THESIS FOR THE DEGREE OF DOCTOR OF PHILOSOPHY
in
THERMO AND FLUID DYNAMICS

Structure of Zero Pressure Gradient High Reynolds Number Turbulent Boundary Layers

MURAT TUTKUN

Division of Fluid Dynamics

Department of Applied Mechanics

CHALMERS UNIVERSITY OF TECHNOLOGY

Göteborg, Sweden, 2008

Structure of Zero Pressure Gradient High Reynolds Number Turbulent Boundary Layers
MURAT TUTKUN

© MURAT TUTKUN, 2008

Doktorsavhandling vid Chalmers tekniska högskola
ISBN: 978-91-7385-166-4
ISSN: 0346-718X
Ny serie nr: 2847

Division of Fluid Dynamics
Department of Applied Mechanics
Chalmers University of Technology
SE-412 96 Göteborg
Sweden
Telephone +46 31 772 1000

Printed at Chalmers Reproservice
Göteborg, Sweden 2008

Structure of Zero Pressure Gradient High Reynolds Number Turbulent Boundary Layers

by

Murat Tutkun
murat.tutkun@chalmers.se
Chalmers University of Technology
Department of Applied Mechanics, Division Fluid Dynamics
SE-412 96 Göteborg, Sweden

Thesis supervisor: Professor William K. George

Abstract

This thesis presents part of the large research program funded by the European Commission called *Wallturb: A European synergy for the assessment of wall turbulence*. The main aim of this research program is to create new experimental and numerical databases on the characteristics of turbulent wall-bounded flows, especially turbulent boundary layers. The goal is that these databases will be used to gain more insight into the physical mechanisms governing the dynamics of these flows. This knowledge is deemed essential for the future development of efficient and physical turbulence modeling strategies, which are in turn crucial to aircraft and other industries for sustainable development, especially under the pressure of high oil prices and operational costs.

The signature experiment of Wallturb was the multi-investigator, multi-system, multi-point investigation carried out in the 20m test section of the boundary layer research facility at LML Lille, France in 2006. This thesis is focused primarily on the part of that investigation which utilized the 143 probe hot-wire array belonging to the Turbulence Research Laboratory of Chalmers, and only on the two zero-pressure gradient boundary layer experiments at Re_θ of 9800 and 19 100.

A new hot-wire calibration method was developed and utilized for this investigation. The method is based on a polynomial curve fitting approximation which expresses the instantaneous velocity as a function of instantaneous voltage. The results showed that even a second order polynomial approximation yields very good agreement between the measured profiles (or computed profiles after the calibration) and the reference profiles used in the calibration. The method also provides an opportunity to do the calibration on the fly as long as the convergence of the high order voltage statistics can be satisfied.

The large scale motions of the turbulence were studied in detail using two-dimensional two-point cross-correlations maps on different planes within the measurement domain. It was observed that the elongated correlations exist at every wall-normal position above the buffer layer. These elongated structures were relatively more significant in the log layer.

The investigation using the proper orthogonal decomposition showed that the POD (in conjunction with Fourier analysis in the statistically homogeneous and stationary directions) can effectively represent the total kinetic energy with a small number of modes. At both Reynolds numbers, it was possible to recover almost 90% of the total turbulence kinetic energy within the entire boundary layer with only four POD modes. The reconstructed velocity fluctuations on the spanwise-wall-normal plane show how organized motions of turbulence with significant amounts of energy interact with each other across the boundary layer. It was also possible to observe the interaction between the inner and outer layers of turbulence using these reconstructed velocity fields.

Keywords: Turbulent boundary layers, high Reynolds number, zero pressure gradient, wind tunnel, hot-wire, calibration, large scale structures, two-point correlations, cross-correlations, proper orthogonal decomposition, Fourier decomposition.

List of Publications

Publications from the thesis:

- M. TUTKUN, W. K. GEORGE, J. M. FOUCAUT, S. COUDERT, M. STANISLAS and J. DELVILLE, In Situ Calibration of Hot-Wire Probes in Turbulent Flows, *Experiments in Fluids*, (under review), 2008.
- M. TUTKUN, W. K. GEORGE, J. DELVILLE, J. M. FOUCAUT, S. COUDERT and M. STANISLAS, Space-Time Correlations in a High Reynolds Number Turbulent Boundary Layer, *Journal of Turbulence*, (to be submitted), 2008.
- M. TUTKUN, W. K. GEORGE, J. DELVILLE, J. M. FOUCAUT, S. COUDERT and M. STANISLAS, Space-Time Correlations from a 143 Hot-Wire Rake in a High Reynolds Number Turbulent Boundary Layer, *AIAA-Paper: 2008-4239, 5th AIAA Theoretical Fluid Mechanics Conference*, Seattle, Washington, USA, June 2008.
- M. TUTKUN, W. K. GEORGE, J. DELVILLE , J. M. FOUCAUT, S. COUDERT AND M. STANISLAS, Cross-Spectral Analysis of Cross-Plane Data from 143 Hot-Wires in Zero-Pressure Gradient Turbulent Boundary Layer at $Re_\theta = 9800$ and 19,100, *Bulletin of the American Physical Society, 60th Annual Meeting of the APS Division of Fluid Dynamics*, Vol. 52, No. 17, pp. 23, November 2007.
- M. TUTKUN, P. B.V. JOHANSSON, W. K. GEORGE, J. KOSTAS, S. COUDERT, J. M. FOUCAUT, M. STANISLAS, C. FOURMENT and J. DELVILLE, Highly Time- and Space-Resolved Experiments on a High Reynolds Number Turbulent Boundary Layer, *ADVANCES IN TURBULENCE XI*, Springer Proceedings in Physics 117, Springer, Heidelberg, Editors: J. M. L. M. Palma and A.Silva Lopes, pp. 346-348, 2007.
- J. DELVILLE, C. FOURMENT, M. TUTKUN, P. B.V. JOHANSSON, W. K. GEORGE, J. KOSTAS, S. COUDERT, J. M. FOUCAUT and M. STANISLAS, High Reynolds Number Flat Plate Turbulent Boundary Layer Experiments Using a Hot-Wire Rake Synchronized with Stereo PIV, *Proceedings of the 5th International Symposium on Turbulence and Shear Flow Phenomena*, Vol. 1, pp. 23-28, TU Munich, 27-29 August 2007.
- M. TUTKUN, P. B.V. JOHANSSON, W. K. GEORGE, M. STANISLAS, J. M. FOUCAUT, J. KOSTAS, S. COUDERT and J. DELVILLE, Zero Pressure Gradient Flat Plate Boundary Layer Experiments Using Synchronized PIV and a Hot Wire Anemometry Rake, *Bulletin of the American Physical Society, 59th Annual Meeting of the APS Division of Fluid Dynamics*, Vol. 51, No. 9, pp. 207, November 2006.

Other publications during the Ph.D. study relevant to the thesis:

- M. TUTKUN, P. B.V. JOHANSSON and W. K. GEORGE, Three-Component Vectorial Proper Orthogonal Decomposition of Axisymmetric Wake behind a Disk, *AIAA Journal*, Vol. 46, No. 5, pp. 1118-1134, 2008.
- M. TUTKUN, P. B.V. JOHANSSON and B. A. P. REIF, Visualization and Measurement of Flow over Cylindrical Surface with a Bump, *AIAA Journal*, Vol. 45, No. 7, pp. 1763-1170, 2007.
- M. TUTKUN, P. B.V. JOHANSSON and W. K. GEORGE, Azimuthal Velocity Correlations in an Axisymmetric Far Wake, *ADVANCES IN TURBULENCE XI*, Springer Proceedings in Physics 117, Springer, Heidelberg , Editors: J. M. L. M. Palma and A.Silva Lopes, pp. 541-543, 2007.
- M. TUTKUN, M. WÄNSTRÖM and W. K. GEORGE, Comparison of the Turbulence Structure in Fully Developed Wakes and Jets, *AIAC Paper: 2007-018, Proceedings of the 4th Ankara International Aerospace Conference*, Middle East Technical University, Ankara, Turkey, 10-12 September, 2007.
- M. TUTKUN, Wind Tunnel Studies of Turbulent Wakes, *Thesis for Licentiate in Engineering*, No 2006:14, Chalmers University of Technology, Göteborg, Sweden, 2006.
- M. TUTKUN, P. B.V. JOHANSSON and W. K. GEORGE, Three-Component POD of an Axisymmetric Wake Behind a Disk, *AIAA-2006-3300, 36th AIAA Fluid Dynamics Conference and Exhibit*, June 5-8, San Francisco, California, USA.
- M. TUTKUN, P. B.V. JOHANSSON and B. A. P. REIF, Flow Visualization, Surface Pressure and Velocity Measurements on a Cylindrical Surface with a Bump. *AIAA-2006-3140, 36th AIAA Fluid Dynamics Conference and Exhibit*, June 5-8, San Francisco, California, USA.
- M. TUTKUN and P. B.V. JOHANSSON, Three-Component POD of an Axisymmetric Wake behind a Disk, *Bulletin of the American Physical Society, 58th Annual Meeting of the APS Division of Fluid Dynamics*, Vol. 50, No. 9, pp. 55, November 2005.

Publications in which M. Tutkun is not the main contributor:

- S. COUDERT, J. M. FOUCAUT, J. KOSTAS, M. STANISLAS, P. BRAUD, C. FOURMENT, J. DELVILLE, M. TUTKUN, F. MEHDI, P. B.V. JOHANSSON and W. K. GEORGE, Double Large Field Stereoscopic PIV in a High Reynolds Number Turbulent Boundary Layer, *Experiments in Fluids* (under review), 2008.
- J. M. FOUCAUT, S. COUDERT, J. KOSTAS, M. STANISLAS, P. BRAUD, C. FOURMENT, J. DELVILLE, M. TUTKUN, F. MEHDI, P. B.V. JOHANSSON and W. K. GEORGE, Study of the Unsteady Aspects of Turbulence in the Near Wall Region of a Boundary Layer Using High Speed SPIV, *Proceedings of 7th International Symposium of Particle Image Velocimetry*, University La Sapienza, Roma, Italy, 11-14 September, 2007.
- P. B.V. JOHANSSON, M. TUTKUN, W. K. GEORGE, M. STANISLAS, J. M. FOUCAUT, J. KOSTAS, S. COUDERT and J. DELVILLE, Adverse Pressure Gradient Boundary Layer Experiments Using Synchronized PIV and a Hot Wire Anemometry Rake, *Bulletin of the American Physical Society, 59th Annual Meeting of the APS Division of Fluid Dynamics*, Vol. 51, No. 9, pp. 207-208, November 2006.

Acknowledgments

I feel myself lucky that I have been surrounded by people who were willing to help, share and support each other. I do not think that I could have managed to finish this thesis and accomplish all the things I have done in past four years without them.

First of all, I would like to express my gratitude to Professor William K. George. I feel myself privileged to have had the chance to meet, work and be friends with him. His enthusiasm, his inspiration, his motivation and his encouragement certainly made this period of my life unique. I appreciate his efforts at trying to provide the best of everything for his students. It is a very nice feeling to be a part of the TRL family established by him over the years.

I would also like to thank my co-supervisor Dr. Peter B. V. Johansson (now at Volvo Aero Corporation) for his help over the years. It was a great experience to stay together with him in France while performing the experiments, which are partly described in this thesis. I appreciate all the time and effort he put into these experiments. I think these experiments could have never been realized without him. His reading my thesis and correcting it right at the very end, just before the submission, is perhaps appreciated the most.

I owe my most sincere gratitude to Dr. Bjørn Anders Pettersson Reif (of FFI) for all his help, time and friendship. He managed to rescue me at the most depressing moments of my Ph.D. studies at Chalmers. His efforts at providing me the best possible working environment at FFI deserve special thanks. He certainly made me and my family feel welcome to Norway. I very much appreciate all the nice things that happened in the last year because of his efforts.

Most importantly, I would like to thank every member of the Wallturb consortium. Special thanks to Michel Stanislas, Jöel Delville, Jean-Marc Foucaut, Sebastien Coudert, Jean-Philippe Laval for all their help during the experiments, and later in the post-processing phase.

I would like to thank especially two of my best friends: Lars-Uno Axelsson and Carlos Arroyo. I enjoyed all the moments we shared over the last six years (including our time as students in the International Turbulence masters program). I also wish to thank Professor T. Gunnar Johansson, Maja Wänström and Abolfazl Shiri for many useful discussions and the nice company. Faraz Mehdi’s help during the LML experiments is very much appreciated.

I would like to thank everybody in my group at FFI, Norway; especially Øyvind Andreassen, Carl-Erik Wasberg and Thomas Elboth for the useful discussions, great company and for helping me solve my daily life practical problems. Also I should not forget Thor Gjesdal, Anders Helgland, Mikael Mortenssen, for all their help and interest. And many thanks to Ronny Horgen from IT-Vakta of FFI for solving all my problems related to the computing system at FFI; otherwise I could not have finished this thesis on-time.

I wish to thank Lars Jernqvist of Chalmers for his help in the laboratory. His motivation and hardworking personality together with his positive attitude were certainly a source of inspiration. Many thanks also to Ulla Lindberg Thieme for helping me out with all sorts of paperwork; but especially, for her smiling face while doing them – it was appreciated a lot.

Meeting with Professor Jonathan Naughton at the beginning of my Ph.D. studies and sharing an office with him were great. As a new Ph.D. student, first I learned a lot from him, second he conveyed his experience in life and work to me. It still helps me to find my direction when needed.

Dr. Brian Brzek certainly deserves many thanks for his friendship and many interesting discussions. Chatting online was used to be a part of our daily life for some years. I would also like to acknowledge the useful discussions on the POD I had with Dr. Vibhav Durgesh.

I would like to express my appreciation Hasan Demirtaş and his family for their friendship during my years at Chalmers.

The person to whom I am the most grateful is my wife, Ayşegül. First of all I would like to thank her for not divorcing me in this past four years. :) I appreciate her unconditional support and love in every aspect of my life. Without her support I do not think I could have succeeded in this. I also want to thank my son for all the fun he has brought into our family. I am grateful to him because of the understanding he showed during the final phase of my Ph.D. studies. I would like to dedicate this thesis to my wife Ayşegül and our son Subutay Usberk. I love you both!

I acknowledge the partial support from the Center of Excellence grant from the Norwegian Research Council to Center for Biomedical Computing.
This work has been performed under the WALLTURB project. WALLTURB (A European synergy for the assessment of wall turbulence) is funded by the CEC under the 6th framework program (CONTRACT No: AST4-CT-2005-516008).

September 4th, 2008
Göteborg, Sweden

Contents

List of Figures

List of Tables

Chapter 1

Introduction

Turbulent boundary layers represent one of the most important fluid flow problems. A boundary layer is the thin layer of fluid closest to the wall when a flow develops over surfaces. It is in this layer that a flow is brought to rest by viscous stresses from its speed in the freestream. Most boundary layers of interest are turbulent. This is mainly because a great portion of industrial flow related problems involve turbulent boundary layers (e.g., the flow over wings and bodies, the flow inside pipes and ducts). Boundary layers are both fundamentally and economically very important, because the thin layer turbulence is greatly responsible for the skin friction resistance of bodies.

1.1 Historical Overview

The turbulent boundary layer idea dates back to the beginning of 20th century, when Prandtl realized that the necessity of a viscosity-dominated thin layer of flow in the vicinity of surfaces. This thin region turned out to be governed by a separate length scale, which characterized changes in the wall-normal direction. This length scale is the boundary layer thickness. Research has been conducted for almost a century on laminar boundary layers. However, at high Reynolds number the viscous forces are not large enough to damp the disturbances, with the result that the flow becomes turbulent (after a transient regime called transition).

Today, most of the industrially important boundary layer problems are high Reynolds number flows and therefore turbulent. The turbulent boundary layer problem has proven to be quite impossible to tackle with simple methodologies. Dependence on the boundary and initial conditions increases the level of complexity. Contrary to the laminar boundary layer, the equations in the turbulent case are not closed. The random character of turbulence makes the problem even more difficult, so that we have to rely on statistical approximations and experimental results.

One of the great interests in turbulent boundary layer research is to find similarity solutions, which produce similar profiles for statistical quantities of turbulent boundary layers, regardless of the external conditions like freestream velocity, development length, boundary layer thickness, surface friction force and so forth. This is especially important because most of turbulence modeling methodologies in computational fluid dynamics are based on assuming similarity solutions. Unfortunately, these approaches have not managed to converge, and remain the subject of great debate. The recent collections of papers by Luciano Castillo (AIAA Journal, Vol 44, 2006) and Beverley J. McKeon (Philosophical Transactions of the Royal Society A, Vol 365, 2007) provide the current state of the knowledge in almost all aspects of canonical turbulent boundary layers. In addition to this, recent reviews first by George (2006) on the scaling issues of boundary layer turbulence and second by Adrian (2007) on the organized motions in wall bounded flows briefly describe evolution of ideas, new findings and possible new directions in wall bounded turbulence research. These volumes and review papers cover all of the recent important contributions in the field with extensive review of literature. Therefore, there will be no attempt made herein to repeat the content of these volumes and papers.

1.2 Turbulence Structure

The large scale motions in turbulent flows have received much attention since Townsend's "large eddy" hypothesis (see Townsend (1976)). These structures were first inferred from his observations of the long tails of the correlation functions of the streamwise velocity fluctuations. Townsend regarded these motions as "inactive" and thought them to be dynamically passive structures. Obvious features of these large scales can be observed by eye in nature and visualized in laboratory environments. Even though quantifying these structured large scale motions, the so-called coherent structures, has proven to be quite difficult, it is now widely realized that these organized motions are actually dynamically important and influence physical processes within the turbulent flows. Examples include the transport of scalars and momentum, turbulent mixing, heat transfer, aerodynamic noise, drag, flow-induced vibration, etc.

The most important aspects of large scale motions in turbulent boundary layers were first documented by Blackwelder & Kovaszny (1972), who suggested they made contributions to the turbulence kinetic energy of 50%, and as much as 80% of the Reynolds shear stress. These large scale motions can range from one boundary layer thickness, δ, to the scales on the order of ten boundary layer thicknesses, or more. Some of the suggested coherent and energetic structures are, for example, low and high momentum streaks, bulges, hairpins, quasi-streamwise vortices, and elongated structures in the log-layer, and even in the wake region of the boundary layer.

1.3 The POD

Lumley (1967) introduced the proper orthogonal decomposition (POD) into the field of turbulence for the purpose of identifying and studying the dynamics of the large scale energy containing features of turbulent flows with finite total energy. The POD provides an optimum deterministic description of the field, the so-called POD eigenvalues and eigenfunctions. These are the solutions obtained by seeking the largest projection onto the stochastic velocity field of turbulence in a mean square sense. Maximization of the projection results in an integral value problem (Fredholm integral equation of the second kind) for which the kernel is the two-point cross-correlations tensor of the stochastic velocity field. The POD has also been found to be very efficient at extracting the most energetic modes of the flow and ordering them according to their energy content.

Even though the POD was introduced more than four decades ago as an optimal and mathematical way of breaking the turbulence scales apart, utilization of the method took some time, mainly due to difficulties associated with the measurement and computation of the two-point cross-correlations tensor. As pointed out by George (1988), the POD needs sufficient information on the two-point cross-correlation tensor so that a complete space-time realization of the turbulence velocity field can be obtained. Computation of the cross-correlation tensor from the measured velocities is also difficult in terms of computing power and speed capabilities.

The first experimental work on wall-bounded flows that utilized the POD was carried out in a turbulent pipe flow in glycerin using hot-film measurement techniques (Bakewell & Lumley

(1967)). They used measurements along a radial traverse inside of $y^+ = 40$. This was followed more than a decade later by the more ambitious experiment of Herzog (1986), who used split-film probes and measured the correlations in a plane transverse to the flow. Almost concurrently, Moin & Moser (1989) applied the POD to a database created by the direct numerical simulation (DNS) of a low Reynolds number turbulent channel flow, and extracted the most energetic characteristics scales of turbulence. With the advent of hardware and software developments, particle image velocimetry (PIV), which provides three-dimensional velocity information on a plane, has recently become a very useful tool in measurements of the two-point cross-correlation with very high spatial resolution. These have been employed by Liu *et al.* (1994, 2001) in a channel flow experiment to produce data sufficient for performing POD analysis. Numerical studies which can be found in the literature also primarily utilize channel flow simulations. There has been no research program carried out prior to the one reported herein for analyzing developing turbulent boundary layers using the powerful features of the POD. In this sense, the work described in this dissertation is unique, and the first application in this direction.

1.4 The scope of this thesis

This thesis is a part of the large research program funded by the European Commission called *Wallturb: A European synergy for the assessment of wall turbulence*. The main aim of this research program is to create new experimental and numerical databases on the characteristics of the turbulent wall-bounded flows, especially turbulent boundary layers. The hope is that these databases will be used to gain more insight into the physical mechanisms governing the dynamics of these flows. This knowledge is deemed essential for the future development of efficient and physical turbulence modeling strategies, which are in turn crucial to aircraft and other industries for sustainable development, especially under the pressure of high oil prices and operational costs.

The signature experiment of Wallturb was the multi-investigator, multi-system, multi-point investigation carried out in the 20m test section of the boundary layer research facility at LML Lille, France in 2006. This thesis is focused primarily on the part of that investigation which utilized the 143 probe hot-wire array belonging to the Turbulence Research Laboratory of Chalmers.

The presentation of the thesis is as follows: The experimental setup and measurement details are described in Chapter 2. The calibration method developed in the course of this study is introduced and discussed in Chapter 3. Chapter 4 presents the single point velocity statistics and spectra. The results of a two-point cross-correlation analysis, together with the integral length and time scales, are presented in Chapter 5. The theory of proper orthogonal decomposition (POD) and the results obtained using the POD theory will be described and discussed in Chapters 6 and 7 respectively. Finally, in the last chapter, Chapter 8, the results will be summarized and some important findings will be emphasized. A detailed literature review and current state of knowledge together with historical development of the relevant ideas are presented at the beginning of each chapter separately.

Chapter 2

Experimental Setup

Two high Reynolds number zero pressure gradient turbulent boundary layer experiments were performed in the large LML (Laboratoire de Mécanique de Lille) wind tunnel in the course of this study. The freestream velocities during the experiments were 10 and 5 m s^{-1} resulting in Reynolds number based on the momentum thickness of 19 100 and 9800 respectively. The boundary layers were measured using a synchronized system of stereo PIVs and a hot-wire rake of 143 probes to be able to obtain both spatial and time history of the turbulent velocity fields. In this thesis, only the hot-wire rake data have been studied even though the complete description of the set-up is described here. The experimental setup and details of the equipment are detailed in the following sections. Most of the information given about the anemometers and data acquisition in this chapter have been compiled from a technical report written for the Wallturb project (c.f., Johansson (2007)).

2.1 Large LML Boundary Layer Wind Tunnel

As it can be seen from the schematic of the wind tunnel in figure 2.1, the LML boundary layer facility is a closed circuit wind tunnel whose dimensions are 21.6 m in length, 2 m in width and 1 m in height. The last part of the wind tunnel, denoted by 7 in the schematic, was equipped with transparent glass walls to be able to provide an optical access for measurements using laser based methods. The opening following the honeycombs in the end of the test section was closed during the measurements to be able to control the concentration level of the seeding particles in the wind tunnel more uniformly. The maximum achievable freestream velocity for this wind tunnel is about 10.5 m s^{-1} $\pm 1\%$. The very long test section provides a high Reynolds number turbulent boundary layer about Re_θ of 20 600. The boundary layer thickness at the end of the test section is about 0.3 m at all freestream velocities. The flow parameters which can be obtained in the large LML wind tunnel at different freestream velocities are compiled in table 2.1.

A Pitot tube with a Furness micromanometer is used to monitor the freestream velocity of the wind tunnel. The tunnel's constant freestream velocity can be regulated within 0.25%. The tunnel has a air/water heat exchanger in the end of the return duct just before the plenum chamber. The heat exchanger works as a temperature control unit which provides a uniform flow temperature within an accuracy of ±0.3°C.

The boundary layer on the bottom wall in the entrance of the test section is tripped using some three-dimensional roughness elements to increase the thickness of turbulent boundary layer. Carlier & Stanislas (2005) observed no effect in the turbulence statistics of the bound-

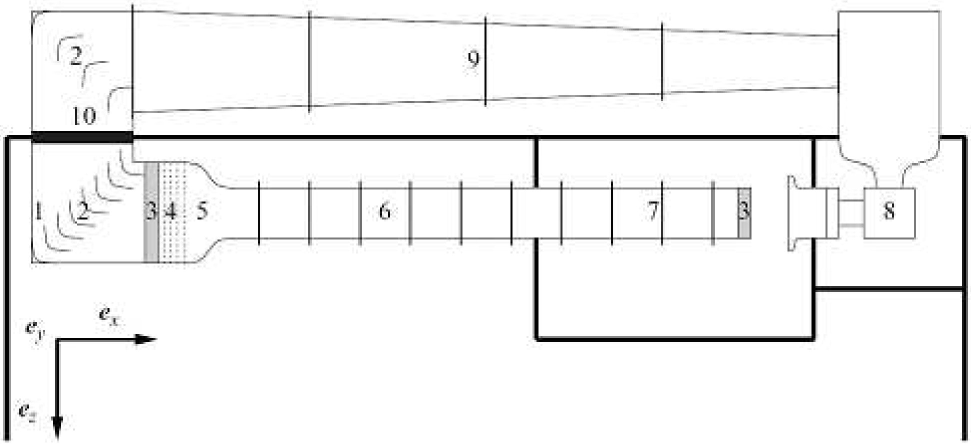

Figure 2.1: Schematic of the LML wind tunnel: 1, plenum chamber; 2, guide vanes; 3, honeycomb; 4, grids; 5, contraction; 6, turbulent boundary layer developing zone; 7, testing zone of wind tunnel; 8, fan and motor; 9, return duct; 10, heat exchanger (air/water).

ary layer due to tripping in the entrance. As mentioned earlier the thickness of the boundary layer at the measurement location which was 18 m downstream of the test section entrance is approximately 0.3 m at both Reynolds numbers tested in this study.

The cross-section area of the tunnel is constant throughout the test section. Previously, Carlier & Stanislas (2005) studied possible effects of having constant cross-section area such as the inhomogeneity in the spanwise direction due to corner vortices developing along the tunnel and the pressure gradient in the streamwise directions. Careful investigations on the turbulence statistics in the spanwise direction revealed that there is no effects on the homogeneity for ±0.35 m in spanwise direction around the symmetry line. In addition to this, the scaled pressure gradients in wall units were found to be very small in comparison in other terms in the streamwise component of the momentum equation and concluded to be negligible.

U_∞ ($\mathrm{m\,s^{-1}}$)	$\partial P/\partial x$ ($\mathrm{Pa\,m^{-1}}$)	$u_\star$ ($\mathrm{m\,s^{-1}}$)	$\nu/u_\star$ (μm)	δ (m)	δ^+ ($-$)	θ (m)	Re_θ ($-$)	ℓ^+ ($-$)	d^+ ($-$)
3	-0.057	0.115	136	0.35	1500	0.041	8171	4	0.02
5	-0.134	0.183	81	0.32	4000	0.035	11 454	6	0.03
7	-0.240	0.249	59	0.30	5100	0.032	14 500	8.5	0.04
10	-0.502	0.354	43	0.30	7000	0.031	20 800	12	0.06

Table 2.1: Characteristics of LML boundary layer wind tunnel as documented by Stanislas *et al.* (2008).

2.2 Hot-Wire Rake of 143 Single-Wire Probes

A hot-wire rake of 143 single wire probes was used in this study to be able to obtain both spatial and temporal information about the turbulent boundary layer simultaneously. The rake, manufactured by Laboratoire d'Etudes Aérodynamiques (LEA), Poitiers, France, covered an area of approximately 30×30 cm^2. All the probes were distributed on an array in a plane normal to the flow as shown in figure 2.2. The rake was comprised of 13 vertical combs staggered in the spanwise direction, and each vertical comb carried 9 single wire hot-wire probes and one

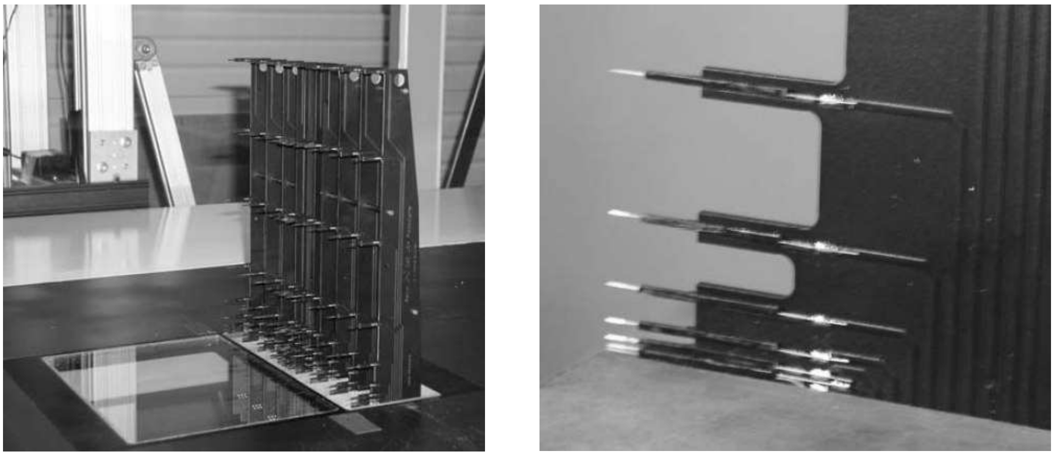

(a) Hot-wire rake in place in the wind tunnel

(b) Close-up of one of the comb at the wall

Figure 2.2: Hot-wire rake in place in the LML wind tunnel and close-up of one of the combs at the wall.

double probe with two single wire sensors spaced logarithmically from wall to freestream in the wall-normal direction. The double probe was at the first wall-normal position very close to the wall and was because of the limited spacing available. The sensing wires of the probes were 0.5 mm in length and 0.25 μm in diameter (see table 2.1 for wire length and diameter as wall units, ℓ^+ and d^+ respectively). The vertical combs were made of double sided conventional circuit boards. The thickness of the circuit boards was 1.8 mm. This method for constructing hot-wire rakes of many probes were previously used for multi-point measurement in turbulent flows by Glauser (1987), Delville (1994) and Delville *et al.* (1999). Special connectors were used between the combs and 5 m long coaxial cables connecting to the hot-wire anemometers. Special attention was given to the comb end of the coaxial cables to prevent any interference with each other.

The vertical combs were distributed symmetrically around the center comb located in the middle of spanwise width of the wind tunnel, corresponding to z=0. Detailed drawings of the hot-wire rake are given in appendix A. The symmetric pairs of the vertical combs were distributed at ±4 mm, ±12 mm, ±28 mm, ±60 mm, ±100 mm and ±140 mm. The logarithmic placing of each probe on the vertical combs from the wall to the freestream was 0.3 mm (corresponds to y^+ of 3.75 and 7 for low and high Reynolds numbers, respectively), 0.9 mm, 2.1 mm, 4.5 mm, 9.3 mm, 18.9 mm, 38.1 mm, 76.5 mm, 153.3 mm, 230.1 and 306.9 mm. These coordinates in both spanwise and wall-normal directions are the coordinates used for mechanical design of the rake. There were some manufacturing imperfections at the probe locations particularly in the wall-normal directions in the vicinity of the wall. The precise coordinates of the probes were found as following: First, the tips of the probes were illuminated with a laser sheet, then a picture of it was taken using a high resolution camera, and finally location of each probe with respect to the wall was found. The uncertainty in finding the precise location of the probes was 0.03 mm with 95% confidence level.

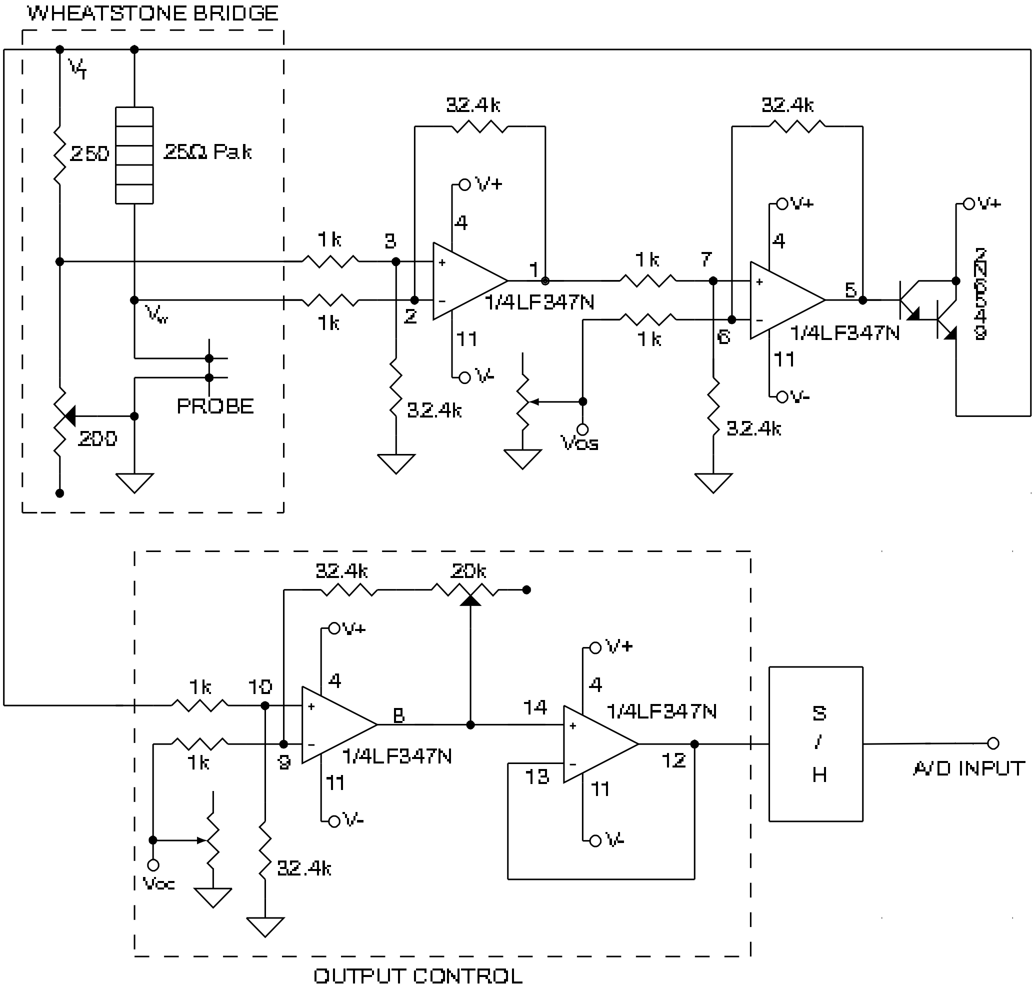

Figure 2.3: Anemometer circuit diagram

2.3 Hot-Wire Anemometers

An in-house developed multiple channel constant temperature hot-wire anemometry system was used for the measurements. Each channel comprised of a Wheatstone bridge, output and sample-and-hold controls. The anemometer circuitry as shown in figure 2.3 was based on simple and stable design given by Perry (1982) with the addition of output signal conditioning part. The system was designed, manufactured and tested in the facilities of the Turbulence Research Laboratory (TRL) in its previous incarnation at the State University of New York at Buffalo, see Woodward (2001). Previously, Citriniti *et al.* (1994), Citriniti (1996), Jung (2001) and Gamard (2002) used and tested the system extensively. As detailed by Woodward *et al.* (2001) the anemometers were capable of measuring the proper spectral statistics with very low noise level better than commercial ones, with no significant thermal drift over time and no cross-talk between the channels. The anemometer system went through a complete overhaul and modification after moving into Sweden in 2001 using some high quality instrumentation amplifiers, frequency compensation and cable inductance compensation. The adaptation to European power grid system was realized by changing the power supplies.

The anemometer system consisted of 144 channels (or anemometers) distributed in 9 racks carrying 16 anemometers on each of them. Every 3 racks, in total 48 anemometers, were powered by a separate power source. Four power supplies for each of these 3 racks were used to operate the anemometers. Two of these four were the main power sources with $+15$ V and -15 V outputs. In addition to these, two smaller power supplies were used with adjustable control output voltages. The second one operated as output offset voltage, V_{oc}, to be able to use maximum range of the A/D converter by tuning the anemometer output voltage.

Setup of the overheat ratio for TRL anemometer system as explained below was different than that for the commercial ones. The overheat ratio is defined as follows:

$$OHR = \frac{R_{wh}}{R_{wc}} \tag{2.1}$$

where R_{wh}, hot resistance, and R_{wc}, cold resistance, represent resistance of the sensor wire at operating and nonoperating temperatures respectively. The cold resistance of the sensor wire is measured before operating the anemometer system, so that the hot resistance of the sensor can be found for the desired overheat ratio using Eq. (2.1). The hot resistance of the wire is set by tuning the adjustable resistance in the Wheatstone bridge once the probe is connected. This is done by monitoring bridge top voltage, V_T, and voltage across the sensor wire, V_w.

Total resistance of the wire, denoted by R_w, can be computed using the measured voltage across the wire as follows:

$$R_w = \frac{V_w}{I_w} \tag{2.2}$$

where I_w is the current passing the sensing wire and $R_w = R_c + R_{wh}$. The current passing the sensing wire is found by measuring the bridge top voltage:

$$I_w = \frac{V_T - V_w}{R_f} \tag{2.3}$$

where R_f is the fixed resistance of 25 Ω in the Wheatstone bridge as shown in figure 2.3. Using the voltage across the wire, the total wire resistance is computed as follows:

$$R_w = \frac{V_w}{V_T - V_w} \times R_f = \frac{V_w}{V_T - V_w} \times 25 \tag{2.4}$$

Therefore, R_w becomes:

$$R_w = R_c + OHR \times R_{wr} \tag{2.5}$$

Combining equations 2.5 and 2.4 results in:

$$\frac{V_w}{V_T} = 1 + \frac{25}{R_c + OHR \times R_{wr}} \tag{2.6}$$

V_T and V_w are measured through the pin holes placed on each anemometer, and desired overheat ratio is achieved by adjusting the voltage ratio in Eq. (2.6) which was computed using the LabView program. An overheat ratio of approximately 1.8 was set for each channel for the experiments carried out in the course of this study.

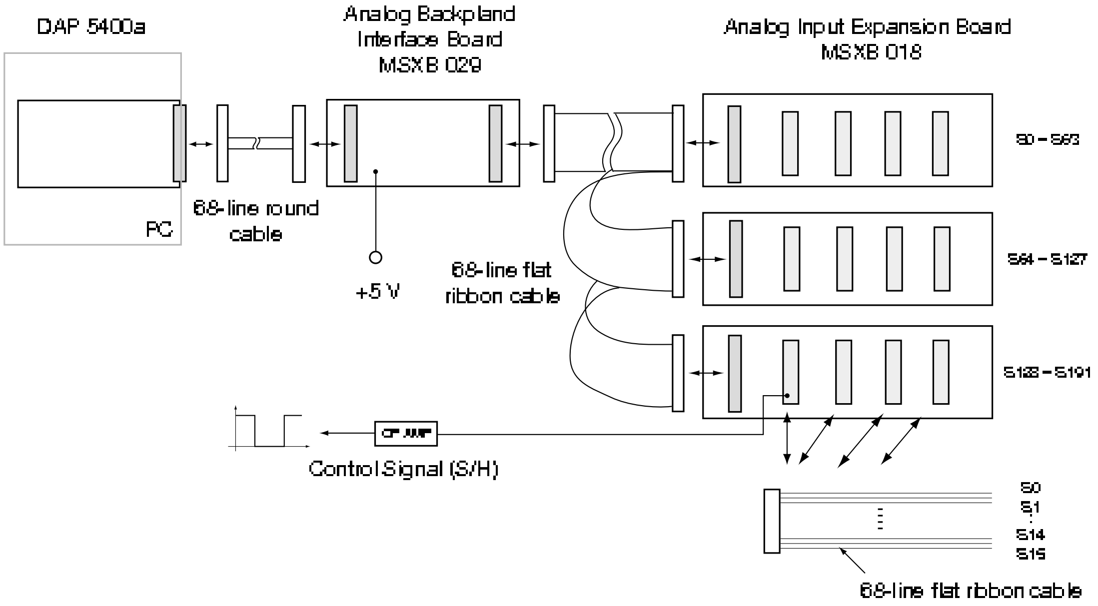

Figure 2.4: DAQ architecture

2.4 Data Acquisition System

Figure 2.4 shows the architecture of the data acquisition system used in the experiments. Data were sampled using a fast A/D converter with an on-board processor and a buffer storing the readings before spooling to the computer disk. A LabView program was developed to be able to control the entire sampling and synchronization processes among the different measurement equipments.

A Microstar Laboratories DAP 5400a processor was used as the data acquisition board. This was an on-board operating system optimized for 32 bit operation in a PC expansion slot. It consisted of an AMD K6$-$III $+$ 400 Mhz CPU with PCI bus interface, 8 separate A/D converters with 14 bits resolution. It provided 20 ns time resolution and simultaneous sample-and-hold at a maximal sampling rate of 1.25×10^6 samples per second per converter with selective input/output range. The DAP 5400a was connected to the analog backplane interface board, MSXB 029, with 68-line round cable to expand the number of channels. Then the system was connected to 3 analog input Microstar Laboratories expansion boards, MSXB 018. The expansion boards were connected to each other by means of 68-line flat ribbon cables. Each expansion board consisted of four 16 channel single-ended connectors, and therefore multiplexed 64 analog inputs. With this architecture it was possible to connect and sample 192 ($=64 \times 3$) channels at a rate of 52 kHz.

In these experiments the hot-wire anemometer output voltages from 143 channels together with tunnel temperature, tunnel dynamic pressure and synchronization signal for the anemometry system and stereo PIV systems were recorded at 30 kHz simultaneously for 6 seconds long blocks. Each anemometer was designed with a sample-and-hold (S/H) amplifier, SHC298, to enable simultaneous sampling at all channels. A 12 bit throughput accuracy was possible for the S/H amplifier with less than 10 μs acquisition time. The wide-band noise level was 10μsV$_{rms}$.

An external clock was used to initialize the sampling and control the sequence of sampling and holding as shown in figure 2.5. The sampling started with the rising front of the control signal which was about 10.2 μs. Due to 30 kHz sampling frequency, the time difference be-

Figure 2.5: Control signal sequence.

tween two successive samples for each channel was 33.3 μs. Therefore, the maximum time for hold phase and conversion was 23.1 μs in total while the control signal was low before the following rising front. As mentioned earlier the fastest sampling rate for Microstar DAP 5400a was 1.25×10^6 samples per second per channel, corresponding 0.8 μs time difference between two successive samples. Since Microstar DAP 5400a has 8 separate A/D converters, the fastest achievable data acquisition for the all channels in the system was $192\times0.8/8=19.2$ μs, meaning 34 kHz maximum sampling frequency for all channels simultaneously. Since only 146 channels sampled simultaneously with the maximum conversion speed of 0.8 μs, total conversion time, or the time between the samples from the first and last channels, was $152\times0.8/8=15.2$ μs.

2.5 Synchronization of Measurement Equipments

An external clock with a special circuitry was designed and used for simultaneous sampling for all the measurement systems employed in the experiments. The signal sequence of the operation can be seen in figure 2.6. The steps of the operation can be detailed as follows:

1. Data acquisition was ready to start on the camera synchronization signal (A) after the laser warm-up signal (B) went low.
2. A trigger signal was sent to initialize the PIV data recordings (C).
3. At the same time as the PIV starting to sample, a sequence was sent to the A/D converter to control hot-wire anemometers for data sampling (D). Every time (D) went high, the A/D converter scanned all the channels and sampled the data.
4. In order to make sure hat all the channels were sampled simultaneously, a positive-edge control signal (E) for the sample-and-hold amplifier was also generated. When the mode control was switched from hold-mode to sample-mode with the positive-edge trigger signal, them sample-and-hold amplifier sampled the data at all the channels simultaneously and held the signal until it switched to the next sample-mode. During the hold-mode (low phase of E), the Microstar DAP 5400a collected the data from the channels, and saved them on the hard disk.

All trigger pulses (C, D and E) have a duration of approximately 10.5 μs. After the current data blocks of 6 seconds was sampled, a re-activation circuit ensured that the system was ready on stand-by and waiting for a new laser warm-up to start sampling of the next data block.

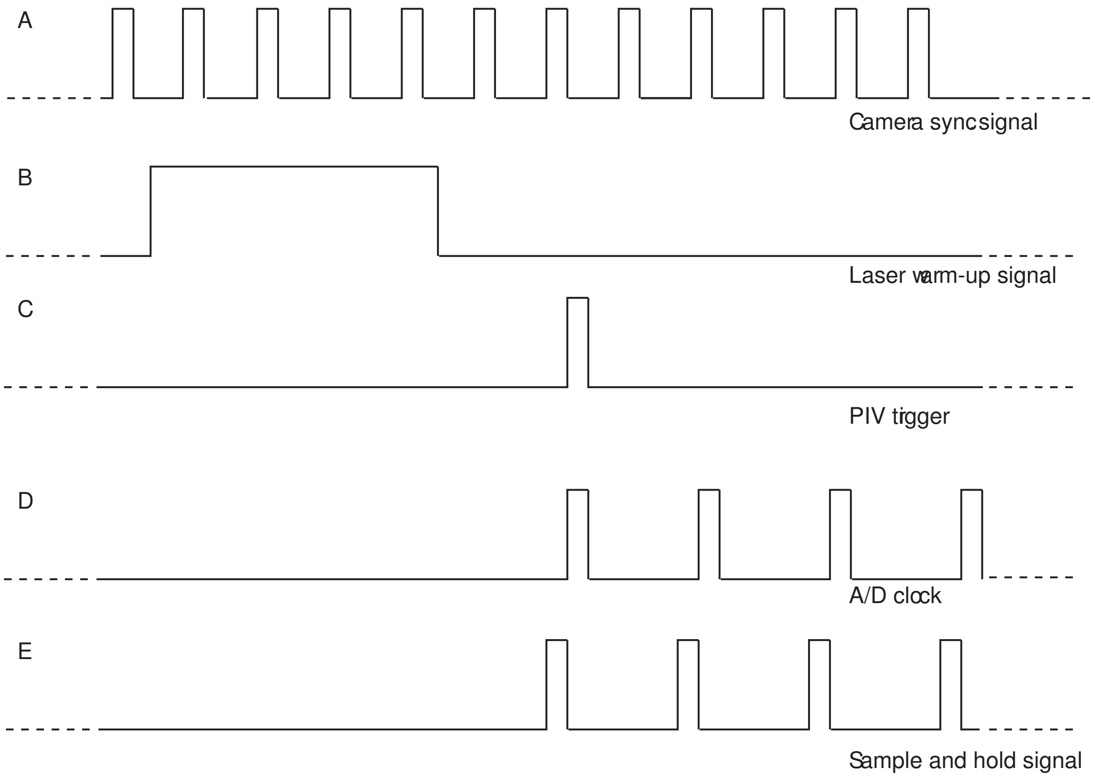

Figure 2.6: Synchronization signal.

2.6 PIV Systems and Experimental Configurations

To be able to extract complete spatial and temporal information on the flow, two different combinations of synchronized PIV and HWR were set up. The first setup (shown in figure 2.7) was comprised of three stereo PIV systems and the hot-wire rake. Two stereo PIV systems were used to record a YZ plane located 1 cm upstream of the hot-wire rake. Each of these two PIV systems covered a field of 30 cm in spanwise direction and 17 cm in wall-normal direction. The total area covered by the PIV systems was 30×32 cm^2 with a small overlap between the two fields. The spatial resolution of each plane was 2 mm, meaning 20 and 40 wall units for Reynolds numbers of 9800 and 19 100, respectively. These two systems used a BMI 2×150 mJ dual cavity Yag Laser and 4 Lavision Image Intense PIV cameras with a CCD of 1376×1024 pixels and a sampling rate of 4 velocity field per second (VF/s). A third stereo PIV system was to record a streamwise-wall-normal (XY) plane in the plane of symmetry ($z=0$). The dimensions of the plane were 10 cm in streamwise direction and 15 cm in wall-normal direction. Twice the spatial resolution for this plane was possible due to a decrease in size of the plane. This plane used a BMI 2×150 mJ dual cavity Yag Laser and 2 Lavision Flowmaster PIV cameras with a CCD of 1280×1024 and a sampling rate of 4 VF/s. Each PIV system recorded 16 samples during each block of hot-wire rake data.

In the second configuration as shown in figure 2.8, one high repetition rate stereo PIV system synchronized with HWR was used in the streamwise-spanwise (XZ) plane to get both the spatial and temporal information in the near-wall region. The fields of view were 6.6×3.4 cm^2 located at y^+ of 50 for the Reynolds numbers of 9800, and 4.2×2.2 cm^2 at y^+ of 100 for the Reynolds number of 19 100. The system was based on a Quantronix dual cavity 2×20 mJ YFL laser and

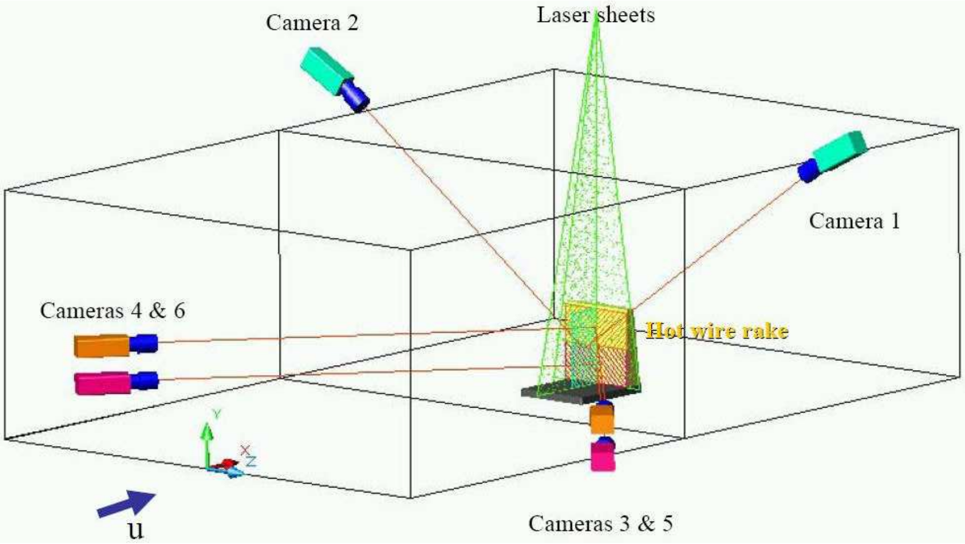

Figure 2.7: Setup 1: Synchronized 3 stereo PIV systems with HWR of 143 probes.

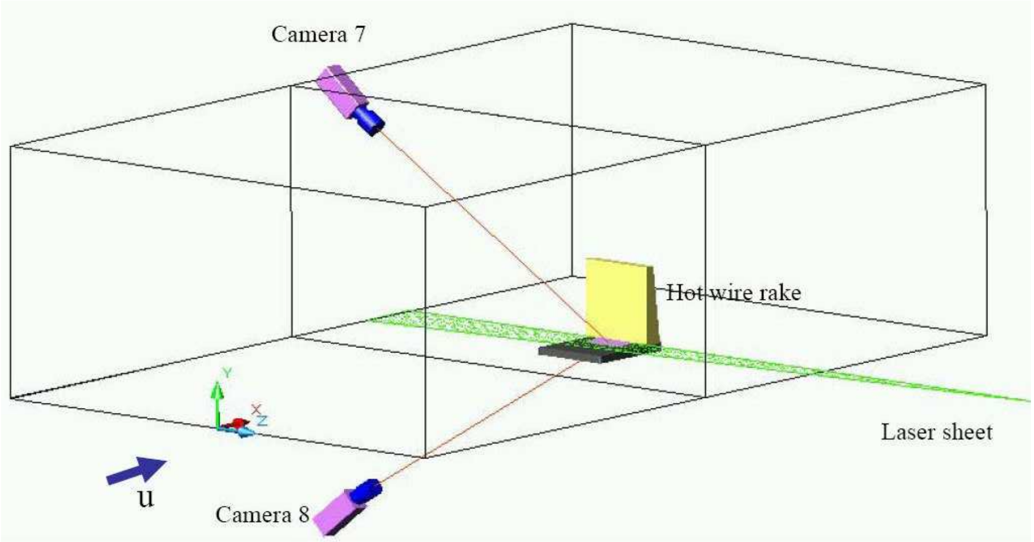

Figure 2.8: Setup 2: Synchronized high repetition stereo PIV system with HWR of 143 probes.

two Vision Research Phantom V9 cameras of 1600×1200 pixels sizing 11.5×11.5 μm^2 each. The operational number of pixels for the experiments were set to 384×592 pixels in the high Reynolds number case and 576×920 pixels in the low Reynolds number case. The sampling frequency of the high repetition PIV system was 3000 VF/s for the high Reynolds number experiment. The sampling frequency was then decreased to 1500 VF/s for the low Reynolds number case. In both cases 40 samples were recorded during each block of hot-wire rake data.

U_∞ (m s^{-1})	Re_θ	Configuration	HWR blocks	PIV records
10	19100	HWR + XY + YZ	600	9600
10	19100	HWR + XZ	1100	1100×40
10	19100	HWR + XZ	1 block of 2.29 s	6880 in 2.29 s
10	19100	HWR	613	0
			Total: 2314	
5	9800	HWR + XY + YZ	600	9600
5	9800	HWR + XZ	1100	1100×40
5	9800	HWR + XZ	1 block of 1.96 s	2943 in 1.96 s
5	9800	HWR	620	0
			Total: 2321	

Table 2.2: Number of synchronized hot-wire rake blocks and PIV recordings collected during the experiments.

2.7 Data Recorded

Table 2.2 summarizes the amount of data recorded during the experiments at the two different Reynolds number with the two different configurations of HWR and stereo PIV systems. For the first setup (figure 2.7), 600 blocks of hot-wire data together with 600×16 velocity fields by the PIV were recorded for both Reynolds numbers. Following this case, 1100 blocks of hot-wire data were recorded with the second setup (e.g., figure 2.8) simultaneously with 1100×40 velocity fields, provided by the high speed stereo PIV system. The same number of blocks of data was collected at both Reynolds numbers in this configuration. In the end one block of synchronized data was recorded by the high speed stereo PIV system with the full memory. This provided 6880 time resolved velocity fields of 2.29 s record length for the high Reynolds number case, and 2943 time resolved fields of 1.96 s record length for the low Reynolds number case. In addition, after completing the synchronized measurements, 613 and 620 blocks of hot-wire data were recorded alone for the high and low Reynolds numbers respectively.

2.8 Seeding Particles

Poly-Ethylene Glycol was used as seeding fluid during the measurements. The size of the particles was of the order of 1 μm. There was no evidence of contamination of the hot-wire sensors during the experiment, nor in the calibration constants, in agreement with the earlier experiments of Buchave (1979), Chatellier & Fitzpatrick (2005) and Ewing *et al.* (2007). Evidence of no contamination can be seen in appendix C.

Chapter 3

Calibration of 143 Hot-Wire Probes *In Situ*

A method for *in situ* calibration of hot-wires in a turbulent flow is presented. The method is particularly convenient (even necessary) for calibrating large probe arrays, like the 143-wire boundary layer probes of the WALLTURB experiment. It is based on polynomial expansion of the velocity statistics in terms of voltage statistics as originally described by George *et al.* (1989). Application of the method requires knowing reference profiles of the mean velocity and higher order central moments (with the array in place) of the turbulent velocity at the probe location at only one freestream velocity. These were obtained in our experiment by a stereo PIV plane just upstream of the probe array. The accuracy of the method is remarkable, even though it is a nonlinear calibration scheme. Both the procedure for implementing the method and sample results are presented in the chapter.

3.1 Introduction

Modern optical measurement techniques (especially stereo PIV) have opened new opportunities for obtaining spatial information about turbulent flows. But in spite of the rapid advance of optical measurement techniques, the hot-wire anemometer is still the first choice of researchers when high frequency response and temporal information on the flow are needed, especially when the turbulence intensities are not too high ($< 30\%$ typically). Our primary interest in WALLTURB has been to combine multi-plane stereo PIV with extensive rakes of hot-wire probes so that temporally resolved hot-wire data can be used to augment and even animate the more slowly sampled spatial and multi-component information from the PIV. Unfortunately the facility being used and the design of the probe array did not allow it to be removed (or at least moved to a region of uniform, low turbulence flow) for the usual external calibration. This chapter discusses one of several challenging aspects of this investigation: how to calibrate the hot-wire rakes *in situ*.

There has been vast amount of research conducted on the basics of the equipment, output data interpretation and calibration since the constant temperature anemometer was introduced into the field in the 1960's (see Perry (1982); Bruun (1995) for excellent reviews). A great deal of attention has naturally been devoted to development of accurate calibration methods of the hot-wire probes. Calibration is particularly important, because the linearization of the output voltages from the anemometers can only be accomplished using coefficients provided by the calibration curves.

The conventional way of calibrating the hot-wire probe sensors requires placing the probes into a laminar flow in a well-controlled laboratory environment; then finding the functional relation between anemometer output voltage and the velocity at the probe location. The reference velocity must be simultaneously measured by an independent device, often by a Pitot-tube in close proximity. This procedure is repeated at different flow velocities and should cover the entire range of velocities (mean and fluctuating) which might occur during the experiment. Depending on the accuracy requirements, there are several alternatives for converting voltages to velocity. Look-up tables are commonly used, but these can be no more accurate than the individual measurements. Significant improvements in accuracy can be obtained by curve-fitting using regression techniques. Common curve fits are variations on King's law (where voltage squared is written as a fractional power of velocity, usually near 1/2) or polynomial curve fits (where the velocity is written as powers of the voltage (usually to 4th order). Since the primary uncertainty in calibration is usually in the velocity and not the voltage, the latter approach is generally more accurate. But none of these calibration schemes work very well if velocity realizations are obtained in the experiment that are outside the range of calibration.

Performing the hot-wire calibration by the conventional methodology is difficult to impossible in some experimental configurations, due to mechanical restrictions, space limitations or simply the absence of a non-turbulent calibration facility. This is especially true when hot-wire rakes of many probes are used for multi-point measurements in a turbulent velocity field. Hot-wire rakes (with up to 139 hot-wires) have been used in axisymmetric mixing layers, planar mixing layers, axisymmetric wakes and axisymmetric jets to be able to extract spatial and temporal information on the turbulent field simultaneously (see Glauser (1987); Delville (1994); Delville *et al.* (1999); Citriniti & George (2000); Jung *et al.* (2004); Johansson & George (2006*a*); Iqbal & Thomas (2007)). All of these applications involved free shear flows, where it was possible to move the hot-wire rakes around and the probes could be calibrated, at least a few at a time, in the laminar flow. For example, Citriniti & George (2000) and Jung *et al.* (2004) divided their rake of 138 probes into five group, fitting each into the laminar calibration jet and performing the calibration of one group at a time.

The situation is more difficult in turbulent boundary layer experiments using the hot-wire rakes of many probes in the wind tunnel, as for example the rake shown in Figure 2.2(a). One of the biggest problem in this case was that it may not be possible to move the rake into the laminar flow which exists outside of the turbulent boundary layer. Nor was it even be possible to traverse rake to a region of the tunnel where the flow was uniform. Therefore, we had no choice but to perform the calibration inside the turbulent flow when the rake is in place.

This problem was first realized by Breuer (1995) and he suggested an *in-situ* calibration method, or the so-called stochastic calibration, using known reference mean velocities measured by an independent device at the probe location. The method is somewhat similar to the quasi-linear hot-wire calibration technique proposed by George *et al.* (1989). It finds a functional relation (polynomial in this case) between the known reference mean velocities and the statistics of the anemometer output voltages including both the mean voltage and the higher order central moments of it. The highest order of voltage statistics needed for calibration depends on the order of polynomial function chosen.

The reference mean velocities (or profiles) in Breuer's method, which are assumed to be known, must have been obtained either in advance before the rake is in place, or from measurements just upstream of the probes when the rake is in place. The former method assumes that the existence of hot-wire probes do not create any blockage on the flow. On the other hand, if the hot-wire rake is comprised of many probes, some blockage to the flow is unavoidable. Therefore calibrating the hot-wire rake against mean velocities obtained in advance before the rake is in place can lead to errors in calibration coefficients due to changes in mean velocity profile created by the rake itself. These errors can be quite significant, especially in the high turbulence and intermittent regions in the flow, because the method forces the coefficients to fit to a different mean velocity distribution than actually exists. In some cases, however, if the blockage is not too severe, the blockage manifests itself as a potential flow disturbance affecting primarily the mean velocity distribution, while leaving the turbulence fluctuations unaffected (at least locally). This can, of course, be justified *a posteriori* by simply comparing the measurements before and after the rake is inserted. Such was the case in our experiments as detailed by Coudert *et al.* (2007). We also developed a simple blockage model based on complex potential for characterizing the effect of the rake on the flow. The blockage model showed that the effect was only potential flow disturbance affecting the mean velocity leaving the turbulence unaffected (see Coudert *et al.* (2007) for further information and complete justification).

In the course of this study, we have developed and performed a new *in situ* hot-wire calibration method using simultaneous particle image velocimetry (PIV) and hot-wire rake measurements. The new method is based on only one single reference freestream velocity at each probe position, together with the higher order voltage statistics computed over the recorded signals at the same location. The proposed calibration finds the best curve fit (in the least-squares sense) to both the mean velocity and central moments of velocity at the probe location.

3.2 The Method and Application

Following George *et al.* (1989), the instantaneous velocity, $\tilde{u}$, can be expressed as a polynomial function of instantaneous voltage, $\tilde{e}$, as follows:

$$\tilde{u} = \sum_{n=0}^{N} a_n \tilde{e}^n \tag{3.1}$$

where N is the order of the polynomial expansion and a_n represents the calibration coefficients. Typically n≤4, but in out experiments n=2 proved to be sufficient. If we set $N = 2$, Eq. (3.1) becomes:

$$\tilde{u} = a_0 + a_1\tilde{e} + a_2\tilde{e}^2 \tag{3.2}$$

Expressing instantaneous quantities as summation of mean and fluctuating parts, the so-called Reynolds decomposition, we obtain following relations: $\tilde{u} = U + u$ and $\tilde{e} = E + e$, where U and E are the ensemble averages of velocity and voltage respectively, and u and e are the fluctuations about the mean values which can be written as: $U = \langle\tilde{u}\rangle$ and $E = \langle\tilde{e}\rangle$. (Note that $\langle\ \rangle$ represents ensemble averaging, and reduces to time averaging in a stationary process by the ergodicity theorem.) Averaging Eq. (3.2) yields the mean velocity equation in terms of voltage statistics:

$$U = a_0 \underbrace{\{1\}}_{\phi_0} + a_1 \underbrace{\{E\}}_{\phi_1} + a_2 \underbrace{\{E^2 + \langle e^2\rangle\}}_{\phi_3} \tag{3.3}$$

Velocity fluctuations about the mean velocity can be obtained by subtracting the mean velocity, Eq. (3.3), from the instantaneous velocity, Eq. (3.2); i.e.,

$$u = a_1 e + a_2\{2Ee + e^2 - \langle e^2\rangle\} \tag{3.4}$$

Second and third order central moments of velocity are given, respectively, by:

$$\begin{aligned}\langle u^2\rangle &= a_1^2\underbrace{\langle e^2\rangle}_{\phi_3}+2a_1a_2\underbrace{\{2E\langle e^2\rangle+\langle e^3\rangle\}}_{\phi_4}\\ &\quad +a_2^2\underbrace{\{4E^2\langle e^2\rangle+4E\langle e^3\rangle+\langle e^4\rangle-\langle e^2\rangle^2\}}_{\phi_5}\end{aligned} \tag{3.5}$$

$$\begin{aligned}\langle u^3\rangle &= a_1^3\underbrace{\langle e^3\rangle}_{\phi_6}+3a_1^2a_2\underbrace{\{2E\langle e^3\rangle+\langle e^4\rangle-\langle e^2\rangle^2\}}_{\phi_7}\\ &\quad +3a_1a_2^2\underbrace{\{4E^2\langle e^3\rangle+4E\langle e^4\rangle-4E\langle e^2\rangle^2+\langle e^5\rangle-2\langle e^3\rangle\langle e^2\rangle\}}_{\phi_8}\\ &\quad +a_2^3\underbrace{\{8E^3\langle e^3\rangle+12E^2\langle e^4\rangle-12E^2\langle e^2\rangle^2+6E\langle e^5\rangle-12E\langle e^3\rangle\langle e^2\rangle+\langle e^6\rangle-3\langle e^4\rangle\langle e^2\rangle+2\langle e^2\rangle^3\}}_{\phi_9}\end{aligned} \tag{3.6}$$

By grouping the right hand side of the Eqs. (3.3), (3.5) and (3.6), we obtain the following nonlinear system of equations:

$$U = a_0\phi_0+a_1\phi_1+a_2\phi_2 \tag{3.7}$$

$$\langle u^2\rangle = a_1^2\phi_3+2a_1a_2\phi_4+a_2^2\phi_5 \tag{3.8}$$

$$\langle u^3\rangle = a_1^3\phi_6+3a_1^2a_2\phi_7+3a_1a_2^2\phi_8+a_2^3\phi_9 \tag{3.9}$$

This nonlinear system of equations can be solved for the calibration coefficients using a nonlinear solver in a least-squares sense. The most important difference calibrating the wire using this method is that the calibration is based on only one freestream velocity. There is no need to change the tunnel (or calibrator) speed and register corresponding output voltages for each calibration point. This method requires two things: (*i*) mean velocity together with the second and third central moment of velocity at the probe location, and (*ii*) central moments of the output voltage of the anemometer, up to sixth order in this case.

High order statistics of the output voltage are crucial to the proposed method, but can be achieved by collecting sufficiently long data using a high resolution analog/digital converter. The highest order of voltage statistics required depends on the order of polynomial fit which is set by Eq. (3.1). Special care has to be taken for the accuracy of the calibration coefficients by ensuring the statistical convergence of high order moments. Care must be taken to insure that clipping of the voltage output by the A/D converter does not affect the higher voltage moments. Thus the probability distribution function and the moment distributions should be carefully examined.

Any nonlinear solver working in a least-squares sense can be used for computing the calibration coefficients. These kind of solvers are already available in some matrix based programs. A Matlab function called ”lsqnonlin” with Levenberg-Marquardt method was used in the present study. Due to nonlinearity in the system of equations, initial conditions to start the computation are important and should be chosen properly.

3.3 Results

To demonstrate the performance of this proposed method, calibrations of single hot-wire probes were performed at two different wind tunnels speeds, 10 m s^{-1} and 5 m s^{-1}, corresponding to

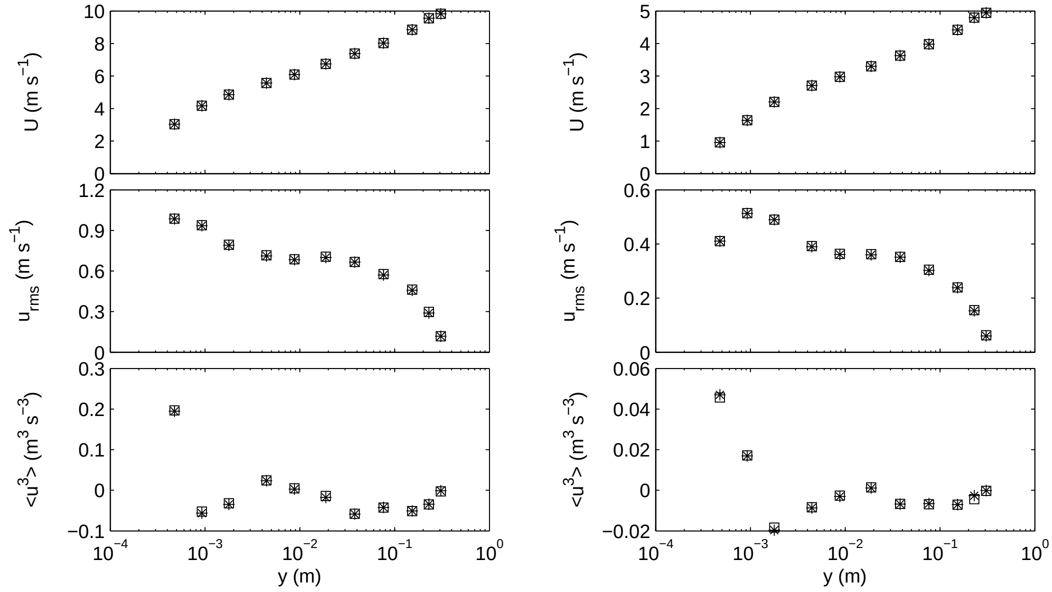

(a) $U_\infty = 10$ m s^{-1}, $Re_\theta = 19100$. (b) $U_\infty = 5$ m s^{-1}, $Re_\theta = 9800$.

Figure 3.1: Comparison between velocity statistics of PIV and hot-wire anemometer measurements. Squares represent the PIV results used for the calibration of probes, and stars represent the results of calibrated probes from the measurement.

Reynolds numbers based on momentum thickness of 19100 and 9800, respectively. The probes were placed in the wall normal direction on a vertical comb made of double-sided circuit board. This vertical comb was a part of an hot-wire rake of 13 vertical comb and 143 probes, in total, distributed on a spanwise-wall-normal plane as shown in Fig 2.2(a).

Simultaneous measurements were performed using both particle image velocimetry (PIV) and hot-wire anemometry rake. PIV planes were normal to the freestream direction and placed 1 cm upstream of the hot-wire rake (see Coudert *et al.* (2007)). High order velocity statistics were achieved by collecting 9600 velocity field at a sampling frequency of 4 velocity field per second (VF s^{-1}). Expressing velocity as a second order polynomial function of voltage required accurate computation of the moments of voltage up to 6th order. The convergence of statistics was ensured by checking the tails of both probability density function (p.d.f.) and p.d.f. multiplied by power of fluctuating voltage from 2nd to 6th, as shown in the following section.

Figure 3.1 compares the reference profiles of mean velocity, root mean square (rms) of velocity fluctuations and third order moments used for the calibration, together with the corresponding profiles based on the results obtained from the hot-wire probes during the experiments. Figures 3.1(a) and 3.1(b) show the profiles for freestream velocity (U_∞) of 10 m s^{-1} and 5 m s^{-1}, respectively. The conversion from voltages to the velocities was done by the coefficient provided the proposed method. As it is seen, there is an excellent agreement between the PIV and hot-wire anemometer results. Further comparison were also performed by checking the fourth order central moment of turbulent velocity at U_∞ of 10 m s^{-1} and 5 m s^{-1}, and are presented in Figs. 3.2(a) and 3.2(b), respectively. The agreement between the PIV data and hot-wire data close to the wall is not as good as the mean velocity, second and third moments

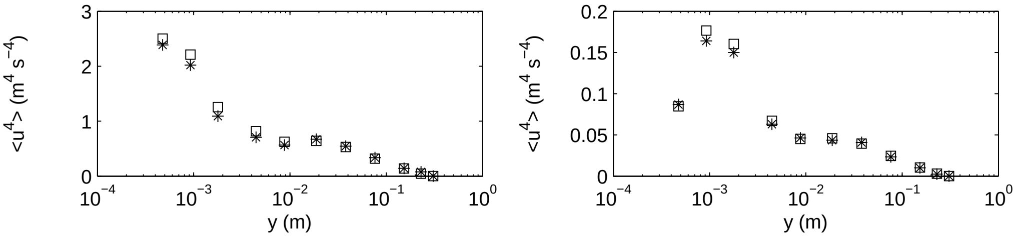

(a) Re_θ =19 100

(b) Re_θ =19 100

Figure 3.2: Fourth moment of velocity field. Squares represent PIV; stars represent hot-wire probes.

shown in figures 3.1(a) and 3.1(b), but these results are mostly due to a convergence problem of the fourth order central moment obtained using the PIV data in the near wall region. To be able to quantify the agreement between the PIV and hot-wire data, computing the relative error was performed for mean and r.m.s. velocity, third and fourth central moments of turbulent velocity using the formula given below:

$$\Upsilon_U = \left| \frac{U_{HW} - U_{PIV}}{U_{PIV}} \right| \tag{3.10}$$

$$\Upsilon_{\sqrt{\langle u^2 \rangle}} = \left| \frac{\sqrt{\langle u^2 \rangle}_{HW} - \sqrt{\langle u^2 \rangle}_{PIV}}{\sqrt{\langle u^2 \rangle}_{PIV}} \right| \tag{3.11}$$

$$\Upsilon_{\langle u^3 \rangle} = \left| \frac{\langle u^3 \rangle_{HW} - \langle u^3 \rangle_{PIV}}{\langle u^3 \rangle_{PIV}} \right| \tag{3.12}$$

$$\Upsilon_{\langle u^4 \rangle} = \left| \frac{\langle u^4 \rangle_{HW} - \langle u^4 \rangle_{PIV}}{\langle u^4 \rangle_{PIV}} \right| \tag{3.13}$$

Computation of the Υ using the calibration based on only one block of data resulted in approximately 1.37×10^{-4} for mean velocities, 0.008 for r.m.s velocities and 0.080 for third moments of the turbulent velocities. Even though the calibration was performed only one block of the data with 180 000 samples, it is very clear that the calibration works accurately with very small errors. The error computed for the fourth central moments was about 0.150, which is higher than the other three moments, however, still small. There are two reasons for relatively higher error in comparison of the fourth order moments; (i) the convergence problem of the PIV data for the fourth moment, (ii) the fourth order moment of turbulent velocity was not included in performing the calibration as it can be seen in Eqs. (3.7), (3.8) and (3.9).

3.4 Accuracy and Applicable Range of the Method

The calibration method developed in the course of this study requires up to 6th order central moment of output voltage read through the anemometers. The convergence of the statistics is necessary for successful implementation to be able to obtain high accuracy in the calibrations. As it can be seen in Eqs. (3.3)-(3.6), the higher order central moments of the voltage are used to compensate the velocity fluctuations around the mean velocity. Therefore, lower order moments, such as mean, variance, third and fourth moments, play a crucial role in the calibration since they account the variation around the mean.

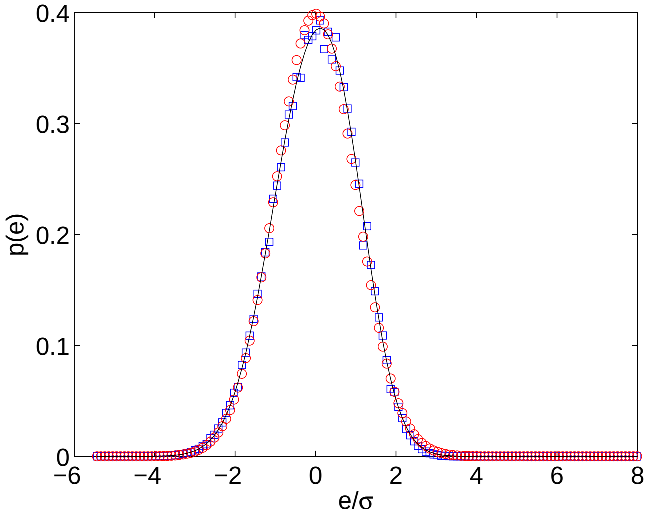

Figure 3.3: Probability distribution function, p.d.f., of voltage in high turbulence region. Circles represent the actual p.d.f. computed from the data; solid line represent the best Gaussian fit to the data in a least-squares sense.

The variability for nth moment estimator, as given by Eq. (3.14), can be studied to investigate the convergence of high order moments computed for a given record length:

$$\varepsilon_{e^n}^2 = \frac{2I}{T}\frac{var\left(e^n\right)}{\langle e^n\rangle^2} = \frac{2I}{T}\frac{\langle e^{2n}\rangle - \langle e^n\rangle^2}{\langle e^n\rangle^2} \tag{3.14}$$

where I and T represent the integral time scale and the record length of measurement in time. The ratio, $2I/T$, equals to number of effective samples separated by twice the integral time scales of turbulence, which means total number of uncorrelated samples within the measurement time window. Therefore, number of samples the statistics are computed over is the most important parameter for the convergence of the statistics. In the present work, we recorded the anemometer output data in 6 second long blocks. Each block contained 180 000 samples because of sampling frequency of 30 kHz for each anemometer channel. In total, we stored more than 2000 blocks of data at each Reynolds number tested in the wind tunnel.

$$p(e) = \frac{1}{\sqrt{2\pi}\sigma} exp\left(-e^2/2\sigma^2\right) \tag{3.15}$$

Figure 3.3 shows a typical probability density function of anemometer out voltage from the rake. The computation of p.d.f. in this figure is based on only 1000 blocks of measured data (which is less than half of the data stored), corresponding to approximately 200 000 integral time scales with 100 000 uncorrelated samples effectively contributing to the convergence of statistics. Here open circles, open squares and solid line present the computed p.d.f. directly from the data, computed Gaussian p.d.f. computed using Eq. (3.15) and the best Gaussian fit to the data using Eq. (3.16). (Note that the coefficients a, b and c Eq. (3.16) are found in the sense of least squares method.) As it can be seen in the figure, the data taken over 1000 blocks have a distribution very similar to the Gaussian one.

$$p(e) = a * exp(-(e-b)^2/c^2) \tag{3.16}$$

Using Eq. (3.14) for the 6th central moment, which is needed for the calibration method developed here, shows that accurate measurement of the 12th moment is required to be able to obtain high accuracy in the computation of the 6th central moment of anemometer output. This requirement can be seen in the numerator of Eq. (3.17) as below:

$$\varepsilon_{e^6}^2 = \frac{2I}{T}\left(\frac{\langle e^{12}\rangle}{\langle e^6\rangle^2} - 1\right) \tag{3.17}$$

One useful and easy way of checking the convergence of the statistics is to study the actual p.d.f.s and their moments (e.g., e×p(e), $e^2\times$p(e),..., $e^{12}\times$p(e)) as shown in figure 3.4. Areas under these curves, which can be computed by taking the integral of the ordinate over the abscissa as given by Eq. (3.18), are equal to the moments of the output signal, $\langle e^n\rangle$:

$$\langle e^n\rangle = \int_{-\infty}^{\infty} e^n p(e)de \tag{3.18}$$

In figure 3.4, computed moments from the data, Gaussian distribution and the best Gaussian fit in the least-squares sense are given by blue, red and black lines respectively. These figures show a remarkable convergence of statistics (even for the 12th moment). The fact is that the moments are similar to the Gaussian distribution up to the 4th moment, and the clipping by analog/digital conversion is not a problem at all. (Note that clipping due to A/D devices is one of the problems for obtaining higher moments.) Departures from the Gaussian behavior are more clear for the odd moments higher than order 7, but the even moments are closer to the Gaussian distribution for the higher modes. We can utilize the relations documented by Lumley (1970) to compute the even moments for a Gaussian distribution as given in Eq. (3.19):

$$\langle e^n\rangle = \frac{n!\sigma^n}{2^{n/2}(n/2)!} \tag{3.19}$$

where σ is the root mean square of the recorded output voltage, $(\sigma = \sqrt{e^2})$. The variability of the estimator for the moments up to 6th order can directly be computed using Eq. (3.14) by plugging the central moments obtained from Eq. (3.19) (e.g., $\langle e^2\rangle = \sigma^2$, $\langle e^4\rangle = 3\sigma^4$, $\langle e^6\rangle = 15\sigma^6$ and so on). Computation of the variability for the 6th moment of output voltage yields ε_{e^6} equal to 0.0212, meaning 2.12% error in the 6th central moment of output voltage. (Note that we also performed computation of the variability of the estimator for the 6th central moment by using the computed 12th and 6th central moments from the data and it resulted in 0.0206, meaning 2.06% error.) As it has been mentioned before, the complete data sets stored during the experiments provide approximately 200 000 uncorrelated samples for each Reynolds number tested. This means that the variability of the 6th moment of the output voltage can be reduced to 0.0150, meaning 1.50%. Therefore, the data studied in this work is capable of providing accurate statistics with high convergence.

As mentioned in the introduction 3.1, one interest in developing these calibration method is to utilize it quickly (or for shorter time records) to take possible changes in calibration into account due to the laboratory environment (e.g., ambient temperature) or measurement equipments (e.g., thermal drift). Therefore, the calibration method has been applied for shorter records instead of the whole record. To be able to show performance of the calibration method in different regions of turbulent boundary layer, one probe from a highly turbulent region close to the wall and one probe from intermittent region very close to the freestream have been studied as shown in figures 3.5 and 3.6 respectively. Open squares present the probability distribution

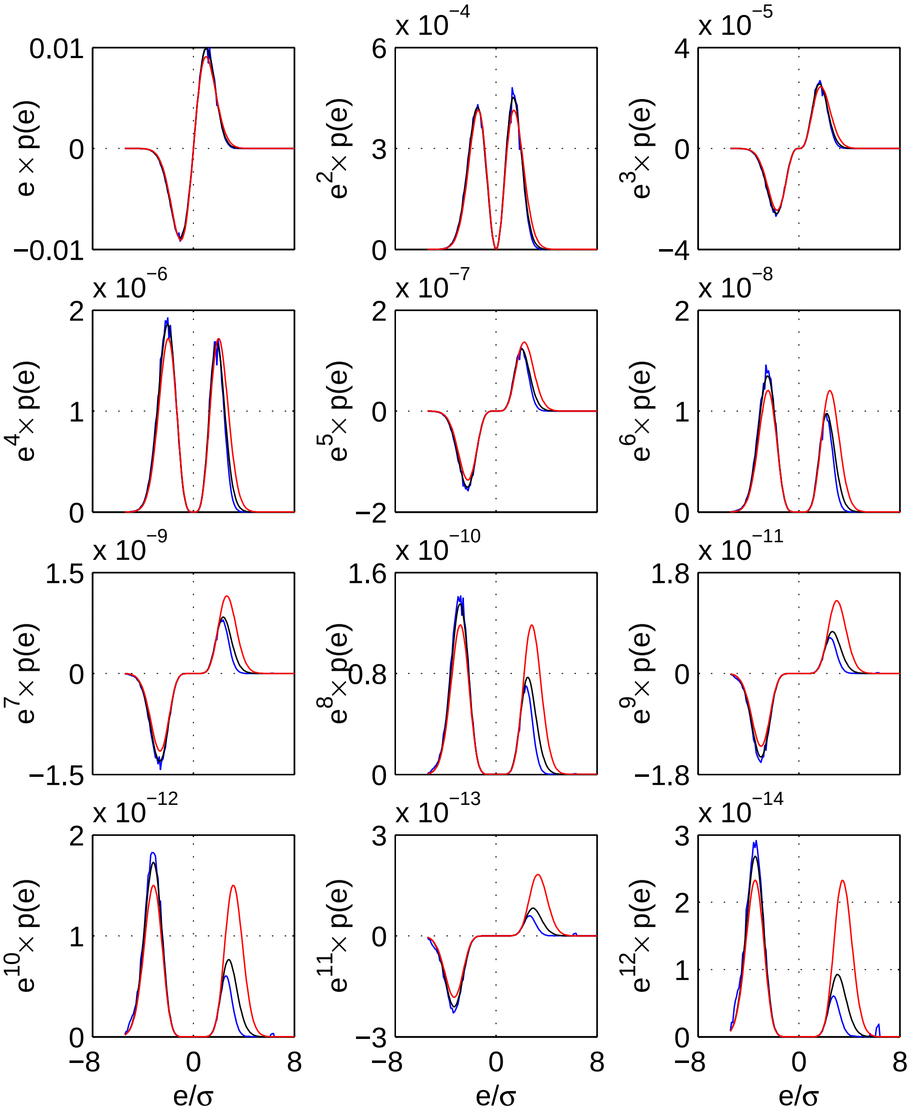

Figure 3.4: Product of output voltage and its powers and probability distribution given in figure 3.3. Circles represent the actual p.d.f. computed from the data times output voltage and its powers; solid line represent the best Gaussian fit to the data in a least-squares sense.

of the moments up to the order 6 obtained from only one block of data containing 180 000 samples. The open circles in the figures are the Gaussian distribution computed using Eq. (3.15) for the root mean square of the output voltage for the same block. The figures show that the convergence of the probability distribution of moments up to order 6 is satisfactory for both highly turbulent and intermittent regions to be able to apply the method developed here. Therefore, the method has been found to be applicable for each block of data resulting almost an on-the-fly calibration scheme.

We further study the time history of the coefficients provided by this nonlinear calibration method as shown in figure 3.7. The results presented here are for four different regions of

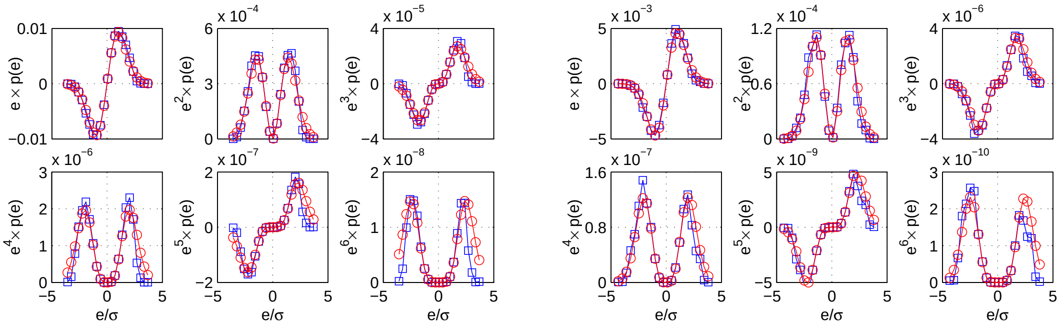

(a) Re_θ =19 100

(b) Re_θ =9800

Figure 3.5: Moments of probability distribution function of the anemometer output voltage near the wall up to 6th order. Blue squares represent the actual p.d.f. computed from the data; red circles represent Gaussian distribution computed using Eq. (3.15) for the same data.

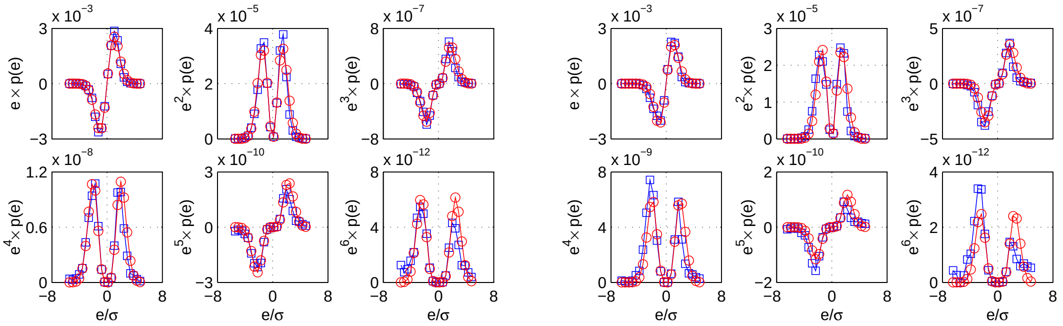

(a) Re_θ =19 100

(b) Re_θ =9800

Figure 3.6: Moments of probability distribution function of the anemometer output voltage in very intermittent region of the turbulent boundary layer up to 6th order. Blue squares represent the actual p.d.f. computed from the data; red circles represent Gaussian distribution computed using Eq. (3.15) for the same data.

turbulent boundary layer, namely (a) near-wall layer, (b) log-layer, (c) outer-layer and the intermittent part very close to the freestream, at two different Reynolds numbers. The calibration coefficients for 500 different blocks showed fluctuations around its mean in both the near-wall layer and log-layer. On the other hand, the calibration coefficients in the outer layer showed different patterns, indicating that the calibration is also sensitive to the intermittent nature of the outer layer of boundary layer. In the outer layer at $y = 0.75\delta$, the coefficients show a linear trend for low Reynolds number case measured here, see figure 3.7(c). The linear trend is different for different coefficients so that when they combined together for converting voltages into velocities, they compensate each other and provide the correct values for velocities. The same is true for the high Reynolds number case, however, the coefficients shows some randomness from blocks to blocks. On the edge of turbulent boundary layer very close to the freestream, the coefficients obtained for both Reynolds number also show a linear trend over the blocks. Again their slopes are organized in a way that they compensate each other to provide correct

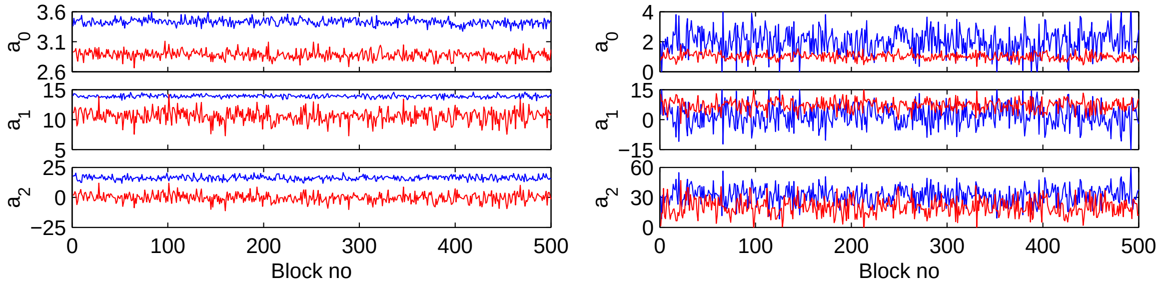

(a) $y^+ = 22$

(b) $y^+ = 450$

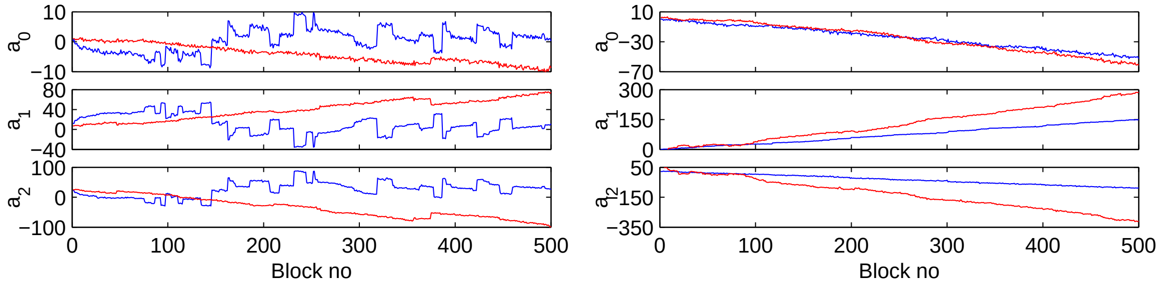

(c) $y = 0.75\delta$

(d) $y = \delta$

Figure 3.7: Time history of the calibration coefficients blocks by blocks for four different regions of the turbulent boundary layer. (a) Near wall, (b) Log-layer, (c) Outer layer, (d) Very close to the freestream. Blue solid lines represents the calibration coefficients of high Reynolds number case ($U_\infty = 19\,100$); red solid lines represent the calibration coefficients of low Reynolds number case ($U_\infty = 9800$).

results. This behavior is attributed to higher demand on the record length required for convergence and accuracy in the intermittent parts of the turbulent boundary layer. As we increase the record length, the random behavior disappears and actually converges to the value which can be obtained if whole 2000 blocks of data are utilized to compute the coefficients.

The range of validity of the calibration coefficients has been studied for four different regions of the turbulent boundary layer at both the Reynolds numbers considered here. Figures 3.8(a) and 3.8(b) present instantaneous and fluctuating velocities computed by both the calibration coefficients obtained from the data recorded at the same freestream velocity (blue solid lines - correct coefficients) and the calibration coefficients obtained from different freestream velocity (red solid lines - incorrect coefficients). As it can be seen in the figures, using the calibration coefficients obtained from 5 m s^{-1} freestream velocity for converting the voltages recorded at 10 m s^{-1} freestream velocity underpredicts the instantaneous velocity at all layers of turbulent boundary layer except for the probes located on the edge of the boundary layer ($y \sim \delta$) at which the prediction is very much larger than the actual velocity. On the other hand, coefficients obtained from 5 m s^{-1} freestream velocity test and used for conversion of voltages recorded at 10 m s^{-1} freestream velocity test yields remarkable agreements for the fluctuating velocities. It is also possible to observe similar agreement for all the probes across the boundary layer. When coefficients computed for the 10 m s^{-1} case are used for converting the voltage output from the

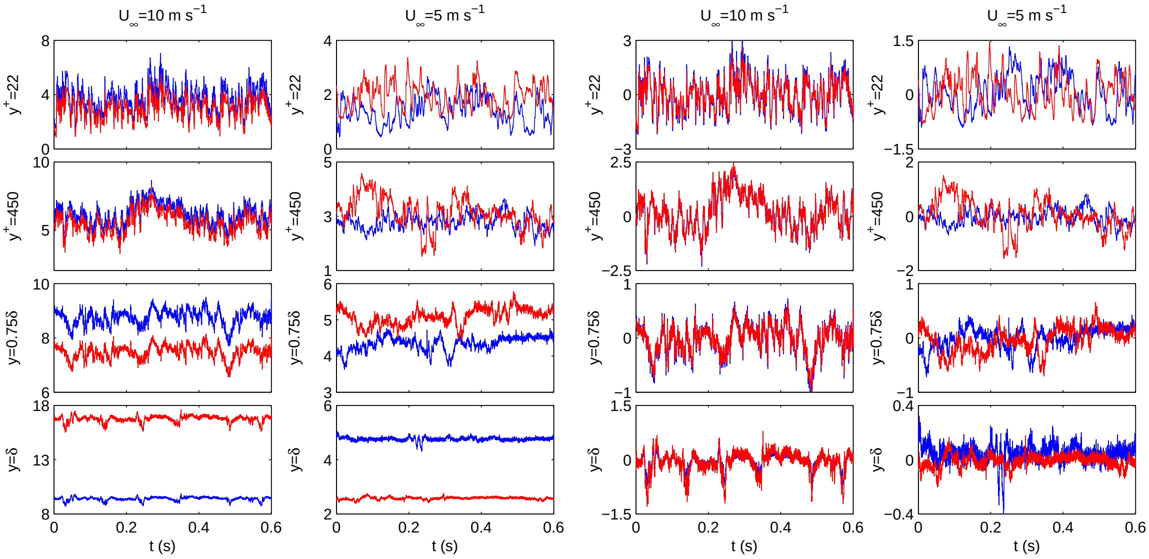

(a) Instantaneous velocities

(b) Fluctuating velocities

Figure 3.8: Comparison of instantaneous and fluctuating velocity converted from voltage using calibration coefficients obtained first at the correct reference velocity and another freestream velocity. Blue solid line show the correct velocity signal created using the proper coefficients. Red solid line show the velocity signal converted using some other calibration coefficients obtained at a different reference velocity.

test case of 5 m s^{-1} freestream velocity, neither the instantaneous velocities nor the fluctuating velocities show any agreement. The velocities linearized using calibration coefficients obtained in a from 10 m s^{-1} case produce overpredictions for all probes except the one very close to the freestream. We also notice a completely reverse situation for the probes placed on the edge of the turbulence boundary layer at 5 m s^{-1} freestream velocity. The instantaneous values in this case are much lower than the values obtained using the correct calibration coefficients. Clearly the calibration coefficients must be obtained for the same freestream velocity tested in the experiments. Use of calibration coefficients obtained at different freestream conditions other than the reference one should definitely be avoided.

3.5 Summary and Discussions

A hot-wire calibration method in the turbulent flow has been presented in this chapter. The method is useful when there is no possibility of performing conventional calibration of hot-wire sensors by means of a laminar flow field. The proposed method assumes the polynomial curve fitting approximation to express instantaneous velocity as a function of instantaneous voltage. There is only one freestream velocity needed in this method; since the method employs the higher order velocity statistics instead of obtaining different freestream velocity versus voltage relations.

High order statistics of voltage are also required to be able to implement the method. Therefore, special care has to be taken to avoid clipping of the tails of the probability distributions

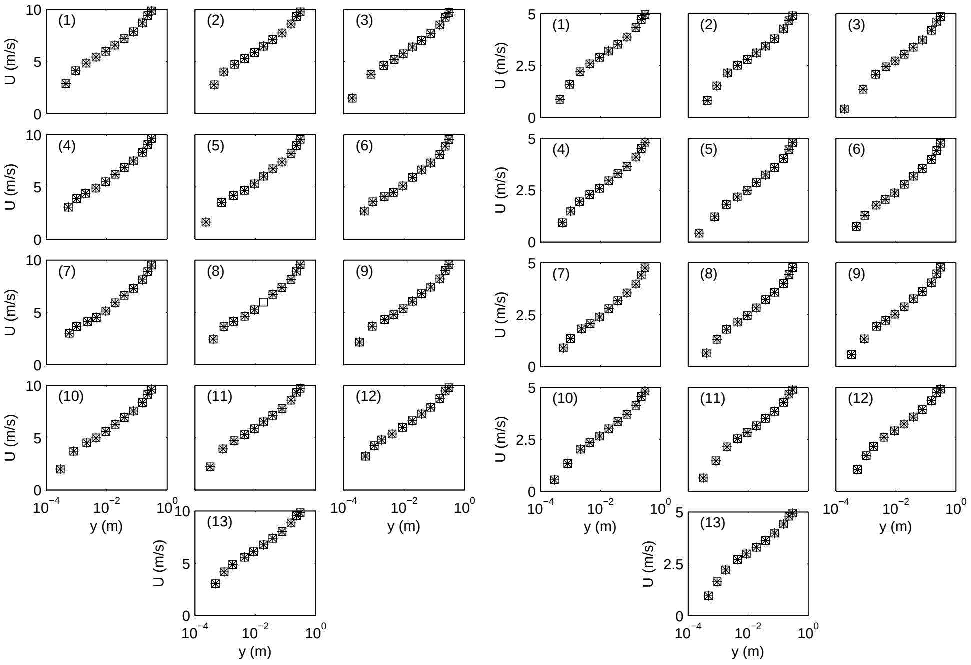

(a) Mean velocity profiles at $\mathrm{Re}_\theta = 19100$.

(b) Mean velocity profiles at $\mathrm{Re}_\theta = 9800$.

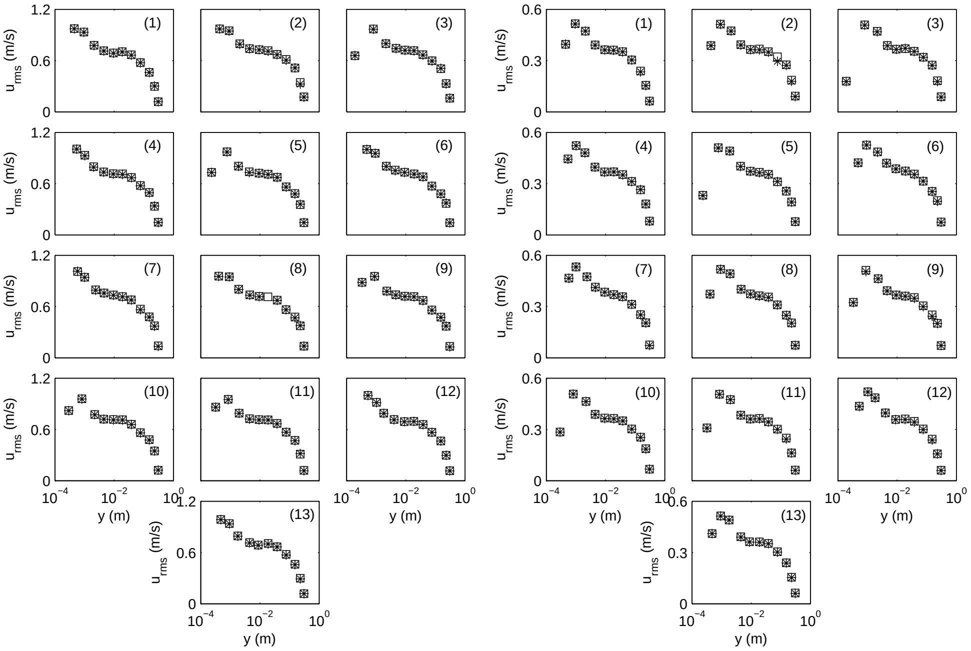

(c) u_{rms} profiles at $\mathrm{Re}_\theta = 19100$.

(d) u_{rms} profiles at $\mathrm{Re}_\theta = 9800$.

Figure 3.9: Mean velocity and r.m.s. velocity profiles from both PIV and HWR. Squares: PIV at HWR probe location, Stars: HWR. Inserted numbers within parenthesis represent the vertical comb numbers in a sequence. (1) is at z=-140 mm and (13) is at z=140 mm.

and ensure the convergence of the voltage statistics. In the present study, instantaneous velocity is expressed as a second order polynomial function of instantaneous voltage. Therefore, central moments of voltage up to sixth order are provided with good accuracy. The results showed that even the second order polynomial approximation results in a remarkable agreement between reference and measured profiles of mean velocity, root mean square of velocity fluctuations and higher moments of turbulent velocity. Therefore, there is no need in this experiment to use third or fourth order polynomial functions, thus avoiding the demands for higher order voltage statistics (see figure 3.9 for mean velocity and r.m.s. profiles for each vertical combs of the hot-wire rake at two different Reynolds numbers). This is undoubtedly because of the lower turbulent intensities of boundary layers (typically $<$30%) than in many free shear flows.

The calibration coefficients when applied smaller data sets exhibit some fluctuations in time from block to block. This is due to the random nature of the statistics computed over the window length taken in time. Three coefficients of the calibration scheme, however, act together to compensate each other to produce the correct values for instantaneous velocities. The range of velocities the calibration can be applied is limited by the reference velocity, freestream velocity in the boundary layer case, at which the experiments are carried out and the calibration coefficients are obtained.

This methods was also found to be very useful way to compensate for the thermal drift of anemometers with time and/or mean ambient temperature variations in the flow during the experiment. The proposed method provides an opportunity to do the calibration on the fly as long as the convergence of the high order voltage statistics can be satisfied. The calibration scheme can be executed for different blocks of hot-wire data to correct the coefficients. Therefore, corrections due to the changes in physical conditions can be eliminated by the proposed method.

Chapter 4

Single Point Statistics and Spectral Analysis

4.1 Introduction

The results reported in this dissertation were a part of the multi-point, multi-system experiment described in chapter 2; in particular, the hot-wire part. And the primary goal of the measurements was to establish the spatial and temporal structure of the high Reynolds number turbulent boundary layer by taking time-resolved data from many points simultaneously over a flow area comparable to the dimensions of the boundary layer itself. The 143 hot-wire array was optimized for this purpose, at some compromise to the mean velocity statistics (as noted in the previous chapter). Nonetheless, the single point statistical quantities from this experiment are of some interest: both in their own right, and because they confirm that the single point statistics are consistent with those that would have been measured without the probe array in place. For these purposes, mean velocity profiles, root-mean-square (rms) velocity profiles, profiles for the third and fourth central moments of turbulent velocity field are presented for all measurement locations. In addition, the spectral characteristics of both turbulent boundary layers are studied by means of power spectral densities (or frequency spectra) and pre-multiplied one-dimensional wave-number spectra. Comparisons are made of the current results with previous measurements in the same wind tunnel. Note that correlation functions, integral length scales and integral time scales are presented in the next chapter, which focuses on the two-point statistics of the turbulent boundary layer.

4.2 Streamwise Velocity Moments

As described in detail in chapters 2 and 3, a hot-wire rake of 143 single-wire probes was used for the experiments investigated in this thesis. These probes were distributed on 13 vertical combs spanning in the spanwise direction. Each of the vertical comb had 11 probes spaced logarithmically in the wall-normal direction from wall to the freestream. This resulted in a matrix of probes 11×13 on the plane normal to the freestream flow. The hot-wire rake was synchronized with PIV systems as shown in chapter 2. The experiments were carried out at Reynolds numbers based on momentum thickness of 9800 and 19 100. These Reynolds numbers were achieved 18 m downstream of the wind tunnel test section entrance with operating freestream velocities for the tunnel of 5 m s^{-1} and 10 m s^{-1}.

The mean velocity profiles, rms velocity distribution, third and fourth central moments in this section were computed using 1000 of 6 seconds long blocks of data at both Reynolds numbers. Each block of data contains 180 000 samples, and a 30 kHz sampling frequency was used throughout the experimental campaign. This block length in time corresponds approximately to 375 and 250 integral times scales for high and low Reynolds number cases respectively (see 5.21). This provides accuracy of the estimator for the mean velocity, using Eq. (3.14), better than 0.094% and 0.115% within the highest turbulence intensity region for Re_θ of 19 100 and 9800 respectively. The maximum error in the estimator for the highest moment discussed in this section, the fourth order central moment of the streamwise turbulent velocity fluctuations, is less than 0.770% and 0.943% for freestream velocities of 10 m s^{-1} and 5 m s^{-1} respectively.

Figure 4.2 shows the scaled mean velocity profiles with inner scaling parameters at different spanwise locations where each of the vertical combs was placed. (Note that u_* is taken from table Carlier & Stanislas (2005).) Each vertical comb is presented in a separate figure, because there is essentially no collapse of the mean velocity profiles across the homogenous direction. This is due to the blockage introduced by the hot-wire rake used for the measurements. The blockage by the rake was quantified by Coudert *et al.* (2007), who found that it creates a potential flow disturbance which affects only the mean velocity profiles while leaving the turbulence unaffected. This blockage effect can be seen easily in subplots from (a) to (l) in figure 4.2 by comparing the profiles against the black solid lines which are the same in every subplots. The black solid line is the velocity profile obtained using the Van Driest formulation for the mean velocity profile as given by Eq. (4.1):

$$U^+(y^+) = \int_0^{y^+} \frac{2}{1+\sqrt{1+4\left[\kappa y^+\left(1-exp(-y^+/c^+)\right)\right]^2}}dy^+ \tag{4.1}$$

where standard values for κ, 0.41, and c^+, 26, are used for computation. The black and magenta dots represent the measurements of Carlier & Stanislas (2005) for Re_θ of 20 600 and 11 500 respectively. Carlier & Stanislas (2005) performed the measurements in the same wind tunnel used in this study. They used single hot-wires to obtain these velocity profiles, which essentially provides very good agreement with Van Driest profile. The blue and red lines show the velocity profiles obtained from the PIV measurements performed one centimeter upstream of the hot-wire rake for the high and low Reynolds numbers tested respectively. (Note that the PIV data are used for calibrating the wires as discussed in chapter 3). The open squares denote the hot-wire data at the probe positions for high (blue) and low (red) Reynolds numbers.

As it can be seen in the figures, there is a very good agreement between the PIV data and hot-wire data. (Details and quantization of this agreement can be found in chapter 3.) On the other hand, the blockage effect on the mean velocity profile is obvious, especially in the middle of the rake. The blockage is negligible for the vertical combs located in both end of the rake in the spanwise direction, see figures 4.2(a,b,l&m). The profiles exhibit a logarithmic region of at least a decade in y, even in the presence of the blockage.

Figures 4.3, 4.4 and 4.5 compare the scaled root-mean-square velocity distributions, scaled third order central moments, and scaled fourth order central moments for each of the vertical combs respectively. The lines in these figures are produced from the same data used by Carlier & Stanislas (2005). All the lines across the rake in the spanwise direction are identical to make comparison possible. We did not place the profiles of different spanwise locations in one figure, because the wall-normal positions close to the wall deviates from the design points, making it difficult to read the figures.

Since inner variables, viscosity, ν, and friction velocity, u_*, are used for normalizing the axes in these figures, there is a very good collapse in the inner wall layer. By contrast, there is a deviation between the profiles in the outer layer of turbulent boundary layer, consistent with the different Reynolds numbers since $u_*\delta/\nu$ differ by a factor of 2. This is especially notable for the rms velocity profiles and fourth order central moments. Note that the boundary layer thicknesses, δ and θ, are nearly the same for both Reynolds numbers and the ratio of friction velocity and freestream velocity, u_*/U_∞, is almost identical. The latter is especially important since it means that the outer scaling parameters from all competing theories are identical.

4.3 Frequency Spectra

Frequency spectra of the streamwise component of the fluctuating turbulent velocity are shown in figures 4.6-4.9 for the high Reynolds number case and in figures 4.10-4.13 for the low Reynolds number case. The spectra are grouped according to their wall-normal position, so that each of the figures has 13 curves in the spanwise direction. Lines indicating the k^{-1} and $k^{-5/3}$ are also drawn in the figures to be able to compare the slopes of the spectra with theory.

The frequency spectra computed here are based on 1000 blocks of data collected during the measurements, yielding 3% statistical error in the estimator for the spectra. Each block contained $131072 = 2^{17}$ samples instead of 180000 (which is the recorded number of samples in each block) to be able to use fast Fourier transformation (FFT) efficiently. This resulted in 4.37 second long blocks, hence a frequency resolution of 0.023 Hz. As mentioned in Balakumar & Adrian (2007), long records of velocity signal at sufficiently high sampling frequency is needed for capturing the contribution due to the very-large scale of motion which appears in the very lower end of the wave number (or frequency) spectra.

As mentioned in the experimental setup chapter, the sampling frequency in the experiments was 30 kHz throughout the measurement campaign. The highest frequency of interest in most turbulence experiments corresponds to the convection past the probe of 2π times the Kolmogorov microscale, η_K; i.e.,

$$f_H = \frac{U_c}{2\pi\eta_k} \tag{4.2}$$

where f_H and U_c are highest frequency at which the turbulence kinetic energy dissipates and the local convecting flow velocity. The Kolmogorov microscale is defined as:

$$\eta_k = \left(\nu^3/\varepsilon\right)^{1/4} \tag{4.3}$$

where ε is the rate of dissipation of turbulence energy per unit mass. Carlier & Stanislas (2005) made estimates of ε in this flow from both PIV and hot-wire data using the assumption of local isotropy. Using their estimates, the highest frequency of interest in this experiment was predicted to be 10 kHz, and would be observed at around y^+ of 30 (actually near where the peak of the rms velocity fluctuations is found). Therefore, in order to to satisfy the Nyquist criterion, a sampling frequency of 30 kHz is chosen.

The finite length of the sensing wire of hot-wire probe, however, acts as a spatial low-pass filter, since the sensing wire only resolves scales larger than twice the wire length. The wire cut-off frequency, as suggested by Glauser & George (1992), can be defined as follows:

$$f_c = \frac{U_c}{2\ell_w} \tag{4.4}$$

where f_c and ℓ_w are the wire cut-off frequency and the wire length respectively. In turbulent boundary layers, the convection velocity increases from the wall to the freestream, so the wire

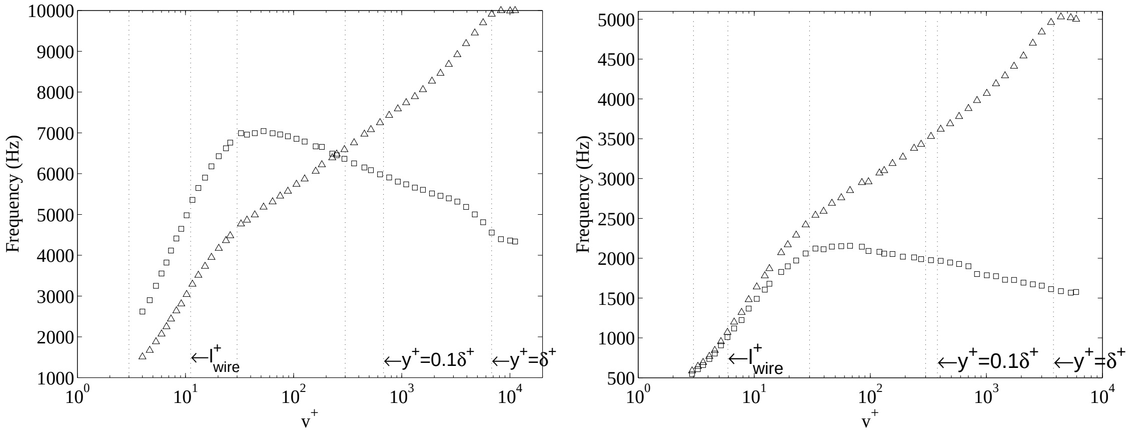

(a) $U\infty = 10$ ms^{-1}, $Re_\theta = 19\,100$.

(b) $U\infty = 5$ ms^{-1}, $Re_\theta = 9800$.

Figure 4.1: Comparison of wire cut-off frequency and highest frequency of turbulence at dissipative scales. Triangles represent the wire cut-off frequency. Squares denote the highest frequency computed using isotropic turbulence assumption.

cut-off frequency also increases in the wall-normal direction. Figure 4.1 compares the wire cut-off frequency with the highest possible frequency in the spectrum (using the aforementioned isotropic turbulence estimates). As can be seen in the figure 4.1(b), the wire is able to resolve all the scales at each wall-normal position in the boundary layer for Re_θ of 9800. For the high Reynolds number case, the wire resolves all the scales above y^+ of 300, but near the peak in the turbulence intensity it only resolves to about $0.6F_H$. This is not of concern in this work, because the aim of this investigation is to study the large scale, energetic features of turbulence, hence low frequency (or wavenumber) motion. Furthermore, we apply a digital filter at 3 kHz and 1 kHz for high and low Reynolds number experiments to remove any noise sources at higher frequencies. Special care was taken in digitally filtering the signal and a precisely zero phase distorting digital filter is applied to the signal. This was especially important in cross-correlation analysis and in building the two-point cross-spectral tensor as the kernel of proper orthogonal decomposition integral equation. The cut-off frequency was not optimized for each channel of hot-wire anemometry, therefore we observe slight differences in the high frequency end of the spectra.

We have detected some negligible low frequency noise in the spectra due to the electronics. These noise contributions are found at 278 Hz and its harmonics at 558 Hz and 834 Hz. The noise is only detectable in the outer layer of turbulent boundary layer, where the turbulence level goes down significantly so that the noise becomes apparent. The noise found in these frequencies is in the form of a spike with no significant area under the spike. We have also observed some noise, also in the form of spikes, very close to the freestream. In the spectra shown in figures 4.6-4.13, these spikes have been removed. The energy due to these spikes was less then 0.07% and 0.20% of the total turbulence kinetic energy at the low and high Reynolds numbers respectively.

The spectra shown in figures 4.6-4.13 are grouped according to their wall-normal position on the vertical rakes as mentioned above. Therefore, it is expected to have a collapse of the spectra from the same wall-normal position in the homogeneous direction. On the other hand, the positions of the probes relative to the wall varies slightly due to mechanical manufacturing imperfections. The variation is relatively larger especially for the first three probes closest to the wall. This is why we observe some variations in the spectra in the spanwise direction.

One common feature of all the frequency spectra shown in these figures is that they have a flat region in the very low frequency part of the spectrum, and fall off monotonically as the frequency increases (like those observed in one-dimensional spectra of homogenous turbulence). This will be seen to be of some interest in the next chapter, since Lumley (1970) states:

> “..., we know that, if $B_{LL}(r)$ is nonnegative, the corresponding one-dimensional spectrum, $F_{LL}^{(1)}(k_1)$ (its Fourier transform sic), will have its maximum at the origin, while if the one-dimensional spectrum has its maximum elsewhere, $B_{LL}(r)$ will have negative regions.”

Note that the inverse is not necessarily true, and we will indeed see negative regions in the streamwise velocity correlations.

There is some limited evidence for the existence of a spectral range where the spectra decay as k^{-1} as suggested, for example, by McKeon & Morrison (2007). For the high Reynolds number case, only figure 4.7(a) ($y^+ = 100$) exhibits about a decade of decay at a rate very close to k^{-1} slope. For the low Reynolds number case, however, it is possible to see almost one decade of k^{-1} range at y^+ of 55 and 114 as shown in figures 4.11(a&b).

The spectra shown in this chapter reveal some interesting facts about the $k^{-5/3}$ range. First of all, there is no such a range below $y^+ = 220$ for the high Reynolds number case, and 230 for the low Reynolds number case as shown in figures 4.7(b) and 4.11(c) respectively. Development of the $k^{-5/3}$ range begins to be observed at y^+ of 445 for Re_θ of 19100. We see approximately two decades of $k^{-5/3}$ range in the outer layer of the boundary layer at this high Reynolds number. The picture is the same for the lower Reynolds number studied in the course of this thesis. The $k^{-5/3}$ range exists at y^+ of 465 and above. These observation suggest that there actually is no significant inertial range, meaning there is no true separation of scales, below approximately y^+ of 450. This is consistent with the arguments of George & Castillo (1997) and George (2006) for the existence of a “mesolayer” in which the viscous stress is negligible, but the energetic scales of turbulence are still influenced by the viscosity.

4.4 Premultiplied Spectra

The premultiplied one dimensional wavenumber spectra of the streamwise velocity fluctuations versus streamwise wave number are presented in figure 4.14. The frequency spectra and frequency can be converted into one-dimensional wavenumber spectra ($F_{1,1}^{(1)}(k_1)$) and streamwise wavenumber (k_1) respectively using the Taylor’s frozen field hypothesis; i.e.,

$$F_{1,1}^{(1)}(k_1) = \frac{U_c}{2\pi} S_{1,1}(f) \tag{4.5}$$

$$k_1 = \frac{2\pi}{U_c} f \tag{4.6}$$

where U_c is the local convecting velocity and f is the frequency. Each subplot of figure 4.14 contains the premultiplied wavenumber spectra of both Reynolds number cases at the same y/δ in the wall-normal direction.

We observe broad peaks at the very low wavenumber end of the premultiplied spectra for the high Reynolds number experiment developing at y^+ of 100. Between y^+ of 100 and 890 ($=0.13\delta^+$) there is a peak in the spectra around $k\delta$ of 1, which corresponds to wavelengths of approximately 7δ. This is certainly in agreement with the wavelengths suggested by Kim & Adrian (1999) for pipe flows and Balakumar & Adrian (2007) for channels and boundary layers. The peak starts moving towards the lower end of wavenumber from wall-normal position of $7y^+$ to $100y^+$. The peaks do not move much within the log layer and move slightly towards higher wavenumbers in the outer layer.

Figure 4.14 also shows that the premultiplied spectra scaled in outer variables collapse outside of the overlap region, (g) - (k). Also the spectra from the position in the viscous sublayer, (a), have the same shape but differ by a factor of 2, almost exactly the difference in δ^+ between the two experiments. Thus, as expected, these spectra should (and do) collapse when plotted using inner parameters for normalization, ν and u_*. There is no scaling, however, that will collapse the spectra in the overlap region, (b) - (f), since these have very different shapes. This provides strong support for the idea this overlap region is really a composite of the inner and outer regions, and not independent of either, at least at finite Reynolds numbers. Whether it can be considered in the limit to be a function of only u_* and y as commonly assumed (c.f., McKeon & Morrison (2007)), or u_* and U_∞ (as argued by George & Castillo (1997)) cannot be established from these experiments since the ratio, u_*/U_∞, is the same for both Reynolds numbers.

4.5 Summary and Discussion

In this section single point statistics obtained using the hot-wire rake have been presented. The measured data by means of some velocity profiles were also compared with the previous measurement done in the same facility. The effect of blockage on the mean velocity profiles was also shown in this section. Single point spectral analysis reveal some important findings. The k^{-1} range is found to be very small in a very narrow region of the turbulent boundary layer around $y^+ = 100$, which might be attributed to the Reynolds numbers tested in this study. The $k^{-5/3}$ range, according the figures presented here, starts developing after y^+ of 220 and becomes an important part of the spectra after y^+ of 450. The premultiplied spectra collapse in the outer layer of turbulent boundary layer. The flat region in the premultiplied spectra is seen only near approximately $y^+ = 100$ for both of the Reynolds number studied here. Also the different shapes of the spectra in the overlap region suggest strongly a dependence on Reynolds number consistent with different inner and outer velocity regions for this developing flow.

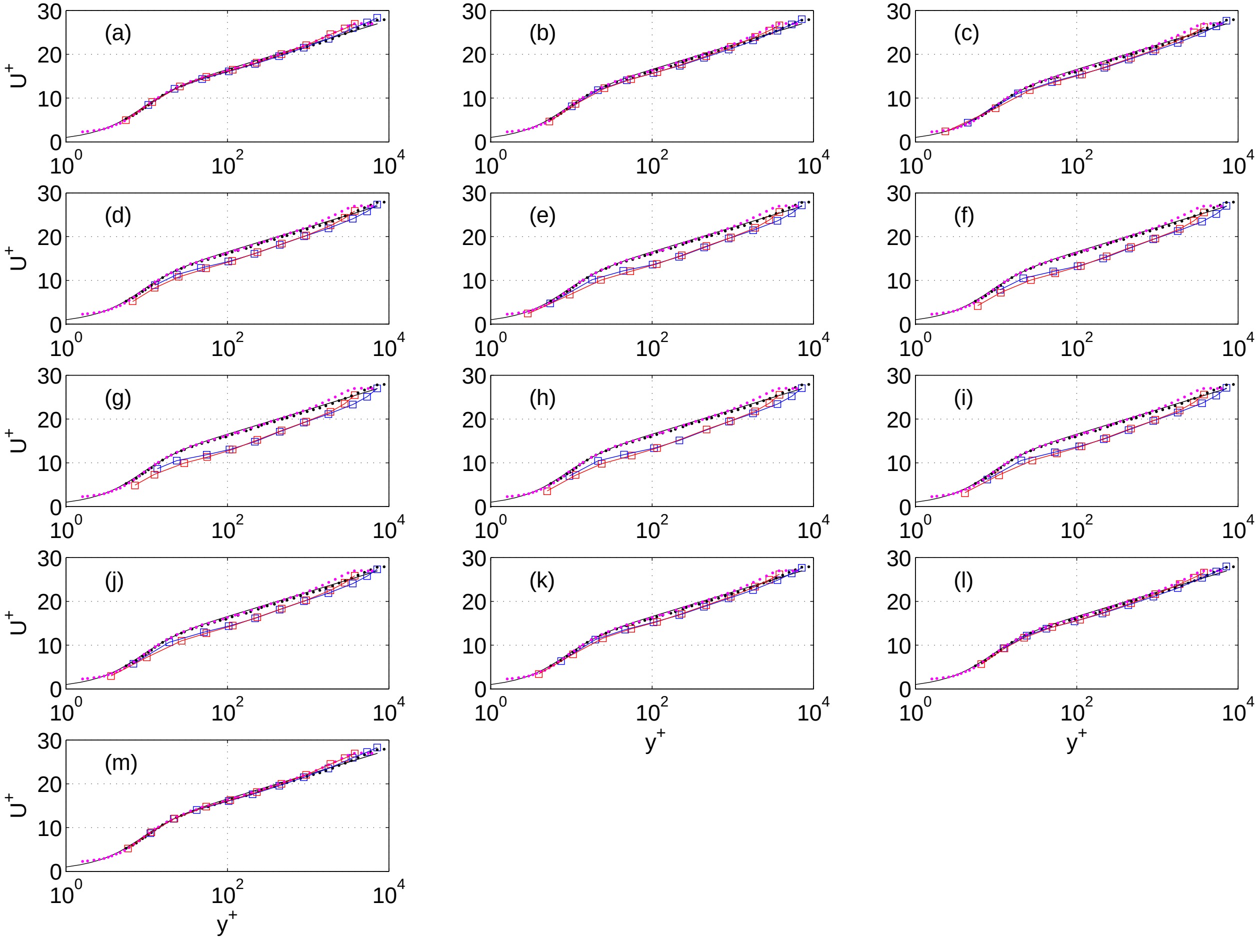

Figure 4.2: Normalized mean velocity profiles. Blue squares and lines: Hot-wire and PIV at $Re_\theta = 19\,100$ respectively, Red squares and line: Hot-wire and PIV at $Re_\theta = 9800$, Black and magenta dots: Measurement by Carlier & Stanislas (2005) at $Re_\theta = 20\,600$ and 11 500 respectively, Black line: Van Driest velocity profile. (a):$z/\delta = -0.46$, (b):-0.33, (c):-0.20, (d):-0.09, (e):-0.04, (f):-0.013, (g):0, (h):0.013, (i):0.04, (j):0.09, (k):0.020, (l):0.33, (m):0.46

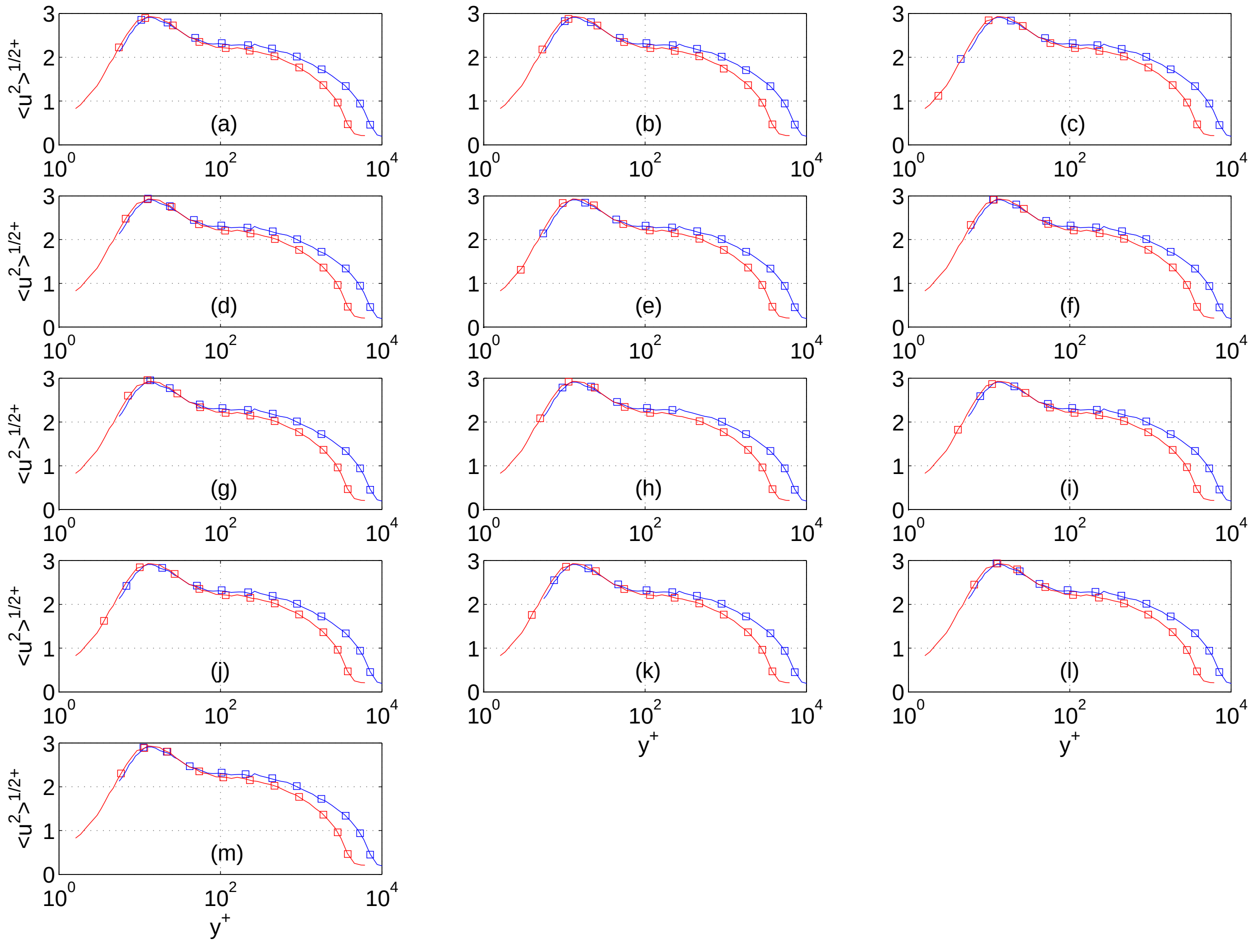

Figure 4.3: Normalized root-mean-square velocity profiles, $\langle u^2\rangle^{1/2}/u_*$. Blue squares: Hot-wire data at Re_θ =19 100, Red squares: Hot-wire data at Re_θ =9800, Blue and red lines: Measurement by Carlier & Stanislas (2005) at Re_θ =20 600 and 11 500 respectively. (a):z/δ =-0.46, (b):-0.33, (c):-0.20, (d):-0.09, (e):-0.04, (f):-0.013, (g):0, (h):0.013, (i):0.04, (j):0.09, (k):0.020, (l):0.33, (m):0.46

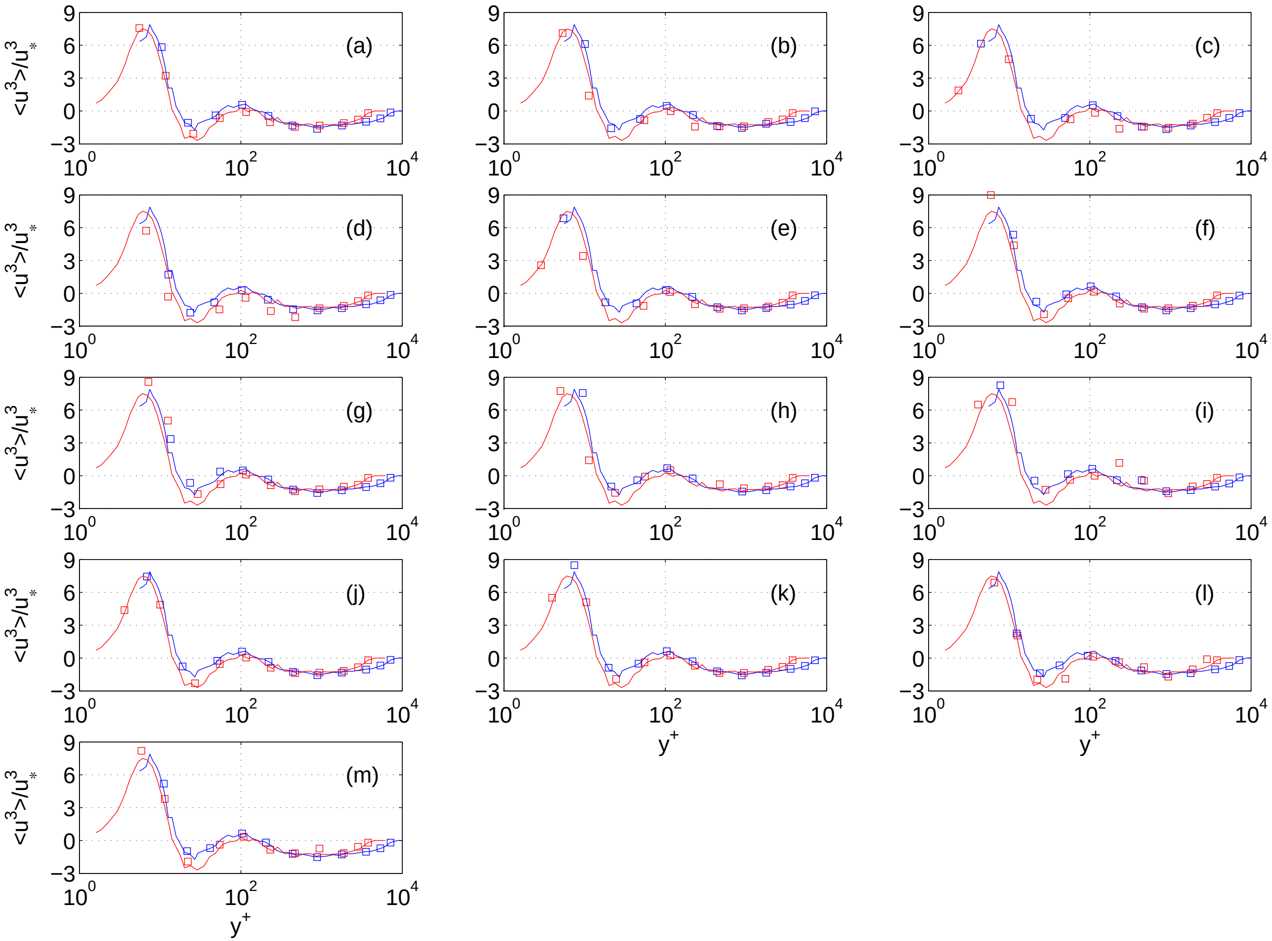

Figure 4.4: Normalized profiles of third central moment of turbulent velocity, $\langle u^3\rangle/u_*^3$. Blue squares: Hot-wire data at $\mathrm{Re}_\theta = 19\,100$, Red squares: Hot-wire data at $\mathrm{Re}_\theta = 9800$, Blue and red lines: Measurement by Carlier & Stanislas (2005) at $\mathrm{Re}_\theta = 20\,600$ and 11 500 respectively. (a):z/δ =-0.46, (b):-0.33, (c):-0.20, (d):-0.09, (e):-0.04, (f):-0.013, (g):0, (h):0.013, (i):0.04, (j):0.09, (k):0.020, (l):0.33, (m):0.46

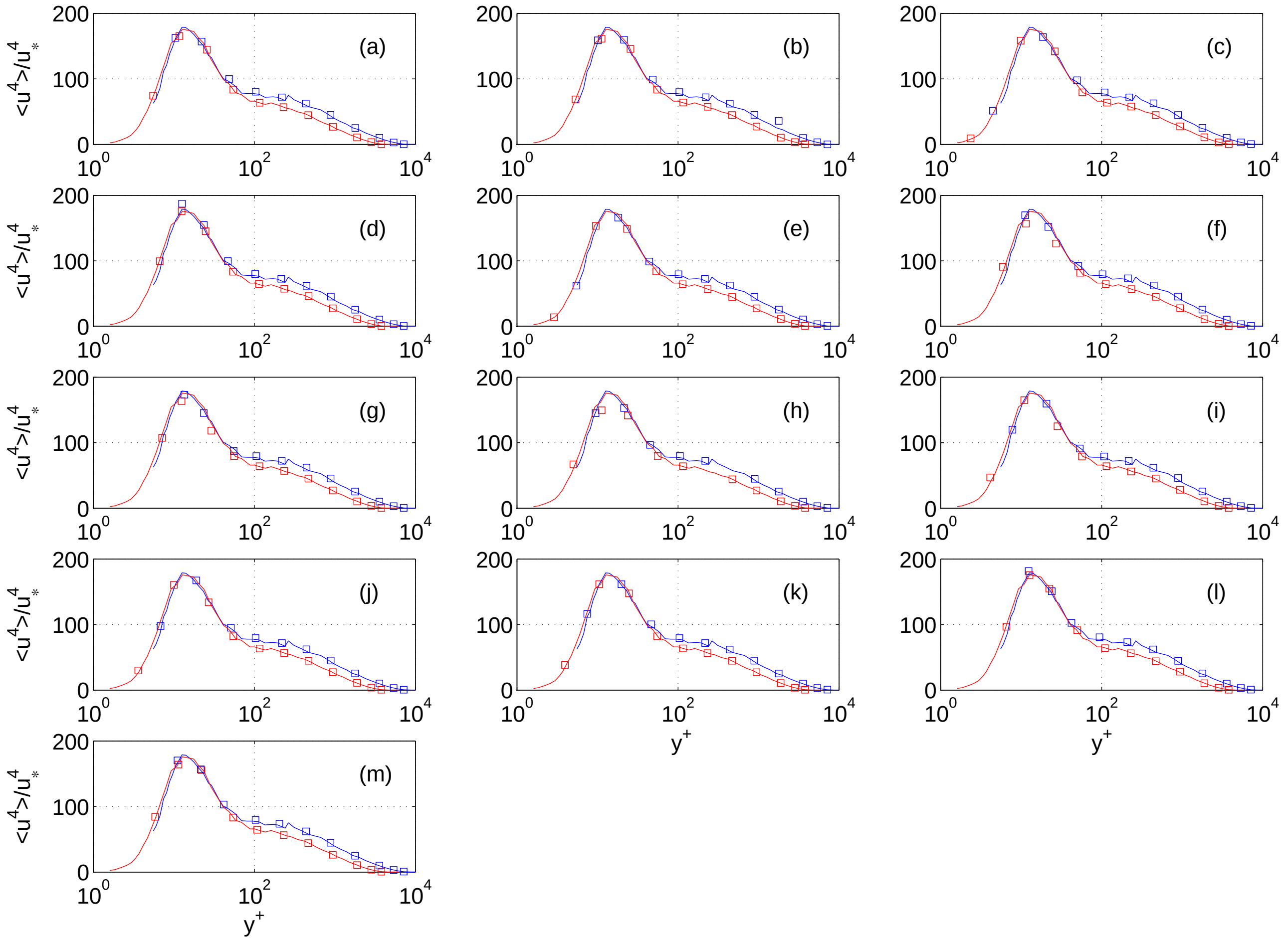

Figure 4.5: Normalized profiles of fourth central moment of turbulent velocity, $\langle u^4 \rangle / u_*^4$. Blue squares: Hot-wire data at Re_θ =19 100, Red squares: Hot-wire data at Re_θ =9800, Blue and red lines: Measurement by Carlier & Stanislas (2005) at Re_θ =20 600 and 11 500 respectively. (a):z/δ =-0.46, (b):-0.33, (c):-0.20, (d):-0.09, (e):-0.04, (f):-0.013, (g):0, (h):0.013, (i):0.04, (j):0.09, (k):0.020, (l):0.33, (m):0.46

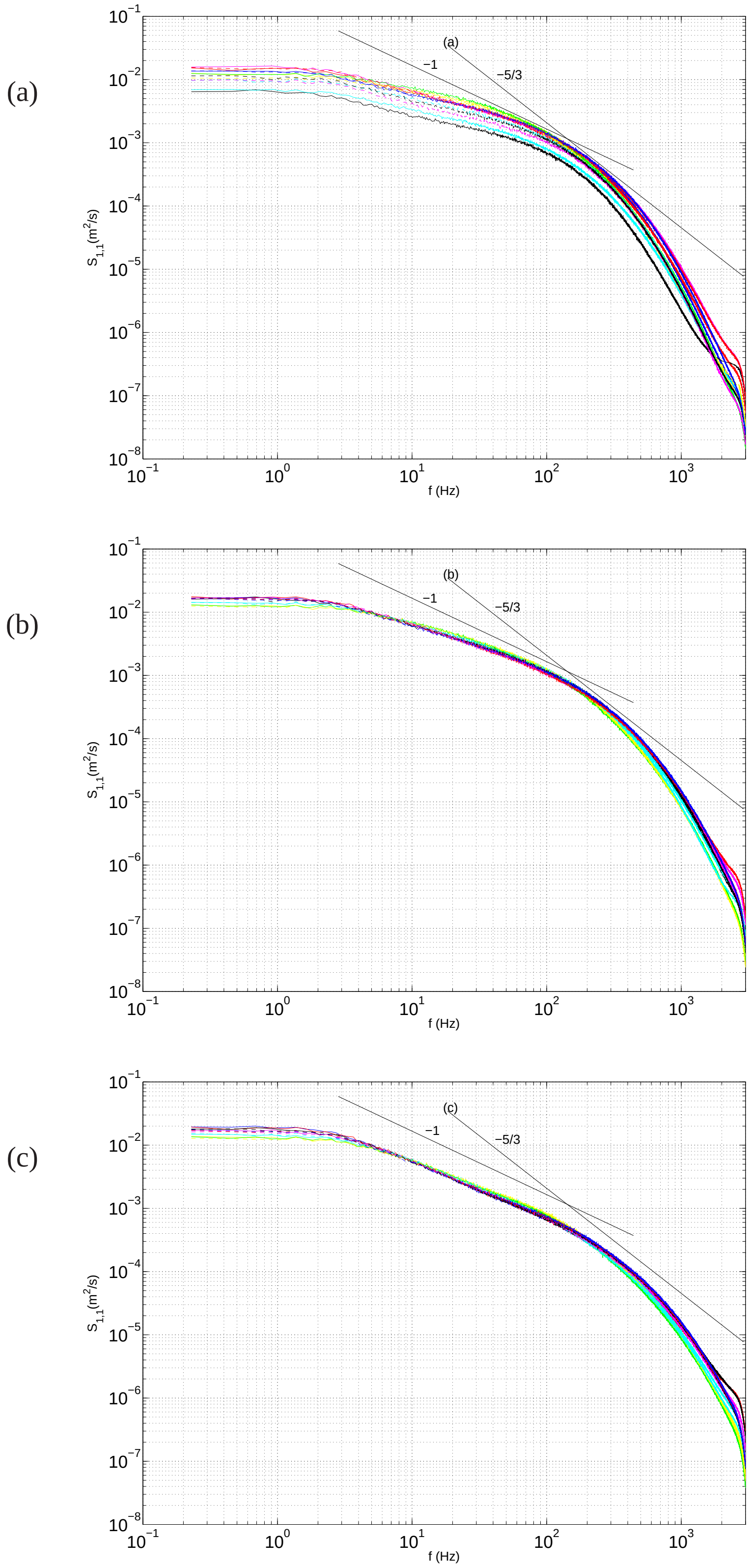

Figure 4.6: Frequency spectra of the first, second and third rows of hot-wire rake about y/δ of (a): 0.001, (b): 0.003 and (c): 0.007 (or y^+ of (a): 7, (b): 22 and (c): 50) at Re_θ of 19 100 respectively. Each color denotes the frequency spectrum of turbulence at different spanwise location.

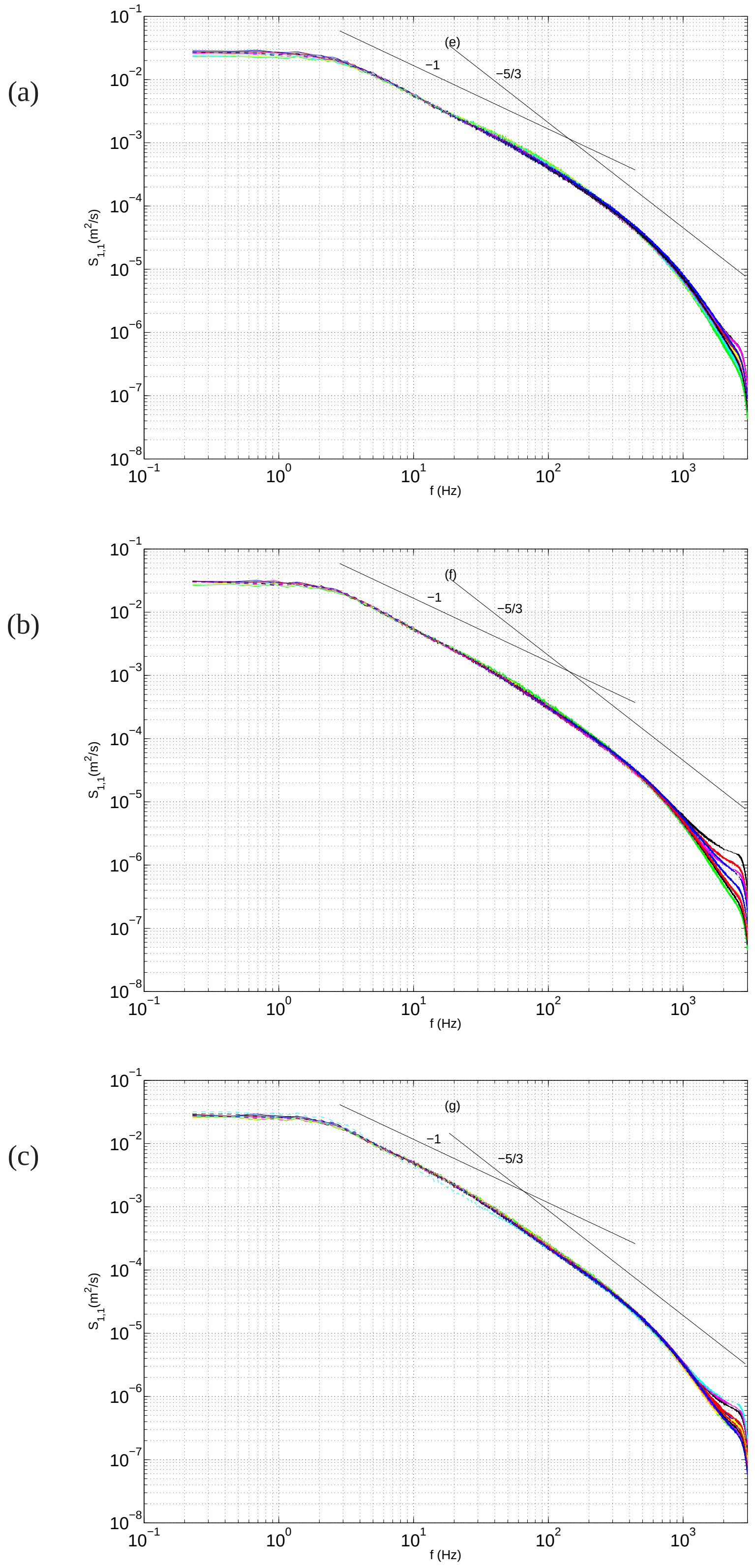

Figure 4.7: Frequency spectra of the fourth, fifth and sixth rows of hot-wire rake about y/δ of (a): 0.015, (b): 0.031 and (c): 0.063 (or y^+ of (a): 100, (b): 220 and (c): 445) at Re_θ of 19 100 respectively. Each color denotes the frequency spectrum of turbulence at different spanwise location.

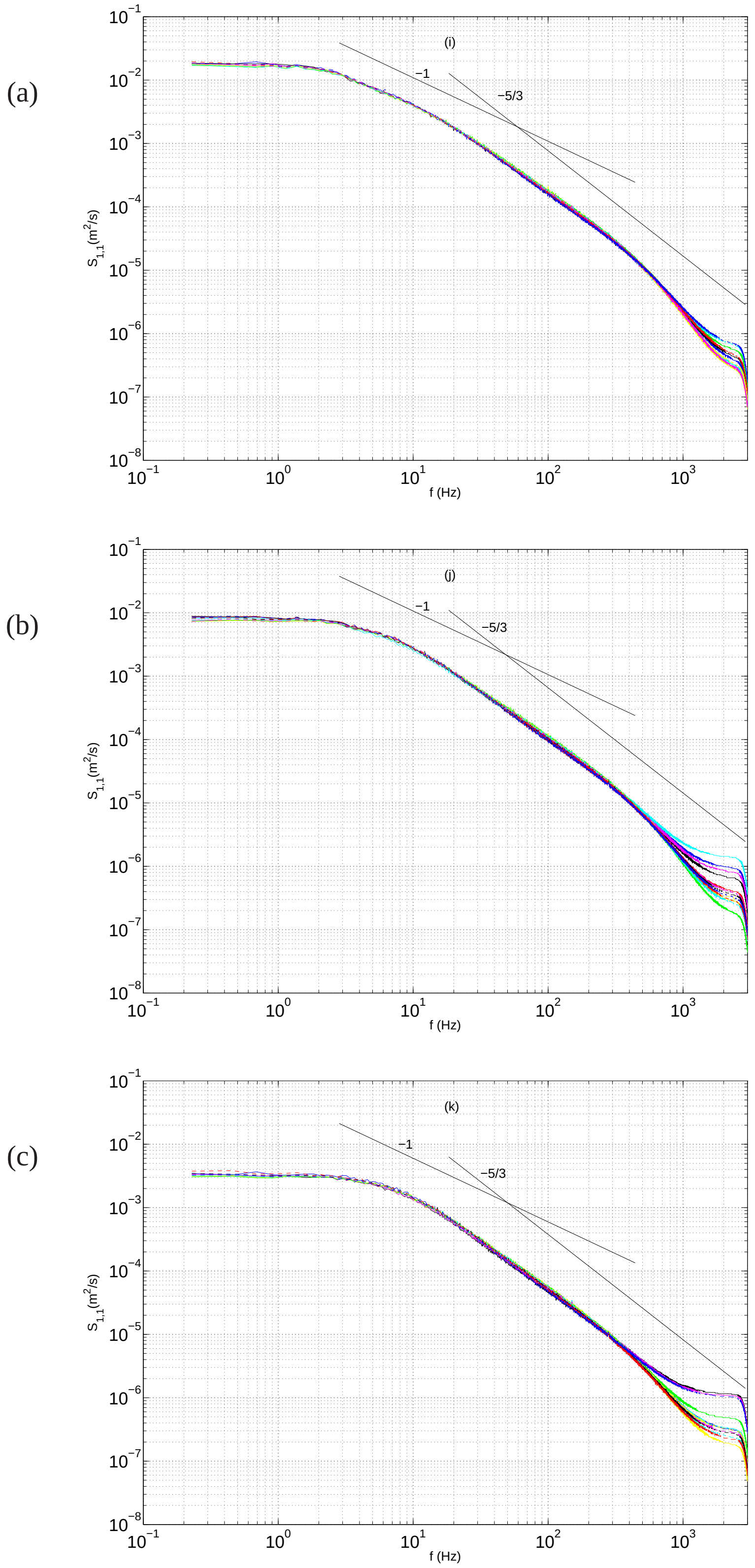

Figure 4.8: Frequency spectra of the seventh, eighth and ninth rows of hot-wire rake about y/δ of (a): 0.127, (b): 0.255 and (c): 0.511 (or y^+ of (a): 890, (b): 1805 and (c): 3618) at Re_θ of 19 100 respectively. Each color denotes the frequency spectrum of turbulence at different spanwise location.

(a)

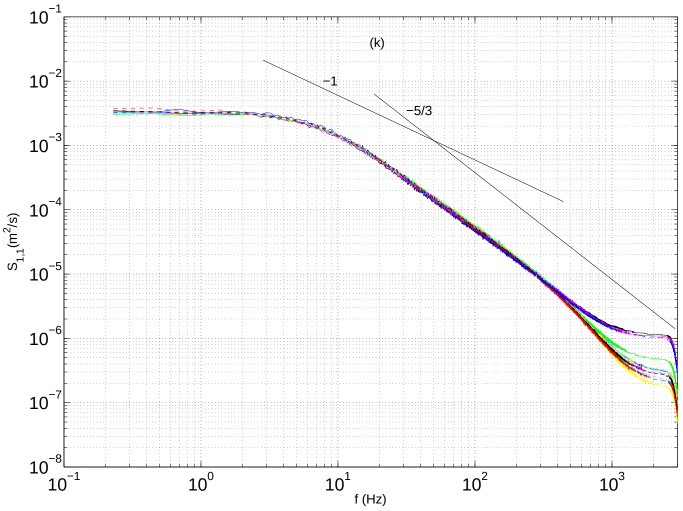

(a)

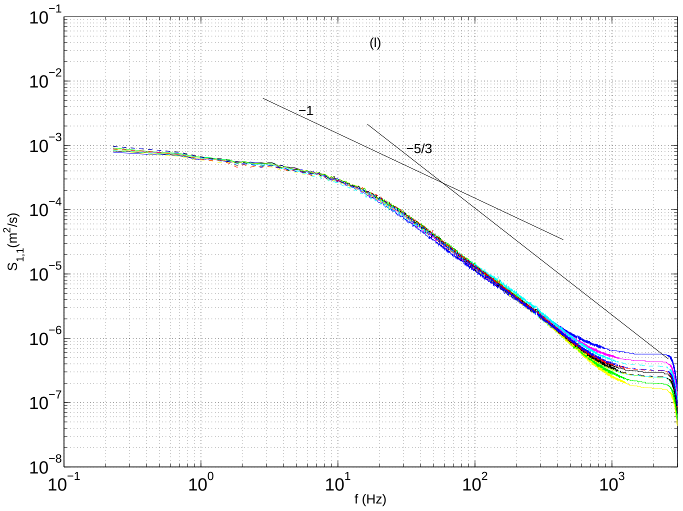

Figure 4.9: Frequency spectra of the tenth and eleventh rows of hot-wire rake about y/δ of (a): 0.767 and (b): 1.0 (or y^+ of (a): 5430 and (b): 7250)at Re_θ of 19 100 respectively. Each color denotes the frequency spectrum of turbulence at different spanwise location.

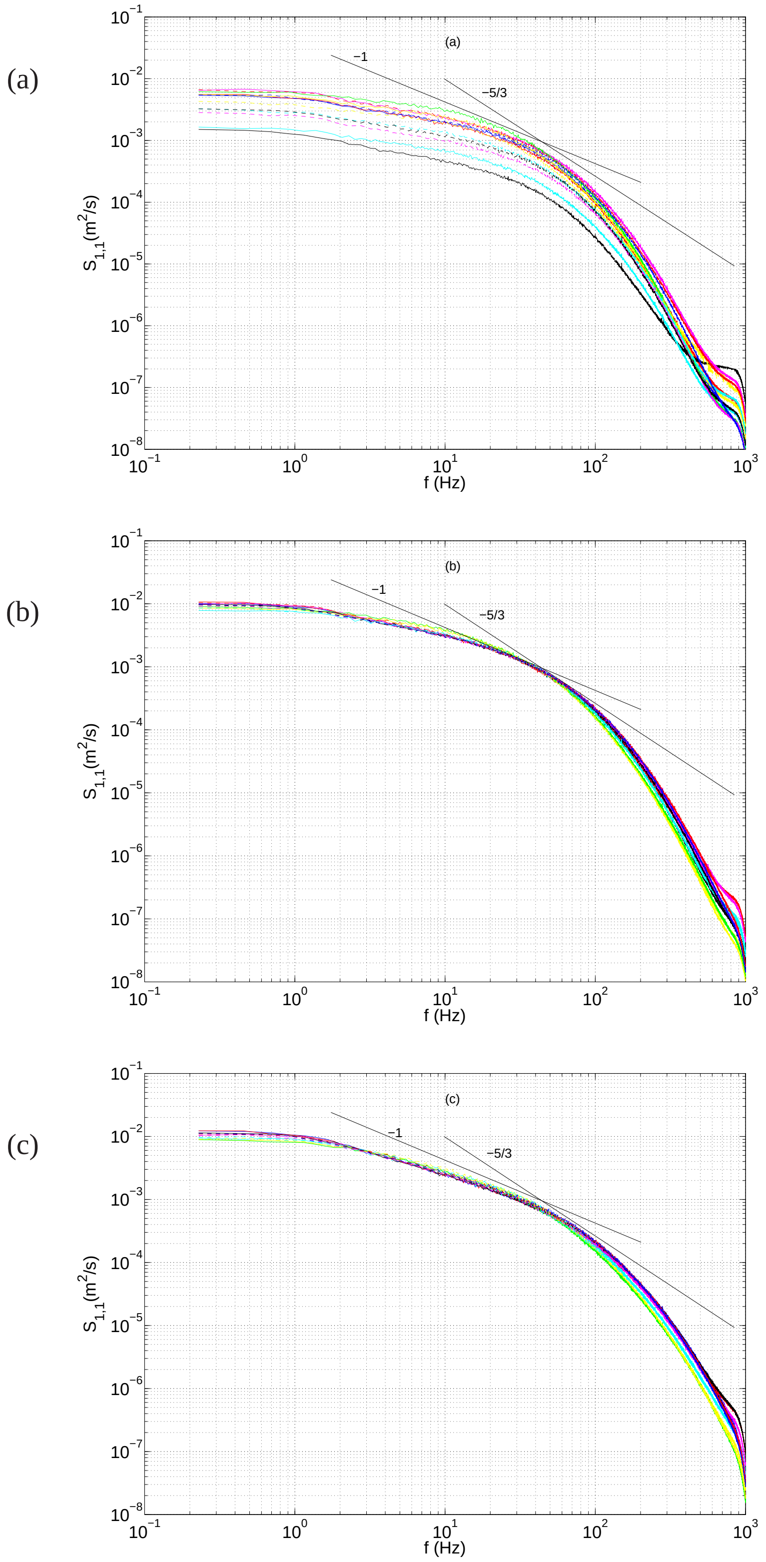

Figure 4.10: Frequency spectra of the first, second and third rows of hot-wire rake about y/δ of (a): 0.001, (b): 0.003 and (c): 0.007 (or y^+ of (a): 3.7, (b): 11 and (c): 26) at Re_θ of 9800 respectively. Each color denotes the frequency spectrum of turbulence at different spanwise location.

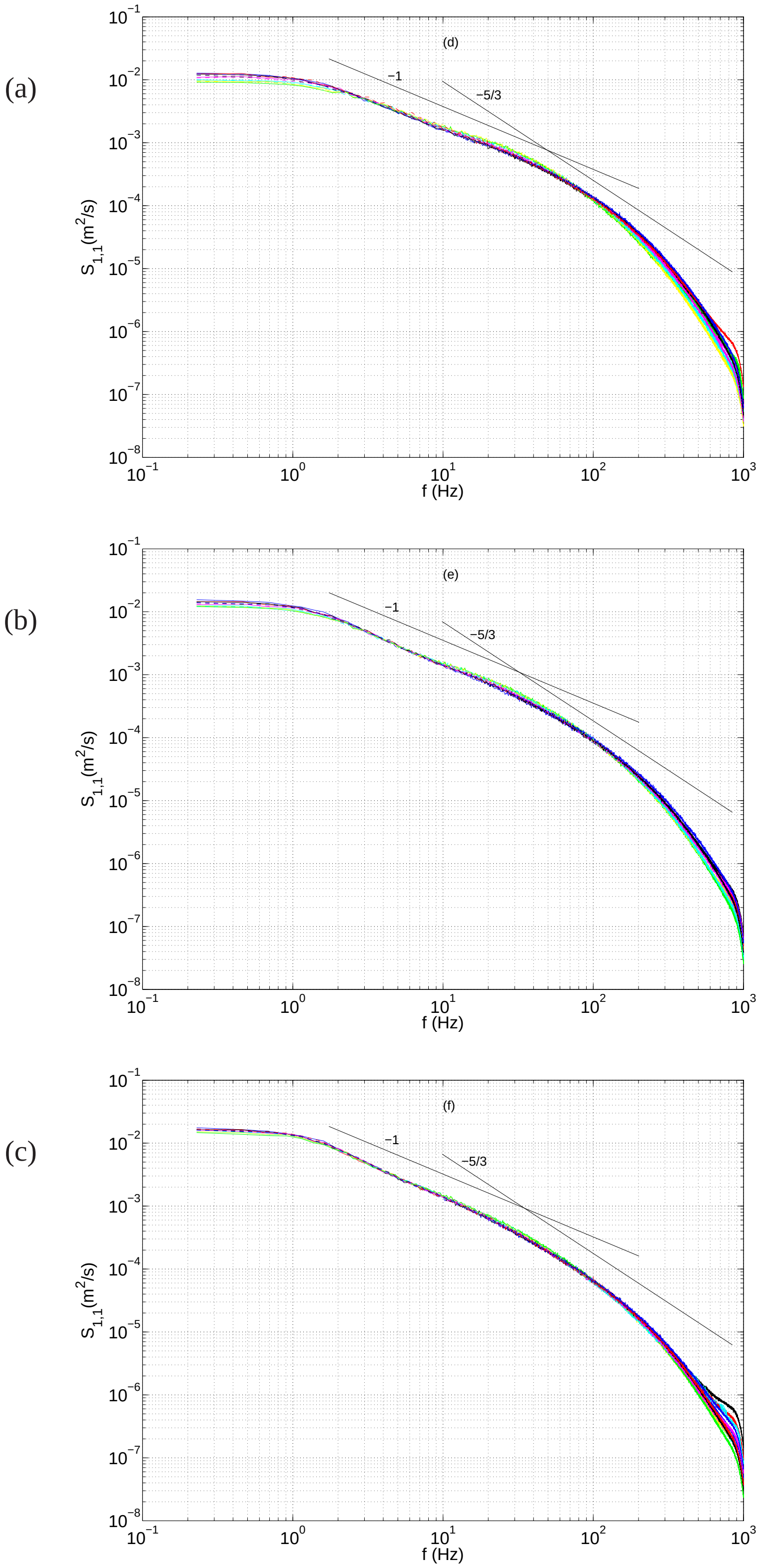

Figure 4.11: Frequency spectra of the fourth, fifth and sixth rows of hot-wire rake about y/δ of (a): 0.014, (b): 0.029 and (c): 0.059 (or y^+ of (a): 55, (b): 114 and (c): 231) at Re_θ of 9800 respectively. Each color denotes the frequency spectrum of turbulence at different spanwise location.

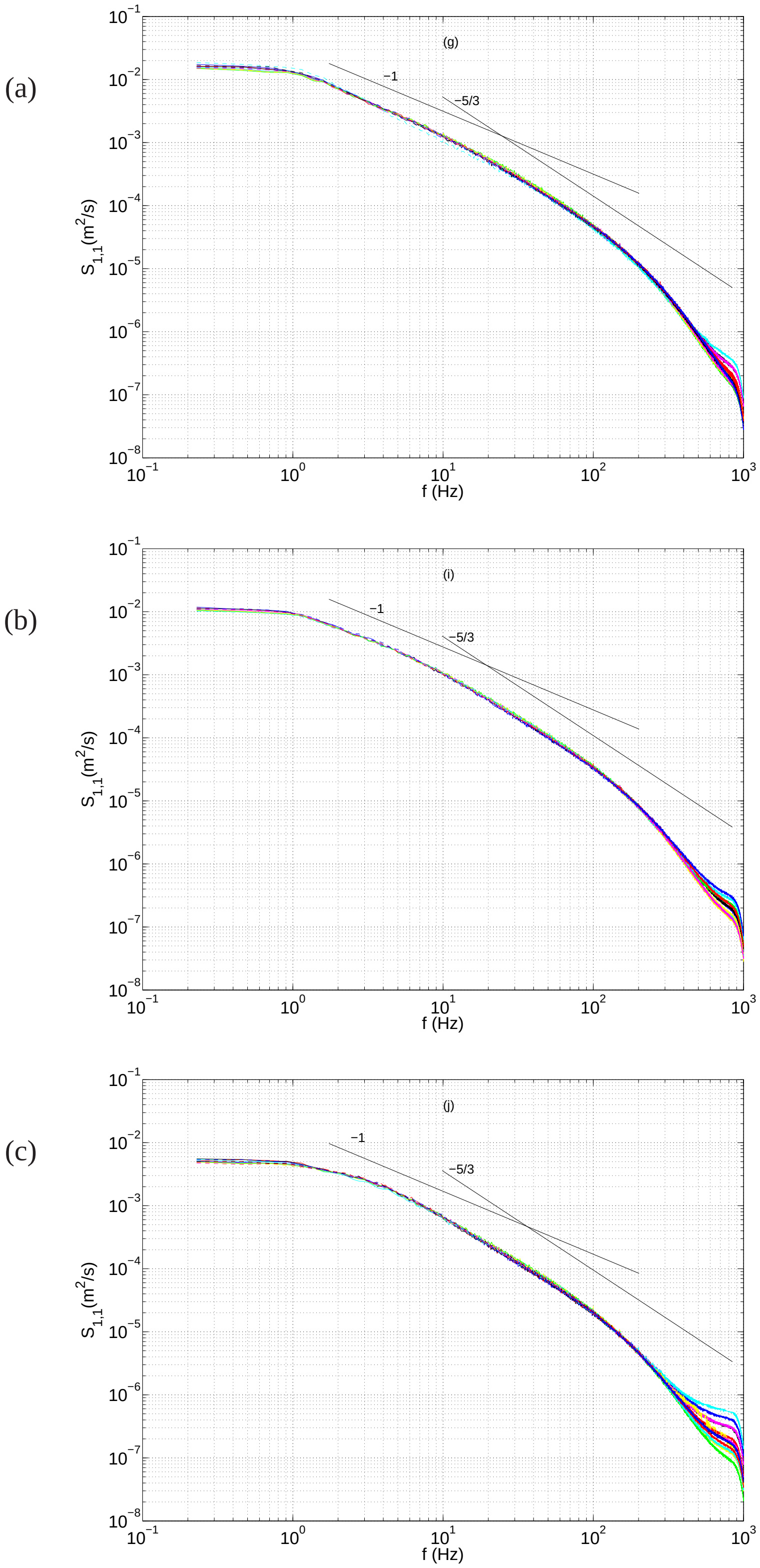

Figure 4.12: Frequency spectra of the seventh, eighth and ninth rows of hot-wire rake about y/δ of (a): 0.119, (b): 0.239 and (c): 0.479 (or y^+ of (a): 465, (b): 933 and (c): 1870) at Re_θ of 9800 respectively. Each color denotes the frequency spectrum of turbulence at different spanwise location.

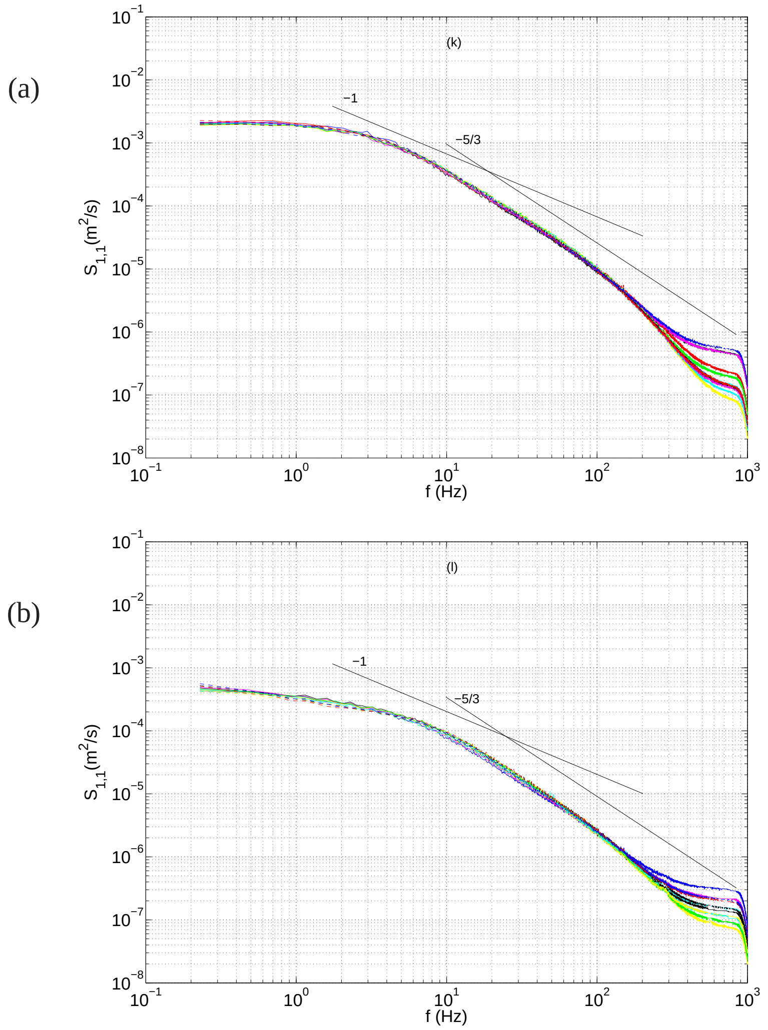

Figure 4.13: Frequency spectra of the tenth and eleventh rows of hot-wire rake about y/δ of (a): 0.719 and (b): 0.960 (or y^+ of (a): 2807 and (b): 3744) at Re_θ of 9800 respectively. Each color denotes the frequency spectrum of turbulence at different spanwise location.

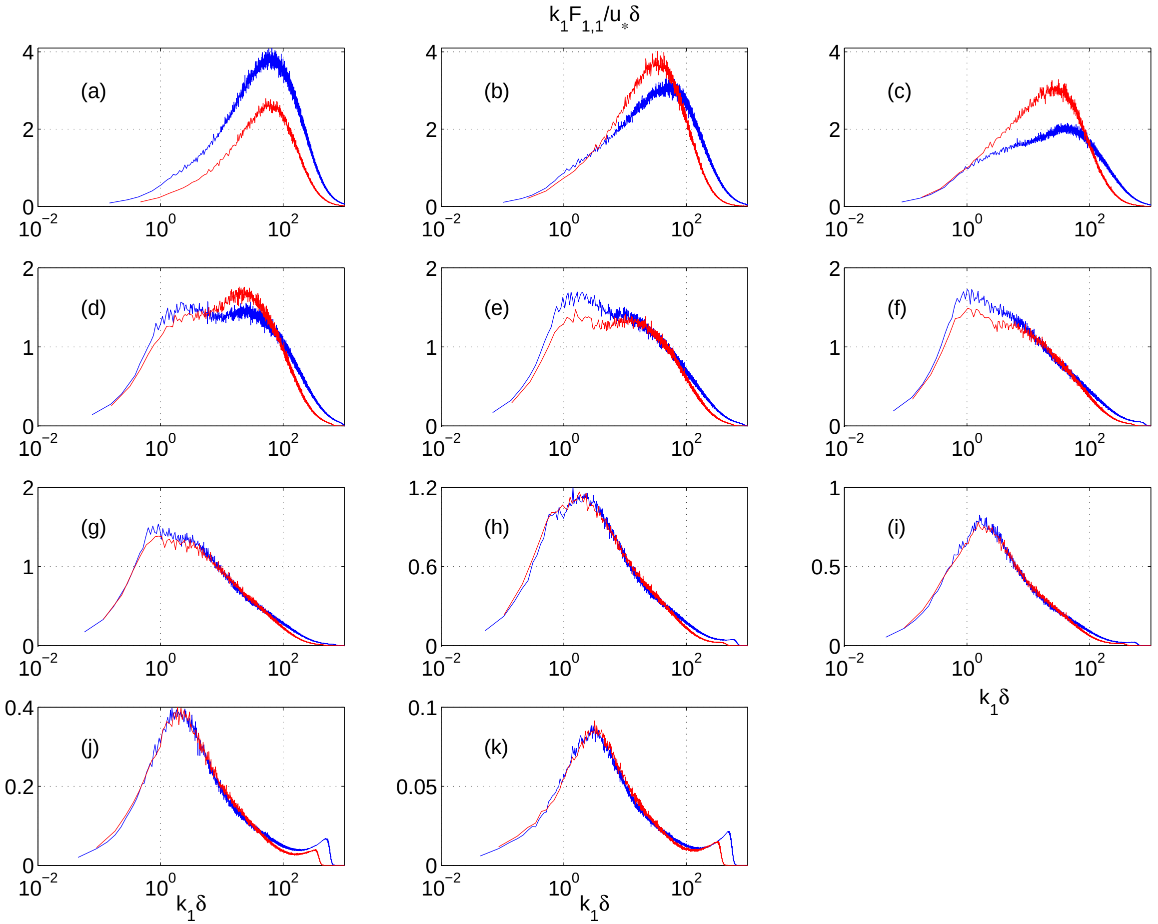

Figure 4.14: Premultiplied one dimensional wave number spectra of streamwise velocity fluctuations versus streamwise wavenumber. Blue lines: $Re_\theta = 19\ 100$; Red lines: $Re_\theta = 9800$. All the probes are located $z/\delta = 0.46$. For $Re_\theta = 19\ 100$ y^+ and y/δ are equal to (a): 7 and 0.001, (b): 22 and 0.003 (c): 50 and 0.007 (d): 100 and 0.015, (e): 220 and 0.031, (f): 445 and 0.063, (g): 890 and 0.127, (h): 1805 and 0.255, (i) 3618 and 0.511, (j) 5430 and 0.767, (k) 7250 and 1.0. For $Re_\theta = 9800$ y^+ and y/δ are equal to (a): 3.7 and 0.001, (b): 11 and 0.003 (c): 26 and 0.007 (d): 55 and 0.014, (e): 114 and 0.029, (f): 231 and 0.059, (g): 465 and 0.119, (h): 933 and 0.239, (i) 1870 and 0.479, (j) 2807 and 0.719, (k) 3744 and 0.960.

Chapter 5

Two-Point Cross-Correlation Analysis

5.1 Introduction

The large scale motion in turbulent flows has received much attention since the Townsend's "large eddy" hypothesis (see Townsend (1976)). These structures were first inferred from his observations of the long tails of the correlation function of streamwise velocity fluctuations. Townsend regarded these motions as "inactive" and thought them to be dynamically passive structures. They contained approximately 20% of the turbulence kinetic energy and made no significant contribution to the Reynolds shear stress due to small wall-normal component of velocity fluctuations occurring at these large scales. Obvious features of these large scales can be observed by eye in nature and visualized in laboratory environments. Multipoint measurements, phase averaging and conditional sampling techniques have been employed to investigate these large scale motions, as researchers have tried to extract more information about these structures other than just shapes of them. Even though quantifying these structured large scale motions, the so-called coherent structures, by the aforementioned methods has been proven to be difficult, it has been realized that these organized motions are actually dynamically important and influence physical processes within the turbulent flows. Examples include transport of scalars and momentum, mixing, heat transfer, aerodynamic noise, drag, flow-induced vibration, etc.

Recent experimental and numerical studies on the large scale features of wall-bounded turbulent flows have revealed some important results regarding the kinematics of these structures. Advancement of particle image velocimetry (PIV) as a measurement tool and the possibility of conducting high-resolution direct numerical simulations (DNS) in large computational boxes have made it possible to address some of the open questions related to these large scale structures. Even though there have been many laboratory experiments and numerical simulations, most of them have actually been performed at small or intermediate Reynolds numbers. However, turbulence scales in wall-bounded flows have a great variety ranging from the viscous length to the boundary layer thickness. Furthermore, this variation also is a function of the Reynolds number so that the higher the Reynolds number, the greater the difference between sizes. Since most of the industrially important problems are high Reynolds number flows, it is very crucial to perform high Reynolds number experiments and simulations to be able to address these issues correctly.

A recent and detailed review by Adrian (2007) provides the current state of knowledge on the large scale organized features in wall bounded flows. These large scale motions can range from one boundary layer thickness, δ, to the scales on the order of ten boundary layer thickness, or more. Some of the suggested coherent and energetic structures are, for example, low and high momentum streaks, bulges, hairpins, quasi-streamwise vortices, and elongated structures in the log-layer, and even in the wake region of the boundary layer. The most important aspects of large scale motions as documented by Blackwelder & Kovaszny (1972) are their contributions to the turbulence kinetic energy, such as approximately 50% of the kinetic energy due to streamwise fluctuations, and almost 80% of the Reynolds shear stress in the outer layer of the turbulent boundary layer.

Early investigations by Favre *et al.* (1957*b*,*a*, 1967) on the large scale structures of turbulent boundary layers using two-point space-time correlation analysis documented a large aspect ratio of the space-time contour lines along the mean flow direction (both upstream and downstream). They also noted transverse and lateral dimension of these elongated contour lines being on the same order of magnitude. Even though the long tails of autocorrelation functions indicated long structures in the streamwise direction, two-point space-time correlations provided a better picture of the dimensions of these scales. For this reason, Kovasznay *et al.* (1970) utilized the two-point space-time correlations maps for very long separations: first identify the largest scale of motions, and second to suppress the contributions of small scale structures. Their study revealed that individual bulges in the turbulent boundary layer were three-dimensional and elongated in the streamwise direction. These elongated structures were on the order of the boundary layer thickness with an aspect ratio of 2:1.

These long structures in the wall bounded flows created a momentum deficit, which is usually referred as low speed streaks. Kline *et al.* (1967) showed the low speed streaky structures in the near wall region and came up with a proposal describing their relation to ejection and sweep phenomena. The break-up of streaks in the near wall region after being lifted-up were thought to be a main turbulence kinetic energy source in the near wall region. These observations supported the counter-rotating vortices proposed by Bakewell & Lumley (1967) of a dominating large scale structure with significant amount of turbulence kinetic energy. The low speed streaks are associated with long quasi-streamwise vortices, which are actually the legs of the hairpin vortices proposed by Theodorsen (1952) as a coherent structure of turbulence in the near wall region (Hommema & Adrian (2002)). The long quasi-streamwise vortices induce a velocity field around itself, resulting in low momentum fluid from the near wall moving upward, hence forming low-speed streaky structures.

PIV measurements of a turbulent boundary layer from the buffer layer to the top of the log layer by Tomkins & Adrian (2003) revealed the large scale low speed structures in the streamwise direction as the dominant feature of turbulence. They were also able to identify the difference between the near-wall streaky structures and highly elongated low speed (or momentum deficit) structures of the log layer. The latter one was found to be larger than 500 viscous wall units in the spanwise direction, which is five times larger than the spacing of low speed streaks in the near wall region as documented by Kline *et al.* (1967). Similar observations were documented by Ganapathisubramani *et al.* (2003, 2005) using PIV measurements in the log layer of turbulent boundary layers. These very long elongated structures have been attributed to the packets of hairpin vortices, which are found to be the largest source of Reynolds shear stress within the log layer (cf., Zhou *et al.* (1996, 1999); Adrian *et al.* (2000); Tomkins & Adrian (2003, 2005); Ganapathisubramani *et al.* (2003)). These findings supported Head & Bandyopadhyay (1981), who essentially visualized the extension of hairpin vortices into the outer layer.

Recent findings on the large scale elongated structures in the log layer suggest that these low speed streaks may have a length scale up to twenty boundary layer thicknesses (or channel width and pipe diameter). The PIV images collected by the experiments mentioned above had a finite window on the order of one boundary layer thickness, so these elongated structures exceeded the limits of the windows. Therefore, hot-wire or hot-film anemometry measurements in connection with the Taylor's frozen field hypothesis have been carried out to find out about the length of these energetic features of the wall bounded turbulence. In this context, Kim & Adrian (1999) studied the large scale features of turbulent pipe flow within the log layer using hot-film measurements. They documented that the streamwise uniform momentum zone had wavelengths up to fourteen pipe radii, and hence named these structures Very Large Scale Motions (VLSM). They also proposed a conceptual model for the VLSM in connection with the hairpin vortex and vortex packets. According to this picture, VLSM appear once the vortex packets line up in the boundary layer and connect the low momentum regions of each of these packets. Following this study, Guala *et al.* (2006) investigated the large and very large scale of motions in the turbulent pipe flow using cross-hot-film measurements and smoke visualizations. They also noted VLSM having wavelengths more than sixteen pipe radii. They made a distinction between the very large and large scale motions such that the latter had characteristic wavelength of two-three pipe radii. One of their important findings was the turbulence kinetic energy and Reynolds stress largely carried by these very large scale motions. In particular, 50% of the turbulence kinetic energy and more than 50% of the Reynolds shear stress are carried by these very large scales, consistent with the earlier observations of Blackwelder & Kovaszny (1972). More recently, meandering of the very large scale motion of wall bounded turbulence revealed that the size of these large scales might go up to 25 boundary layer thickness, channel width or pipe radius (Hutchins & Marusic (2007); Monty *et al.* (2007)). Hutchins & Marusic (2007) also showed how deficient the single point statistics are for capturing the VLSM and its meandering features. Like the experimental studies showing the VLSM in wall bounded flows, the very large DNS simulation by J. Jimenez and his group reported similar findings from the numerical experiments on the fully developed channel flows (e.g., del Álamo & Jimenez (2003); del Álamo *et al.* (2004)).

The current study aims to investigate these large and very large scales of motion in a high Reynolds number turbulent boundary layer using the novel hot-wire rake of 143 single wire probes. Most of the aforementioned investigations are low Reynolds number experiments, and as pointed out earlier, there is a clear need for investigating these large scale structures and understanding their kinematical and dynamical properties in a high Reynolds number turbulent boundary layer. The current study also aims to fill the gap between these intermediate Reynolds number and high Reynolds numbers. The large LML wind tunnel provides a very thick boundary layer of about 30 cm with resolvable small scales. The hot-wire rake with many probes distributed on an array enables us to look at both spatial and temporal characteristics of the turbulent boundary layers by means of multiple-point cross-correlation analysis. The results presented in this chapter are of two-point cross-correlations observed in a turbulent boundary layer at Reynolds number based on momentum thickness, Re_θ, of 19 100 and 9800.

5.2 Computation of Two-Point Cross-Correlations

The two-point cross-correlation tensor for turbulent boundary layers in a Cartesian coordinate system can be written as follows:

$$R_{i,j}(x,x',y,y',z,z',t,t') = \langle u_i(x,y,z,t)u_j(x',y',z',t')\rangle \tag{5.1}$$

where the subscripts i and j present different components of fluctuating turbulent velocity (u, v, w). Here u, v and w are the turbulent velocity components in the streamwise, wall-normal, and spanwise directions respectively. $\langle\,\rangle$ represent the ensemble averaging, and $'$ denotes different spatial positions in x, y, z coordinates and a different time. Since the turbulent boundary is stationary in time, and statistically homogeneous in the spanwise direction, the two-point cross-spectral tensor is a function of separation in these directions. Since $\tau = t' - t$ and $\Delta z = z' - z$, therefore Eq. (5.1) becomes:

$$\widetilde{R}_{i,j}(x,x',y,y',\Delta z,\tau) = \langle u_i(x,y,z,t)u_j(x',y',z+\Delta z,t+\tau)\rangle \tag{5.2}$$

Due to stationarity, Fourier transformation of the two-point cross-correlation in time yields the two-point cross-spectral tensor which can be written as below:

$$S_{i,j}(x,x',y,y',\Delta z,f) = \int_{-\infty}^{\infty} \widetilde{R}_{i,j}(x,x',y,y',\Delta z,\tau)e^{-i2\pi f\tau}d\tau \tag{5.3}$$

where f is the frequency corresponding to τ.

Considering only one downstream position results in treating the $x = x'$ in Eq. (5.3) as a parameter. Thus, Eq. (5.3) reduces to:

$$S_{i,j}(y,y',\Delta z,f) = \int_{-\infty}^{\infty} R_{i,j}(y,y',\Delta z,\tau)e^{-i2\pi f\tau}d\tau \tag{5.4}$$

As mentioned in the experimental setup section (chapter 2) the hot-wire rake was comprised of single wire probes, hence only the streamwise component of turbulent velocity was measured. Therefore, the subscripts i and j in the equations above will be omitted for simplicity.

The analysis technique following the equations listed before can be described as follows:

1) Instantaneous streamwise velocities were measured at 143 point simultaneously by the hot-wire rake which was also synchronized with stereo-PIV systems.

2) Fourier transformation of velocity signals was performed in time for finite size record length:

$$\hat{u}(y,z,f) = \int_{-T/2}^{T/2} u(y,z,t)e^{-i2\pi ft}dt \tag{5.5}$$

where T is the record length for each block of data taken into Fourier transformation. Even though the length of each block of hot-wire data was 6 seconds with 180,000 samples, for computational efficiency each block was divided into more blocks with 16,384 samples corresponding to 0.55 seconds record length each. A fast Fourier transformation (FFT) algorithm was used to obtain the Fourier coefficients.

3) These steps were repeated for all possible configuration obtained from the hot-wire rake which was 143^2 =20,449 in our case.

4) Two-point cross-spectral estimates were computed and then ensemble (or block) averaging was performed:

$$S_{1,1}(y,y',z,z',f) = \frac{\langle \hat{u}(y,z,f)\hat{u}^*(y',z',f)\rangle}{T} \tag{5.6}$$

where $\langle\ \rangle$ and * represent the ensemble averaging and complex conjugate respectively. In this study the total number of blocks was 1000, resulting in 3% error of the estimator for the two-point cross-spectral tensor, $S_{1,1}(y,y',z,z',f)$.

5) To map the two-point cross-spectra from frequency domain back to the time domain, inverse Fourier transformation was performed to obtain the two-point cross-correlation as a function of separation in time, τ:

$$R_{1,1}(y,y',z,z',\tau) = \int_{-T/2}^{T/2} S_{1,1}(y,y',z,z',f)e^{i2\pi f\tau}df \tag{5.7}$$

6) The frozen field hypothesis of Taylor is implemented and two-point cross-correlation with separation Δx in streamwise coordinate was obtained:

$$R_{1,1}(\Delta x, y, y', z, z') = R_{1,1}(y, y', z, z', \tau = -\Delta x / U_c) \tag{5.8}$$

where U_c is the convection velocity. As documented by Krogstad *et al.* (1998) using two-point correlations in a turbulent boundary layer, the local mean velocity is a good approximation to the convective flow velocity. A recent study by Dennis & Nickels (2007) on the use of Taylor's hypothesis showed how accurate the field can be represented using the frozen field idea, and it was found to work very well in the log-layer of wall bounded flows.

5.3 Two-Point Correlations in the Streamwise - Spanwise Plane

In this section we present streamwise-spanwise (XZ-plane) correlations. The correlations were obtained for constant wall normal positions, meaning that $y=y'$. Spanwise coordinate of the reference probe was always $z=0$. The data, or the correlation maps, are the two-point cross-correlation coefficients defined as follows in its most general form as:

$$\rho_{1,1}(\Delta x, \Delta y, \Delta z, \tau) = \frac{R_{1,1}(x, x', y, y', z, z', t, t')}{R_{1,1}(x, x, y, y, z, z, t, t)} = \frac{\langle u_1(x, y, z, t) u_1(x', y', z', t') \rangle}{\langle u_1(x, y, z, t) u_1(x, y, z, t) \rangle} \tag{5.9}$$

This was simply computed by dividing the two-point cross-correlations by its maximum value on the plane, which was found when the separation in space and time were zero. The maximum value in each two-point correlation map is one, therefore the actual maximum correlation found in each plane will be displayed separately below.

Figures 5.1 and 5.2 presents the two-point cross-correlation coefficients in the XZ-plane. The first figure shows the correlation contour lines from y^+ of 7 to 1805 ($\sim 0.2\delta$) for the high Reynolds number case. The second figure shows the correlation coefficients for the last three wall-normal locations closest to the edge of the boundary layer. Since these are the correlation coefficients, the maximum value found in each of these figures is 1, representing the value for the correlation of the probe by itself at the same instant in time, or at the same streamwise location (with use of Taylor's hypothesis). Therefore, these figures should be discussed together with figure 5.5, where a slice through the real correlation contour lines at $\Delta z = 0$ is performed along the x direction for different wall-normal positions. The peak found in each of these figures represents the denominator of Eq. (5.9), which is the variance of the streamwise velocity fluctuations at the corresponding wall-normal position.

As it can be seen in the figures, the size of the positive correlations contour lines within the viscous sublayer is quite limited between $\pm 0.5\delta$ in length in the streamwise direction, and $\pm 0.25\delta$ in width in the spanwise direction. We observe almost no negative correlation in the planes shown in figures 5.1(a&b). The contour lines are slightly elongated in the streamwise direction. Elongation of the contour lines becomes more obvious as the plane moves away from the wall. Once the plane is above the buffer layer, shown in figure 5.1(c), very long elongated correlations appear. These elongated large correlation contours are negative, which actually corresponds to the long tails of autocorrelation functions observed by Townsend (1976).

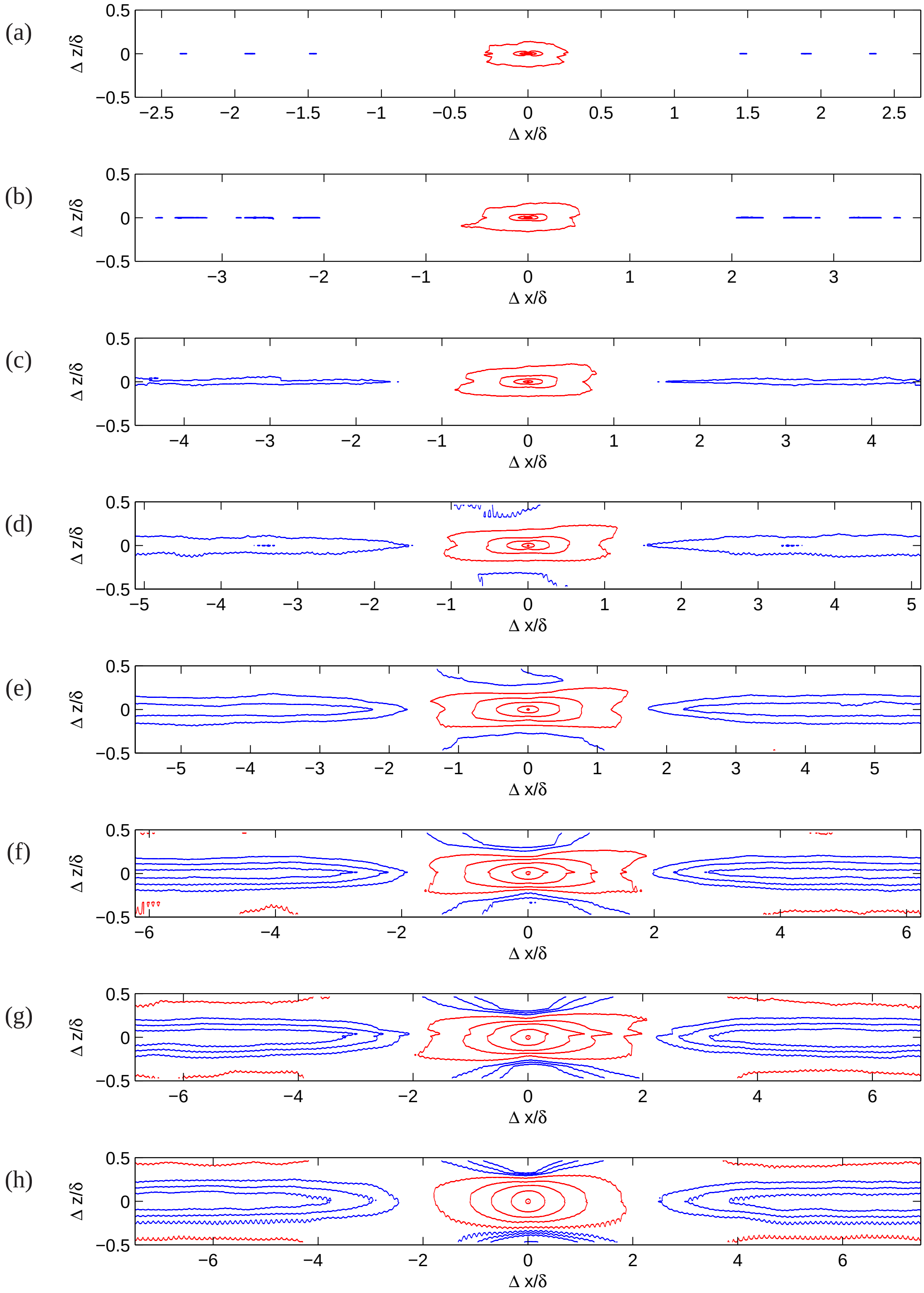

Figure 5.1: Two-point cross-correlation coefficients (XZ-plane) at constant wall-normal positions at Re_θ of 19 100. The figures present the correlations between the probe located at z=0 and the probes at the same y^+ location on each plane. (a) $y^+ = 7$, (b) $y^+ = 22$, (c) $y^+ = 50$, (d) $y^+ = 100$, (e) $y^+ = 220$, (f) $y^+ = 445$, (g) $y^+ = 890$, (h) $y^+ = 1805$, $y = 0.2\delta$. Red contour lines denote positive values [0.025 0.1 0.2 0.4 0.8 1.0]; Blue contour lines denote negative values [-0.025 -0.05 -0.075 -0.15 -0.20].

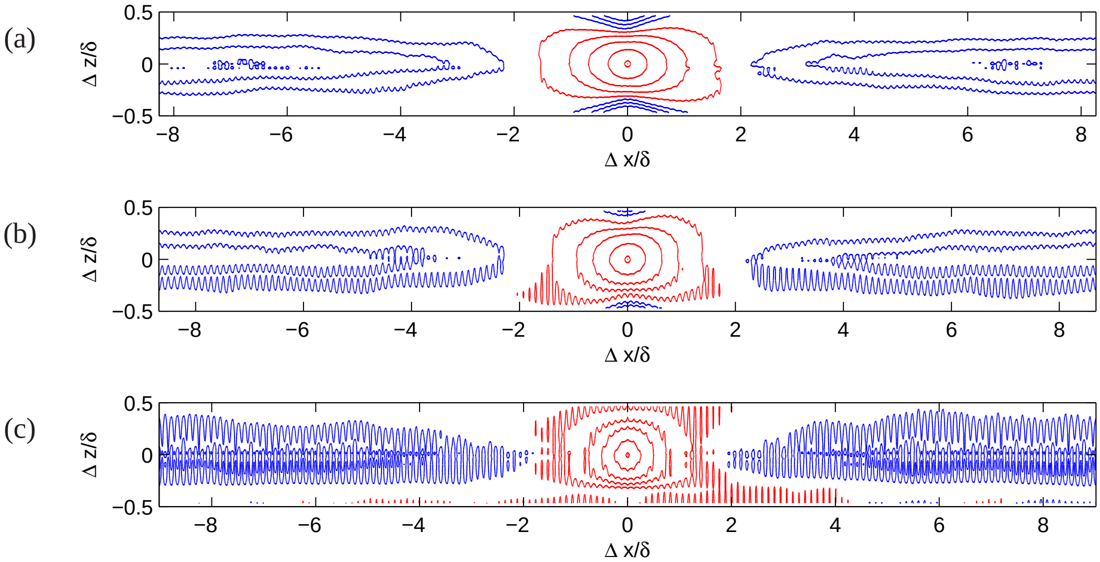

Figure 5.2: Two-point cross-correlation coefficients (XZ-plane) at constant wall-normal positions. The figures present the correlations between the probe located at z=0 and the probes at the same wall-normal location on each plane at Re_θ of 19 100. (a) y= 0.5δ, (b) y= 0.75δ, (c) y= δ. Red contour lines denote positive values [0.025 0.1 0.2 0.4 0.8 1.0]; Blue contour lines denote negative values [-0.025 -0.05 -0.075 -0.15 -0.20].

The contour lines representing the correlation coefficients get wider in the spanwise direction as the plane moves within the log layer towards the freestream. If the strength of the two-point cross-correlations are not taken into account, the elongated structures exists everywhere in the turbulent boundary layer from the top of the buffer layer to the freestream (or simply in the region where outer equations are the governing equations for mean momentum equations). Figure 5.5 shows that within the log layer, the maximum positive correlation on the plane is between 0.5 and 0.6. This suggests that the upper part of the log layer and the bottom part of the outer layer are the regions with the strongest elongated negative correlations. In this region, the ratio of the smallest correlation (largest blue correlation) to the peak at $\Delta x = \Delta z = 0$ has its maximum value, meaning they are very strong relative to the maximum correlation. Even at the wall-normal position of 0.2δ, as presented by figure 5.1(h), there is significant strength and length in these structures elongated in the streamwise direction.

Since the turbulence intensity goes down substantially in the upper part of the boundary layer (as shown by the peaks of the two-point cross-correlations in figure 5.5(i,j&k), the correlation coefficients presented in figure 5.2 demonstrate the weakness of the correlations in the region of half of the boundary layer thickness to the top of the boundary layer compared to the other XY-planes within the log layer. Interestingly, the footprints of the elongated structures still exist in the second half of the turbulent boundary layer. The last two planes close to the freestream show some oscillation in the contour lines. This is mainly due to two reasons; first very low level of turbulence at these wall-normal positions so that electronic noise becomes visible and correlations are very sensitive to the disturbances from the freestream only, and second the high level of intermittency in the region. Even though the statistics presented here are computed over 1000 ensembles, the oscillations are still present, suggesting that the source of oscillations is not lack of samples. In fact, the same electronic noise exists at each probe; however, due to high levels of turbulence and correlation, they do no appear in the figures.

5.4 Correlations in the Streamwise - Wall-normal Plane

Figures 5.3 and 5.4 present the two-point cross-correlation coefficients of the high Reynolds number case in the same fashion as shown in figures 5.1 and 5.2. Here the contour lines show the two-point cross-correlation coefficients on the streamwise-wall-normal plane located at $z=z'=0$. Each of the subplots presents the cross-correlations computed using one reference probe and all the other probes in the wall-normal direction at the same spanwise location, thus, $\Delta z=0$. Note that the abscissa shows the streamwise distance, both upstream and downstream, and the extent of the axis increases as the reference probe moves away from the wall. This is due to increasing convection velocity from wall to freestream.

One interesting observation is that the contour lines for the XY-plane are confined into a relatively small field within the buffer layer, which is consistent with figure 5.1(a&b). The smallest area covered by the contour lines is found for the two-point correlations computed using the probe closest to the wall as a reference probe, as can be seen in figure 5.3(a). The correlation contours cover larger areas as the reference probe moves away from the wall. Similar to the previous XZ-plane correlations, elongated correlations covering almost the entire boundary layer are observed once the reference probe is in the log-layer and above. The area covered by the contour lines representing the positive correlations on this plane is always larger than that on the XZ-plane. This is attributed to the velocity gradient that exists along the wall-normal axis. Higher convective velocities with an increasing wall-normal distance result in faster propagation of the information for higher wall-normal position. The other important large scale structure is the bulge, which shows up in the shape of the positive contour lines. In the log layer, the positive correlations denoted by red contour lines suggests a length scale on the order of five boundary thicknesses in the streamwise direction and up to 0.75 boundary layer thicknesses in the wall normal direction.

Similar to the elongated structure correlations found on the XZ-plane, negative correlations appear above the buffer layer. They get stronger as the reference probe moves into the log layer and the bottom part of the outer layer. Since the values of the contour lines and the peak values on each of the figures are the same as in figures 5.1 and 5.2, we see the same elongated structures; however, they are clustered in this case, because each XY-plane covers the entire boundary layer.

Figure 5.4 displays important features. First of all, the correlation values at each subplot is very small compared to the ones obtained in the log layer. Nevertheless, they show how the intermittent flow in the outer region of boundary layer turbulence penetrates into the entire boundary layer, including the near wall region.

A better picture of the relative strength of these elongated correlations with respect to the peak found on each XZ-plane, together with the relative size of the peaks among themselves, is provided by figure 5.5. Even though there are long tails in the correlations for within the buffer layer, their magnitudes are very small in comparison to the peaks found at the other wall-normal positions, see for instance figures 5.5(a&b). In the log layer, the magnitude of the tails becomes larger, but in the negative direction. Also the peak values go down, hence the relative importance increases significantly. The last three cross-sections obtained from the planes above half of the boundary layer thickness are substantially smaller than the others presented.

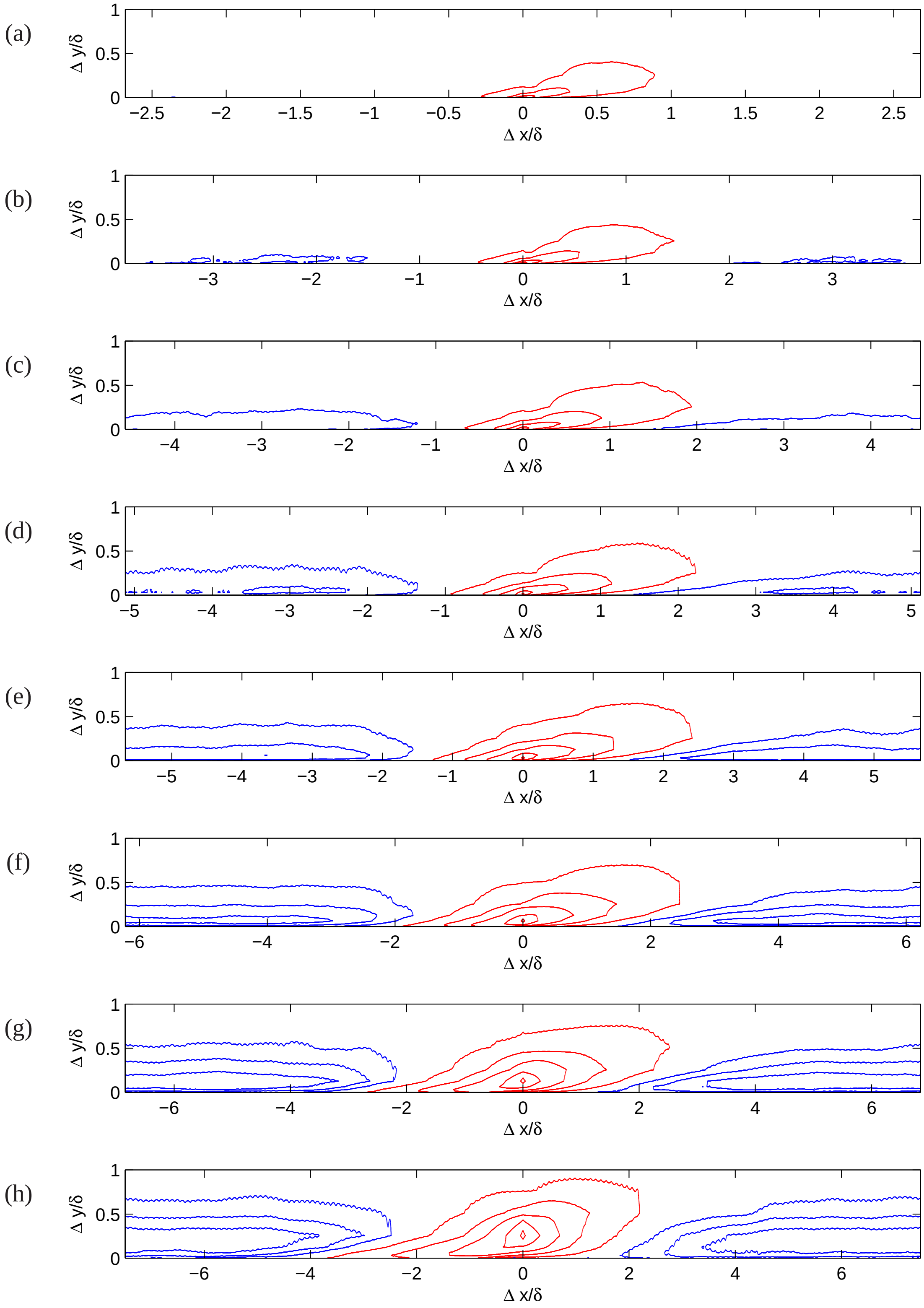

Figure 5.3: Two-point cross-correlations (XY-plane) at z=0. The figures present the correlation between the probe at one wall-normal position and the rest the probes at the same spanwise location at Re_θ of 19 100. (a) $y^+ = 7$, (b) $y^+ = 22$, (c) $y^+ = 50$, (d) $y^+ = 100$, (e) $y^+ = 220$, (f) $y^+ = 445$, (g) $y^+ = 890$, (h) $y^+ = 1805$, $y = 0.2\delta$. Red contour lines denote positive values [0.025 0.1 0.2 0.4 0.8 1.0]; Blue contour lines denote negative values [-0.025 -0.05 -0.075 -0.15 -0.20].

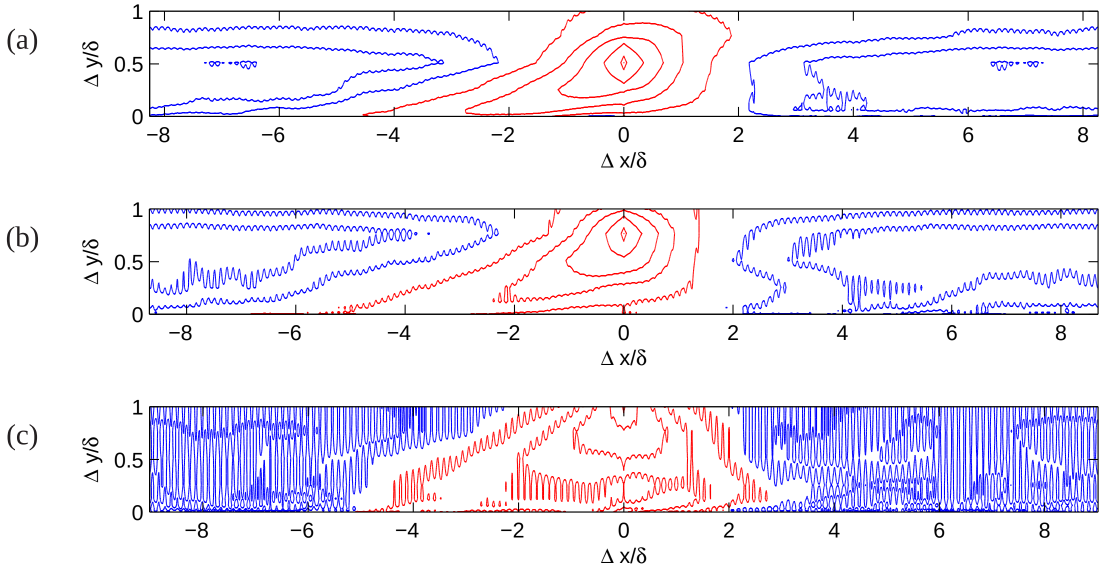

Figure 5.4: Two-point cross-correlations (XY-plane) at z=0. The figures present the correlation between the probe at one wall-normal position and the rest the probes at the same spanwise location at Re_θ of 19 100. (a) y= 0.5δ (b) y= 0.75δ (c) y= δ. Red contour lines denote positive values [0.025 0.1 0.2 0.4 0.8 1.0]; Blue contour lines denote negative values [-0.025 -0.05 -0.075 -0.15 -0.20].

5.5 Correlations in the Wall-normal - Spanwise Plane

Two-point cross-correlation coefficients for the wall-normal-spanwise (YZ) plane of the high Reynolds number experiment are shown in figures 5.6 and 5.7. These figures represent the correlation coefficients computed for a reference probe and all the other probes on the same plane. The reference probe is always at z=0 and moves from the wall to the freestream. The scale used in each of the subplots is the same, and varies between -0.1 and 1. The cross-correlations are normalized by the maximum correlation on the same plane, which is the same as in the previous figures, simply the variance at the point of the reference probe. The y axes in the figures are normalized by the viscous scale, δ_ν.

Figures 5.6(a&b) present the results within the buffer layer of the turbulent boundary layer. We see very a very narrow correlation between the first two probes located at y^+ of 7 and 22 and the third probe on the same row located at y^+ of 50. The correlation between these two positions in the buffer region is very large because the maximum variance of fluctuating velocity is also found in this region. The correlation does not extend very far in either the spanwise direction or in the wall-normal direction. Once the reference probe moves to y^+ of 100, we see the development of correlations between the probes, covering a larger field on the plane. Since the variance within the log layer does not change much, we can conclude that the largest structures are found in this layer. Above y^+ of 100 and below of wall-normal distance of 0.2δ, the large scale motions are quite active as can be seen in figures 5.6(e&f) and 5.7(a&b).

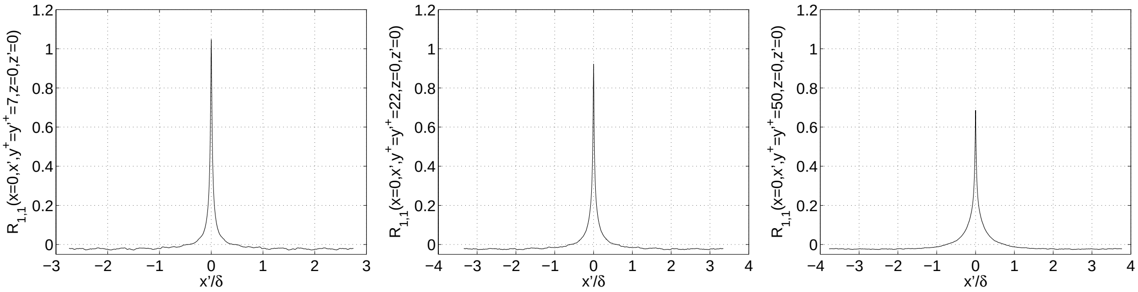

(a) $y^+ = 7$, $y/\delta = 0.001$.

(b) $y^+ = 22$, $y/\delta = 0.003$.

(c) $y^+ = 50$, $y/\delta = 0.007$.

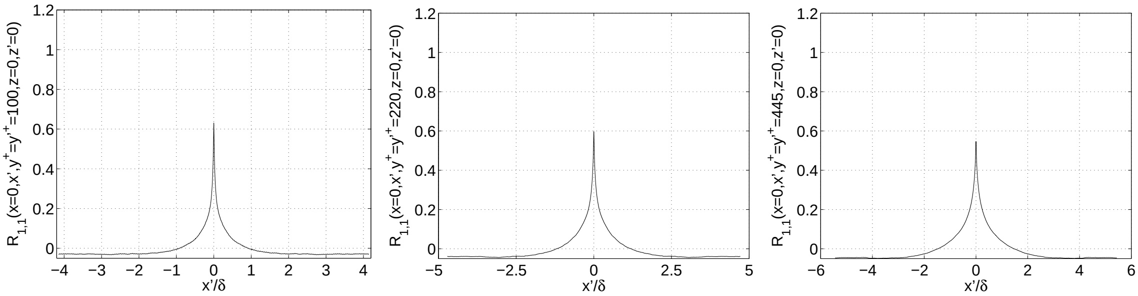

(d) $y^+ = 100$, $y/\delta = 0.015$.

(e) $y^+ = 220$, $y/\delta = 0.031$.

(f) $y^+ = 445$, $y/\delta = 0.063$.

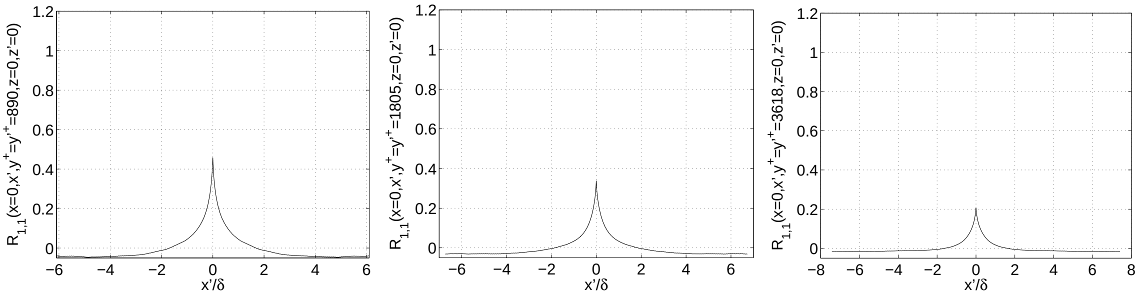

(g) $y^+ = 890$, $y/\delta = 0.127$.

(h) $y^+ = 1805$, $y/\delta = 0.255$.

(i) $y^+ = 3618$, $y/\delta = 0.511$.

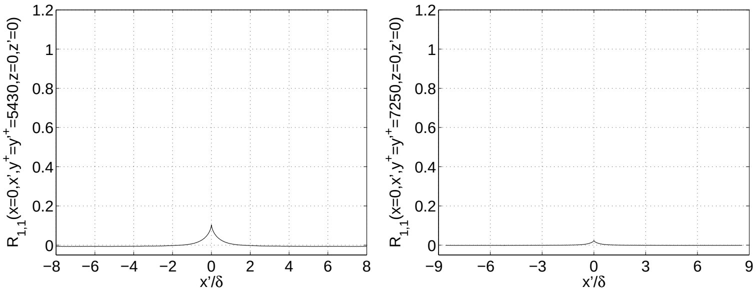

(j) $y^+ = 5430$, $y/\delta = 0.767$.

(k) $y^+ = 7250$, $y/\delta = 1.0$.

Figure 5.5: Cross-section of figures 5.1 and 5.2 at $\Delta z = 0$ at $Re_\theta = 19\,100$.

The correlations within the outer layer as shown in figures 5.7(b,c,d&e) seems to be confined only into this region. There does not appear any significant correlation between the outer layer and inner layer. This is somewhat confusing because it is difficult to observe any of the large scale or very large scale motions on the two-point cross-correlations constructed on these planes. This might be due to how the computation is performed. The contour lines are obtained using the cross-correlations between each and every probe used in the rake. Some subset of these correlations are presented in figures 5.3-5.4. To be able to compute the correlations on the YZ-plane, the two-point cross-spectra between different probes are integrated over frequency, which finally produced the two-point cross-correlations with zero time-lag, $\tau = 0$, as given by Eq. (5.10).

$$R_{1,1}(y,y',z,z',\tau=0) = \int_{-\infty}^{\infty} S_{1,1}(y,y',z,z',f)\,df \tag{5.10}$$

The integration smears out the details and yields an average picture. Therefore, in this plane we do not observe the previous finding about the elongated large scale structures.

Figure 5.8 shows the cross-section along the spanwise direction taken from the two-point cross-correlation coefficients presented in figures 5.6 and 5.7. Each subplot of figure 5.8 represents the cross-section taken from the wall-normal position at which the reference probe was placed. Therefore, 5.8(a) is the cross section of 5.6(a) at y^+ of 7, 5.8(b) is the cross section of 5.6(b) at y^+ of 22 and so on. Here we present the actual cross-correlation values instead of the coefficients. This information is also useful in evaluating the relative strengths of each subfigure of YZ-plane cross-correlation coefficients discussed earlier. Again, the peak of each subplot of 5.8 is the correlation with zero separation both in space and time, hence it is the variance of velocity fluctuations. These peaks are equal to the peaks presented in figure 5.5.

As with the contour plots of the two-point cross-correlation coefficients with zero time-lag, each wall-normal position, or each layer of turbulent boundary layer in more general, produces distinct contour lines in the boundary layer. The picture becomes more clear in the cross-section plots presented in figure 5.8. In the buffer region, shown by figures 5.8(a&b), there is a sudden drop of correlation even with the smallest possible separation in the spanwise direction for the hot-wire rake. This strong decrease at z=0 gets weaker as the reference probe moves along the wall-normal direction toward the freestream. In the log layer the cross-section of the two-point cross-correlation is rather broad with no abrupt changes in magnitude between successive separations in space 5.8(d,e,f&g). For the last three subplots which are the cross-section of the two-point cross-correlation for which the reference probes were between 0.5-1.0δ, the correlation is very weak compared to the other cross-sections taken closer to the wall. The last subfigure, figure 5.8(l), shows the peak of each cross-section to compare their relative magnitudes.

Other cross-sections of the correlation coefficient on the YZ-plane along the wall-normal direction are presented in figure 5.9. This figure shows how different wall-normal positions of boundary layer turbulence are correlated with the other wall-normal locations on the same vertical axis. As it can easily be seen, the cross-correlations always go to zero when the probe located at y' approaches the freestream as expected. On the other hand, the correlation curves between the probes located anywhere in the boundary layer and the ones located within the near wall region reveal some finite, significant correlations. These suggest that from the very near wall region to the first half of the outer layer of the turbulent boundary layer, there are active scales covering the bottom half of the boundary layer. This can be attributed to the bulges and hairpin vortices, because legs of the hairpin vortices are found to be in the near wall region, while the heads of the hairpin vortices have also been observed within the outer layer, mostly

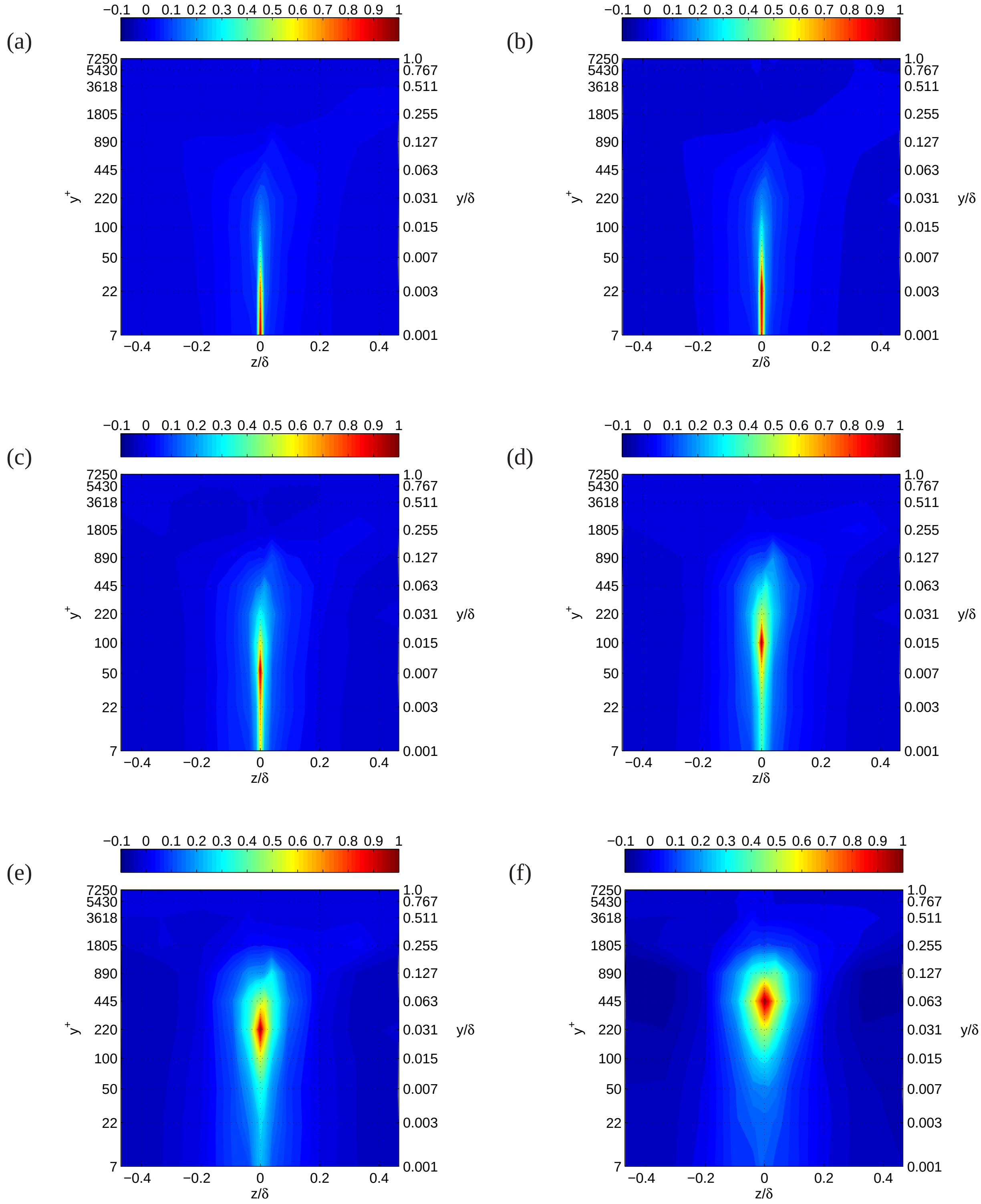

Figure 5.6: Two-point cross-correlation coefficients on the YZ-plane at $Re_\theta = 19\,100$. (a) $y^+ = 7$, (b) $y^+ = 22$, (c) $y^+ = 50$, (d) $y^+ = 100$, (e) $y^+ = 220$, (f) $y^+ = 445$.

inside the log layer.

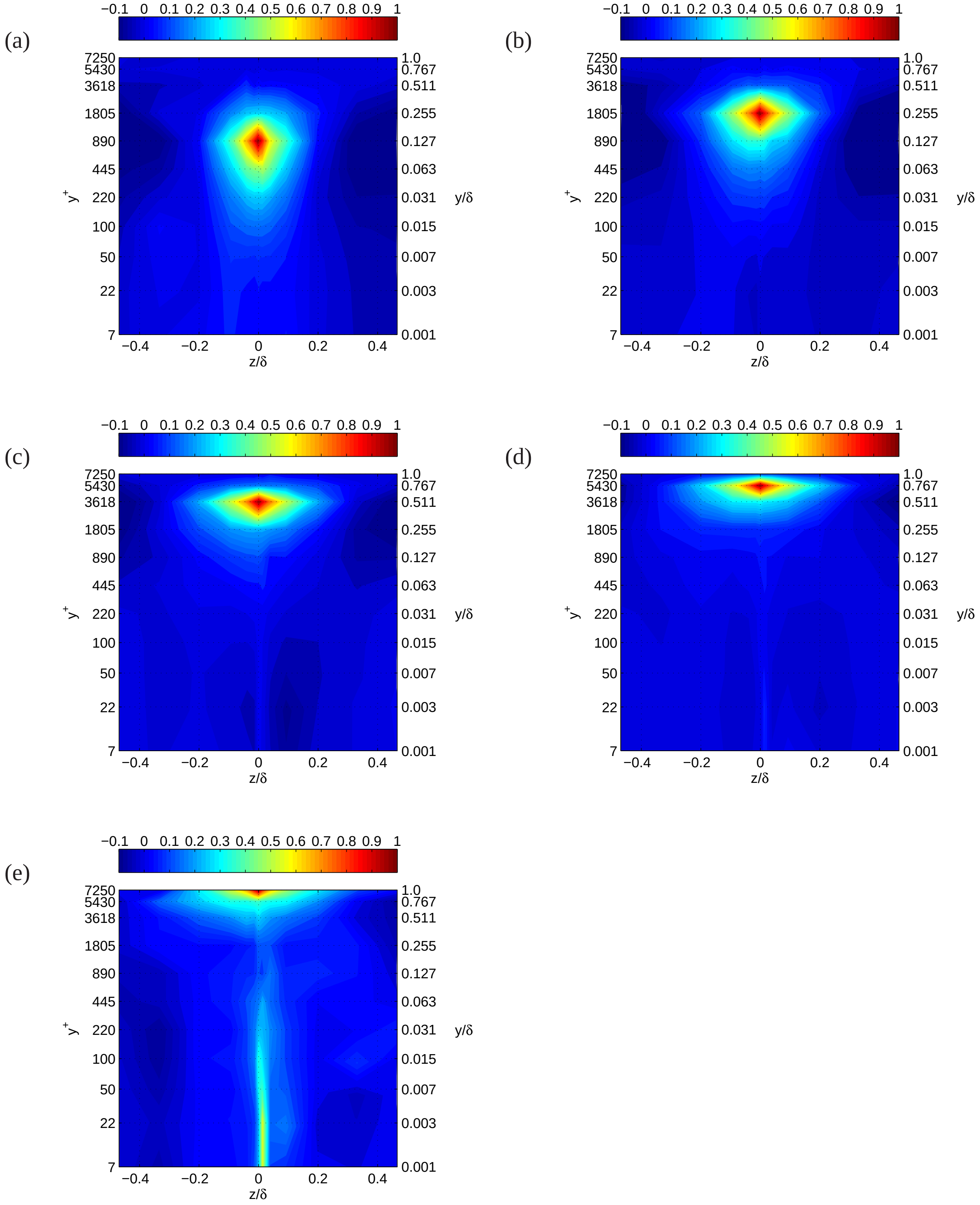

Figure 5.7: Two-point cross-correlation coefficients on the YZ-plane at Re_θ =19 100. (a) y^+ =890, (b) y^+ =1805, (c) y^+ =3618, (d) y^+ =5430, (e) y^+ =7250.

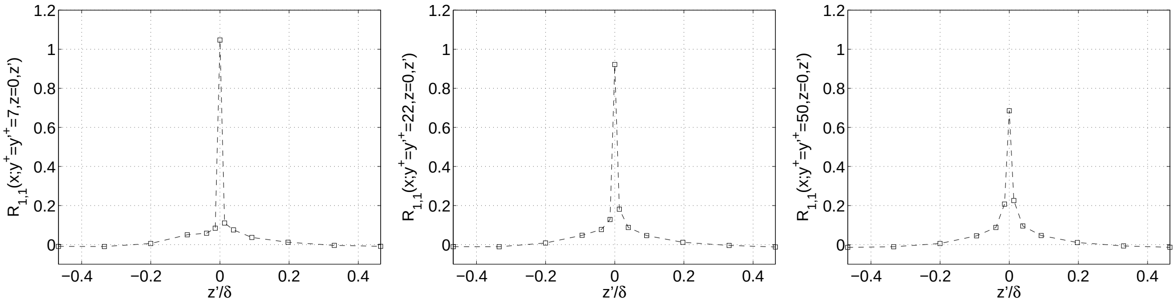

(a) $y^+ = 7$, $y/\delta = 0.001$.

(b) $y^+ = 22$, $y/\delta = 0.003$.

(c) $y^+ = 50$, $y/\delta = 0.007$.

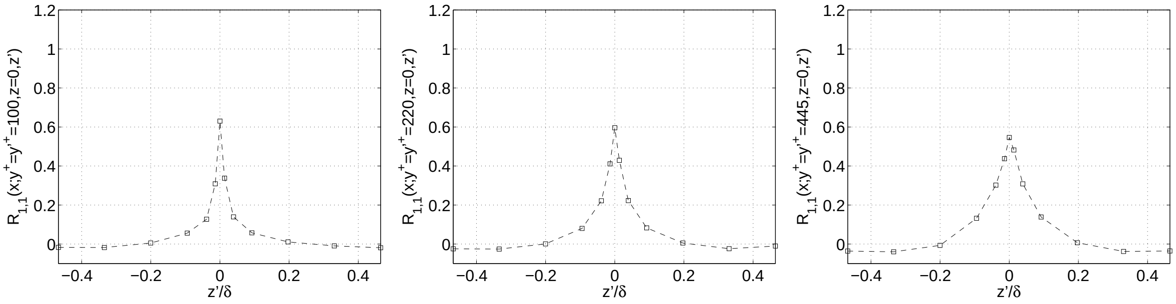

(d) $y^+ = 100$, $y/\delta = 0.015$.

(e) $y^+ = 220$, $y/\delta = 0.031$.

(f) $y^+ = 445$, $y/\delta = 0.063$.

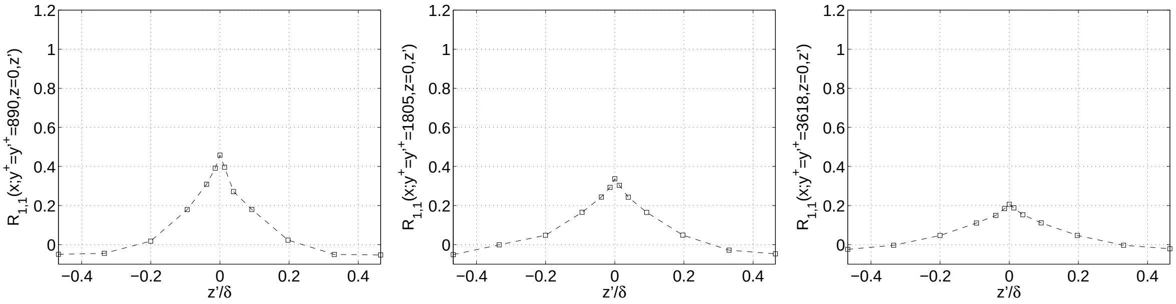

(g) $y^+ = 890$, $y/\delta = 0.127$.

(h) $y^+ = 1805$, $y/\delta = 0.255$.

(i) $y^+ = 3618$, $y/\delta = 0.511$.

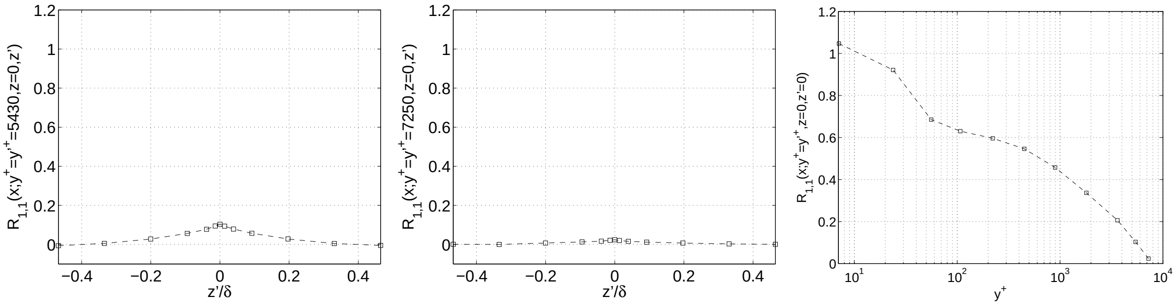

(j) $y^+ = 5430$, $y/\delta = 0.767$.

(k) $y^+ = 7250$, $y/\delta = 1$.

(l) Peaks at z=0

Figure 5.8: Cross-section of figures 5.6 and 5.7 at constant wall-normal positions at $Re_\theta = 19\,100$.

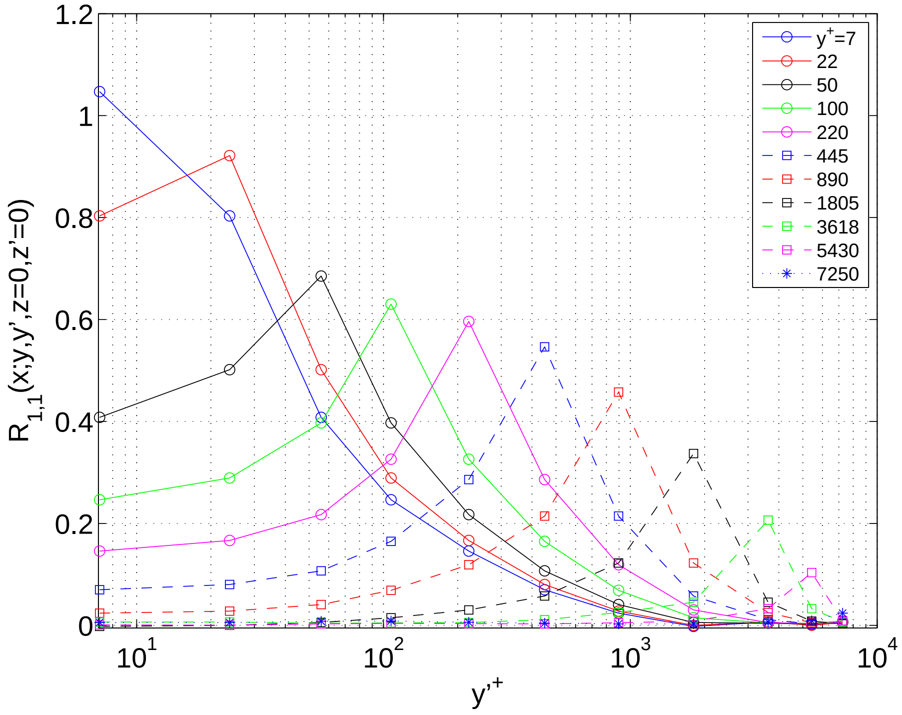

Figure 5.9: Cross-section of figures 5.6 and 5.7 at z=z'=0 positions at Re_θ =19 100.

5.6 Two-Point Cross-Correlations for Re_θ of 9800

The two-point cross-correlation coefficients from the lower Reynolds number measurement are presented in this section. The figures are ordered as in the previous sections for the high Reynolds number case. The planes used for presenting the cross-correlation coefficients and actual values of cross-correlations are obtained at the same wall-normal locations. Since the viscous length scale for the low Reynolds number case is twice the viscous length scale of the high Reynolds number case as shown in table 2.1, the corresponding y^+ values for the low Reynolds number case are almost half those for high Reynolds number case. The contour line levels in these figures are the same as the ones used for the high Reynolds number case and this is noted in the caption of the figures.

Figures 5.10 and 5.12 present the two-point cross-correlation coefficients on the XZ-plane for the low Reynolds number case. One obvious fact from these figures is that the size of the correlations at this Reynolds number is smaller than the size of the correlations observed in the high Reynolds number case. The abscissa in the figures is the streamwise separation and obtained using the Taylor's frozen field hypothesis. Since the convection velocity is evaluated at each wall-normal position where the probe is located, the axis is actually stretched because of the higher convection, even though the events happen at the same scale in the time domain. At this Reynolds number, it is even possible to see some elongated correlations in the near wall region at y^+ of 3.5, which is essentially in the linear sublayer, and 11. We observe a significant strength in these elongated contour lines within the viscous sublayer of the turbulent boundary layer as shown in figures 5.10(a,b&c). As the planes move away from the wall and pass the buffer layer, the elongated correlations both increase in magnitude and expand in the spanwise direction. Another interesting feature observed at this Reynolds number is that the two-point cross-correlations exist everywhere within the domain taken into consideration here. The ratio of the size of the positive correlation and negative correlation is as it is for the high Reynolds number case. Even though the correlations are very weak in the top half of the boundary layer shown in figure 5.12, it is easy to detect the presence of the underlying elongated structures at every wall-normal position up to the freestream.

The two-point cross-correlations in the XY-plane for this Reynolds number are shown in figures 5.11 and 5.13. In the near wall regions shown in figures 5.11(a,b&c), the positive correlations are shorter in height compare to the ones observed in the high Reynolds number case. The aspect ratio of the positive correlations are also larger in this case, because of extension of correlation in the streamwise direction. At this Reynolds number, we observe elongated negative correlation coefficients even in the linear sublayer, similar to the ones from the correlation on the XZ-plane shown in figure 5.10. The most significant activity, hence the largest and relatively strongest correlations, exist within the log layer, supporting the previous findings. Figure 5.12 shows how the top half of the boundary layer is actually correlated with the bottom part of the boundary layer. Even though the correlations are weak, they show that there are large scale very weak structures linking these two different layers. On top of these, the intermittency of the upper part of the boundary layer penetrates down to the wall and shows itself within the entire boundary layer.

The cross-sections of the two-point cross-correlations shown in figures 5.10 and 5.12 at $\Delta z = 0$ are displayed in figure 5.14 with the actual correlation values. The peaks present the probe correlated with itself with no separation in space and time, thus the variance of turbulence fluctuations. As it is clear from these figures, the peak of the variance is shifted to the second wall-normal position which is actually at the same y^+ position of the first wall-normal position of the high Reynolds number case. The ratio of the magnitude of negative elongated correlations to the peak correlation found in the same plane is maximum in the log layer at this Reynolds number, similar to the ones shown for high Reynolds number case (e.g., 5.14(e,f,g&h)). These figures are useful especially for comparing the relative importance of the two-point cross-correlation coefficients given in figures 5.10-5.13, because they are normalized by the maximum correlation found on the same plane, which are essentially the peaks presented in figure 5.14.

Figure 5.15 and 5.16 show the two-point cross-correlation coefficients on the YZ-plane. The correlations present no significant difference if the comparison is made using the wall-normal coordinate scaled with the boundary layer thickness, because at both Reynolds number the boundary layer thicknesses are approximately the same. However, when the comparison is made using the wall-normal coordinate scaled with the viscous length scale, then everything simply shifts down by factor of 2 for the low Reynolds number case. These figures actually show that the lateral (or spanwise) extent of the large scale motions are bounded within $\pm 0.35\delta$.

Similar to figure 5.8, we present the cross-section of the two-point cross-correlation plots on the YZ-plane at each wall-normal position in figure 5.17. The only notable difference is that the peak of the correlations near the wall for the low Reynolds number case shifts away from the wall, but remains at the same wall-normal position when scaled by the viscous length scale.

5.7 Integral Length and Times Scales

The cross-correlation data shown in figures 5.5 and 5.8 for the high Reynolds number case and figures 5.14 and 5.17 for the low Reynolds number case are used for computing the integral length scale in both streamwise (L_x) and spanwise (L_z) directions, as well as the integral time scale (T_{int}). The integral time scale is deduced from the integral length scale in the streamwise direction by dividing it by the local mean convecting velocity. Computations of the integral length scales are performed as follows:

$$L_x = \int_0^{R_0} \frac{R_{1,1}(x=0,x')}{R_{1,1}(x=0,x'=0)} dx' \tag{5.11}$$

where the upper limit of integration, R_0, is taken as the first zero crossing of the correlation function following O'Neill *et al.* (2004). Otherwise, the integral length scale obtained after integration is very small due to very long tails of the correlation function. Similarly,

$$L_z = \int_0^{\infty} \frac{R_{1,1}(z=0,z')}{R_{1,1}(z=0,z'=0)} dz' \tag{5.12}$$

where the upper limit was covering the entire domain, hence ∞, because the correlation functions have a very small portion on the negative side. The integration up to first zero crossing does not change the result at any wall-normal position.

Figure 5.18 shows that the integral length scale in the streamwise direction increases with increasing wall-normal distance except very close to the freestream. The increase in the length scale is almost linear in a semi-logarithmic plot within the log layer. Then for the high Reynolds number case there is a region of almost constant value for the integral length scale between y/δ of 0.1-0.75. By contrast, this does not appear for the low Reynolds number case and the integral length scale continues to increase up to y/δ of 0.7. For the last wall-normal position there is a significant drop in magnitude of the integral length scale. This is due to the high level of intermittency at this height.

The integral length scale in the spanwise direction increases with increasing wall-normal location, except at the last wall-normal position for the low Reynolds number case. The integral length scales, L_x and L_z, do not show any dependence on the Reynolds number, since they at each wall-normal position are approximately the same. The largest length scale was about 0.15δ, meaning that the extent of the rake in the spanwise direction is about 7 integral length scale in this direction.Therefore, the extent of the rake is sufficient to compute the integral length scale correctly at every wall-normal position. (Note that O'Neill *et al.* (2004) suggested that the extend of the field should be at least 6 times the integral length scale for computing the correct integral length scale.).

The integral Eulerian time scales for both Reynolds number cases in normalized forms are presented in figure 5.21. The trend in these figures are approximately the same as for the integral length scale if the wall normal position is below 10% of the boundary layer thickness. After this point we observe a sudden drop in the integral time scale due to the large mean convection velocity. The maximum integral time scale was about 15 and 20 microseconds for the high and low Reynolds number cases respectively. This means that the original data recording record sizes correspond to 400 and 300 integral time scale for each block. The data shown in this section is based on first 16 384 samples of 180 000 sample long blocks, therefore each subblock analyzed here is about 40 and 30 integral time scales long for the high and low Reynolds numbers respectively.

5.8 Summary and Discussions

In this section the two-point cross-correlation of the turbulent boundary layer at Re_θ of 19 100 and 9800 were presented. The data investigated in this chapter was the streamwise component of the turbulent velocity field obtained using the hot-wire rake of 143 probes sampled simultaneously. Taylor's frozen field hyperostosis was utilized to be able to convert the time dependence into spatial dependence in the streamwise direction when it needed.

The two-point cross-correlation coefficients in the streamwise-spanwise plane at different wall-normal positions showed that the elongated structures develop after the buffer layer. The most significant elongated correlations are within the log layer. These long correlations are always negative and their magnitude is small compared to the peak correlation found at the same wall-normal positions. As the streamwise-spanwise plane moves in the wall-normal direction toward the freestream, the strength of these weak negative correlations gets weaker. On the other hand, these long features of turbulence are visible even at the last 25% of the boundary layer thickness towards the freestream.

Analysis of the two-point cross-correlation on the streamwise-wall-normal direction also showed that the elongated correlations appear above the buffer layer. They have negative values and extended in the streamwise direction covering the entire field. The area covered by these negative correlations increase as the reference probe moves away from the wall. The positive correlations have an inclined features. The contour lines representing the correlations coefficients above wall-normal position of 0.2δ showed that the outer layer is physically connected to every layer of the boundary layer down to the wall, even though the correlation is very weak. The intermittency effects the entire boundary layer including the near wall region.

There appear slight differences between Re_θ of 19 100 and 9800. First of all, it is possible to detect these elongated correlations in the near wall region for the low Reynolds number case, contrary to the high Reynolds number case. However, they are very thin in the transverse directions until the end of buffer layer. Once the streamwise-spanwise plane or the reference probe in the case of streamwise-wall-normal plane are above the buffer layer, these correlations cover the entire domain. At the low Reynolds number case, they are relatively stronger compared to the peak correlation of the same plane. The correlations between intermittent region and near wall region are also observed at the lower Reynolds number.

Cross-section of the two-point correlations on different planes were used to study the integral scales of the boundary layer. Integral scales in the streamwise direction for the high Reynolds number case is higher than that for the low Reynolds number case. The size of the integral scale is small close to the wall and increases with increasing wall-normal position. In the very intermittent region of the boundary layer there is a drop in size of the integral length scale in the streamwise direction. The integral length scale in the spanwise direction is approximately the same, indicating no Reynolds number dependence. The time scale for the high Reynolds number case is approximately twice the time scale for the low Reynolds number case because of the ratio of freestream velocities between these two Reynolds number and approximately equal boundary layer thicknesses.

The high Reynolds number turbulent boundary layers studied here has very long elongated structures. Our investigations showed that these elongated correlations get longer and longer as the record length of the measurement increases. Both the fast way of computing these two-point cross-correlations using FFT algorithms and much slower computation using the time-lag products produce the same results, suggesting that these long correlations are not due to the algorithm used in computations. However, our longest record show that it is possible to see these correlations up to 120 boundary layer thickness and more. This cannot be physical either because the wind tunnel test section is about 65 boundary layer thicknesses long. Therefore, there must be some other reason for these very long correlations. This is not a problem of utilization of Taylor's frozen field hypothesis either, because then the same very long correlations exist in time domain. Therefore, the physical reasoning of these long correlations needs further investigations, and no attempt made in that direction in the course of this thesis, other than comparing the algorithms used to compute these correlations.

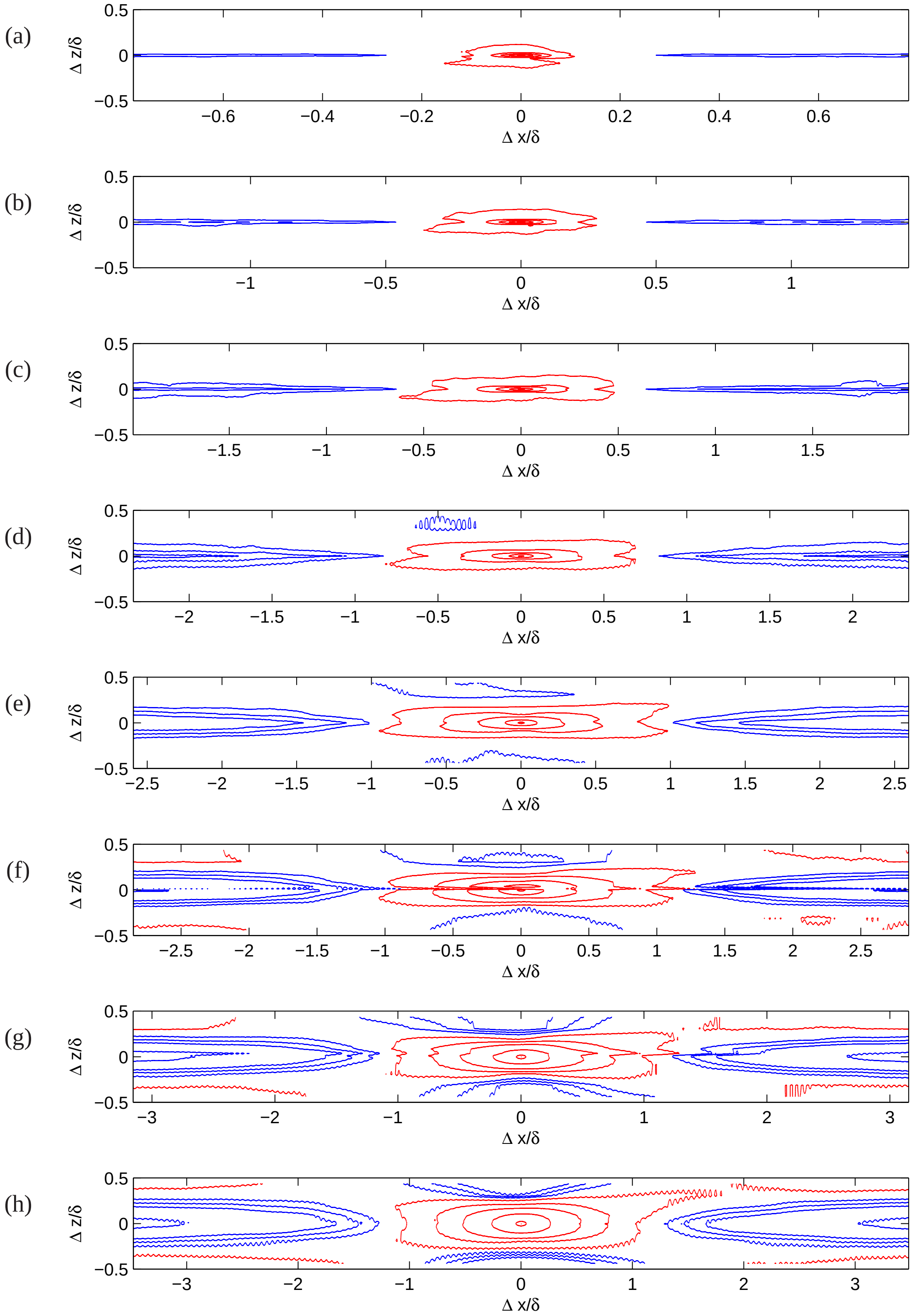

Figure 5.10: Two-point cross-correlation coefficients (XZ-plane) at constant wall-normal positions at Re_θ of 9800. The figures present the correlations between the probe located at z=0 and the probes at the same y^+ location on each plane. (a) $y^+ = 3.7$, (b) $y^+ = 11$, (c) $y^+ = 26$, (d) $y^+ = 55$, (e) $y^+ = 114$, (f) $y^+ = 231$, (g) $y^+ = 465$, (h) $y^+ = 933$, $y = 0.239\delta$. Red contour lines denote positive values [0.025 0.1 0.2 0.4 0.8 1.0]; Blue contour lines denote negative values [-0.025 -0.05 -0.075 -0.15 -0.20].

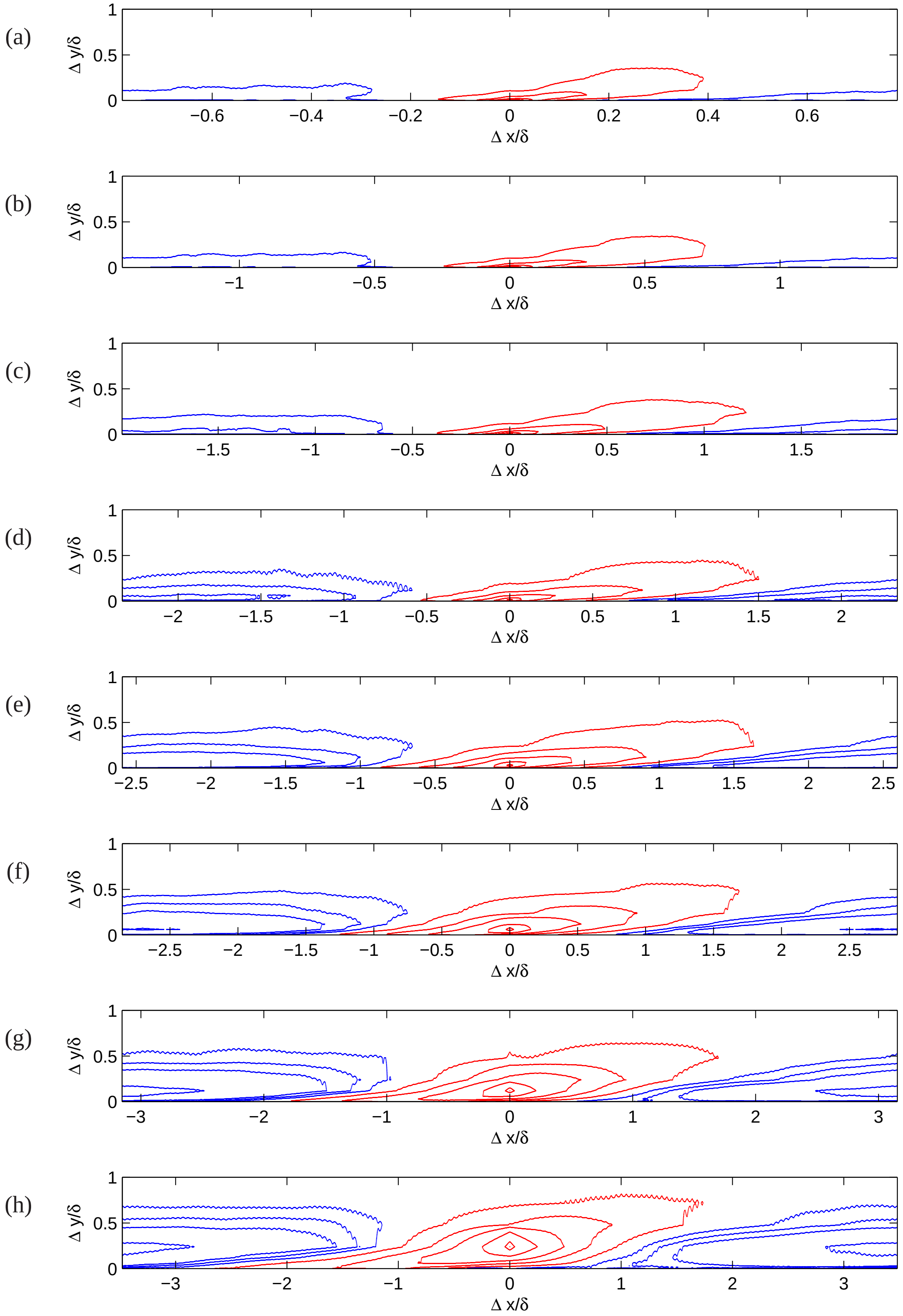

Figure 5.11: Two-point cross-correlations (XY-plane) at z=0. The figures present the correlation between the probe at one wall-normal position and the rest the probes at the same spanwise location at Re_θ of 9800. (a) $y^+ = 3.7$, (b) $y^+ = 11$, (c) $y^+ = 26$, (d) $y^+ = 55$, (e) $y^+ = 114$, (f) $y^+ = 231$, (g) $y^+ = 465$, (h) $y = 0.2\delta$. Red contour lines denote positive values [0.025 0.1 0.2 0.4 0.8 1.0]; Blue contour lines denote negative values [-0.025 -0.05 -0.075 -0.15 -0.20].

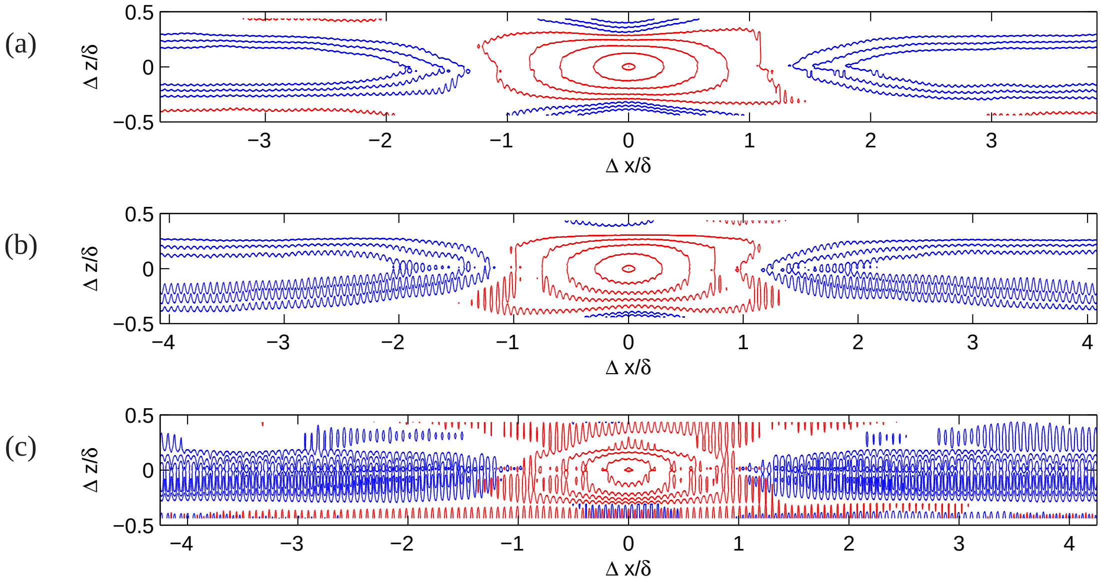

Figure 5.12: Two-point cross-correlation coefficients (XZ-plane) at constant wall-normal positions at Re_θ of 9800. The figures present the correlations between the probe located at z=0 and the probes at the same y^+ location on each plane. (a) y= 0.479δ, (b) y= 0.719δ (c) y= 0.960δ. Red contour lines denote positive values [0.025 0.1 0.2 0.4 0.8 1.0]; Blue contour lines denote negative values [-0.025 -0.05 -0.075 -0.15 -0.20].

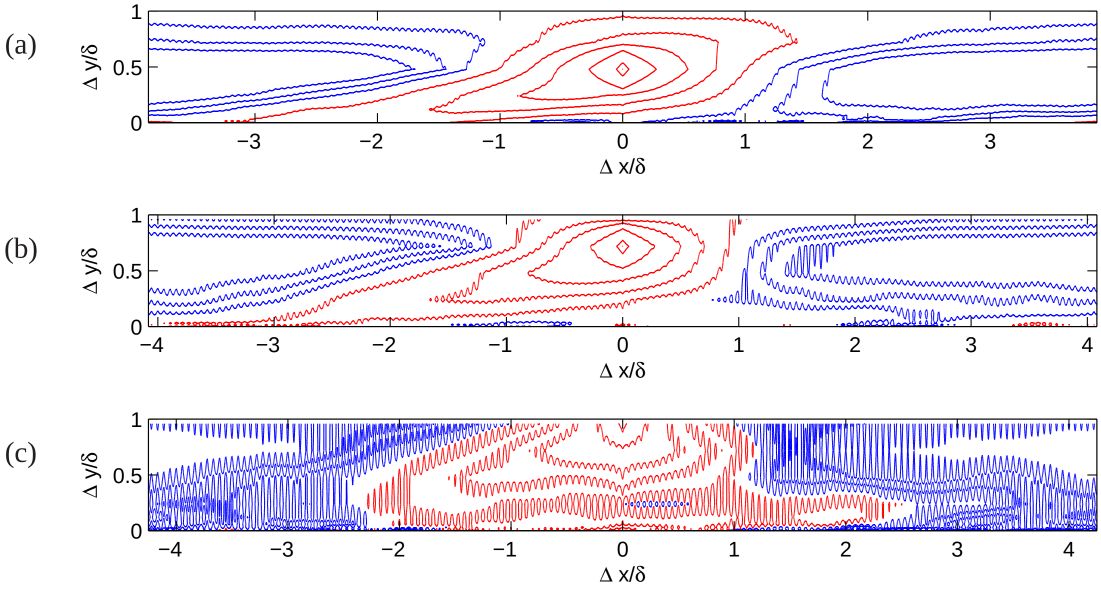

Figure 5.13: Two-point cross-correlations (XY-plane) at z=0. The figures present the correlation between the probe at one wall-normal position and the rest the probes at the same spanwise location at Re_θ of 19100. (a) y= 0.479δ (b) y= 0.716δ (c) y= 0.960δ. Red contour lines denote positive values [0.025 0.1 0.2 0.4 0.8 1.0]; Blue contour lines denote negative values [-0.025 -0.05 -0.075 -0.15 -0.20].

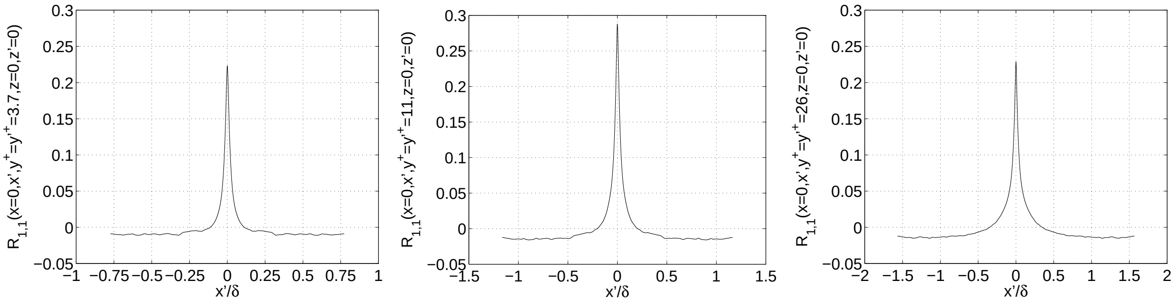

(a) $y^+ = 3.7$, $y/\delta = 0.001$.

(b) $y^+ = 11$, $y/\delta = 0.003$.

(c) $y^+ = 26$, $y/\delta = 0.007$.

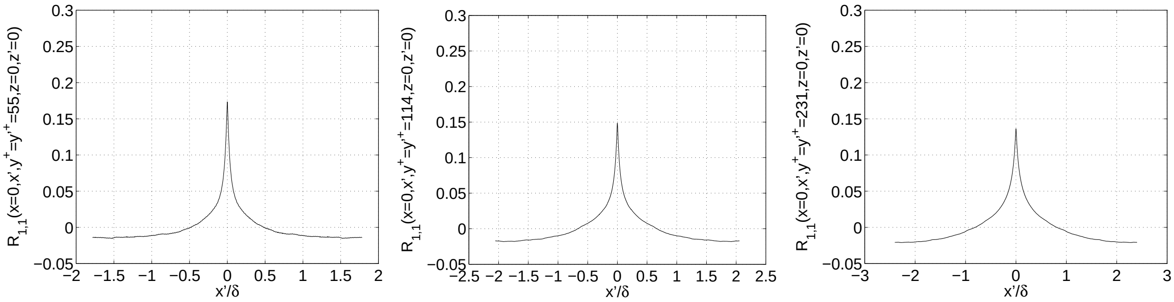

(d) $y^+ = 55$, $y/\delta = 0.014$.

(e) $y^+ = 114$, $y/\delta = 0.029$.

(f) $y^+ = 231$, $y/\delta = 0.059$.

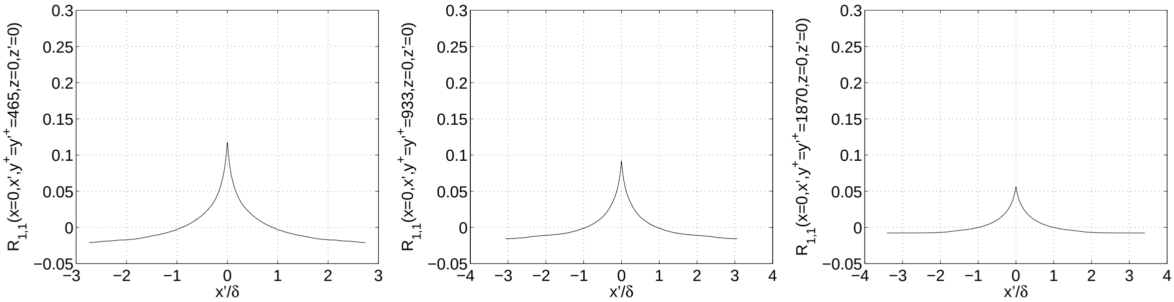

(g) $y^+ = 465$, $y/\delta = 0.119$.

(h) $y^+ = 933$, $y/\delta = 0.239$.

(i) $y^+ = 1870$, $y/\delta = 0.479$.

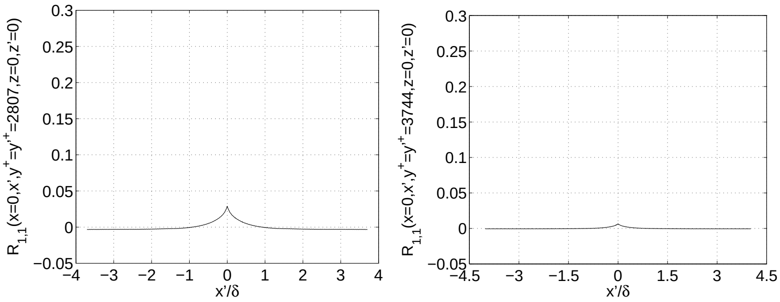

(j) $y^+ = 2807$, $y/\delta = 0.719$.

(k) $y^+ = 3744$, $y/\delta = 0.960$.

Figure 5.14: Cross-section of figures 5.10 and 5.12 at $\Delta z = 0$ at $Re_\theta = 9800$

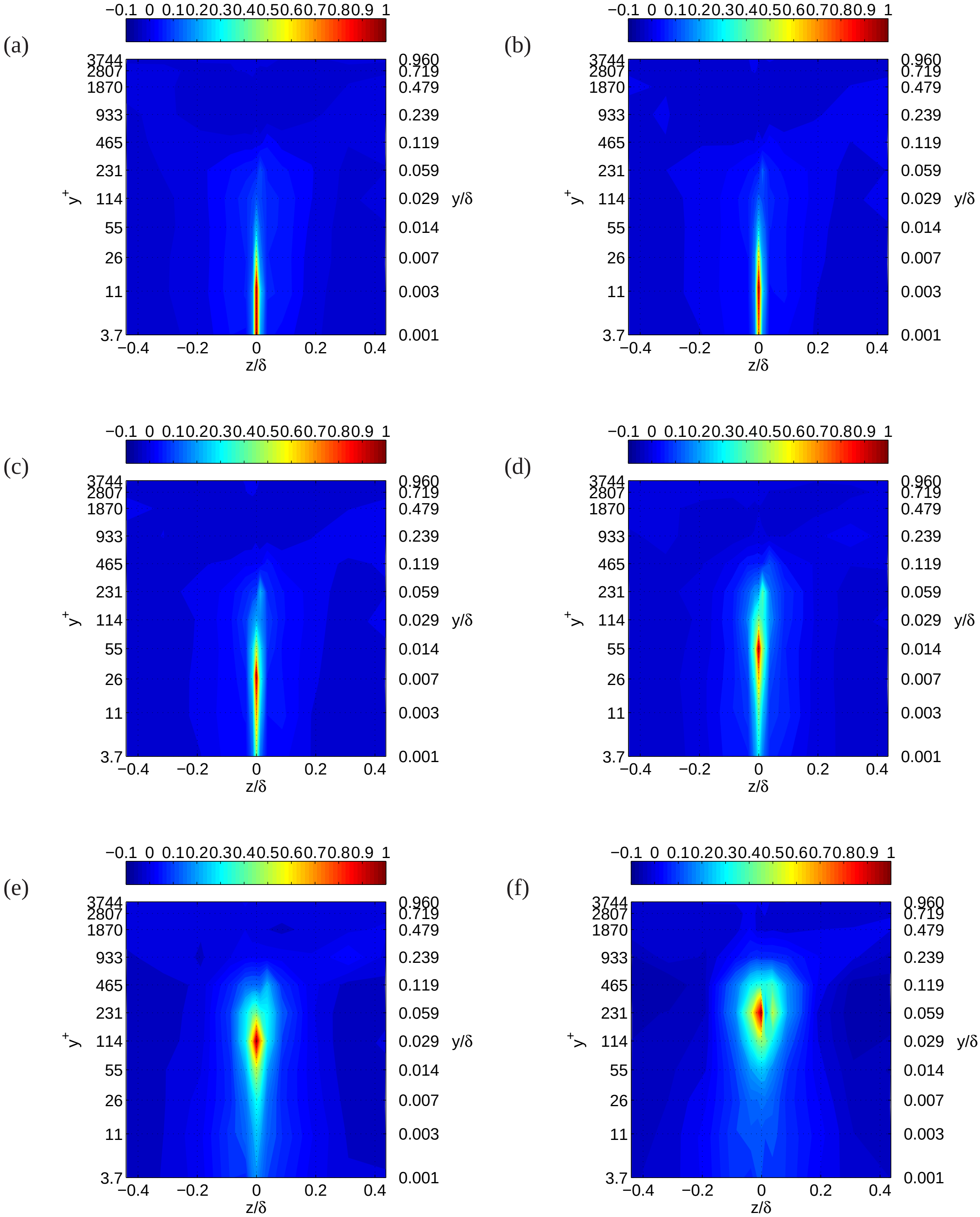

Figure 5.15: Two-point cross-correlation coefficients on the YZ-plane at $Re_\theta = 9800$. (a) $y^+ = 3.7$, (b) $y^+ = 11$, (c) $y^+ = 26$, (d) $y^+ = 55$, (e) $y^+ = 114$, (f) $y^+ = 231$,

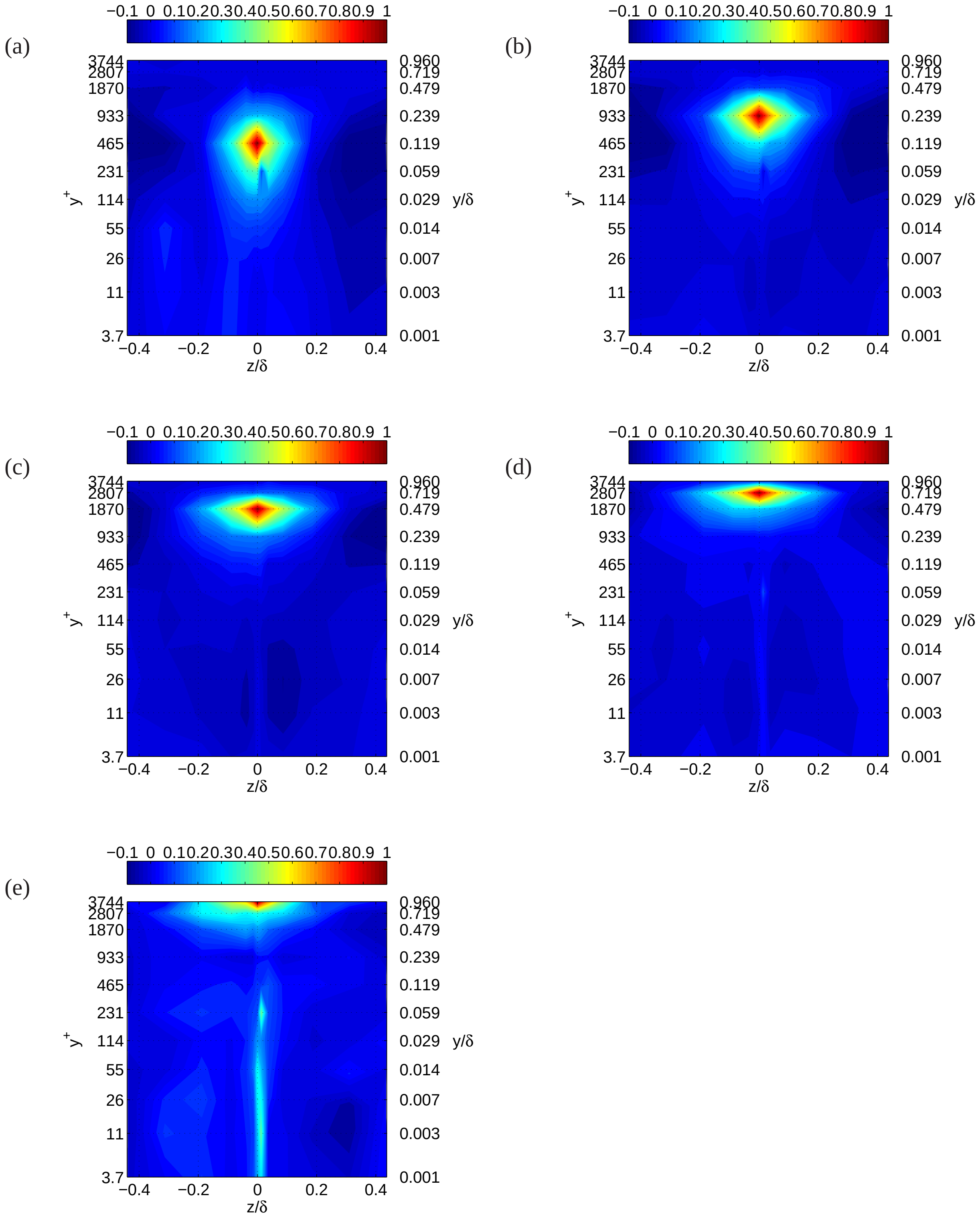

Figure 5.16: Two-point cross-correlation coefficients on the YZ-plane at $Re_\theta = 9800$. (a) $y^+ = 465$, (b) $y^+ = 933$, (c) $y^+ = 1870$, (d) $y^+ = 2801$, (e) $y^+ = 3744$

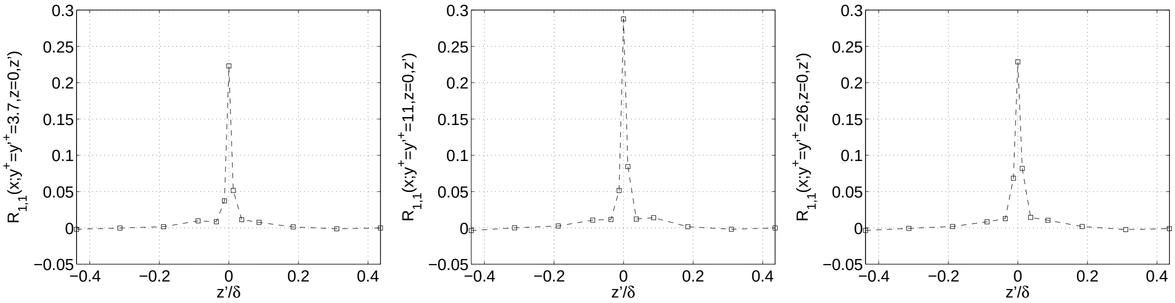

(a) y$^+$ =3.7, y/δ =0.001.

(b) y$^+$ =11, y/δ =0.003.

(c) y$^+$ =26, y/δ =0.007.

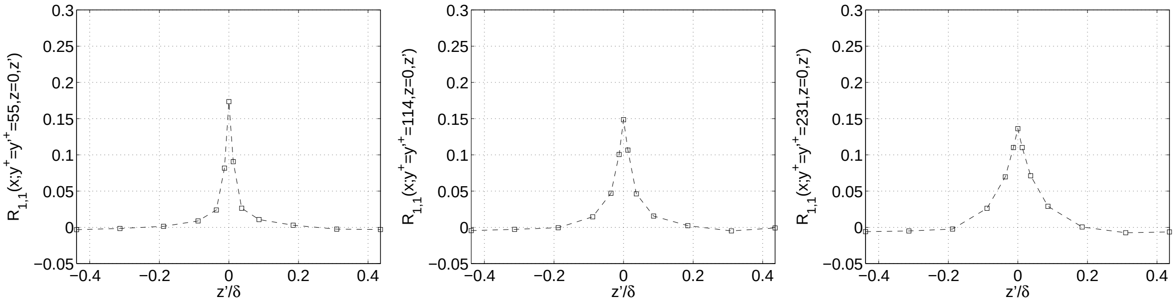

(d) y$^+$ =55, y/δ =0.014.

(e) y$^+$ =114, y/δ =0.029.

(f) y$^+$ =231, y/δ =0.059.

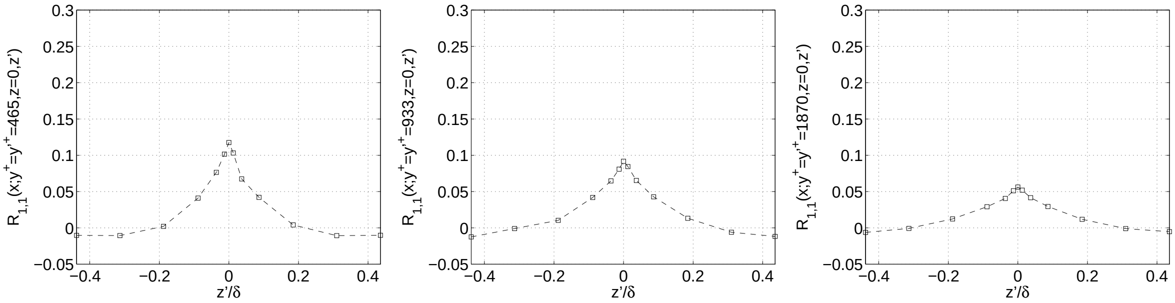

(g) y$^+$ =465, y/δ =0.119.

(h) y$^+$ =933, y/δ =0.239.

(i) y$^+$ =1870, y/δ =0.479.

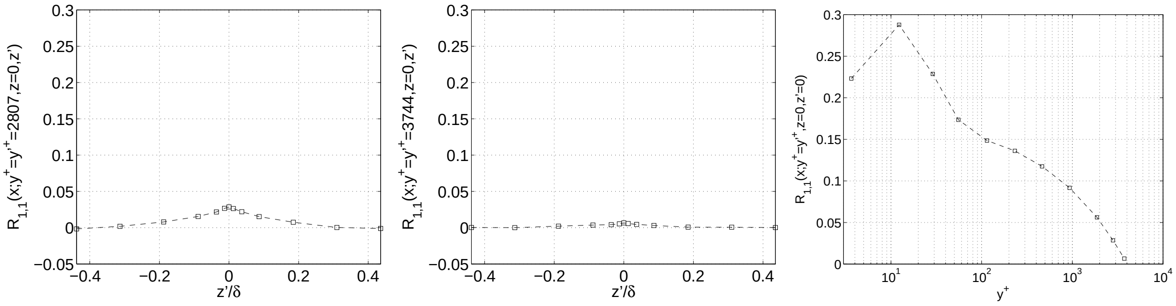

(j) y$^+$ =2807, y/δ =0.719.

(k) y$^+$ =3744, y/δ =0.96.

(l) peaks at z=0.

Figure 5.17: Cross-section of figures 5.15 and 5.16 at constant wall-normal positions at Re_θ =9800.

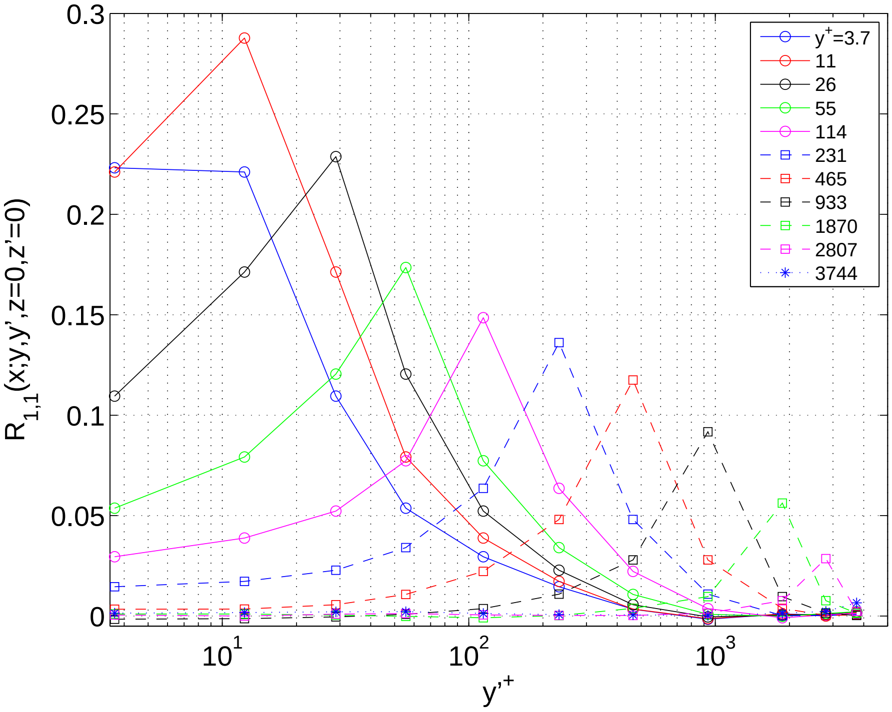

Figure 5.18: Cross-section of figures 5.15 and 5.16 at z=z'=0 positions at Re_θ =9800

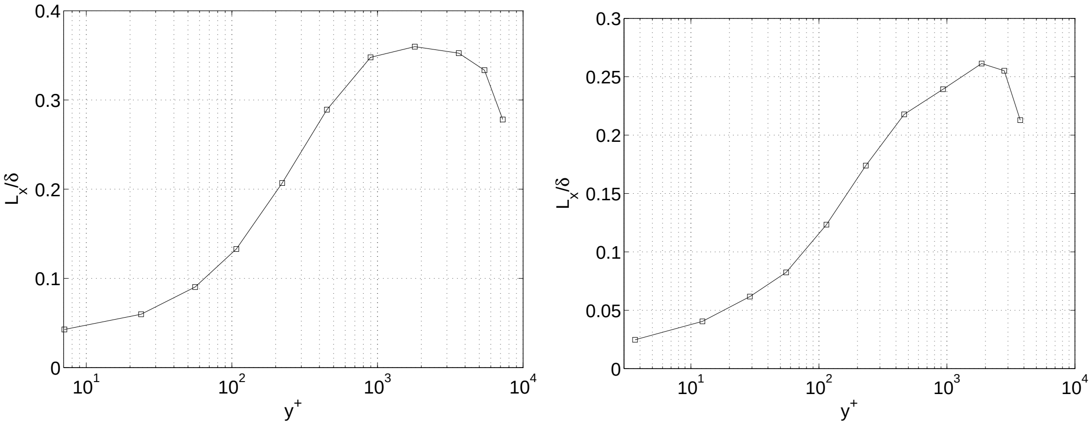

Figure 5.19: Integral length scales in the streamwise direction, L_x. Left and right figures show Re_θ of 19100 and 9800 respectively

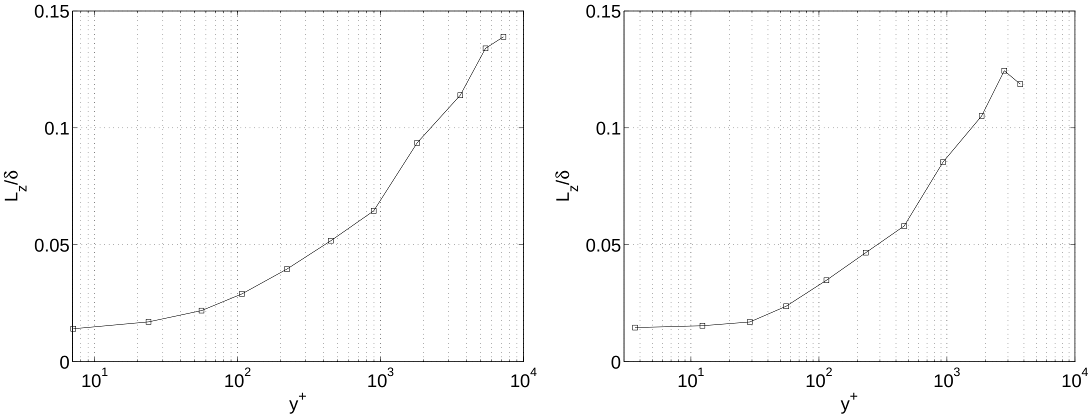

Figure 5.20: Integral length scales in the spanwise direction, L_z. Left and right figures show Re_θ of 19100 and 9800 respectively

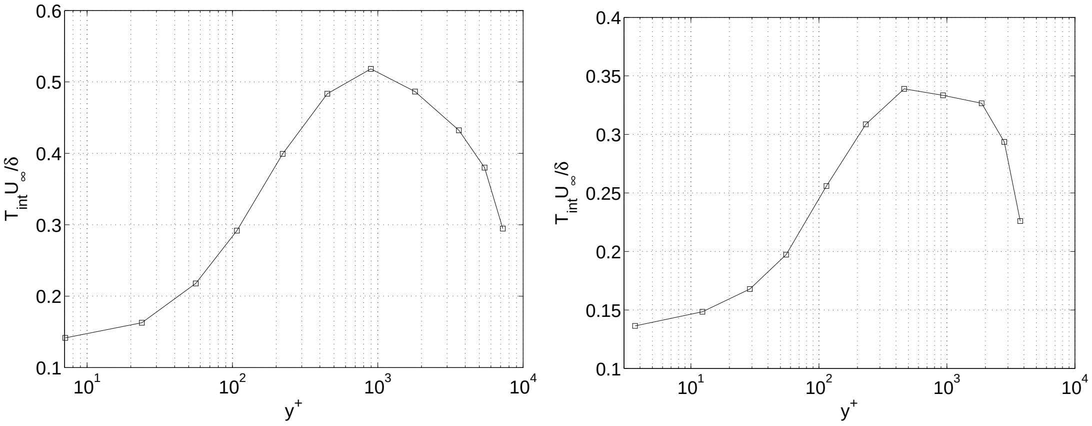

Figure 5.21: Integral times scales, T_{int}. Left and right figures show Re_θ of 19100 and 9800 respectively

Chapter 6

Proper Orthogonal Decomposition: Theory

6.1 Introduction

As a quantitative and unbiased method, Lumley (1967) introduced the proper orthogonal decomposition (POD) into the field of turbulence to identify and study the dynamics of the large scale energy containing features in turbulent fields with finite total energy. The POD provides an optimum deterministic description of the field, the so-called POD eigenvalues and eigenfunctions. These are the solutions obtained by seeking the largest projection onto the stochastic velocity field of turbulence in a mean square sense. Maximization of the projection results in an integral value problem (Fredholm integral equation of the second kind) for which the kernel is the two-point cross-correlations tensor of the stochastic velocity field. The POD has also been found to be very efficient at extracting the most energetic modes of the flow and ordering them according the their energy content.

Even though the POD was introduced as an optimal and mathematical way of breaking the turbulence scales apart, utilization of the method took some time, mainly due to difficulties associated with the measurement and computation of the two-point cross-correlations tensor. As pointed out by George (1988), the POD needs sufficient information on the two-point cross-correlation tensor so that a complete space time realization of the turbulence velocity field can be obtained. Computation of the cross-correlation tensor from the measured velocities is also difficult in terms of computing power and speed capabilities.

The first successful experimental implementation of the POD was made by Bakewell & Lumley (1967) for the pipe flow. It was almost two decades after Lumley (1967)'s proposal in the 1980s that the full potential of the POD began to be realized, e.g., Leib *et al.* (1984); Glauser *et al.* (1985); Glauser & George (1987) (see also Glauser (1987)) for high Reynolds number axisymmetric mixing layer and Herzog (1986) for low Reynolds number pipe flow. Since then, experimental utilization of the POD has been widely used to break the turbulence scales apart. Following these experimental utilization of the POD, Moin & Moser (1989) applied the POD on a database created by the direct numerical simulation (DNS) of turbulent channel flow and extracted the most energetic characteristics scales of turbulence.

One of the most striking features of the POD is its ability to describe the energetic large scale structures with only a few eigenmodes in an optimal manner, especially if the flow is first Fourier decomposed in periodic or homogeneous directions. Glauser (1987) showed that the orthogonal decomposition was very efficient in organizing the large scale structures in the axisymmetric mixing layer. The first POD mode contained 40% of the total turbulence kinetic energy. The energy content of the first three POD modes was about 80% in total. These initial results were based on measurements using hot-wire rakes of single wire probes. The capability of the POD to capture most of the turbulence kinetic energy by a few orthogonal eigenmodes led a number of research group to apply this technique, initially to canonical flows, but later to flows in more complex geometries. Especially, free shear turbulent flows have been investigated extensively using the POD technique (i.e., Glauser & George (1987); Glauser *et al.* (1985); Delville (1994); Delville *et al.* (1999); Gordeyev & Thomas (2000, 2002); Citriniti & George (2000); Johansson *et al.* (2002); Jung *et al.* (2004); Gamard *et al.* (2004); Johansson & George (2006*b*); Wänström *et al.* (2006); Iqbal & Thomas (2007); Tutkun *et al.* (2008)).

By contrast to the amount of research conducted using the POD in turbulent free shear flow (mainly experimental), there have been only a limited number of applications carried out for the wall bounded flows. This is mainly because of the experimental difficulties in such flows imposed by the required number of hot-wire rakes of many probes, or the statistical convergence problem of numerical simulations.

The early experimental work was carried out in turbulent pipe flows using hot-film measurement techniques. With the advent of hardware and software developments, particle image velocimetry (PIV), which provides three-dimensional velocity information on a plane, has recently become a very useful tool in measurements of the two-point cross-correlation with very high spatial resolution. These have been used for some channel flow experiments to be able to perform POD analysis on the obtained data. Numerical studies which can be found in the literature is also primarily for channel flow simulations. There has been no research program carried out for analyzing the turbulent boundary layers using the powerful features of the POD. In this sense, our work described in this dissertation is unique, and the first application in this direction.

The first POD application on the wall bounded flows, Bakewell & Lumley (1967) investigated the the near wall region of turbulent pipe flow up to y^+ of 40. The Reynolds number based on the pipe diameter was 8700, and glycerine was used as working fluid to be able to study the viscous sublayer near the wall. Hot-film anemometers were employed for measurements of the streamwise velocity fluctuations only and then only along a single line. They extracted the most dominant large scale structure of the flow using the mixing length theory and the continuity equation. They were able to obtain only the first eigenmode because of the inaccuracy of the measurements of two-point space-time correlations. In an experiment initiated by W. K. George, Herzog (1986) carried out some measurements in the same facility at Reynolds number of 8750. At this time, he measured two components of the velocity, namely the azimuthal and the streamwise components. The missing five members of the cross-correlation tensor were obtained utilizing the general symmetry properties in connection with the continuity equation. The measurement grid was established using six points in wall-normal direction up to y^+ of 40, seven points in the streamwise direction of to x^+ of 49, six points in the azimuthal direction up to z^+ of 136. He reported that the dominant mode contained 50% or more of the kinetic energy due to streamwise velocity component, and first three POD modes contained more than 90% of the turbulence kinetic energy because of streamwise fluctuations.

Following these experimental studies, the most detailed POD study in the wall bounded turbulence came from Moin & Moser (1989) in which they studied DNS of turbulent channel flow data using both scalar and vectorial decompositions in one or more dimensions. The Reynolds number based on the friction velocity and half channel height was 180, corresponding to the Reynolds number of 3200 based on centerline mean velocity and half channel height. They were able to show that the energy carried by the first eigenmode, regardless of the number of dimension included in the analysis, was 30-50% of the total kinetic energy when the half channel was taken into account. The contribution of the first three POD modes to the total turbulence kinetic energy changed from 50 to 75% depending on the number of dimensions. They also used a shot-noise decomposition and extracted the most dominant characteristic eddy, which had 76% of the total turbulence kinetic energy.

Recently Liu *et al.* (1994, 2001) studied the turbulent channel flow by experimental utilization of the POD method. The Reynolds numbers tested were much higher than the previous investigations listed above. They were 5378 and 29 935 when computed using bulk velocity and the channel height. The PIV was used as an experimental tool with high spatial resolution to measure the two components of turbulent velocity field, namely streamwise and wall-normal components. The first of these studies focused on the similarity of the eigenspectra and eigenfunctions in the outer layer of the turbulent channel flow, and showed that the proper scaling of the eigenspectra using the friction velocity and outer length scale results in a collapse in the eigenspectra. The second paper was more thorough and did detailed analyzes on the energy and Reynolds stress distribution over different eigenfunctions. For both of the Reynolds number investigated, they reported that the energies of first 6 and 12 eigenmodes were approximately 35 and 50% of the total kinetic energy respectively. They also noted the Reynolds stresses due to the these 6 and 12 eigenmodes being approximately 50% and 70% of the total Reynolds stress of the domain respectively. The large scale motions of turbulence represented by the low eigenmodes with high turbulence kinetic energy had wavelengths longer than three times the half channel height.

As it is clear from above discussions, the POD is very efficient in capturing the maximum amount of turbulence kinetic energy with minimum number of modes in wall bounded flows too. We therefore implement this methodology to analyze velocity measurements of the streamwise component of high Reynolds number zero pressure gradient turbulent boundary layer data obtained using a hot-wire rake of 143 single wire probes. Our data set and analyses are different than the previous research conducted on the wall bounded flows: first because it is a high Reynolds number turbulent boundary layer flow, and second because it is of very large extent so that a large probe array can be utilized. In the following sections, the background theory and implementation of the method are discussed first. And in the next chapter, the eigenspectra and turbulence kinetic energy distributions from the POD analysis are presented and discussed. Finally, the instantaneously measured streamwise velocity fluctuations are projected back onto the empirical eigenfunction in order to reconstruct the velocity field, and break it different scales of motions.

6.2 Background Theory

6.2.1 General Formulation of POD

The POD is a mathematical tool to decompose stochastic turbulent velocity field into deterministic scales of motion. This decomposition is done by finding a deterministic field which has the maximum projection onto the stochastic field of interest. Details of the methodology can be summarized as below:

Let $u_i(\cdot)$ and $\phi_i(\cdot)$ be the stochastic turbulent velocity fluctuations and the deterministic field the POD seeks respectively. The maximization of the projection can be performed by finding the largest inner product of the fields in a mean square sense as follows:

$$\langle| \alpha |^2\rangle = \langle| (u_i(\cdot), \phi_i^*(\cdot)) |^2\rangle \tag{6.1}$$

where $\langle\ \rangle$ denotes the ensemble averaging. "$\cdot$" represents any spatial and/or time dependence of these fields. The result of inner product in Hilbert space, α, can be written as:

$$\alpha = (u_i(\cdot), \phi_i^*(\cdot)) = \int_D u_i(\cdot)\phi_i^*(\cdot)d(\cdot) \tag{6.2}$$

where the integration is performed over the entire domain of interest, which is represented by D. Normalization of the mean square projection can be obtained dividing Eq. (6.1) by the magnitude of the deterministic field:

$$\lambda = \frac{\left[\int_D u_i(\cdot)\phi_i^*(\cdot)d(\cdot)\right]\left[\int_D u_i(\cdot)\phi_i^*(\cdot)d(\cdot)\right]^*}{\left[\int_D \phi_l(\cdot)\phi_l^*(\cdot)d(\cdot)\right]\left[\int_D \phi_l(\cdot)\phi_l^*(\cdot)d(\cdot)\right]^*} \tag{6.3}$$

As shown by Lumley (1967), maximization of the normalized mean square projection results in a Fredholm integral equation of the second kind given by:

$$\int_D R_{i,j}(\cdot,\cdot')\phi_j(\cdot')d(\cdot') = \lambda\phi_i(\cdot) \tag{6.4}$$

The kernel of Eq. (6.4), $R_{i,j}(\cdot,\cdot')$, is the two-point cross-correlation tensor which is defined as:

$$R_{i,j}(\cdot,\cdot') = \langle u_i(\cdot)u_j(\cdot')\rangle \tag{6.5}$$

where $'$ denotes any different position and/or time. The subscripts i and j are indices and represent appropriate velocity components.

As detailed in many other sources (e.g., Lumley (1967), George (1988), Holmes *et al.* (1996)), if the field of interest is bounded and of finite total turbulence kinetic energy, then the Hilbert-Schmidt theory applies. Solution of the integral equation given in Eq. (6.4) in the domain of finite energy produces denumerably many solutions ($\phi_i(\cdot)$s in this case) instead of a single solution. There is a pair of λ (eigenvalue) and $\phi_i(\cdot)$ (eigenfunction, or eigenmode) for each of these denumerable solutions. Therefore, Eq. (6.4) can be written as

$$\int_D R_{i,j}(\cdot,\cdot')\phi_j^{(n)}(\cdot')d(\cdot') = \lambda^{(n)}\phi_i^{(n)}(\cdot) \tag{6.6}$$

where n= $1,2,3,\ldots$ and represents the solution index, which is called POD mode number.

For fields of finite total energy, the properties of the solutions to the POD integral equation, Eq. (6.6) can be listed as follows:

1. Solutions to the POD integral, or eigenfunctions, are orthogonal:

$$\int_D \phi_i^{(n)}(\cdot)\phi_i^{*(m)}(\cdot)d(\cdot) = \delta_{nm} \tag{6.7}$$

2. For each eigenfunction there is a corresponding eigenvalue. These eigenvalues are ordered in a sense that the solution is optimum, meaning that the first eigenvalue is larger than the second one, and the second one is larger the third one and so on; $\lambda^{(1)} > \lambda^{(2)} > \lambda^{(3)} > \cdots$

3. Eigenvalues are real and positive.

4. The stochastic velocity field can be reconstructed using the eigenfunctions:

$$u_i(\cdot) = \sum_n a_n \phi_i^{(n)}(\cdot) \tag{6.8}$$

where a$_n$ represent the set of random coefficients which is obtained by back projection of eigenfunction onto the stochastic field of turbulence,

$$a_n = \int_D u_i(\cdot)\phi_i^{*(n)}(\cdot)d(\cdot) \tag{6.9}$$

5. Random coefficients given by Eq. (6.9) are uncorrelated because of orthogonality of the eigenfunctions:

$$\lambda^{(n)} = \langle a_n a_m^* \rangle \delta_{nm} \tag{6.10}$$

6. The two-point cross-correlation tensor, $R_{i,j}(\cdot,\cdot')$, can also be reconstructed using the reconstructed velocities given by Eq. 6.8:

$$R_{i,j}(\cdot,\cdot') = \sum_n \lambda^{(n)}\phi_i^{(n)}(\cdot)\phi_j^{(n)}(\cdot') \tag{6.11}$$

7. Contraction of the reconstructed two-point cross-correlation tensor shows that the total energy within the finite domain equals to summation of eigenvalues:

$$E = \int_D \langle u_i(\cdot)u_i(\cdot)\rangle d(\cdot) = \sum_n \lambda^{(n)} \tag{6.12}$$

Thus the POD provides a set of eigenfunctions that optimally decompose the turbulence energy in the domain, and each eigenvalue measures the energy associated with the corresponding eigenfunction. This implies that the largest eigenvalue represent the eigenfunction with the largest energy content and so forth.

6.2.2 Field of Homogeneous and Periodic Domains

As mentioned in the previous section, the POD is applicable to fields which are statistically inhomogeneous and of finite total energy. If the field of interest is homogenous in space, or stationary in time (or periodic in space and/or time), then the field is not bounded so that the energy is infinite. Therefore, Hilbert-Schmidt theory does not apply. On the other hand, Lumley (1967) showed that the POD formulation in the homogenous or stationary directions reduces to Fourier decomposition and eigenfunctions become exponential functions (see also George (1988, 1999) for useful reviews). The reconstruction of the original velocity in this case is performed by the same way of reconstruction of velocity using the POD. However, the random coefficients, a_n, are obtained by projecting the exponential functions onto the velocity field. This actually results in Fourier transformation of the velocity field. The velocity field therefore is reconstructed as a linear sum of the multiplication of Fourier coefficients and exponential eigenfunctions. Therefore, the reconstruction part is essentially an inverse Fourier transformation process.

The POD in the periodic directions also reduces to Fourier decomposition, but in this case the Fourier transformation used for finding the eigenfunction in homogeneous direction becomes a Fourier series expansion. The main difference between these two cases is the number of possible solutions to the problem. The homogeneous fields do not have finite extent; hence the field is a continuous field so the resulting wavenumbers, or frequencies, are also continuous. In contrast, the periodic fields are field of finite extent within one period, therefore the field can be treated as a field of finite extent, which makes Hilbert-Schmidt theory applicable.

As shown by Lumley (1967) and George (1988), it is more convenient to first perform Fourier transformation and/or Fourier series expansion of the two-point cross-correlation tensor of the POD integral equation in the homogenous (or stationary) and/or periodic direction, and then to apply the POD on the resulting two-point cross-spectral tensors.

6.2.3 Formulation of POD for Turbulent Boundary Layer

The full four dimensional representation of the POD integral given by Eq. (6.6) in Cartesian coordinate system becomes:

$$\int_D R_{i,j}(x,x',y,y',z,z',t,t')\phi_j^{(n)}(x',y',z',t')dx'dy'dz'dt' = \lambda^{(n)}\phi_i^{(n)}(x,y,z,t) \tag{6.13}$$

where x, y, z and t denote coordinates in streamwise, wall-normal and spanwise directions and time respectively. $'$ represents different position in space and time. The kernel of the equation can be written as:

$$R_{i,j}(x,x',y,y',z,z',t,t') = \langle u_i(x,y,z,t)u_j(x',y',z',t')\rangle \tag{6.14}$$

Because the turbulent boundary layer is stationary in time and homogenous in the spanwise direction, the two-point cross-correlation tensor is only function of separations in space and time, i.e.,

$$\widetilde{R}_{i,j}(x,x',y,y',\Delta z,\tau) = R_{i,j}(x,x',y,y',z,z',t,t') \tag{6.15}$$

where $\Delta z = z' - z$ and $\tau = t' - t$. Since the POD reduces to the harmonic decomposition in the homogenous and stationary directions, these directions can be removed by taking the Fourier transform of the two-point cross-correlation tensor given by Eq. (6.15). Therefore, Fourier transformations in time, t, and homogenous direction, z, are performed to obtain Fourier coefficients of the two-point cross-spectral tensor:

$$S_{i,j}(x,x';y,y';k;f) = \int_{-\infty}^{\infty}\int_{-\infty}^{\infty}\widetilde{R}_{i,j}(x,x';y,y',\Delta z,\tau)e^{-i(2\pi f\tau+k\Delta z)}d\tau d(\Delta z) \tag{6.16}$$

where f is the frequency corresponding to τ and k is the spanwise Fourier mode number corresponding to Δz.

If only one downstream location is considered, streamwise, x, dependence of the two-point cross-spectral tensor in Eq. (6.16) can be treated as a parameter. The resulting POD integral equation is therefore called the slice-POD (c.f., Glauser & George (1987); Jung *et al.* (2004); Citriniti & George (2000); Johansson & George (2006*b*); Gordeyev & Thomas (2000, 2002); Johansson *et al.* (2002); Tutkun *et al.* (2008)). As detailed by Krogstad *et al.* (1998) utilizing the Taylor hypothesis in connection with the convection velocities across the boundary layer is a reasonable assumption to convert spatial dependence to the time dependence. Therefore, x dependence essentially is the same as time dependence, and the slice POD equation can be written as:

$$\int_{y'} S_{i,j}(y,y';k;f)\phi_j^{*(n)}(y';k;f)dy' = \lambda^{(n)}(k;f)\phi_i^{(n)}(y;k;f) \tag{6.17}$$

where $\lambda^{(n)}(k;f)$ and $\phi_i^{(n)}(y;k;f)$ represent the eigenspectra and eigenfunctions for each spanwise mode and frequency, respectively. Since the integration is performed over the wall-normal coordinate direction, which is an inhomogeneous direction, the domain is bounded by the boundary layer thickness, δ, hence it is of finite total energy. Therefore, the Hilbert-Schmidt theory applies.

6.3 POD Analysis Procedure and Numerical Implementation

The POD integral equation given by Eq. (6.17) can be solved numerically by approximating the integral as follows:

$$\int_{y'} f(y')dy' \approx \sum_{i=1}^{N} f_i \Delta y'_i \tag{6.18}$$

where f_i and Δy_i represent the values of the function f at the grid points (or measurement points in this case) and value of the integrand around these grid points respectively. A common practice is to use trapezoidal rule to perform the integration. Justification of using the trapezoidal rule in computing the POD integral equation is detailed by Moin & Moser (1989). The numerically discretized form of the POD integral equation, Eq. (6.17), results in an eigenvalue problem, which can be written as follows:

$$\mathbf{A}\phi^{(n)} = \lambda^{(n)}\phi^{(n)} \tag{6.19}$$

The solution to eigenvalue problem given by Eq. (6.19) is easy to obtain using standard numerical eigenvalue solvers if the kernel, **A**, is Hermitian symmetric. Because of the logarithmic stretching of the probes along the wall-normal direction, the **A** in this experiment is not Hermitian symmetric as shown below:

$$\mathbf{A} = \begin{bmatrix} S_{1,1}(y_1,y'_1;k;f) & S_{1,1}(y_1,y'_2;k;f) & \cdots & S_{1,1}(y_1,y'_N;k;f) \\ S_{1,1}(y_2,y'_1;k;f) & S_{1,1}(y_2,y'_2;k;f) & \cdots & S_{1,1}(y_2,y'_N;k;f) \\ \vdots & \vdots & \ddots & \vdots \\ S_{1,1}(y_N,y'_1;k;f) & S_{1,1}(y_N,y'_2;k;f) & \ldots & S_{1,1}(y_N,y'_N;k;f) \end{bmatrix} \begin{bmatrix} \Delta y'_1 & 0 & 0 & 0 \\ 0 & \Delta y'_2 & 0 & 0 \\ \vdots & \vdots & \ddots & \vdots \\ 0 & 0 & 0 & \Delta y'_N \end{bmatrix} \tag{6.20}$$

where the first matrix is the two-point cross-spectral tensor and the second matrix is the diagonal matrix with the integrands. The remedy to make the kernel Hermitian symmetric is to rearrange Eq. (6.19) and multiply both side of it with the diagonal matrix of square-roots of the integrands as follows:

$$\underbrace{\mathbf{wSw}}_{\mathbf{H}}\underbrace{\mathbf{w}\phi^{(n)}}_{\psi^{(n)}} = \lambda^{(n)}\underbrace{\mathbf{w}\phi^{(n)}}_{\psi^{(}n)} \quad \Rightarrow \mathbf{H}\psi^{(n)} = \lambda^{(n)}\psi^{(n)} \tag{6.21}$$

where **w**, **S** and $\phi^{(n)}$ are:

$$
\begin{aligned}
\mathbf{w} &= \begin{bmatrix} \sqrt{\Delta y'_1} & 0 & 0 & 0 \\ 0 & \sqrt{\Delta y'_2} & 0 & 0 \\ \vdots & \vdots & \ddots & \vdots \\ 0 & 0 & 0 & \sqrt{\Delta y'_N} \end{bmatrix} = \begin{bmatrix} \sqrt{\Delta y_1} & 0 & 0 & 0 \\ 0 & \sqrt{\Delta y_2} & 0 & 0 \\ \vdots & \vdots & \ddots & \vdots \\ 0 & 0 & 0 & \sqrt{\Delta y_N} \end{bmatrix} \\
\mathbf{S} &= \begin{bmatrix} S_{1,1}(y_1,y'_1;k;f) & S_{1,1}(y_1,y'_2;k;f) & \cdots & S_{1,1}(y_1,y'_N;k;f) \\ S_{1,1}(y_2,y'_1;k;f) & S_{1,1}(y_2,y'_2;k;f) & \cdots & S_{1,1}(y_2,y'_N;k;f) \\ \vdots & \vdots & \ddots & \vdots \\ S_{1,1}(y_N,y'_1;k;f) & S_{1,1}(y_N,y'_2;k;f) & \dots & S_{1,1}(y_N,y'_N;k;f) \end{bmatrix} && (6.22) \\
\phi^{(n)} &= \begin{bmatrix} \phi^{(n)}(y'_1;k;f) \\ \phi^{(n)}(y'_2;k;f) \\ \vdots \\ \phi^{(n)}(y'_N;k;f) \end{bmatrix} = \begin{bmatrix} \phi^{(n)}(y_1;k;f) \\ \phi^{(n)}(y_2;k;f) \\ \vdots \\ \phi^{(n)}(y_N;k;f) \end{bmatrix} && (6.23)
\end{aligned}
$$

The solution to Eq. (6.21) does not produce the correct eigenfunctions because of multiplying both sides of Eq. (6.19) by **w**. Therefore, the eigenfunctions, ψ, which will be obtained from the solutions are:

$$
\psi^{(n)} = \begin{bmatrix} \sqrt{\Delta y'_1} & 0 & 0 & 0 \\ 0 & \sqrt{\Delta y'_2} & 0 & 0 \\ \vdots & \vdots & \ddots & \vdots \\ 0 & 0 & 0 & \sqrt{\Delta y'_N} \end{bmatrix} \begin{bmatrix} \phi^{(n)}(y'_1;k;f) \\ \phi^{(n)}(y'_2;k;f) \\ \vdots \\ \phi^{(n)}(y'_N;k;f) \end{bmatrix} \tag{6.24}
$$

The correct eigenfunctions can be found by multiplying the solutions with the inverse of the diagonal matrix formed by the square-root of the integrand elements as follows:

$$
\phi^{(n)} = \begin{bmatrix} \phi^{(n)}(y_1;k;f) \\ \phi^{(n)}(y_2;k;f) \\ \vdots \\ \phi^{(n)}(y_N;k;f) \end{bmatrix} = \begin{bmatrix} \sqrt{\Delta y_1} & 0 & 0 & 0 \\ 0 & \sqrt{\Delta y_2} & 0 & 0 \\ \vdots & \vdots & \ddots & \vdots \\ 0 & 0 & 0 & \sqrt{\Delta y_N} \end{bmatrix}^{-1} \begin{bmatrix} \psi^{(n)}(y_1;k;f) \\ \psi^{(n)}(y_2;k;f) \\ \vdots \\ \psi^{(n)}(y_N;k;f) \end{bmatrix} \tag{6.25}
$$

The number of eigenfunctions and eigenvalues depends on the size of the kernel which is the two-point cross-spectral tensor. The kernel is a square matrix of (M×N)×(M×N), where M is the number of velocity components included in the analysis and N is the number of grids, or measurement locations within the field of interest (c.f., Delville (1994)). In our experiments, we had 11 probes in the wall-normal direction, y, spaced logarithmically and only the streamwise velocity component of turbulent velocities was measured. Therefore, the size of the the kernel is 11×11 for each pair of spanwise Fourier mode, k, and frequency, f. Thus, the maximum number of POD modes which can be extracted from the current setting is 11 for each k and f.

6.4 Spectral Analysis Technique and Forming the Kernel

This section is compiled from Tutkun *et al.* (2008) to describe the steps towards establishing the final POD equation, Eq. (6.17), following previous experimental utilization of the POD documented by Glauser & George (1987); Citriniti & George (2000); Gordeyev & Thomas (2000); Jung *et al.* (2004); Johansson *et al.* (2002); Gordeyev & Thomas (2002); Johansson & George (2006*b*):

1. Instantaneous velocities are measured simultaneously at two points in space.
2. Fourier transformation of the instantaneous velocities is performed in time for the finite size record length; i.e.,

$$\hat{u}_i(y,z,f) = \int_{-T/2}^{T/2} e^{-i2\pi ft} u_i(y,z,t)dt \tag{6.26}$$

   where $\hat{u}_i(y,z,f)$ is called the Fourier coefficients and T represents the record length for each block of data. An FFT (Fast Fourier Transformation) algorithm is used to compute the Fourier coefficients efficiently.
3. Steps (1) and (2) are repeated for all pairs of points.
4. Cross-spectra are computed and block averaging is performed as follows:

$$\widetilde{S}_{i,j}(y,y';\Delta z;f) = \frac{\langle \hat{u}_i(y,z,f)\hat{u}_j^*(y',z+\Delta z,f)\rangle}{T} \tag{6.27}$$

   where $\langle\ \rangle$ and * denote the block averaging and complex conjugate respectively.
5. The doubly transformed cross-spectra are computed by the Fourier transformation of Eq. (6.27) in the spanwise direction; i.e.,

$$S_{i,j}(y,y';k;f) = \int_{-Z/2}^{Z/2} \widetilde{S}_{i,j}(y,y';\Delta z;f) e^{-ik\Delta z} d(\Delta z) \tag{6.28}$$

   where Z is the width of the hot-wire rake in the spanwise direction.
6. The final eigenvalue problem is solved for each frequency and spanwise Fourier mode after construction of the Hermitian symmetric kernel as described in the previous section.

Chapter 7

Proper Orthogonal Decomposition: Results

7.1 Eigenvalue Distribution over POD Modes

First, the eigenvalue distribution is presented in Figure 7.1 to show how POD is efficient and optimumal in terms of capturing the largest amount of turbulence kinetic energy with the fewest modes. The high and low Reynolds number cases are given in Figures 7.1(a) and 7.1(b) respectively. Each of the bars in these figures represents the normalized eigenvalues integrated over frequency and summed over the spanwise Fourier modes. The distribution of eigenvalues is computed using using Eq. (7.1) as follows:

$$\zeta^{(n)} = \frac{\sum_{k=1}^{M} \int_{-\infty}^{\infty} \lambda^{(n)}(k,f)\,df}{\sum_{n=1}^{N} \sum_{k=1}^{M} \int_{-\infty}^{\infty} \lambda^{(n)}(k,f)\,df} \tag{7.1}$$

where the denominator is, as it can also be seen from Eq. (6.12), the total turbulence kinetic energy at the plane normal to the streamwise direction. These results together with all the POD results given in following sections are based on a one-component scalar proper orthogonal decomposition of the streamwise turbulence fluctuations, since that only component of the velocity was measured in the experiments. (Note that hereafter all reference to the proper orthogonal decomposition will mean the one-component scalar decomposition.)

Each bar in figure 7.1 indicates the contribution of the corresponding POD modes to the total kinetic energy of the domain. We observe slightly higher ($\sim$0.4%) energy captured by the first POD mode in high the Reynolds number case, whereas the second POD mode of the low Reynolds number case is found to be approximately the same amount higher than that of the high Reynolds number case.

The results show that the first six POD modes contain more than 97% of the total energy. If the energy content of the first four POD modes is investigated, we see that approximately 90% of the total energy is carried by these three modes. Table 7.1 presents the percentage of each POD mode in terms of its contribution to the overall energy. Note that these normalized values are integrated and summed over frequency and spanwise Fourier modes. There are 16384 Fourier coefficients in the frequency domain and 71 modes in spanwise Fourier mode domain in total, so that it actually consists of many more modes due to Fourier coefficients in these domains.

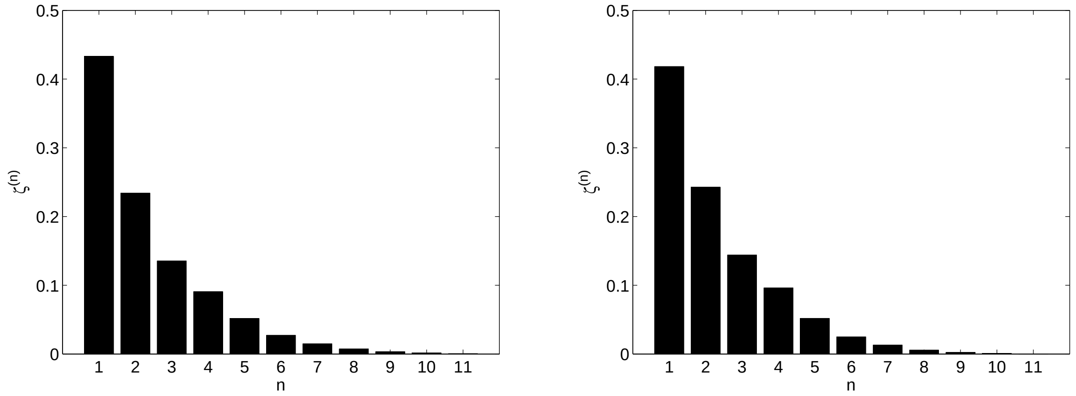

(a) Re_θ =19 100.

(b) Re_θ =9800.

Figure 7.1: Normalized eigenvalue distribution, ζ^n, for each POD mode, *n*.

Percentage of turbulence kinetic energy	Re_θ =19 100	Re_θ =9800
$\lambda^{(1)}$	43.32	41.83
$\lambda^{(1)}+\lambda^{(2)}$	66.72	66.10
$\lambda^{(1)}+\lambda^{(2)}+\lambda^{(3)}$	80.27	80.51
$\lambda^{(1)}+\lambda^{(2)}+\lambda^{(3)}+\lambda^{(4)}$	89.35	90.13
$\lambda^{(1)}+\lambda^{(2)}+\lambda^{(3)}+\lambda^{(4)}+\lambda^{(5)}$	94.52	95.30
$\lambda^{(1)}+\lambda^{(2)}+\lambda^{(3)}+\lambda^{(4)}+\lambda^{(5)}+\lambda^{(6)}$	97.25	97.80

Table 7.1: Percentage of turbulence kinetic energy captured by the POD modes.

The ratios of each pair of successive eigenvalues are given in Table 7.2. As it is clear from both Figure 7.1 and Tables 7.1 and 7.2, it is difficult to see any strong Reynolds number dependency at this point. This might be attributed to the integration and summation performed over frequency and spanwise Fourier mode number respectively, because these operations tend to smooth things out, hence leading to an average picture. But it could also be because of the dominant contribution of the outer part of the boundary layer to the overall energy at these high Reynolds numbers.

Re_θ	$\frac{\lambda^{(1)}}{\lambda^{(2)}}$	$\frac{\lambda^{(2)}}{\lambda^{(3)}}$	$\frac{\lambda^{(3)}}{\lambda^{(4)}}$	$\frac{\lambda^{(4)}}{\lambda^{(5)}}$	$\frac{\lambda^{(5)}}{\lambda^{(6)}}$	$\frac{\lambda^{(6)}}{\lambda^{(7)}}$	$\frac{\lambda^{(7)}}{\lambda^{(8)}}$	$\frac{\lambda^{(8)}}{\lambda^{(9)}}$	$\frac{\lambda^{(9)}}{\lambda^{(10)}}$	$\frac{\lambda^{(10)}}{\lambda^{(11)}}$
19 100	1.85	1.73	1.49	1.76	1.89	1.85	2.05	2.12	2.27	2.50
9800	1.73	1.68	1.50	1.86	2.07	1.92	2.28	2.38	3.00	8.00

Table 7.2: Ratios of turbulence kinetic energy captured by each POD mode.

7.2 Eigenspectra over Spanwise Fourier Modes, *k*, and Frequency, *f*

Figures 7.2 and 7.3 show the eigenspectra, $\lambda^{(n)}(k,f)$, as function of spanwise Fourier mode number (k) and frequency (f) for Reynolds numbers of 19 100 and 9800 respectively. The first 6 POD modes are presented in these figures from (a) to (f) in ascending order, even though fewer modes would be enough to capture most of the total kinetic energy. The amount of energy found in POD mode-5 (Figures 7.2(e) and 7.3(e)) and POD mode-6 (Figures 7.2(f) and 7.3(f)) are almost negligible compared to the energy of the first four POD modes. The highest spanwise Fourier modes and frequency considered in these figures are 6 and 100 Hz respectively, because the contributions of higher modes and frequencies are very small in terms of magnitude.

Most of the energy is in spanwise Fourier mode-1 and mode-2: first because the peaks at the near zero frequency are large, and second because there is a broadband decay of the energy compared to rest of the POD modes. The eigenspectra have peaks at near zero frequency, a distinct feature at all POD and spanwise modes. For the first POD mode at both Reynolds numbers, the near zero frequency peaks are found to be the largest in spanwise Fourier mode-2. By contrast, the second POD modes at near zero frequency are larger for the first spanwise mode than for the second spanwise mode. This also is observed for both of the Reynolds numbers investigated here. It is again difficult to see any dependence on the Reynolds number in these figures.

The features of the eigenspectra in general are almost the same at both Reynolds numbers. Since the eigenspectra presented here are not scaled by the total energy, the only difference between the two Reynolds numbers studied here is the magnitude of the eigenvalues. This is an expected result because higher Reynolds number was created by increasing the tunnel speed, which also caused an almost directly proportional increase in the turbulence kinetic energy.

In a similar manner, the eigenspectra of the first six spanwise Fourier modes as functions of POD modes and frequency are presented in Figures 7.4 and 7.5 for the high and low Reynolds numbers respectively. Only the first six POD modes and first 100 Hz of the spectra are shown, because of almost negligible activity at the higher modes and frequencies as discussed previously. Since one of the axes is the POD mode number, the eigenspectra at each frequency is ordered from the largest to the smallest for each spanwise Fourier modes. This is due to the optimality property of the POD, which we did not observe for in the previous Figures 7.2(f) and 7.3(f). For the harmonic decomposition performed in the spanwise direction or frequency the Fourier modes are not ordered.

$$\chi^{(n)}(k,f) = \frac{\lambda^{(n)}(k,f)}{\sum_{n=1}^{N}\sum_{k=1}^{M}\int_{-\infty}^{\infty}\lambda^{(n)}(k,f)df} \tag{7.2}$$

To be able to compare the eigenspectra of the dynamically most important eigenmodes of both Reynolds numbers we present normalized eigenspectra, $\chi^{(n)}(k,f)$ of the first six POD modes versus frequency for the first four spanwise Fourier modes in Figures 7.6−7.11. We compute $\chi^{(n)}(k,f)$ using Eq. (7.2). The frequency axes in these figures extend to 1000 Hz, even though there are actually no large scale energy containing eddies left in the spectrum. Furthermore, a log-log scale is chosen to show how the energy is distributed, and especially how it decays with increasing frequency. As shown in the Section 4.3, the power spectra of turbulence energy have some small spikes around 278 Hz and its harmonics around 556 Hz and 834 Hz. The largest area under these spike, which is the contribution of the spike to the total turbulence energy, is found to be at 278 Hz. The energy due to the spikes in the spectra is negligible when compared with the total turbulence energy. Since these spikes are caused by noise sources due to electronics and synchronization of different measurement systems, the noise exists at every anemometer channel. Even though these spikes are much weaker than turbulence, and only show up when turbulence level decreases with increasing wall-normal distances close to the freestream, the POD finds them at every measurement position and treats them as a very large scale filling up the whole domain. That is why we also observe the same spikes in the eigenspectra. Moreover, we observe most of the spikes at the first POD modes for the same reason. If the noise at different channel occurred at different frequencies, then the POD would not be able to link them as an energy containing scale and would place them toward the end of spectrum as some other noise.

The area under these spikes in the power spectra is negligible, hence they should also be negligible in the eigenspectra. Therefore, we remove spikes from the eigenspectra shown in Figures 7.6−7.11 to be able to provide clearer picture. Justification of this can be seen in Figures 7.12 and 7.13 which actually is equivalent to Figure 7.6, but in a linear-linear scale with additional curves showing the normalized eigenspectra double summed over spanwise and POD modes, and that summed over only spanwise Fourier modes. It is obvious from this linear plot that even the largest contribution is very small compared to the total area under the curves. More quantitatively, the area under the spike-removed curves and the area under the original curves can be compared; the difference when the integration is performed for the entire frequency domain (for which the higher frequencies are much noisier) never exceeds 5% in the worst case, which is POD mode-1.

Figures 7.6−7.11 show that a significant part of the spectra collapse for both of the Reynolds numbers. But the eigenspectra of high and low Reynolds numbers collapse on different curves. On the other hand, since the collapsing curves are almost parallel to each other, it suggests that proper scaling of the frequency axis may lead to eigenspectra of the two Reynolds number tested here collapsing on a single curve. As can be seen in these figures, the collapsing part of the spectra is around 100 Hz and 50 Hz for high and low Reynolds number cases. Furthermore, the collapse is observed after at least two decades of decay of turbulence from the largest values in the spectra which are near at zero frequency. Therefore, the scales of the collapsing part are not the most energetic scales, which are found at rather low frequencies. The collapse occurs at the frequencies where the inertial range of the energy cascade begins. Even though the collapse is observed at slightly different frequencies for different POD modes, there is always a factor of 2 between the starting points of collapsing frequencies of high and low Reynolds number cases. This is an expected result, because the freestream velocity of $Re_\theta = 19\,100$ is twice the freestream velocity of $Re_\theta = 9800$. Since the boundary layer thickness is almost the same for both cases, the integral time scale of the low Reynolds number case is approximately half of that of the high Reynolds number case.

The low frequency part of the eigenspectra contains the scales with the largest amount of energy. In its current form, there is no collapse in this part of the spectra at all, even for different spanwise Fourier modes at the same POD mode. It seems that this part of the spectra will not collapse by any means, because there are many crossings of different spanwise modes for each POD modes. In addition to this, the eigenspectra of different Reynolds number at the same spanwise and POD modes sometimes cross each other which makes any scaling attempt more difficult.

7.3 Eigenvalue Distribution over POD and Spanwise Fourier Modes

The eigenspectra of the POD modes are integrated over frequency to investigate the kinetic energy distribution only over azimuthal Fourier modes. These results are presented in normalized form using Eq. (7.14), which actually is equal to the integration of Eq. (7.2) over frequency as follows:

$$\xi^{(n)}(k) = \frac{\displaystyle\int_{-\infty}^{\infty} \lambda^{(n)}(k,f)df}{\displaystyle\sum_{k=1}^{M}\sum_{n=1}^{N}\int_{-\infty}^{\infty} \lambda^{(n)}(k,f)df} = \int_{-\infty}^{\infty} \chi^{(n)}(k,f)df \tag{7.3}$$

where M and N are the maximum number of Fourier modes in the spanwise direction and POD modes respectively. Each bar denotes the contribution to the turbulence kinetic energy of the POD mode at the spanwise Fourier mode shown by the abscissa of the plots. Only the first 6 POD modes and only 12 spanwise modes are shown to clearly identify the relative contribution of the most important POD and spanwise modes. Since this is the integrated eigenvalue distribution, it can be easily seen that spanwise Fourier modes higher than number six have relatively insignificant contribution to the total energy. The asterisk sign in the figures indicate the total contribution of each POD mode to the total turbulence kinetic energy at each spanwise Fourier mode. The $*$ signs are computed by summing all the POD modes for each spanwise mode. Note that there are 71 spanwise Fourier modes, which are actually symmetric pairs of 35 modes plus the first Fourier mode. Therefore, the second spanwise Fourier mode and the spanwise Fourier mode-71 are identical. In these figure, we do not show the symmetric part.

Figures 7.14(a) and 7.14(b) show the normalized eigenvalue distribution for high and low Reynolds numbers respectively. The distribution of eigenvalues for these two cases are very close to each other; hence there is no apparent dependence on Reynolds number. There are some common features in both of these figures; namely: (i) Most of the energy is found at spanwise Fourier mode-1 and mode-2, (ii) Spanwise Fourier mode-2 is slightly larger than spanwise Fourier mode-1 as shown by the asterisk signs, (iii) The first POD modes of the first and second spanwise Fourier modes of the high Reynolds number case are larger than those of the low Reynolds number case, whereas the second POD modes of the first and second Fourier modes of the high Reynolds number case are smaller than those of the low Reynolds number case.

7.4 Reconstruction of Velocity Field

Using Eqs. (6.8) and (6.9), it is possible to reconstruct the instantaneous velocity field of the turbulence using the deterministic POD eigenmodes together with their the random coefficients, which are obtained by projecting the velocity field onto the deterministic eigenmodes. Only the streamwise velocity component can be reconstructed in our study because only the streamwise fluctuations are included in our construction of the kernel of the POD integral equation, Eq. (6.17). Since the kernel, $\mathrm{S}_{1,1}(y,y';k;f)$, is written as a function of both spanwise Fourier mode number, k, and frequency, f, the resulting eigenfunctions and eigenvalues are also functions of these two parameters as described in the previous sections. Therefore, reconstruction of velocity field begins by finding the random coefficients, $\mathrm{a}_n(k,f)$, by projecting the eigenfunction onto the double Fourier transformed velocity fluctuations as follows:

$$a_{(n)}(k,f) = \int_0^{\infty} \hat{\hat{u}}(y,k,f)\phi^{(n)*}(y,k,f)dy \tag{7.4}$$

where the integration is performed in the inhomogeneous wall-normal direction using the trapezoidal rule. The upper limit of integration is actually replaced by the boundary layer thickness, δ. The fluctuating velocity is transformed into Fourier domain, first in time and second in the homogeneous spanwise direction to obtain $\hat{\hat{u}}(y,k,f)$; i.e.,

$$\hat{\hat{u}}(y,k,f) = \int_{-\infty}^{\infty}\int_{-\infty}^{\infty} u(y,z,t)e^{-i(2\pi ft+kz)}dzdt \tag{7.5}$$

The experimental utilization of the second Fourier transformation in the spanwise direction is rather difficult because of the nonuniform grid of hot-wire rake probes as detailed in the experimental setup chapter. To be able to perform the second Fourier transformation in z, linear interpolation of the fluctuating velocities at each constant wall-normal location is performed by the smallest increment available in z-direction. In this way, a uniform grid spaced by 4 mm is created and subsequent Fourier transformation is applied on this grid. Note that construction of the kernel, $\mathrm{S}_{1,1}(y,y';\Delta z;f)$, (and the resulting eigenfunctions and eigenvalues) are already on a uniformly spaced grid of 4 mm, because it is possible to create this grid size using different vertical combs in connection with the homogeneity of the statistical quantities in the spanwise direction.

The doubly Fourier transformed streamwise component of fluctuating velocities are obtained as a linear combination of eigenfunction using the random coefficients obtained by Eq. (7.4):

$$\hat{\hat{u}}_{rec}(y,k,f) = \sum_{n=1}^{N} a^{(n)}(k,f)\phi^{(n)*}(y,k,f) \tag{7.6}$$

where subscript *rec* stands for “reconstructed”. The reconstructed velocity expressed in terms of spanwise Fourier modes and frequency can be mapped back into real space in two steps:
(i) Inverse Fourier transformation in frequency:

$$\hat{u}_{rec}(y,k,t) = \int_{-\infty}^{\infty} \hat{\hat{u}}_{rec}(y,k,f)e^{i2\pi ft}df \tag{7.7}$$

(ii) Inverse Fourier transformation in spanwise Fourier index:

$$u_{rec}(y,z,t) = \int_{-\infty}^{\infty} \hat{u}_{rec}(y,k,t)e^{ik\Delta z}dk \tag{7.8}$$

The fluctuating velocity given by Eq. (7.8) can also be reconstructed using some subset of the POD and spanwise Fourier modes to investigate the dynamics associated with that subset of modes. This can be achieved by setting the random coefficients of all the modes out of the subset of interest to zero, and following the same route from Eq. (7.5) to Eq. (7.8). If all the POD and spanwise Fourier modes are used for reconstruction, the original velocity signal can be recovered within the numerical accuracy. By selecting only the most energetic POD and Fourier modes, it is possible to study large scale energetic structures using the reduced velocity reconstruction which does not count the intermediate and small scales.

Figures 7.15 and 7.16 compare the original velocity signal and the reconstructed velocity signal using a number of POD modes. These figures show the reconstruction of velocity fluctuations measured by one probe in the middle of the hot-wire rake as an example. Similar features are observed for the other probes of the rake. These reconstructed signals shown in figures 7.15 and 7.16 are computed using all spanwise Fourier modes and frequencies. Here, we just show a very small portion of the signal to be able to present the details. The data are plotted for the first 1500 samples of a randomly chosen single block of velocity recordings. Therefore the time axis extends up to 0.05 seconds from the beginning of the block, as it can be seen in the figures. The reconstructed velocities converge to the original signal, and all the small details of the signal emerge as the number of POD modes involved in the reconstruction increases. Most of the recovery of the original signal is accomplished using only the first five modes. Adding higher POD modes do not change the reconstruction significantly as can be seen in figure 7.15.

Since large scale features of turbulent boundary layers are of much interest, low-pass filtering of the data to remove the contributions due to high frequency (or wavenumber) (i.e., small scale features of turbulence) is performed by setting the random coefficient, $a_n(k, f)$, to zero for those high frequencies. Figures 7.17 and 7.18 compare the reconstruction with and without filtering of the small scale contribution to turbulence kinetic energy at higher frequencies. The location of the cut-off frequency in the spectrum was decided using the eigenspectra shown in figures 7.2−7.11; 100 Hz for the high Reynolds number case and 49.4 Hz for the low Reynolds number case. The left columns of figures 7.17 and 7.18 present the reconstructed velocity fluctuations on the spanwise-wall-normal plane with all the frequency components, while right columns represent the same reconstructions with filtering through the random POD coefficients. Here we present reconstruction using all POD and spanwise Fourier modes, the first POD mode and all spanwise Fourier modes, and the first POD mode and only the second spanwise Fourier mode. As evidenced in these figure, the filtering only removes the high frequency and small scale contributions, and does not affect the large scale features of turbulence.

Since it is possible to retain all the large scale energetic features of turbulence with only frequencies up to 100 Hz and 49.4 Hz for the high and low Reynolds numbers studied here, it provides a great reduction in number of frequency modes. This means that only 112 spanwise and 54 frequency Fourier modes are kept in the reconstruction of the velocity fluctuations for high and low Reynolds numbers, instead of 16384 frequency modes. Therefore, we only use and show velocity reconstruction with low-pass filtering in the subsequent discussions and figures. The difference because of filtering in any kind of partial or full reconstruction is negligible and similar to the ones shown in figures 7.17 and 7.18.

Figures from 7.19 to 7.42 show the reconstructed velocity in the spanwise-wall-normal (YZ) plane for both of the Reynolds numbers tested here. These figures can be divided into four main sections: Reconstruction of velocity using (i) first POD mode at $Re_\theta = 19\,100$ (figures 7.19-7.24); (ii) first four POD modes at $Re_\theta = 19\,100$ (figures 7.25-7.24); (iii) first POD mode at $Re_\theta = 9800$ (figures 7.31-7.36); and (iv) first four POD modes at $Re_\theta = 9800$ (figures 7.37-7.42). These four main groups enable us to see the effect of most energetic modes on the reconstructions at the different Reynolds numbers. Each of these four main groups are formed by reconstruction using only first, second, third, fourth, fifth and sixth spanwise Fourier modes for corresponding POD modes included in the computations. Moreover, each of these figures show the evolution of these reconstructed velocities by presenting the velocity fluctuations at different time of realizations. In total, each figure contains nine different time steps and demonstrates how things change as the flow evolves. Figures representing different time steps are portions of real time movies of the reconstructed velocity fields. The time step are selected to show some of the important events happening within the boundary layer, and it is on the order of integral time scale of turbulence.

Figures 7.19, 7.25, 7.31 and 7.37 show the reconstruction of velocity fluctuations using only the first spanwise Fourier mode. Since only the first spanwise Fourier mode is included in these computations, there is no variation (or zero crossings) along the spanwise direction. (Note that the first spanwise Fourier mode represent the first coefficient of the Fourier transformation performed in the corresponding directions. It usually is called the zeroth Fourier mode in some other applications such as POD performed on axisymmetric flows.) It seems that there are layers of positive and negative fluctuations throughout the boundary layer.. As the number of POD modes increases as in figures 7.25 and 7.37, the complexity of these layers in the wall-normal direction increases as well. This complexity, or an increase in number of zero crossings in the inhomogeneous direction, is associated with the fact that as the POD mode number increases the eigenfunction across the inhomogeneous direction varies a lot, hence so do the reconstructed velocity fluctuations. From these figures it is hard to say anything about the interaction between different layers of fluctuations across the boundary layer.

Reconstructed velocity fluctuations using only the second spanwise Fourier mode are presented in figures 7.20, 7.26, 7.32 and 7.38. Similar to the previous figures, they represent the reconstruction based on first POD mode and first four POD modes for the high Reynolds number case and those for the low Reynolds number case respectively. The variation in velocity fluctuations across the spanwise direction is clear this time, because of the second spanwise Fourier mode. In addition to this, the features are not fixed in space and move along the spanwise direction back and forth. There is no trend or tendency observed in neither direction nor the sequence of motion. The large scale features (notice that two lobes fill almost entire extent of the view in the spanwise direction, which is about one boundary layer thickness) observed in these figures are dynamically active such that they get stronger, weaker, sometimes merge with other large scale features and break into different pieces. More interestingly, these figures show how the inner and outer layer of turbulent boundary layer, including the near wall region, interact with each other.

For the high Reynolds number case, first of all, we observe strong positive and negative momentum sources in the outer layer as shown in figure 7.20, especially between y/δ of 0.1 and 0.8. These are one of the most dominant features if only the reconstruction based on spanwise Fourier mode 2 is considered. The time-resolved reconstruction of this POD and spanwise Fourier mode show that once there is large enough momentum developed in the inner layer including both log layer and near wall layers, then these high momentum sources located outer layer and inner layer merges. This initially results in a very large scales of motion occupying the entire outer layer and log layer. While these large scale fluctuations are formed, there is no significant activity existing in the near wall region. As the flow evolves, then this large scale, high momentum motion of turbulence starts extending down to the wall, and filling the entire boundary layer again as it is in figure 7.20(i) and some subsequent snapshots. Reconstruction based on only one POD and spanwise mode shows that there is a strong coupling between the inner and outer layer. Furthermore, the velocity profiles along the spanwise direction change significantly between positive and negative fluctuations and most probably creates inflection points in the profile and corresponding instability mechanisms. These speculations need to be investigated further with some detailed analysis, but no attempt has been made to do this in the course of this thesis.

Reconstruction based on the same spanwise mode-2, but including the first four POD modes in figure 7.26 provide a clearer picture about what really is going on in the boundary layer. First, there is an increase in size and magnitude of both positive and negative fluctuations, which is particularly related to the number of POD modes taken into account. As can be seen from the contour plots of the spanwise-wall-normal plane, the highly energetic features in the outer layer merge with the energetic events in the near wall region and breaks apart. When the energetic events merge, they cover the entire span from the very near wall to almost the top of the boundary layer. Since there are four POD modes are included in the reconstruction, there appears a more complex behavior in the wall-normal direction. Similar observations from figures 7.32 and 7.38 are possible for the low Reynolds number velocity fluctuations reconstruction based on spanwise mode-2.

Reconstructed velocities for high Reynolds number experiment using spanwise Fourier mode-3 together with only the first POD mode and first four POD modes are plotted in figures 7.21 and 7.27 respectively. First of all, there are more variations in velocity profiles and zero crossings along the spanwise direction. As the number of POD modes involved in the reconstruction increases, the strength of the large scale energetic events increases together with the complexity of the profiles in the wall-normal direction. Reconstruction based only on the first POD mode in figure 7.21 shows that the organized motions extend from half-way in the outer region to the end of buffer layer. As the time step increases we see more and more influence in the near wall region due to these energetic features of turbulence, mostly occupying the entire log layer. At some point, these features lose strength and are "turned off"; then they activate again. Figure 7.27 provides a better picture and stronger evidences of the coupling between the inner and outer layers. The large scale features in the wake region and log layer first become strong and then they penetrate down to the wall. Once they cover the entire boundary layer, they stay active for many integral time scales. Equally strong and important coupling between inner and outer layers using the reconstructed velocity field in the low Reynolds number case is observed in figures 7.33 and 7.39. However, the strength of the energetic events very close to the wall is slightly weaker compared to the maximum momentum sources in the turbulent boundary layer.

Figures 7.22 and 7.28 show the velocity contour lines of the reconstructed turbulent fluctuations using the fourth spanwise Fourier mode together with the first and first four POD modes respectively. The positive and negative momentum sources in one POD based reconstructions appear to be fixed in space and they do not change their location substantially. On the other hand, they are active and inactive in a cycle. They are weak, get stronger, then get weaker, and get stronger again. The footprints of these events extending to the wall can also be seen in these figures. However, they are not as significant as for the lower spanwise Fourier modes. Inclusion of more POD modes increases the complexity in the wall-normal direction as can be seen in figure 7.28. In addition to this, we observe smaller features of positive and negative momentum sources due to higher POD modes, even though the magnitude is not affected substantially. The connection between the log layer and the near wall region is more obvious in this case than the coupling between the inner and outer layer of turbulent boundary layer. We essentially do not see any significant difference between the velocity reconstruction of the high and low Reynolds number cases, as it can be seen in figures 7.34 and 7.40.

Even though the magnitude of the large scale events go down substantially for higher Fourier mode number in spanwise direction, it is still possible to see how the velocity profiles vary in both spanwise and wall normal direction. Figures 7.23, 7.24, 7.29, 7.30, 7.35, 7.36, 7.29 and 7.30 essentially show that there are weak organized motions starting near the wall and extending into the log layer of the turbulent boundary layer.

7.5 Summary and Discussion

In this chapter, we showed the experimental utilization of the proper orthogonal decomposition for the high Reynolds number zero pressure gradient turbulent boundary layer. The normalized eigenvalue distribution shows that the first POD mode has more than 40% of the turbulence kinetic energy, while the second one has about 20% of the total turbulence kinetic energy. It is possible to recover about 90% of the kinetic energy only using the first four POD modes. Similar figures are obtained at both Reynolds number with no significant indication of Reynolds number dependence.

The eigenspectra always peak near zero frequency and most of the large scale features are found below 100 Hz and 50 Hz for the high and low Reynolds number cases studied here respectively. Even though no attempt was made to find a suitable similarity parameter for the eigenspectra of the two different Reynolds number made in this investigation, the results indicate that it might be possible to scale the eigenspectra especially in the inertial range of turbulence similar to the similarity of the eigenfunctions and eigenspectra within the outer layer of turbulent wall flow shown by Liu *et al.* (1994) using inner velocity and outer length scales.

The kinetic energy distribution is maximum at spanwise Fourier mode-2, while there is a slight difference between spanwise Fourier mode-1 and-2. The normalized eigenvalue distribution obtained from two different Reynolds number have almost the same distribution and features.

The low-pass filtering of turbulence kinetic energy by means of the random coefficients of POD is very effective with no significant change in the large scale features of the turbulent boundary layer. The reconstructed velocity fluctuations on the spanwise-wall-normal plane show how organized motions of turbulence with significant amounts of energy interact with each other across the boundary layer. It is also possible to observe the strength of the interaction between the inner and outer layer using these reconstructed velocity fields. The reconstructed fields suggest strongly that any attempt to develop uncoupled models for different layers of turbulence will result in failure, since strong interactions exist between the large scale energetic scales of turbulence in the entire boundary layer. Moreover they appear to dispute the classical view that it is the inner layer that drives the outer. In fact, the opposite appears to be true.

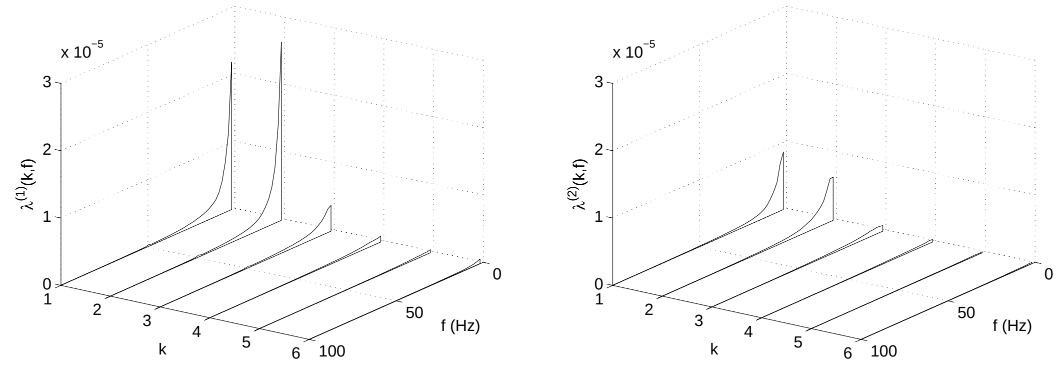

(a) Eigenspectra of the first POD mode.

(b) Eigenspectra of the second POD mode.

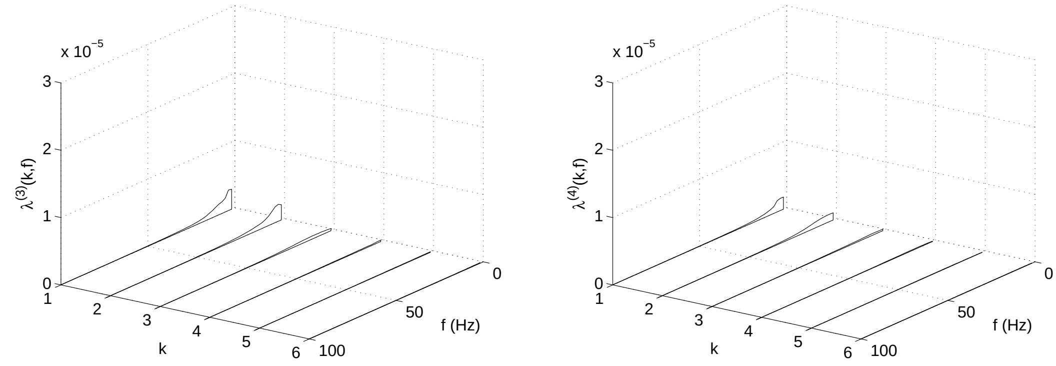

(c) Eigenspectra of the third POD mode.

(d) Eigenspectra of the fourth POD mode.

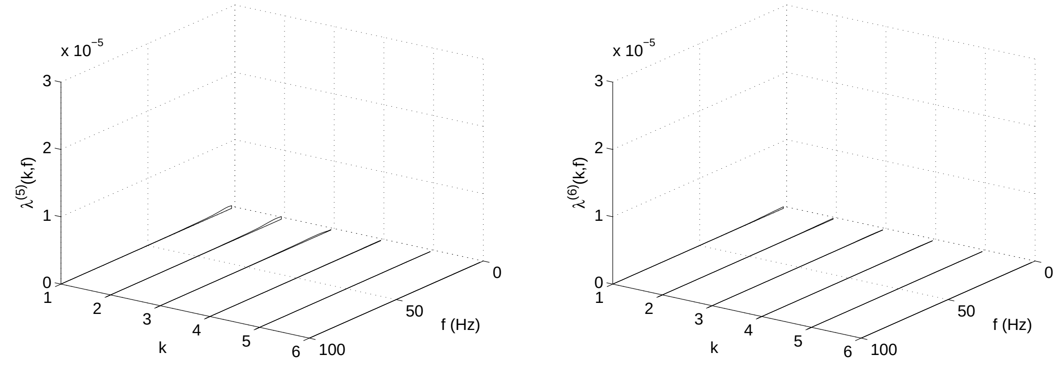

(e) Eigenspectra of the fifth POD mode.

(f) Eigenspectra of the sixth POD mode.

Figure 7.2: Eigenspectra, $\lambda^{(n)}(k,f)$, of the first 6 POD modes (n=1,$\cdots$, 6) for different spanwise Fourier modes, k, and frequencies, f, at Re_θ =19 100.

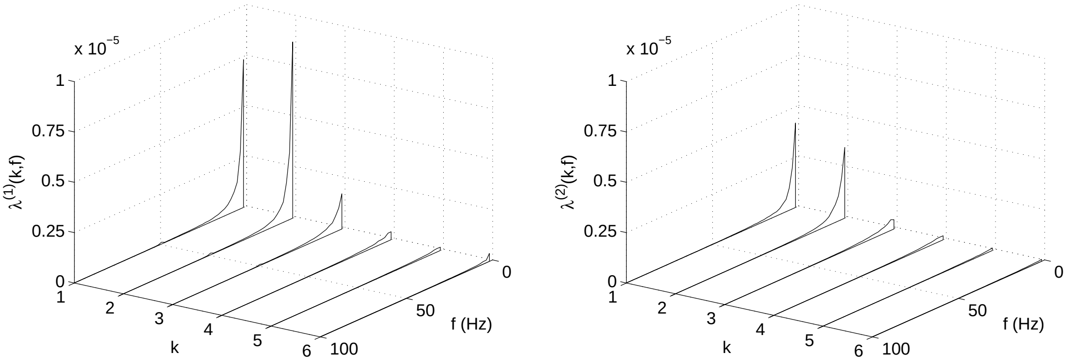

(a) Eigenspectra of the first POD mode.

(b) Eigenspectra of the second POD mode.

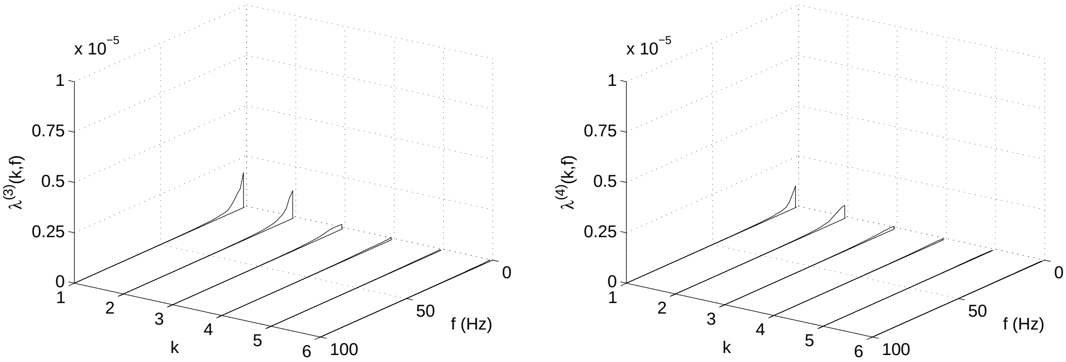

(c) Eigenspectra of the third POD mode.

(d) Eigenspectra of the fourth POD mode.

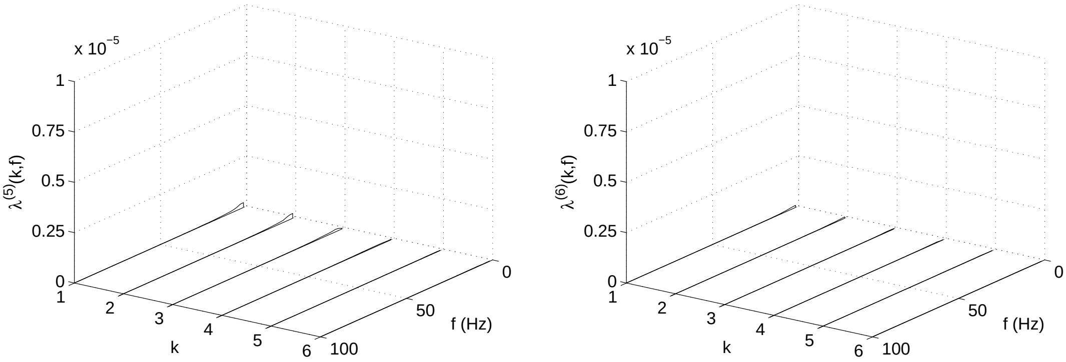

(e) Eigenspectra of the fifth POD mode.

(f) Eigenspectra of the sixth POD mode.

Figure 7.3: Eigenspectra, $\lambda^{(n)}(k, f)$, of the first 6 POD modes (n=1,$\cdots$, 6) for different spanwise Fourier modes, k, and frequencies, f, at Re_θ =9800.

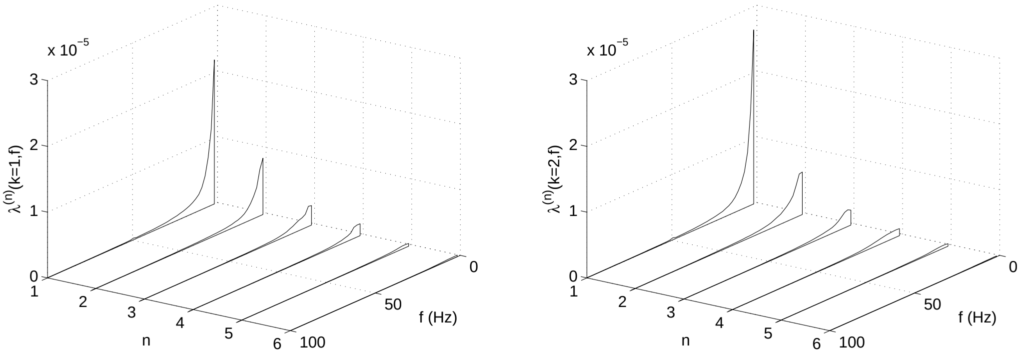

(a) Eigenspectra of the first spanwise Fourier mode.

(b) Eigenspectra of the second spanwise Fourier mode.

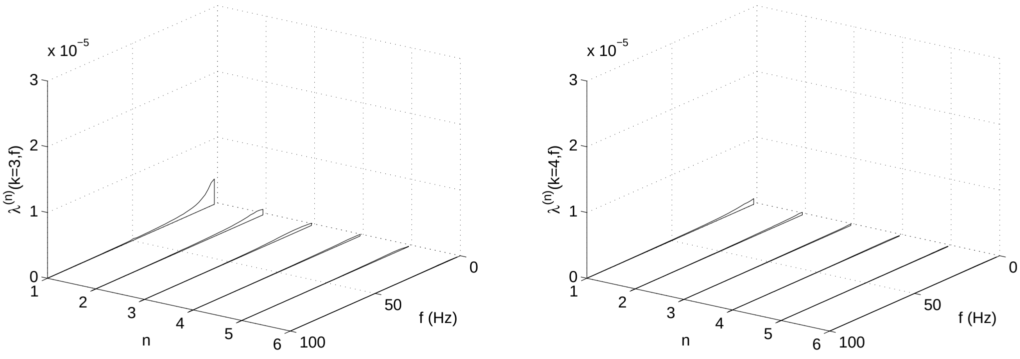

(c) Eigenspectra of the third spanwise Fourier mode.

(d) Eigenspectra of the fourth spanwise Fourier mode.

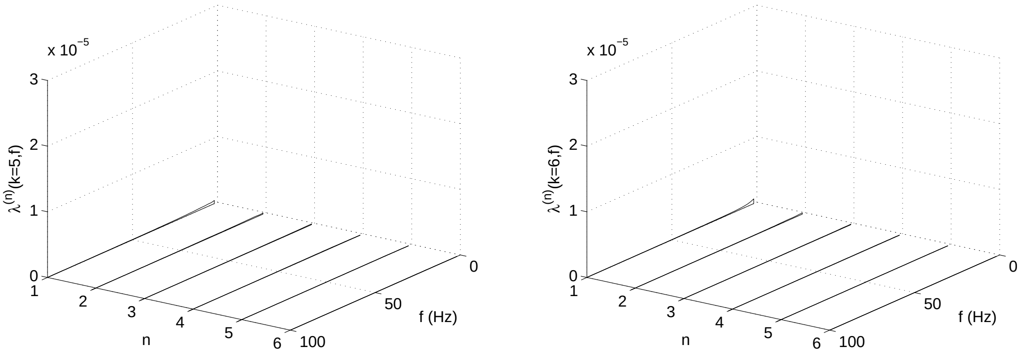

(e) Eigenspectra of the fifth spanwise Fourier mode.

(f) Eigenspectra of the sixth spanwise Fourier mode.

Figure 7.4: Eigenspectra, $\lambda^{(n)}(k, f)$, of the first 6 spanwise Fourier modes ($k = 1, \cdots, 6$) for different POD modes, n, and frequencies, f, at $Re_\theta = 19\,100$.

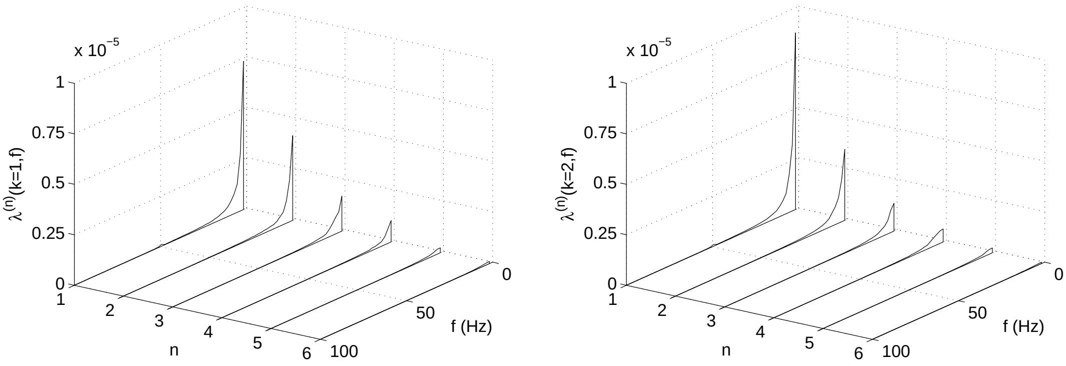

(a) Eigenspectra of the first spanwise Fourier mode.

(b) Eigenspectra of the second spanwise Fourier mode.

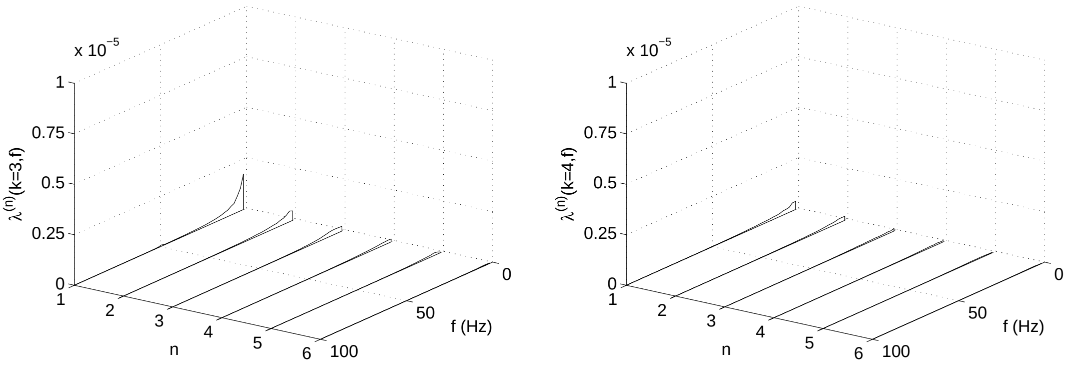

(c) Eigenspectra of the third spanwise Fourier mode.

(d) Eigenspectra of the fourth spanwise Fourier mode.

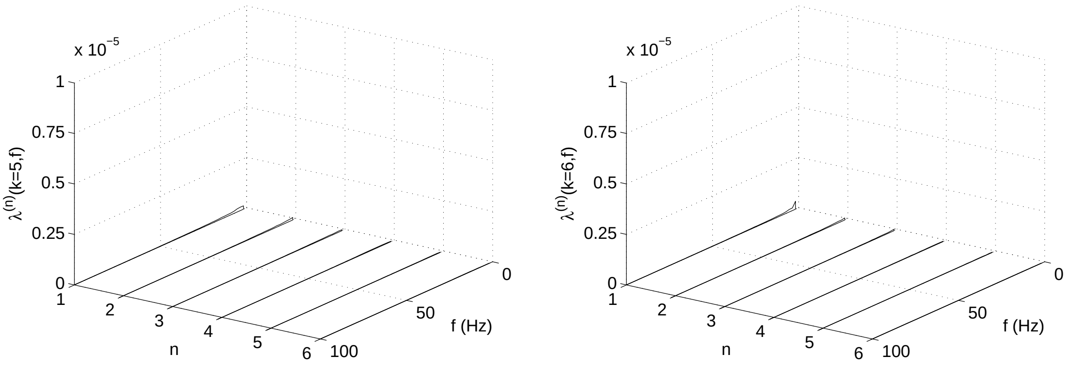

(e) Eigenspectra of the fifth spanwise Fourier mode.

(f) Eigenspectra of the sixth spanwise Fourier mode.

Figure 7.5: Eigenspectra, $\lambda^{(n)}(k, f)$, of the first 6 spanwise Fourier modes ($k = 1, \cdots, 6$) for different POD modes, n, and frequencies, f, at $\mathrm{Re}_\theta = 9800$

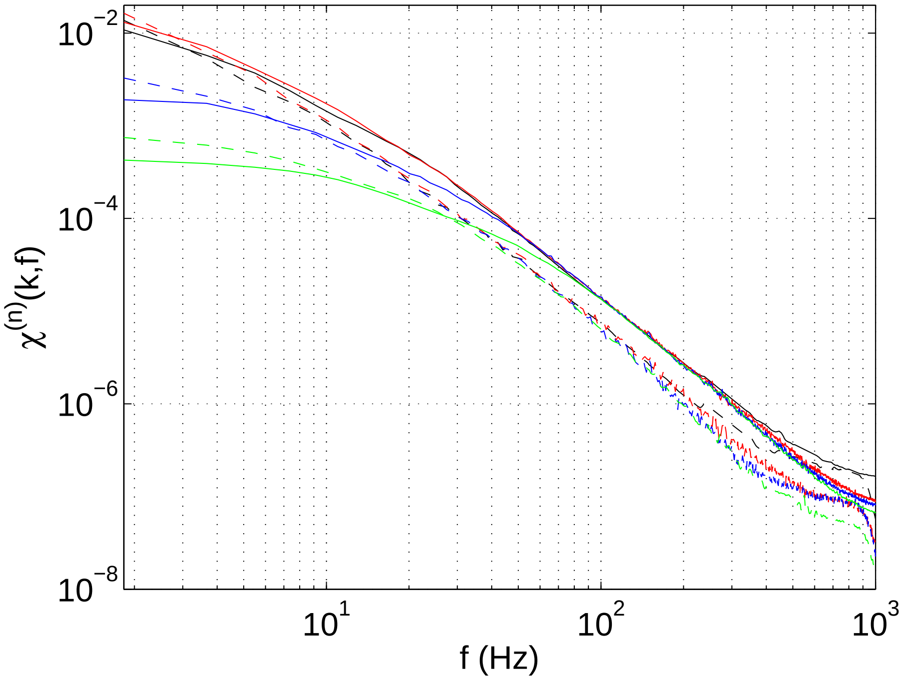

Figure 7.6: Normalized eigenspectra of the first POD mode. Black, red, blue and green lines present $\chi^{(1)}(k,f)$ for $k=$1, 2, 3, and 4 respectively.

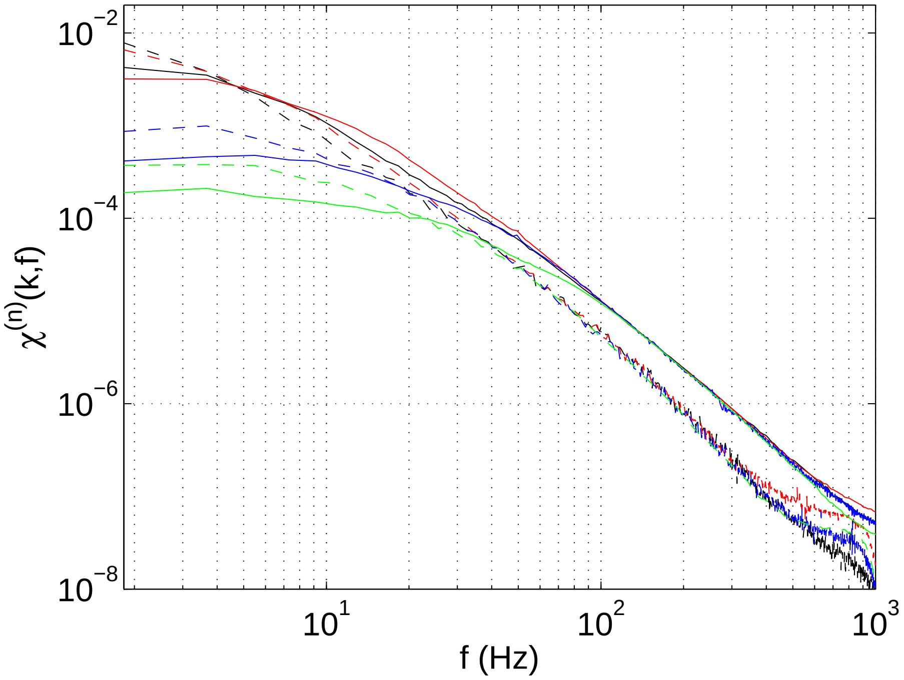

Figure 7.7: Normalized eigenspectra of the second POD mode. Black, red, blue and green lines present $\chi^{(1)}(k,f)$ for $k=$1, 2, 3, and 4 respectively.

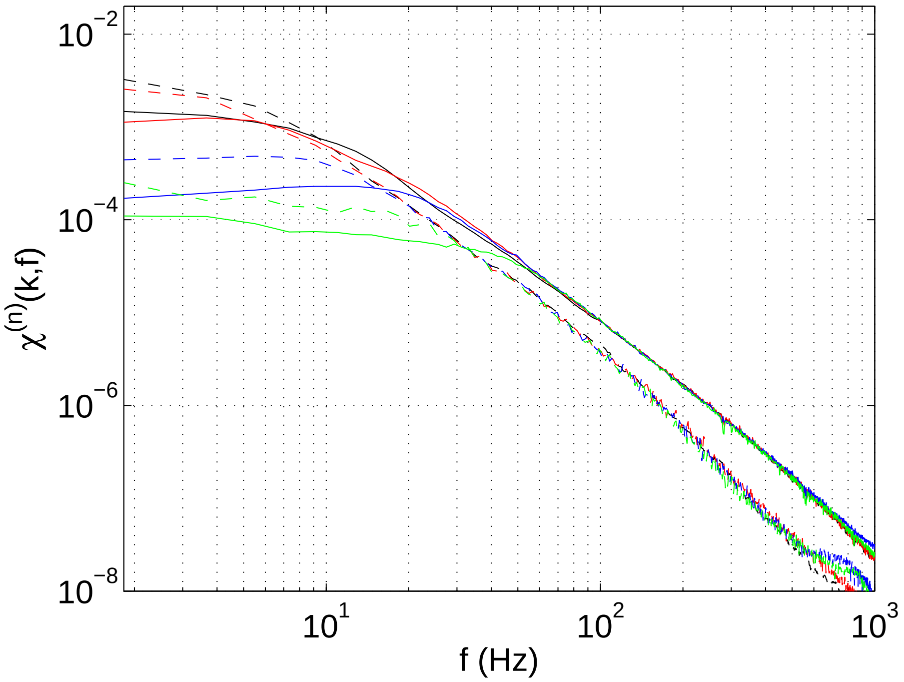

Figure 7.8: Normalized eigenspectra of the third POD mode. Black, red, blue and green lines present $\chi^{(1)}(k, f)$ for $k = 1, 2, 3,$ and 4 respectively.

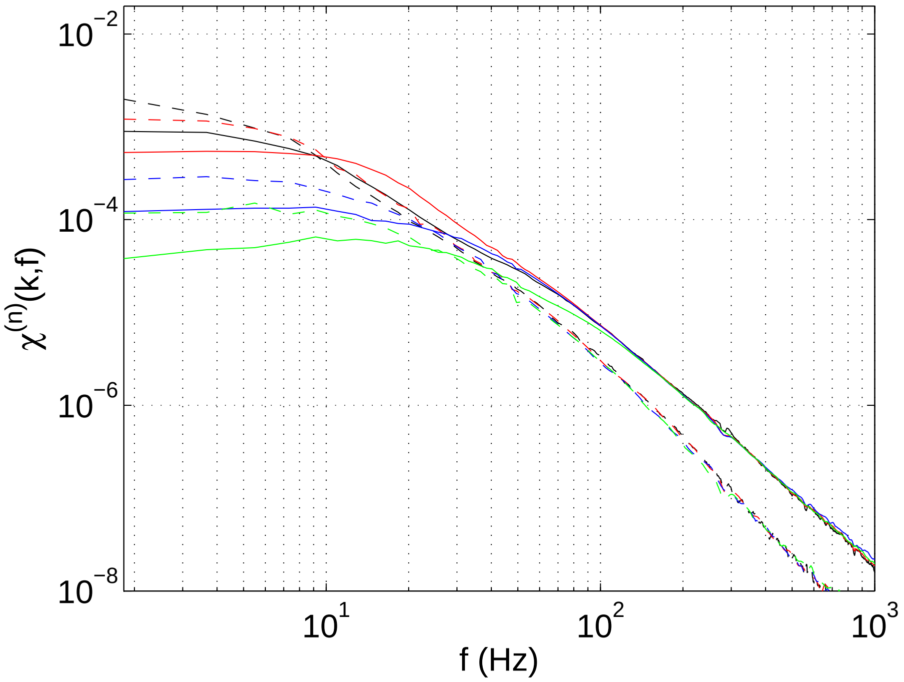

Figure 7.9: Normalized eigenspectra of the fourth POD mode. Black, red, blue and green lines present $\chi^{(1)}(k, f)$ for $k = 1, 2, 3,$ and 4 respectively.

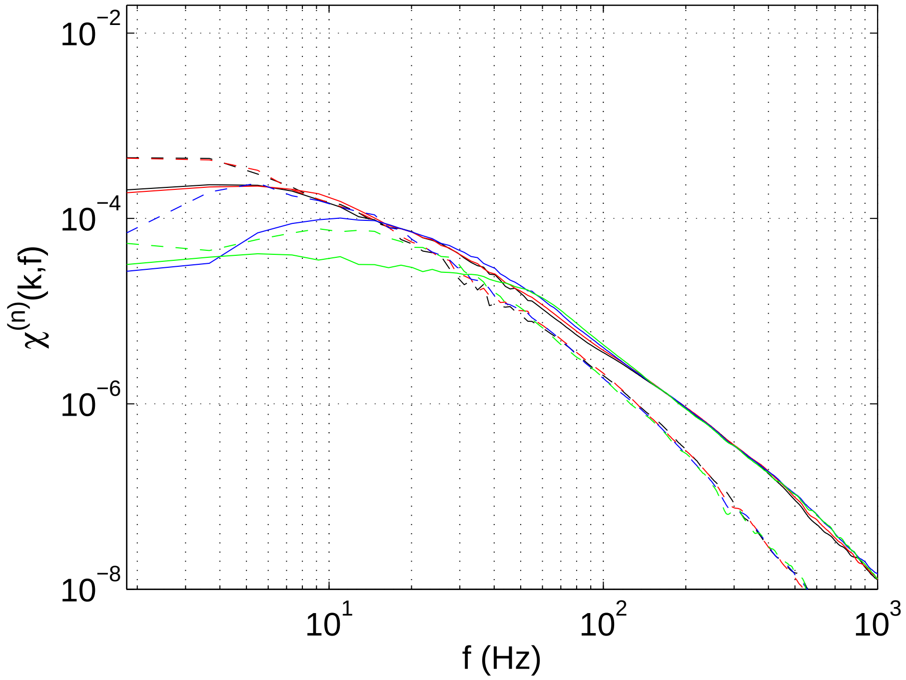

Figure 7.10: Normalized eigenspectra of the fifth POD mode. Black, red, blue and green lines present $\chi^{(1)}(k,f)$ for $k = 1, 2, 3$, and 4 respectively.

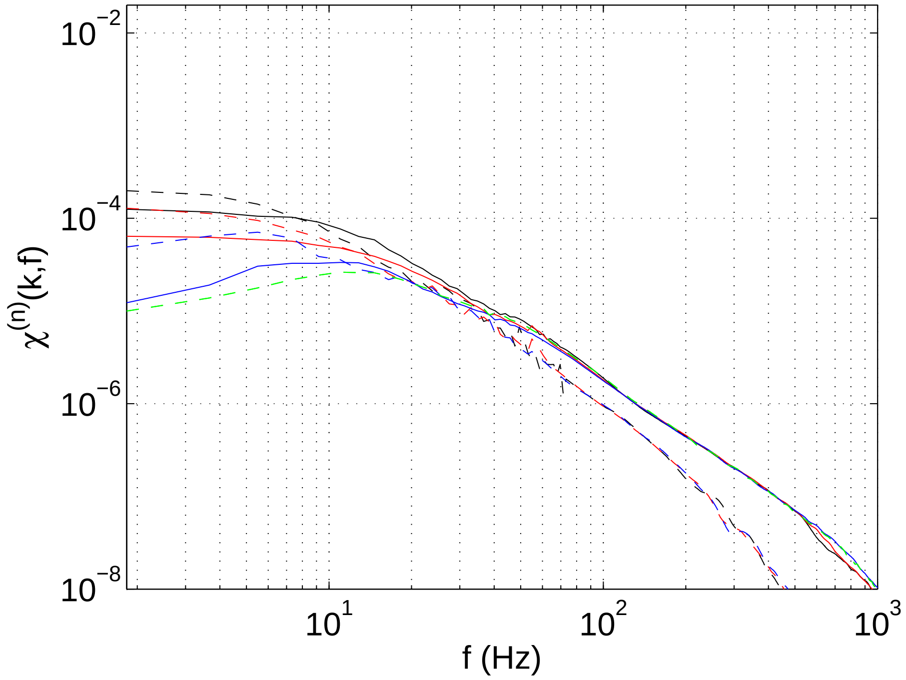

Figure 7.11: Normalized eigenspectra of the sixth POD mode. Black, red, blue and green lines present $\chi^{(1)}(k,f)$ for $k = 1, 2, 3$, and 4 respectively.

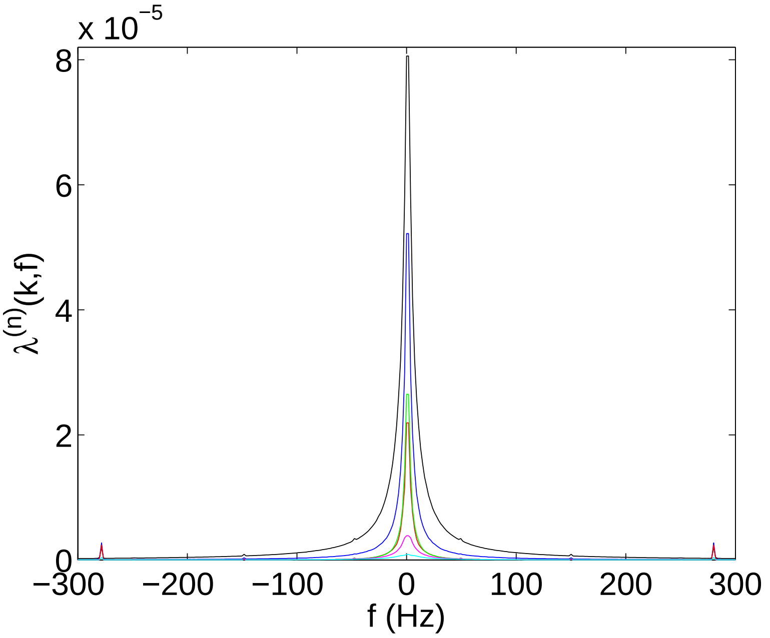

Figure 7.12: Eigenspectra for Re_θ =19 100 in linear-linear scale. Black lines: Eigenspectra summed over all POD and spanwise Fourier modes; Blue lines: Eigenspectra of the first POD mode summed over all spanwise Fourier modes; Red, green, magenta and cyan lines represent eigenspectra of the first POD mode with first, second, third and fourth spanwise Fourier modes respectively.

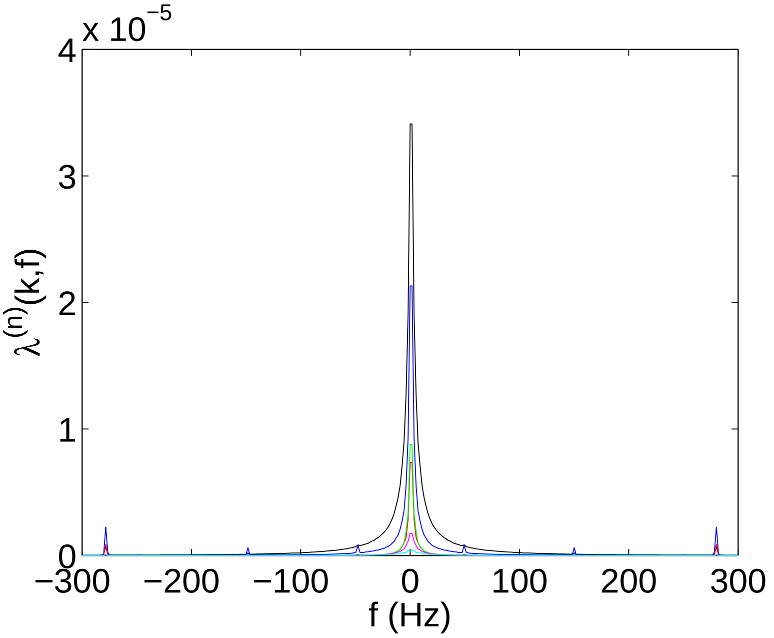

Figure 7.13: Eigenspectra for Re_θ =9800 in linear-linear scale. Black lines: Eigenspectra summed over all POD and spanwise Fourier modes; Blue lines: Eigenspectra of the first POD mode summed over all spanwise Fourier modes; Red, green, magenta and cyan lines represent eigenspectra of the first POD mode with first, second, third and fourth spanwise Fourier modes respectively.

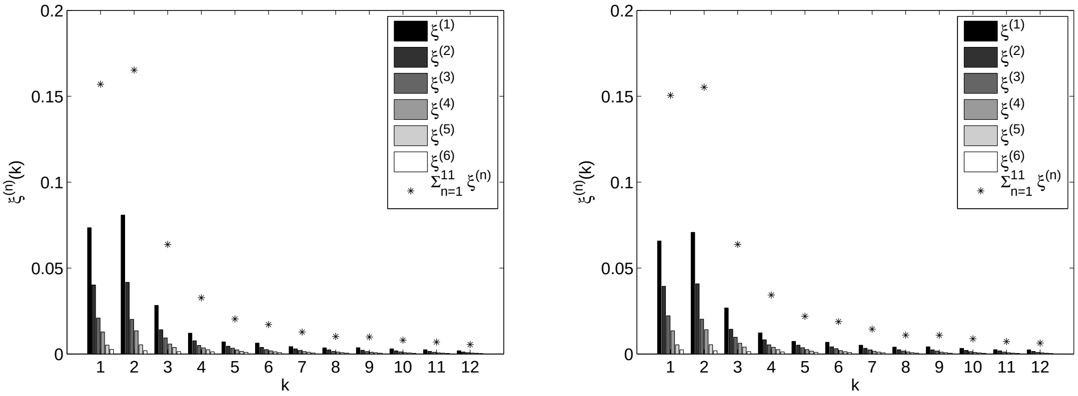

(a) Re_θ =19 100.

(b) Re_θ =9800.

Figure 7.14: Normalized eigenvalue distribution, ξ^n, for POD modes, *n*, and spanwise Fourier modes, *k*.

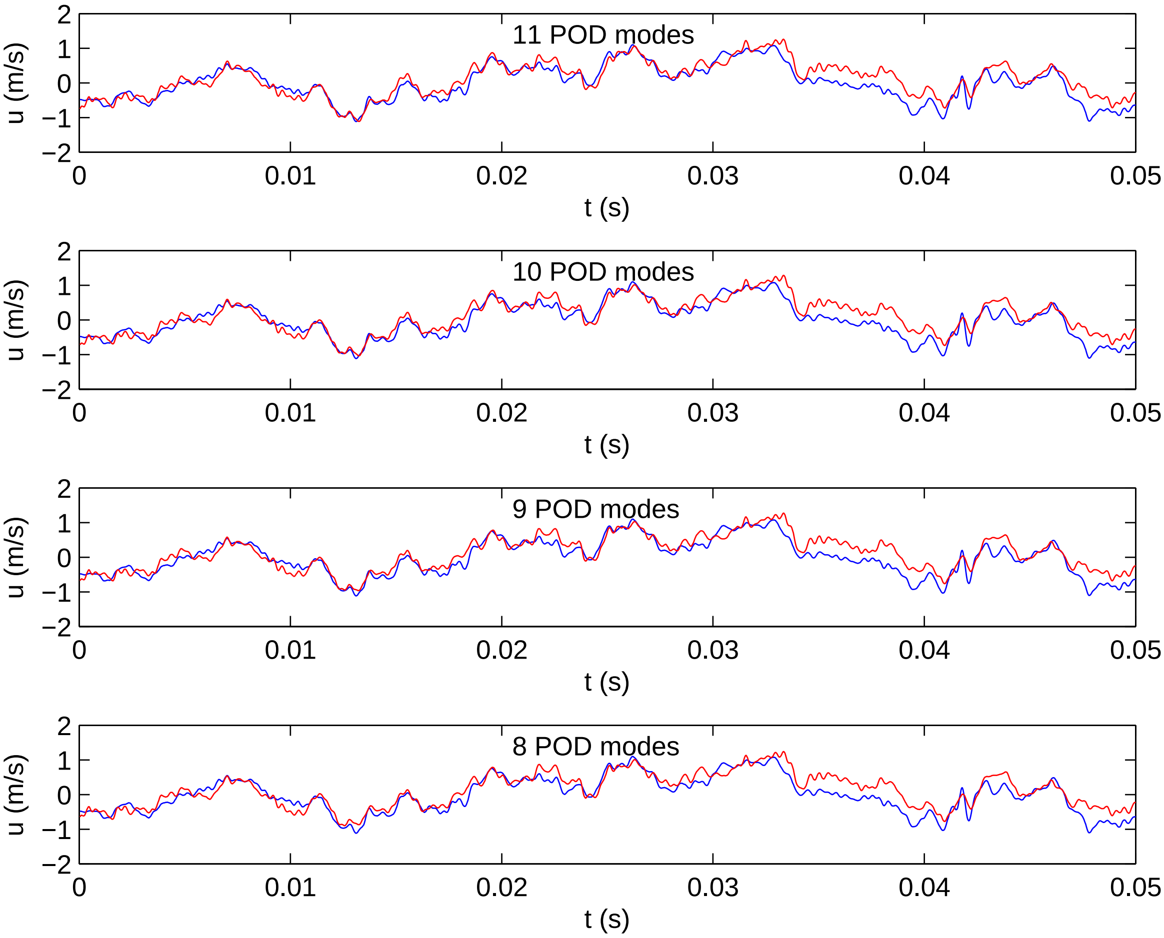

Figure 7.15: Reconstructed instantaneous velocity signal at Re_θ =19 100. Blue lines denote the original velocity fluctuations and red lines denote the reconstructed velocity fluctuations using some numbers of POD modes as inserted in figures.

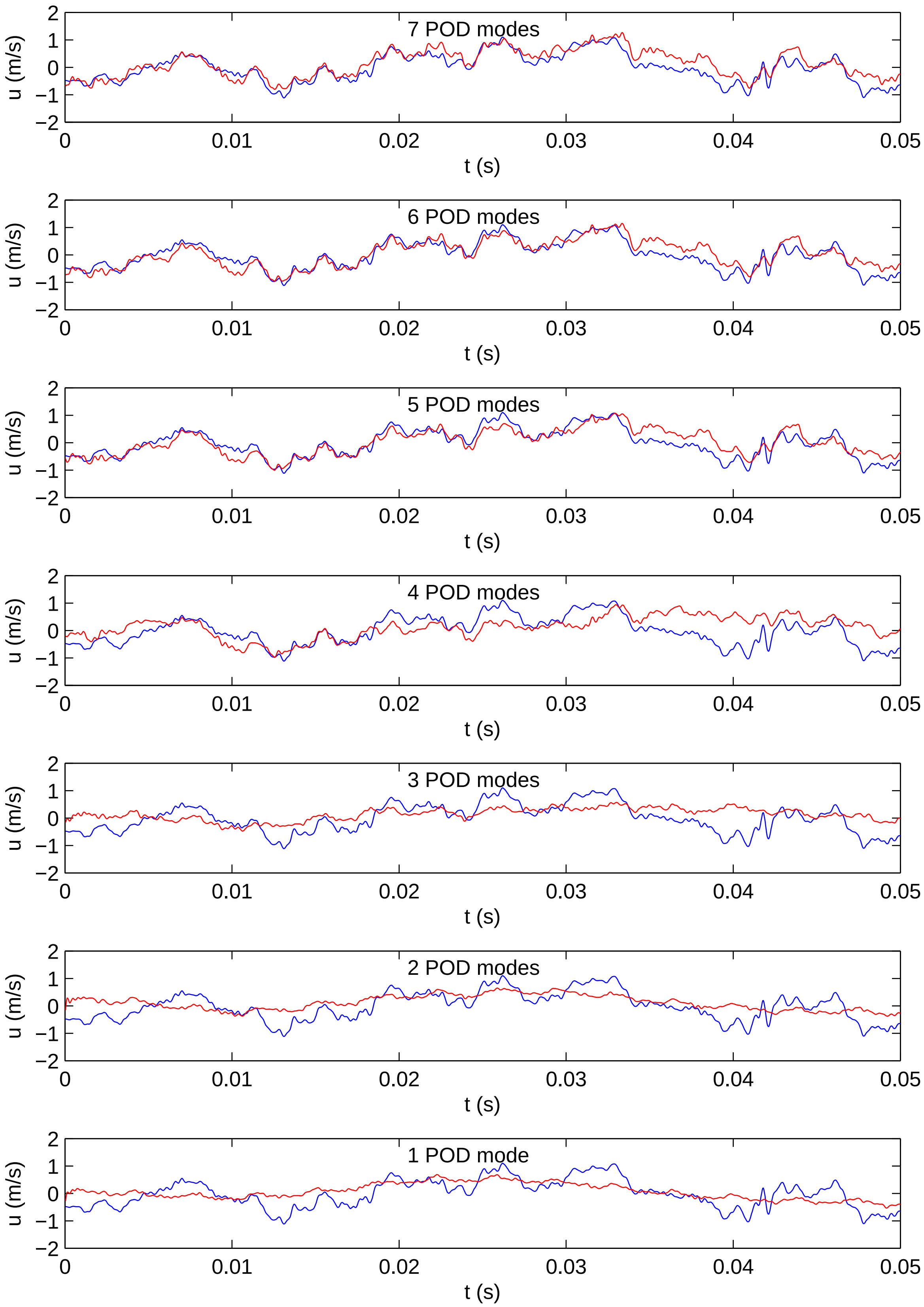

Figure 7.16: Reconstructed instantaneous velocity signal at $Re_\theta = 19\,100$. Blue lines denote the original velocity fluctuations and red lines denote the reconstructed velocity fluctuations using some numbers of POD modes as inserted in figures.

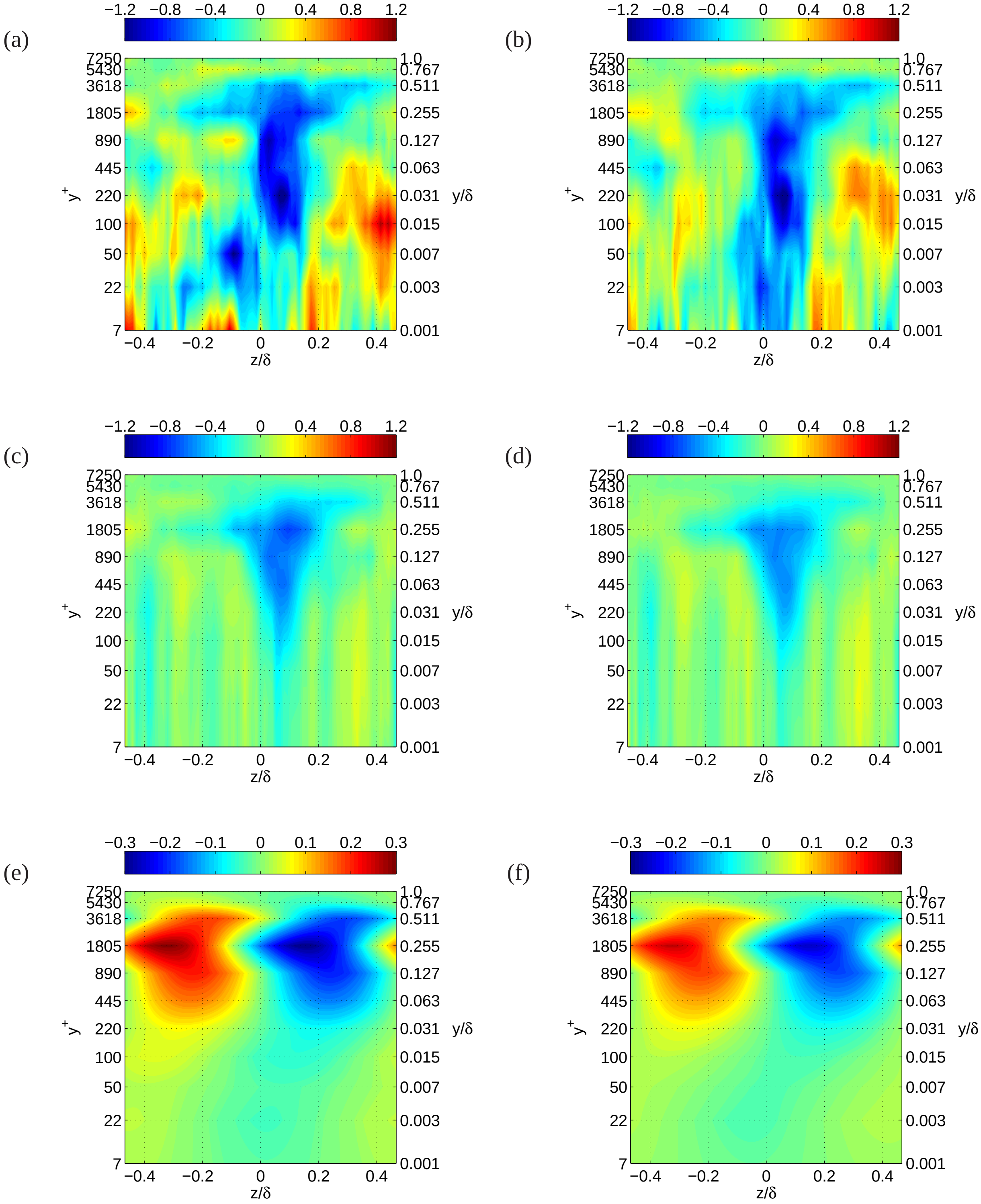

Figure 7.17: Comparison of reconstructed velocity field using both all frequencies and only frequencies lower than 100 Hz at Re_θ of 19 100. Left column (figures (a), (c) and (e)) and right column (figures (b), (d) and (f)) represent the reconstruction without and with low-pass filtering at 100 Hz respectively. (a-b): all POD and spanwise modes; (c-d): First POD modes and all spanwise modes; (e-f): First POD modes and second spanwise modes.

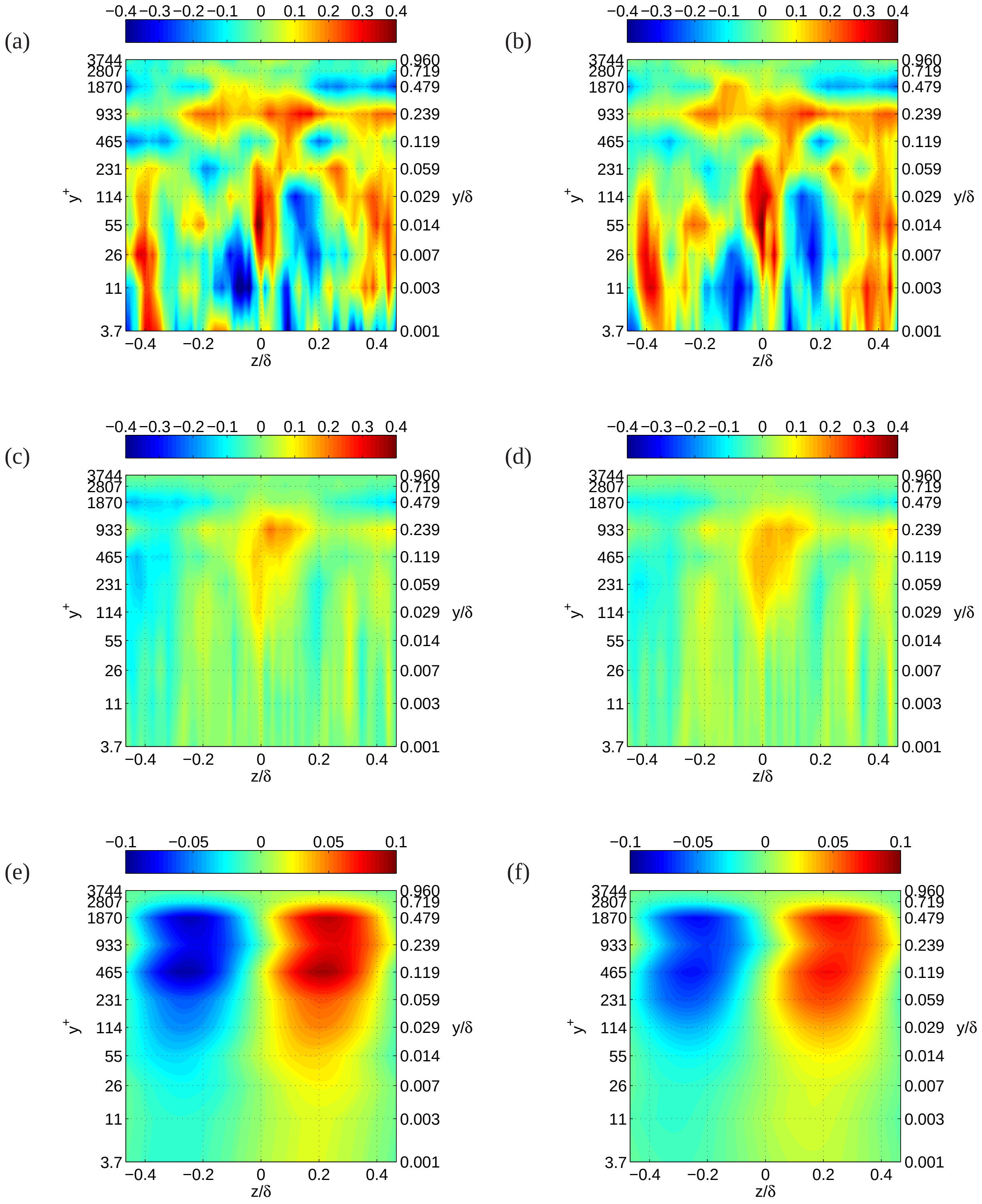

Figure 7.18: Comparison of reconstructed velocity field using both all frequencies and only frequencies lower than 49.5 Hz at Re_θ of 9800. Left column (figures (a), (c) and (e)) and right column (figures (b), (d) and (f)) represent the reconstruction without and with low-pass filtering at 49.5 Hz respectively. (a-b): all POD and spanwise modes; (c-d): First POD modes and all spanwise modes; (e-f): First POD modes and second spanwise modes.

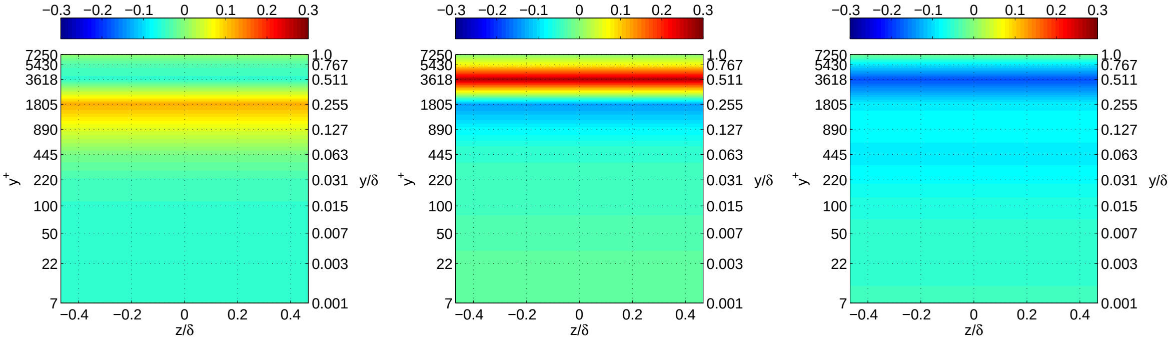

(a) t=0.016 s. (b) t=0.066 s. (c) t=0.116 s.

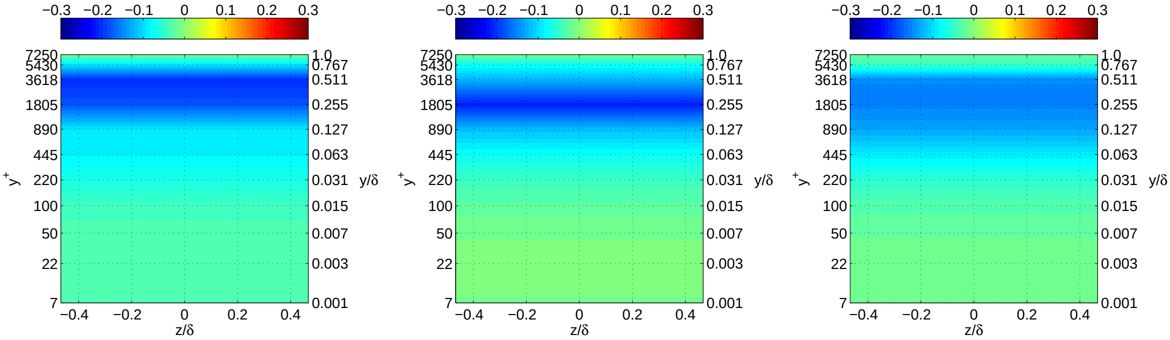

(d) t=0.133 s. (e) t=0.150 s. (f) t=0.183 s.

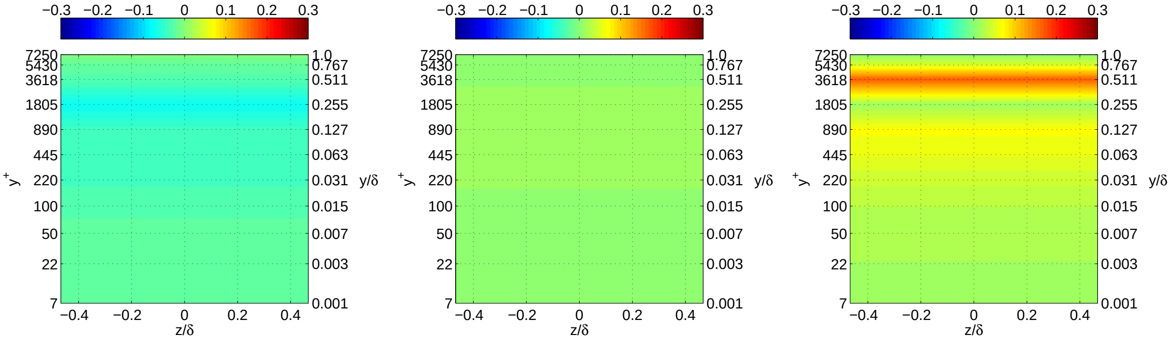

(g) t=0.233 s. (h) t=0.283 s. (i) t=0.333 s.

Figure 7.19: Reconstructed velocity fluctuations using only the first POD and first spanwise Fourier modes at Re_θ =19 100. Different time steps are as given in the captions.

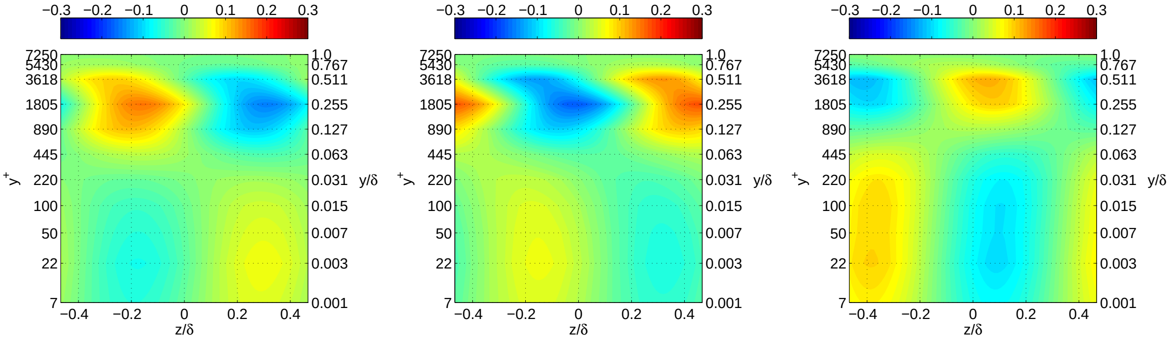

(a) t=0.016 s.

(b) t=0.066 s.

(c) t=0.116 s.

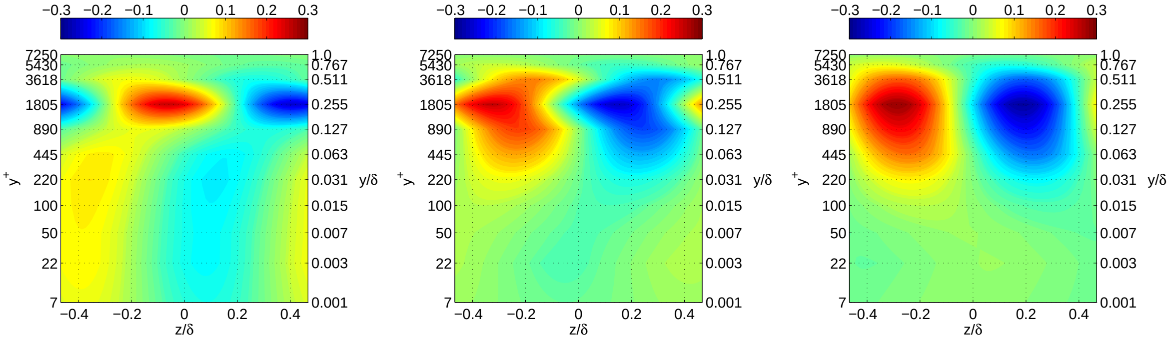

(d) t=0.133 s.

(e) t=0.150 s.

(f) t=0.183 s.

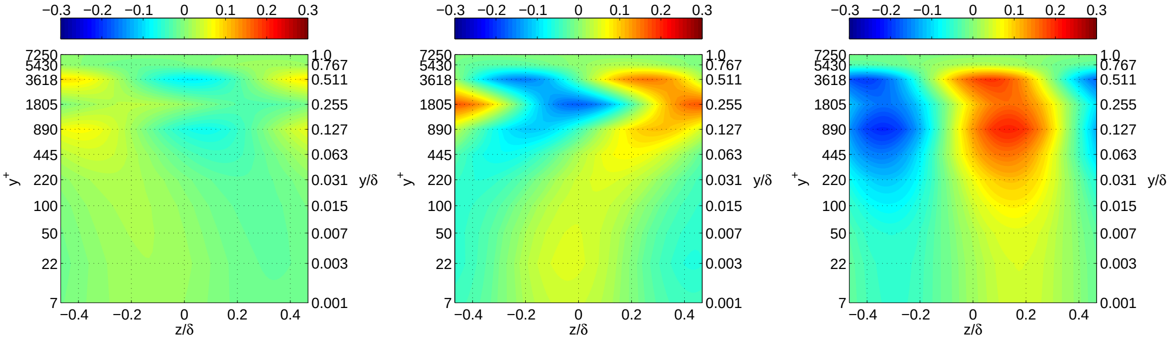

(g) t=0.233 s.

(h) t=0.283 s.

(i) t=0.333 s.

Figure 7.20: Reconstructed velocity fluctuations using only the first POD and second spanwise Fourier modes at $Re_\theta = 19\,100$. Different time steps are as given in the captions.

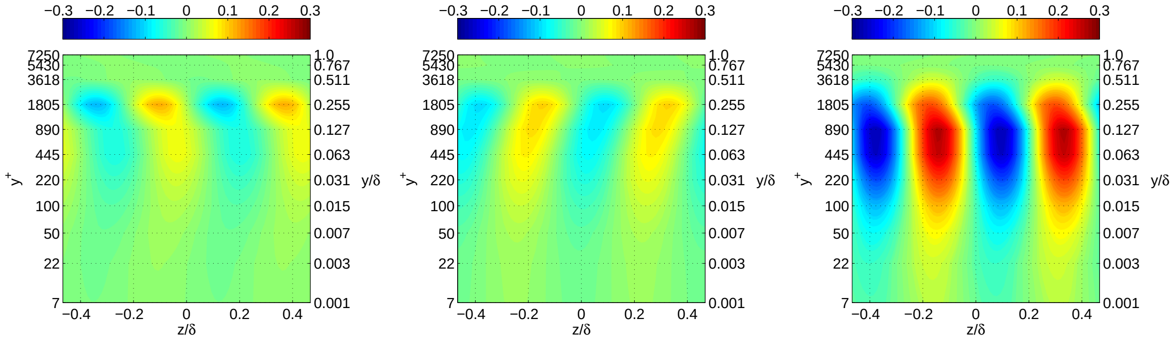

(a) t=0.016 s.

(b) t=0.066 s.

(c) t=0.116 s.

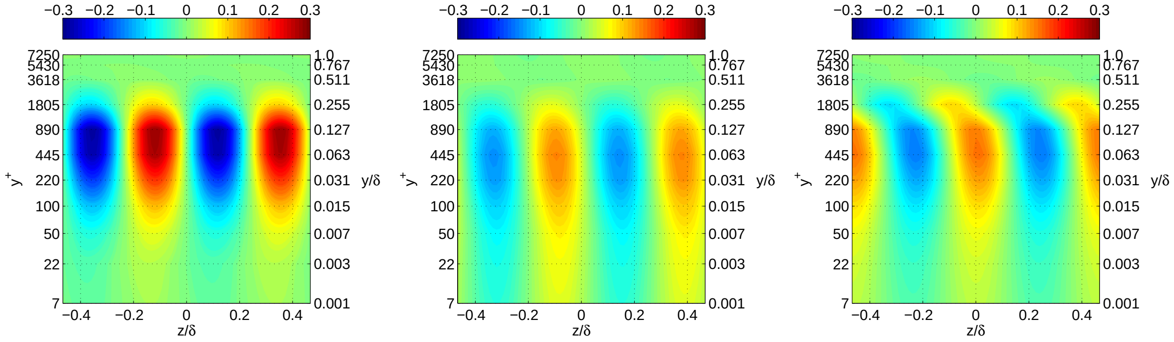

(d) t=0.133 s.

(e) t=0.150 s.

(f) t=0.183 s.

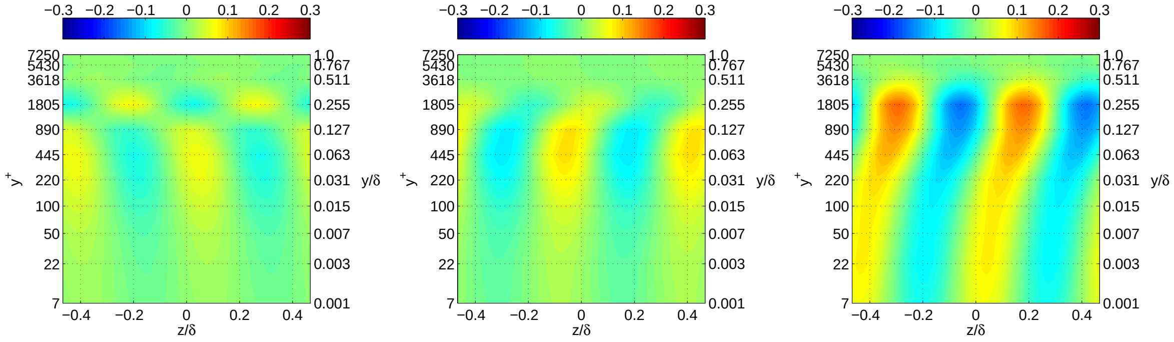

(g) t=0.233 s.

(h) t=0.283 s.

(i) t=0.333 s.

Figure 7.21: Reconstructed velocity fluctuations using only the first POD and third spanwise Fourier modes at $Re_\theta = 19\,100$. Different time steps are as given in the captions.

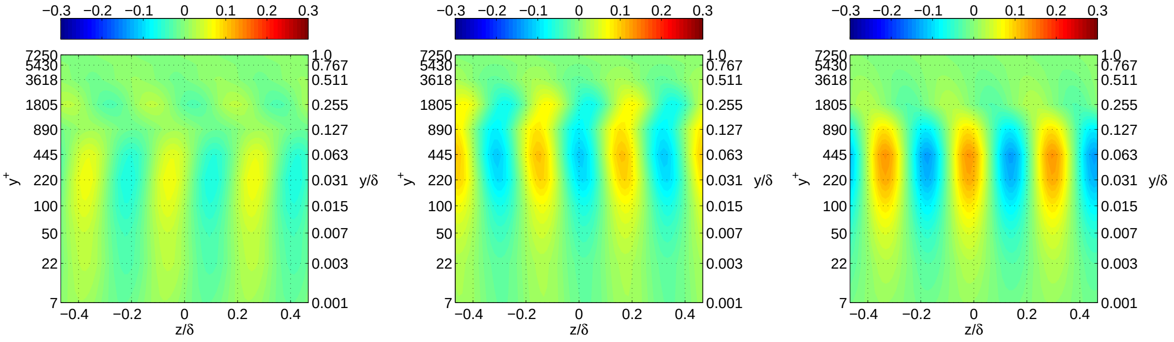

(a) t=0.016 s. (b) t=0.066 s. (c) t=0.116 s.

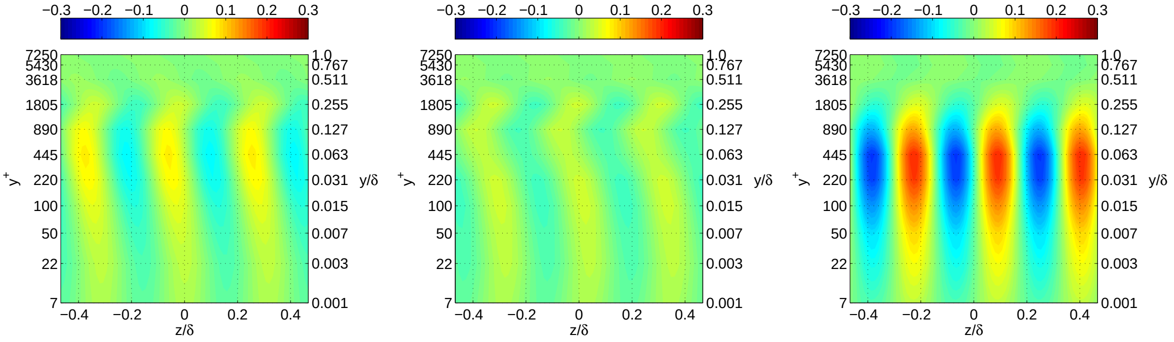

(d) t=0.133 s. (e) t=0.150 s. (f) t=0.183 s.

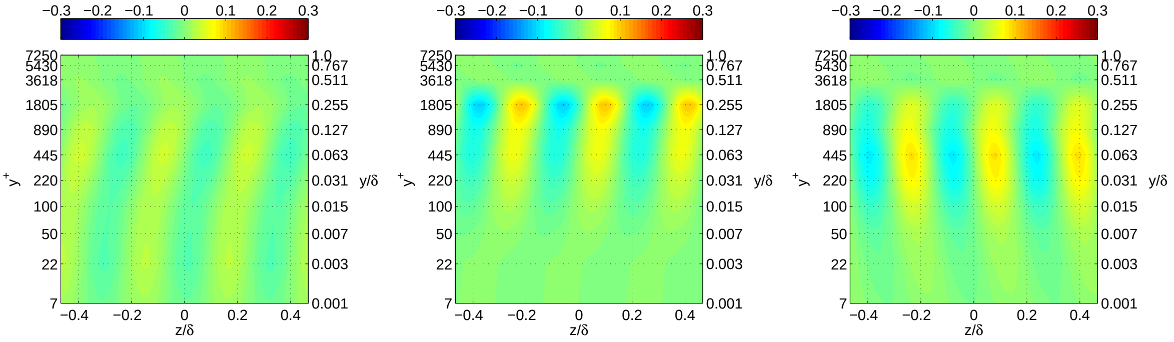

(g) t=0.233 s. (h) t=0.283 s. (i) t=0.333 s.

Figure 7.22: Reconstructed velocity fluctuations using only the first POD and fourth spanwise Fourier modes at $Re_\theta = 19\,100$. Different time steps are as given in the captions.

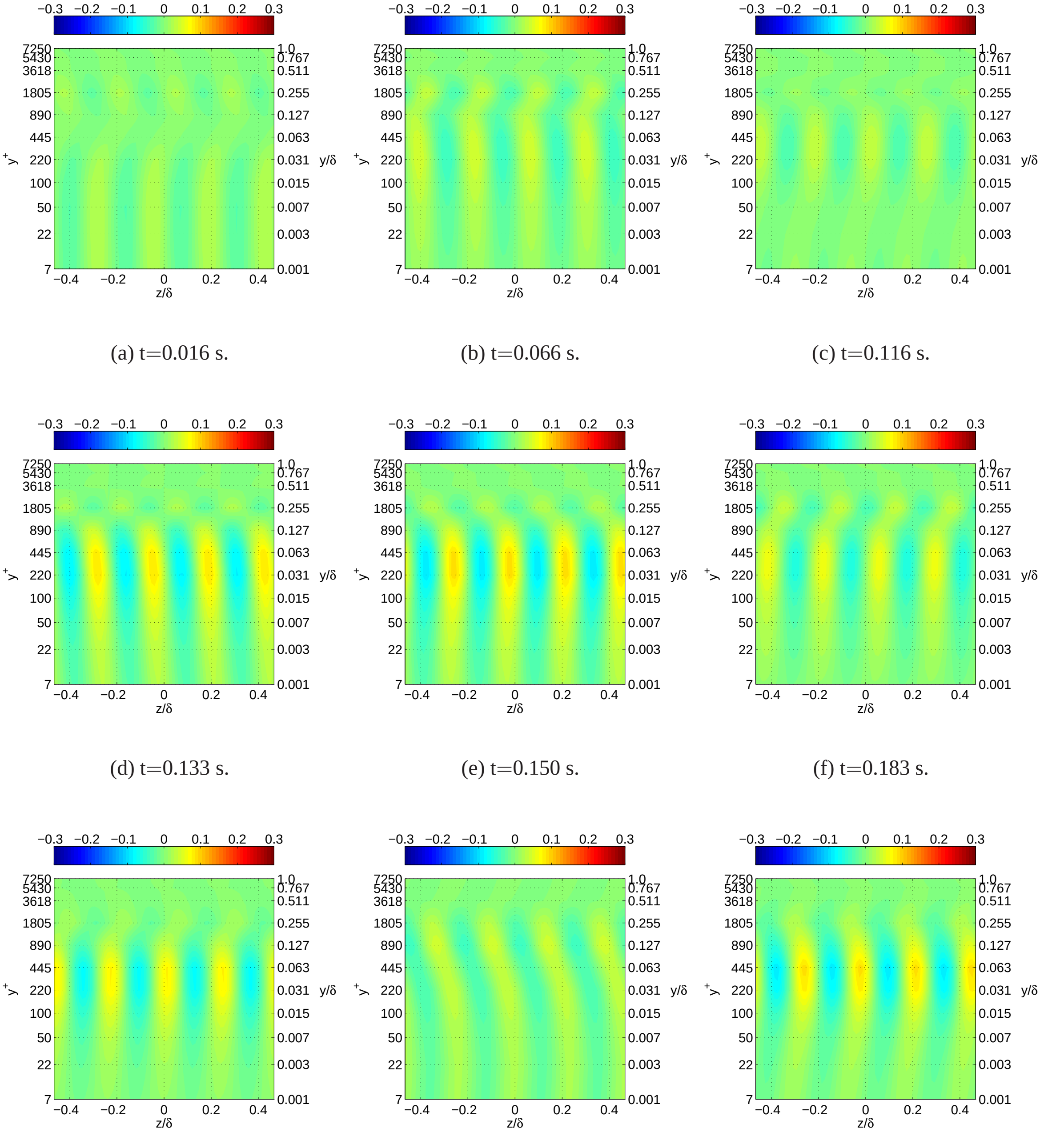

(a) t=0.016 s.

(b) t=0.066 s.

(c) t=0.116 s.

(d) t=0.133 s.

(e) t=0.150 s.

(f) t=0.183 s.

(g) t=0.233 s.

(h) t=0.283 s.

(i) t=0.333 s.

Figure 7.23: Reconstructed velocity fluctuations using only the first POD and fifth spanwise Fourier modes at Re_θ =19 100. Different time steps are as given in the captions.

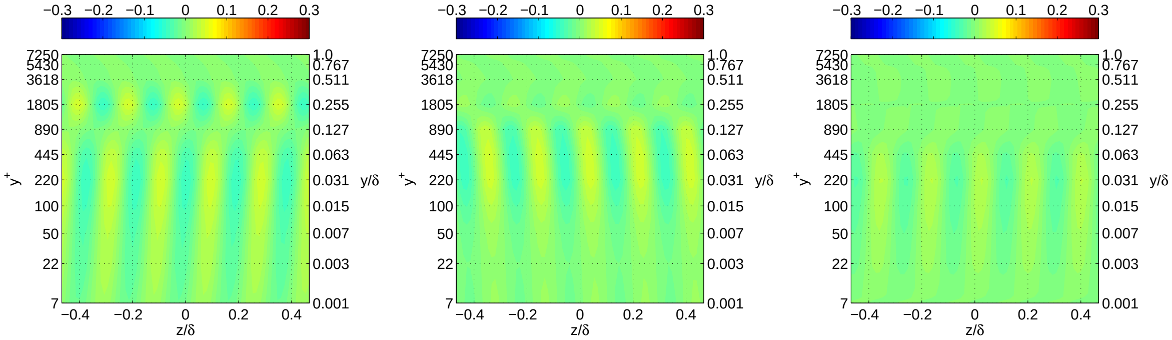

(a) t=0.016 s.　(b) t=0.066 s.　(c) t=0.116 s.

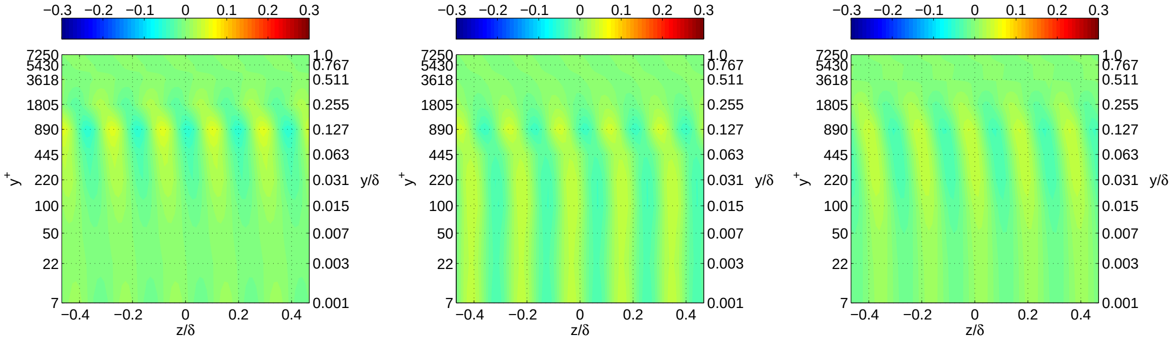

(d) t=0.133 s.　(e) t=0.150 s.　(f) t=0.183 s.

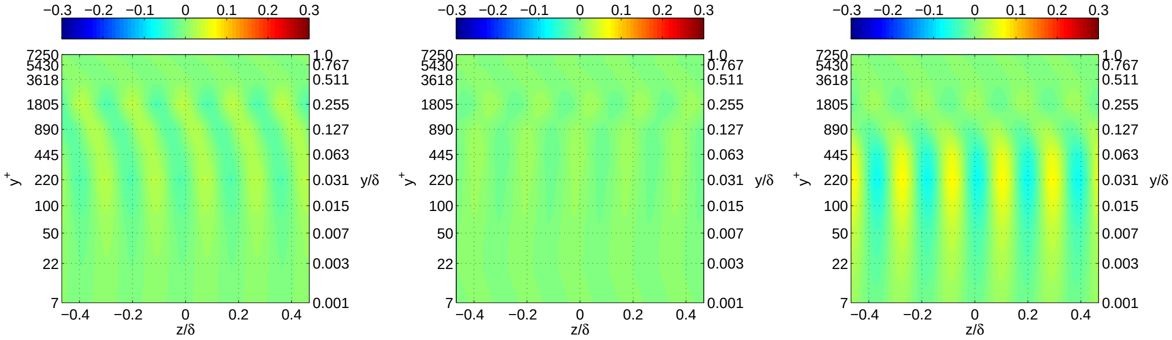

(g) t=0.233 s.　(h) t=0.283 s.　(i) t=0.333 s.

Figure 7.24: Reconstructed velocity fluctuations using only the first POD and sixth spanwise Fourier modes at $Re_\theta = 19\,100$. Different time steps are as given in the captions.

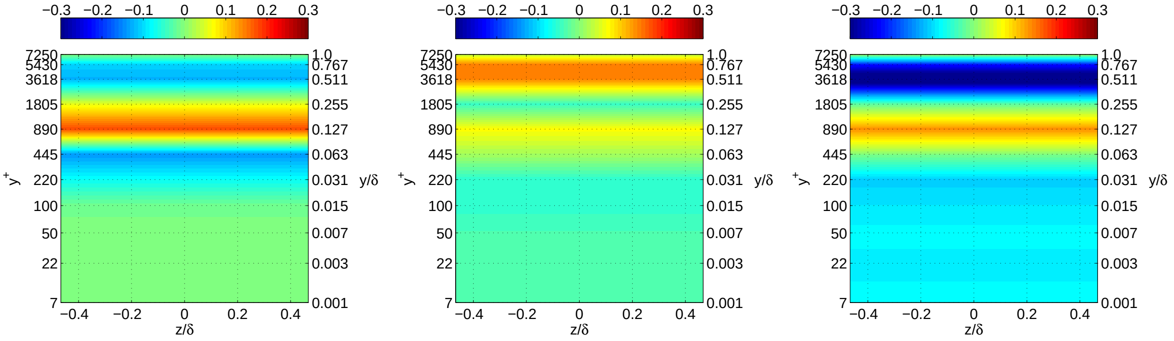

(a) t=0.016 s.

(b) t=0.066 s.

(c) t=0.116 s.

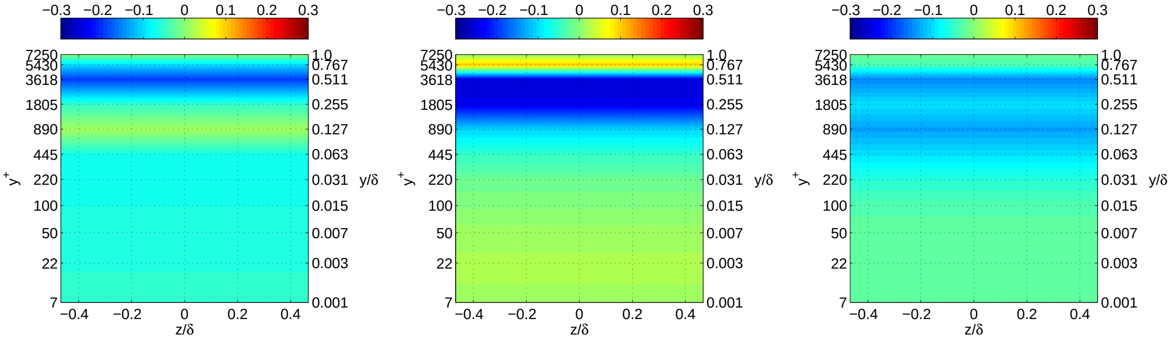

(d) t=0.133 s.

(e) t=0.150 s.

(f) t=0.183 s.

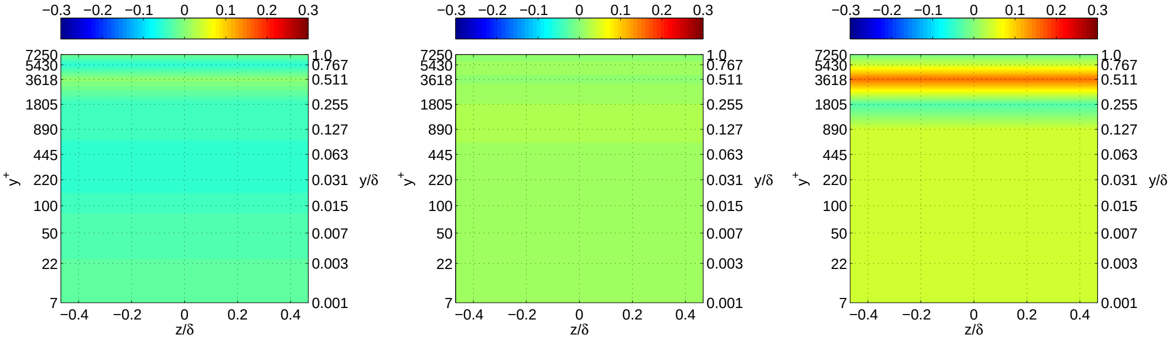

(g) t=0.233 s.

(h) t=0.283 s.

(i) t=0.333 s.

Figure 7.25: Reconstructed velocity fluctuations using the first four POD and first spanwise Fourier modes at Re_θ =19 100. Different time steps are as given in the captions.

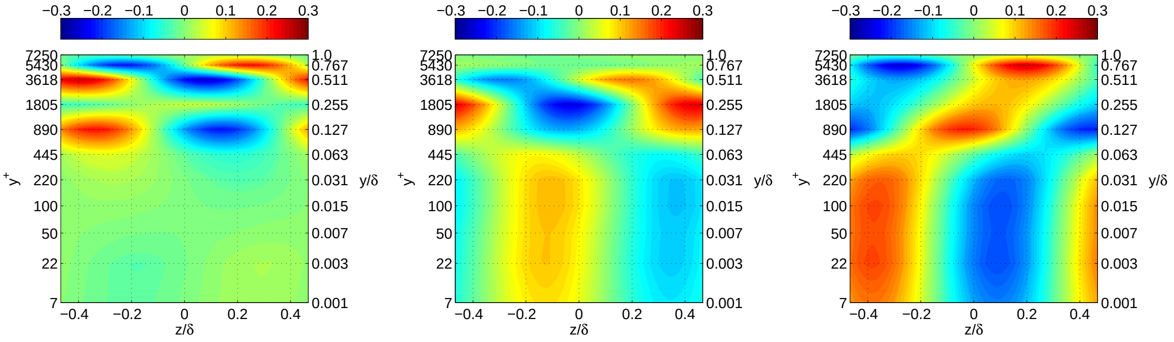

(a) t=0.016 s.

(b) t=0.066 s.

(c) t=0.116 s.

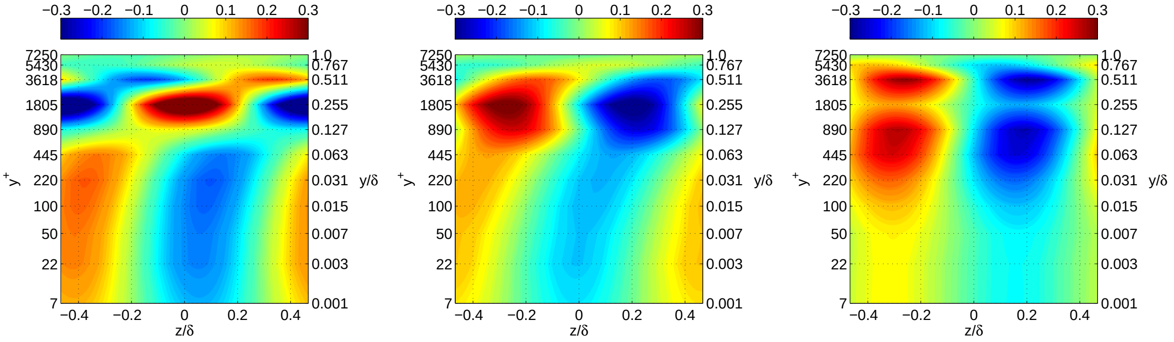

(d) t=0.133 s.

(e) t=0.150 s.

(f) t=0.183 s.

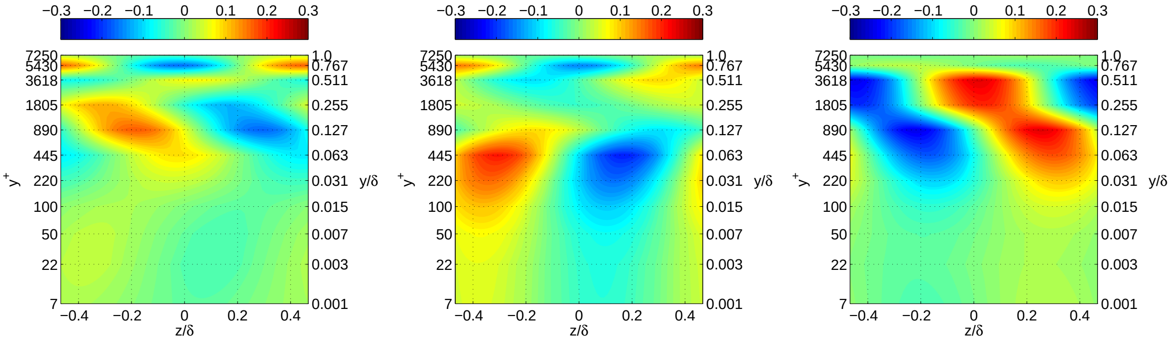

(g) t=0.233 s.

(h) t=0.283 s.

(i) t=0.333 s.

Figure 7.26: Reconstructed velocity fluctuations using the first four POD and second spanwise Fourier modes at Re_θ =19 100. Different time steps are as given in the captions.

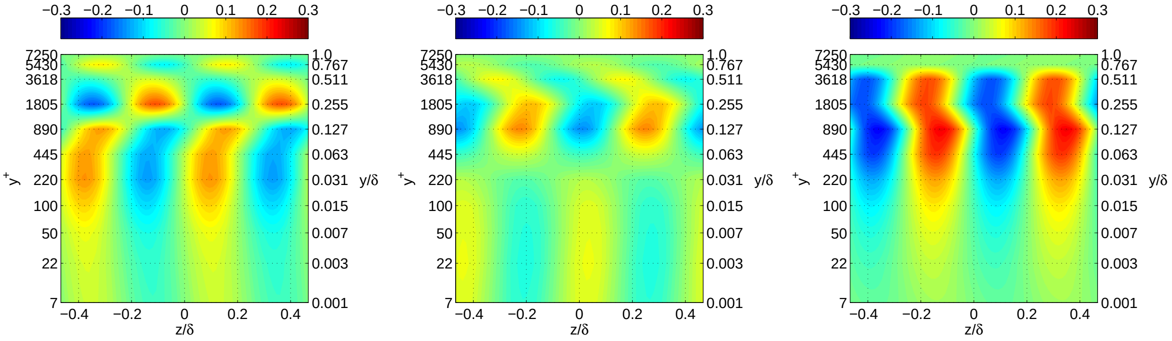

(a) t=0.016 s.

(b) t=0.066 s.

(c) t=0.116 s.

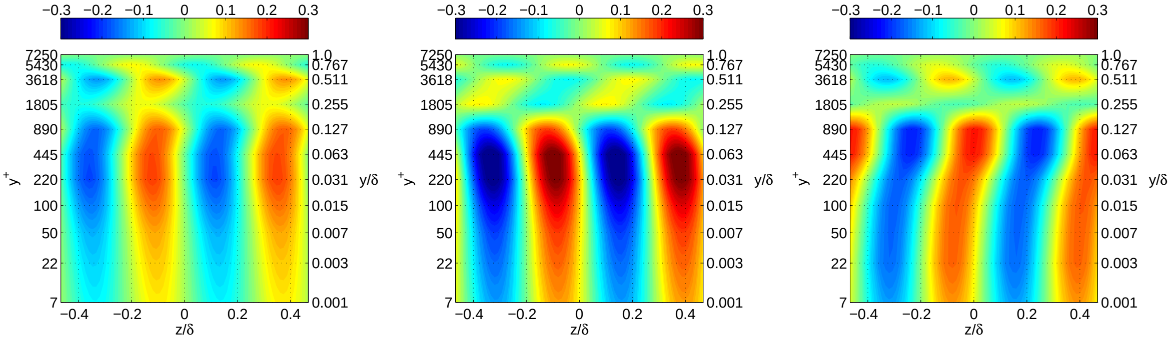

(d) t=0.133 s.

(e) t=0.150 s.

(f) t=0.183 s.

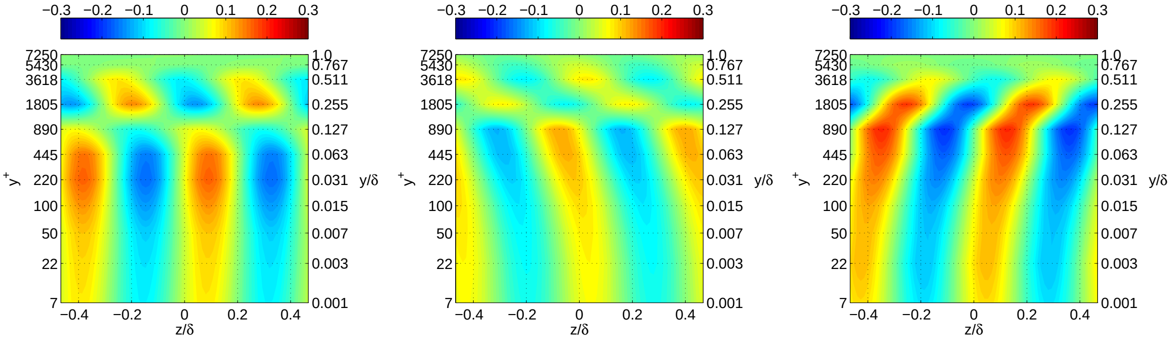

(g) t=0.233 s.

(h) t=0.283 s.

(i) t=0.333 s.

Figure 7.27: Reconstructed velocity fluctuations using the first four POD and third spanwise Fourier modes at $Re_\theta = 19\,100$. Different time steps are as given in the captions.

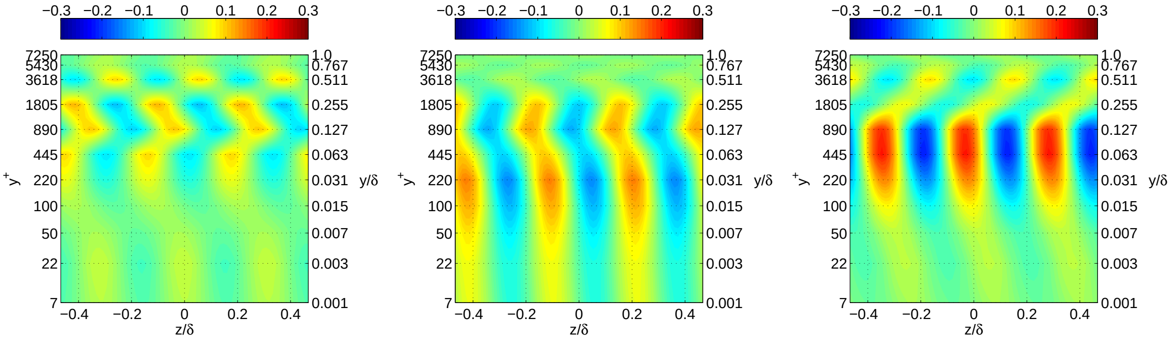

(a) t=0.016 s.

(b) t=0.066 s.

(c) t=0.116 s.

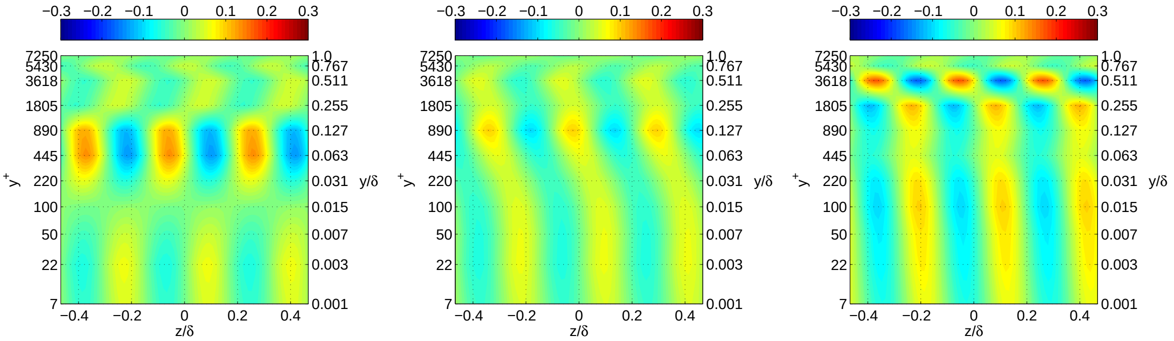

(d) t=0.133 s.

(e) t=0.150 s.

(f) t=0.183 s.

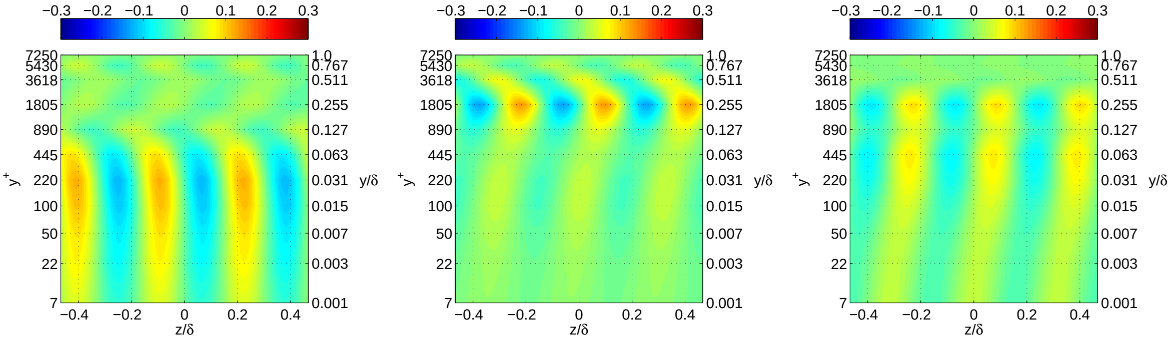

(g) t=0.233 s.

(h) t=0.283 s.

(i) t=0.333 s.

Figure 7.28: Reconstructed velocity fluctuations using the first four POD and fourth spanwise Fourier modes at $Re_\theta = 19\,100$. Different time steps are as given in the captions.

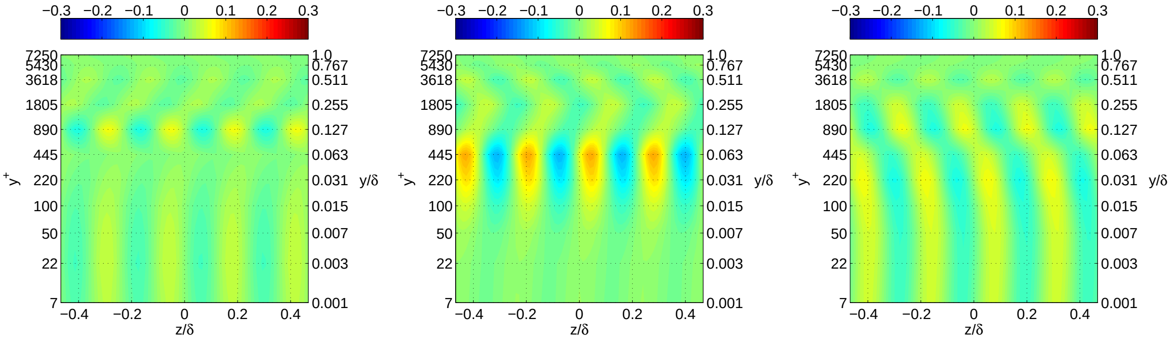

(a) t=0.016 s.

(b) t=0.066 s.

(c) t=0.116 s.

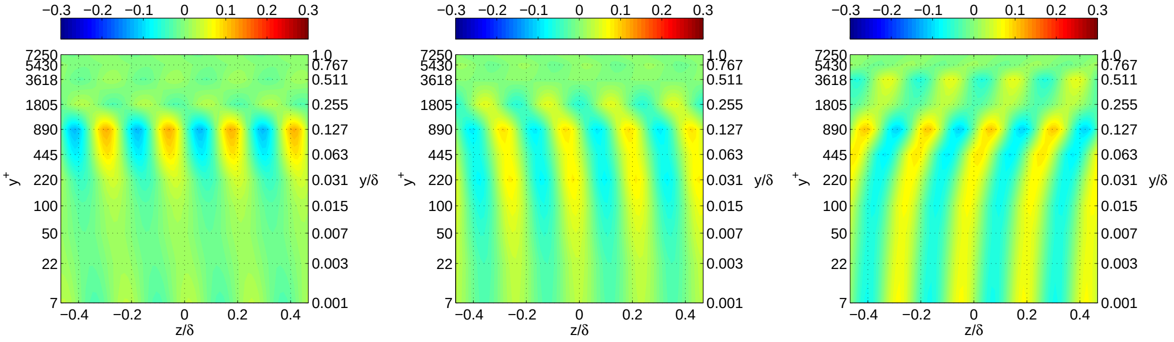

(d) t=0.133 s.

(e) t=0.150 s.

(f) t=0.183 s.

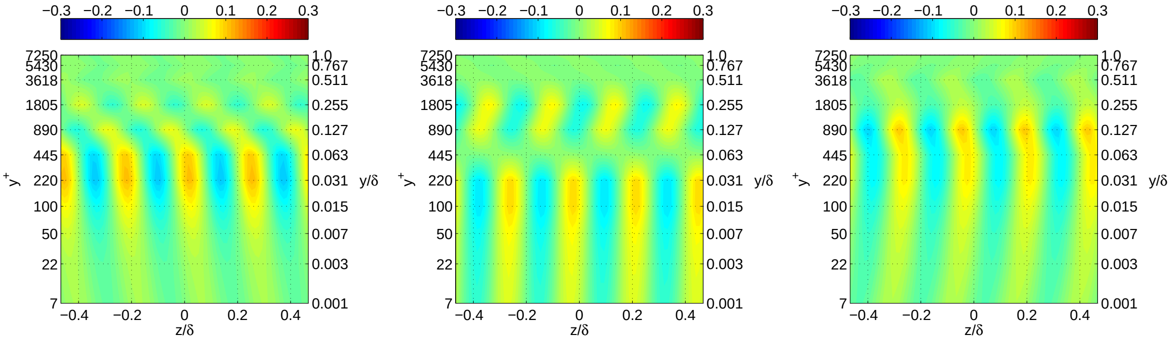

(g) t=0.233 s.

(h) t=0.283 s.

(i) t=0.333 s.

Figure 7.29: Reconstructed velocity fluctuations using the first four POD and fifth spanwise Fourier modes at Re_θ =19 100. Different time steps are as given in the captions.

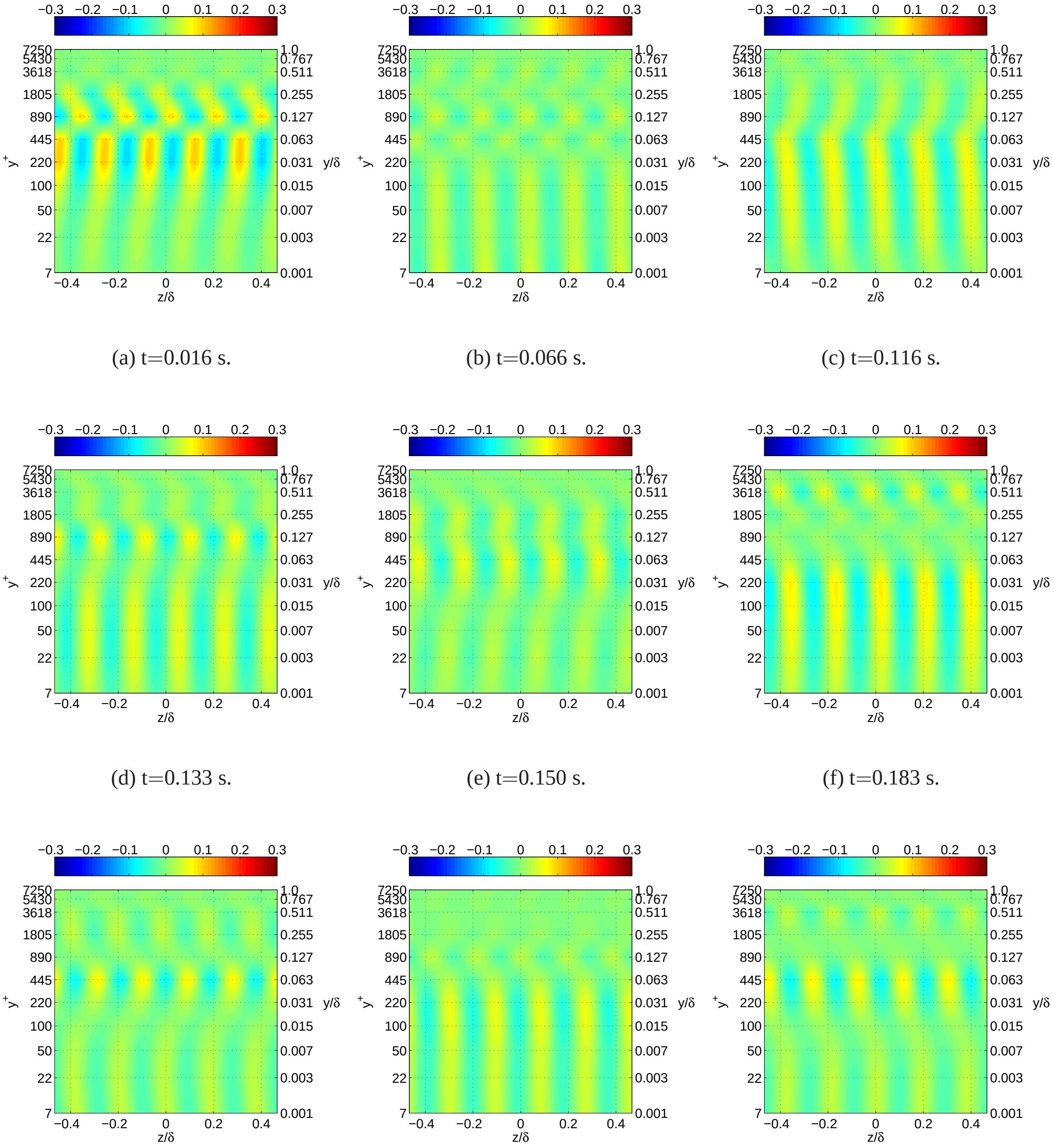

(a) t=0.016 s.

(b) t=0.066 s.

(c) t=0.116 s.

(d) t=0.133 s.

(e) t=0.150 s.

(f) t=0.183 s.

(g) t=0.233 s.

(h) t=0.283 s.

(i) t=0.333 s.

Figure 7.30: Reconstructed velocity fluctuations using the first four POD and sixth spanwise Fourier modes at Re_θ =19 100. Different time steps are as given in the captions.

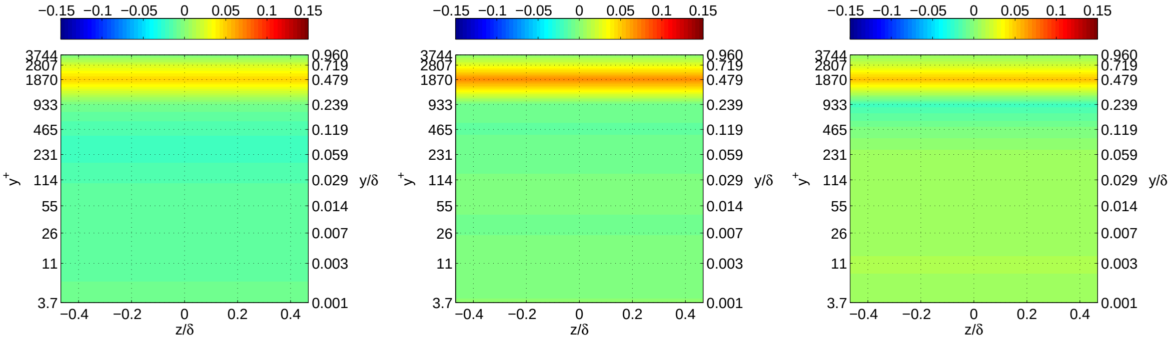

(a) t=0.033 s. (b) t=0.050 s. (c) t=0.066 s.

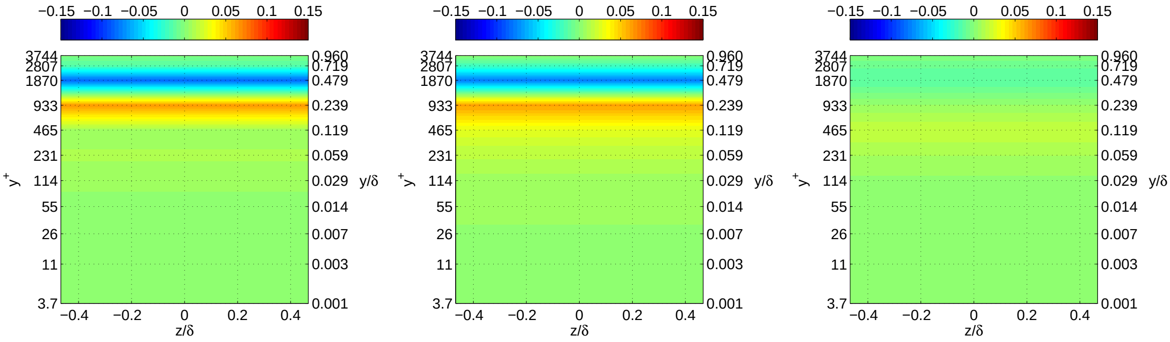

(d) t=0.133 s. (e) t=0.150 s. (f) t=0.200 s.

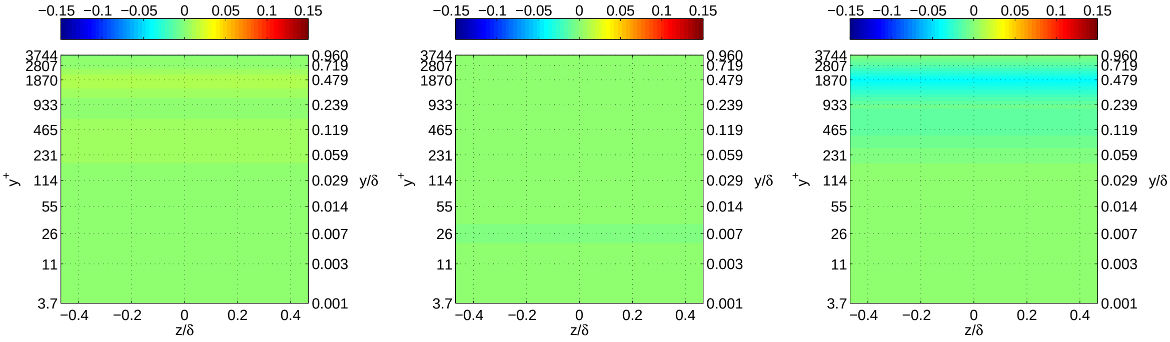

(g) t=0.233 s. (h) t=0.266 s. (i) t=0.316 s.

Figure 7.31: Reconstructed velocity fluctuations using only the first POD and first spanwise Fourier modes at $Re_\theta = 9800$. Different time steps are as given in the captions.

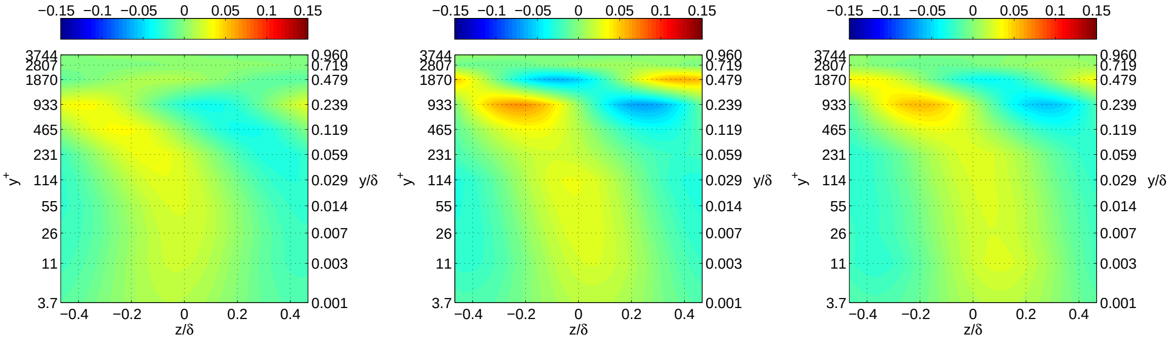

(a) t=0.033 s.
(b) t=0.050 s.
(c) t=0.066 s.

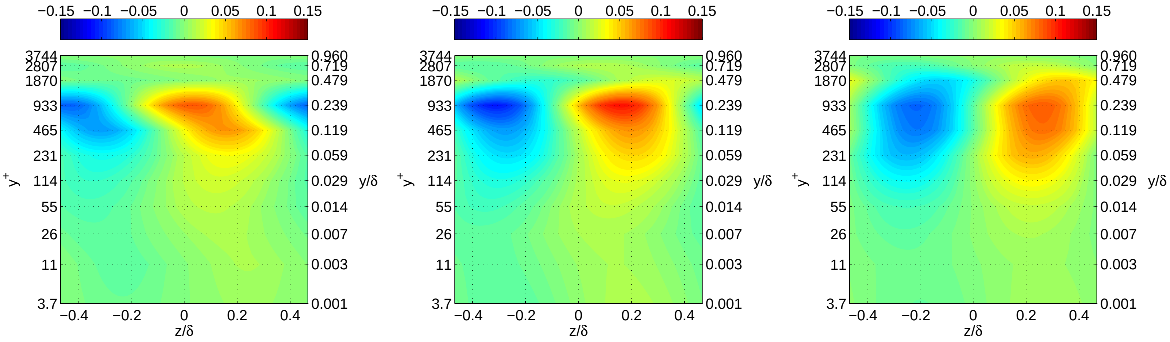

(d) t=0.133 s.
(e) t=0.150 s.
(f) t=0.200 s.

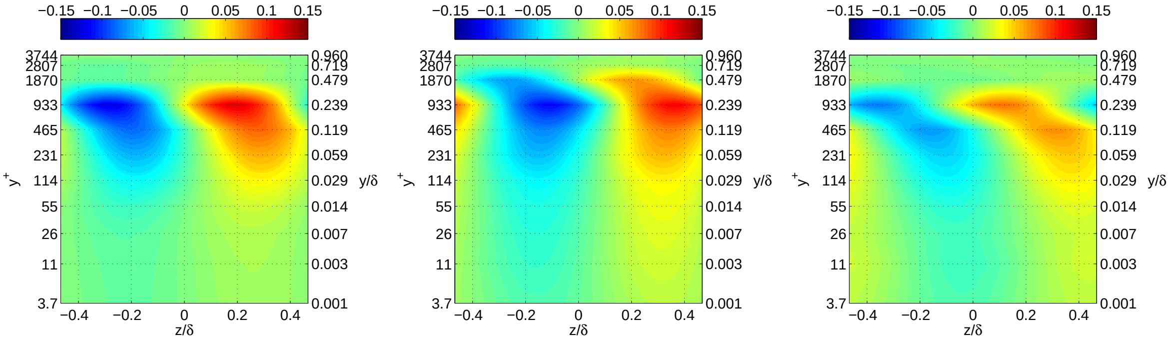

(g) t=0.233 s.
(h) t=0.266 s.
(i) t=0.316 s.

Figure 7.32: Reconstructed velocity fluctuations using only the first POD and second spanwise Fourier modes at $Re_\theta = 9800$. Different time steps are as given in the captions.

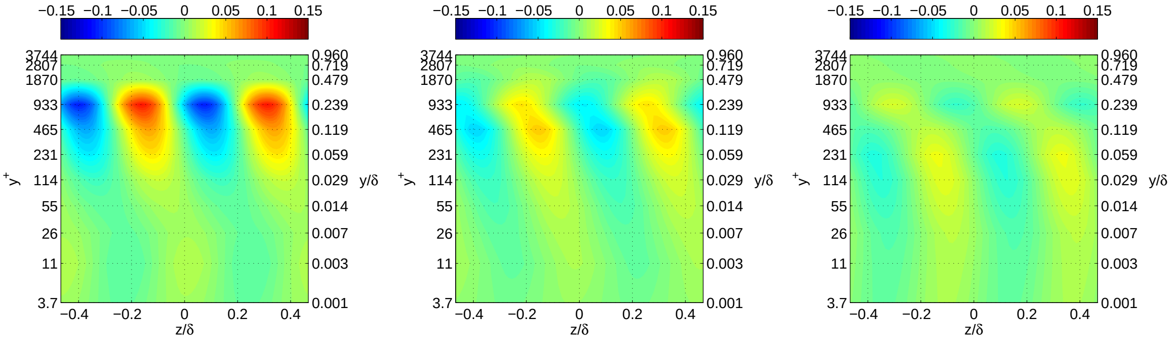

(a) t=0.033 s. (b) t=0.050 s. (c) t=0.066 s.

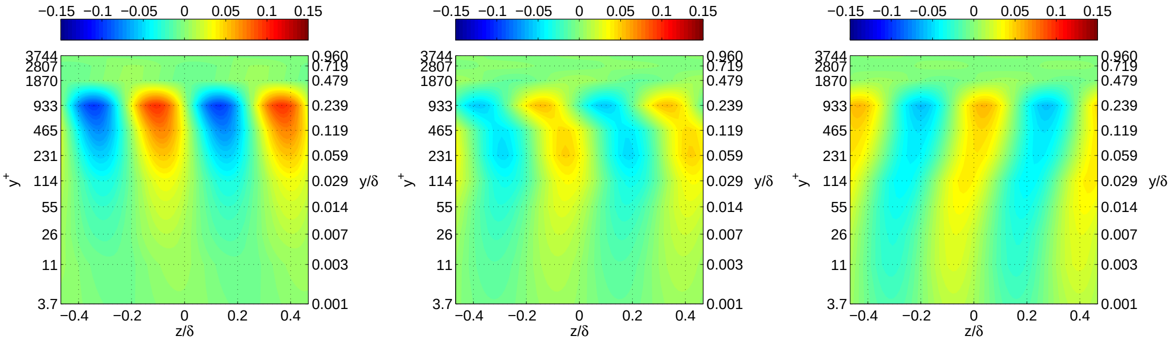

(d) t=0.133 s. (e) t=0.150 s. (f) t=0.200 s.

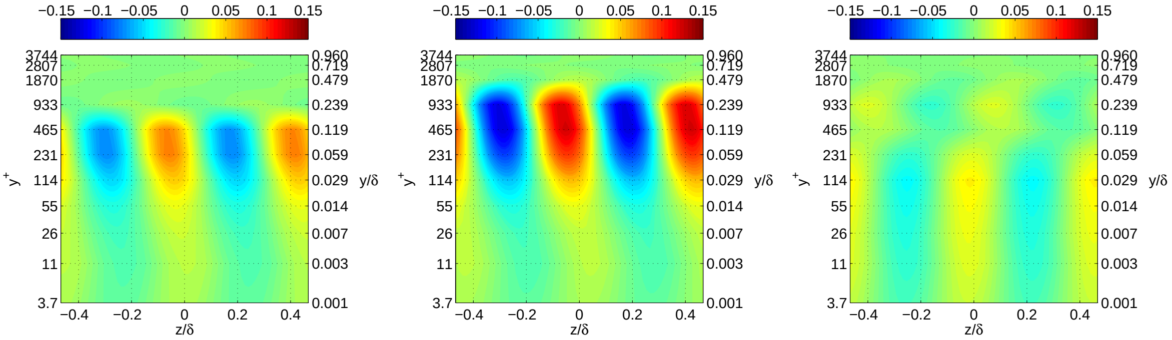

(g) t=0.233 s. (h) t=0.266 s. (i) t=0.316 s.

Figure 7.33: Reconstructed velocity fluctuations using only the first POD and third spanwise Fourier modes at Re_θ =9800. Different time steps are as given in the captions.

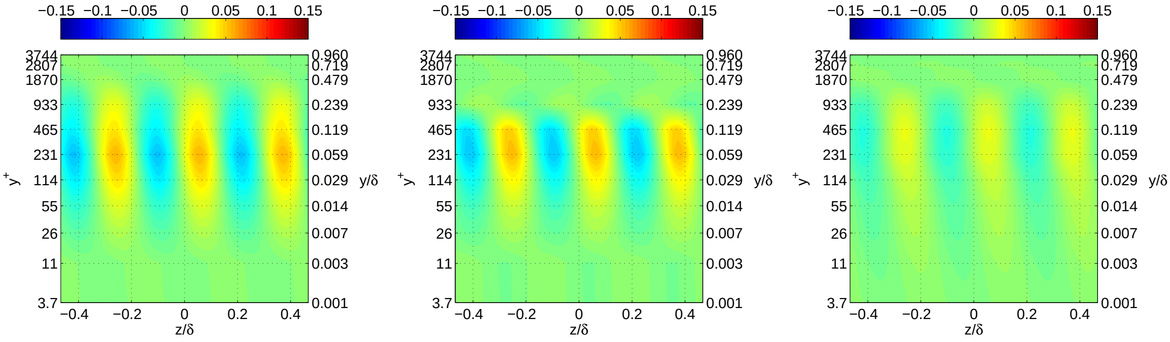

(a) t=0.033 s.

(b) t=0.050 s.

(c) t=0.066 s.

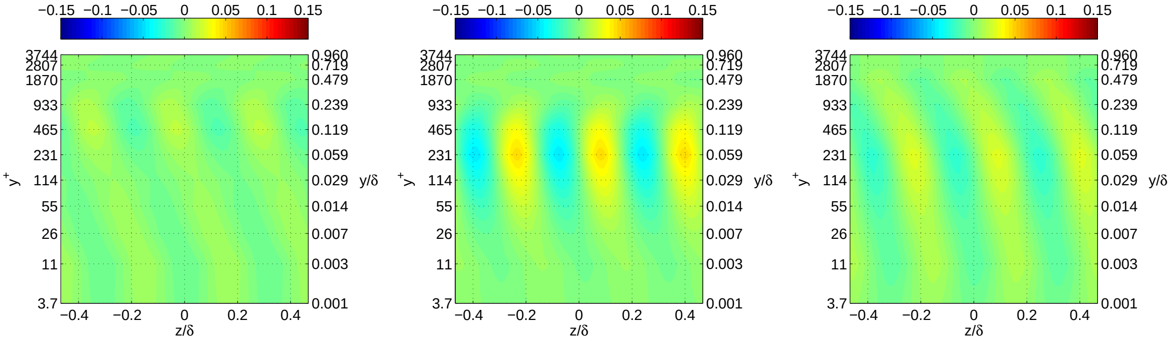

(d) t=0.133 s.

(e) t=0.150 s.

(f) t=0.200 s.

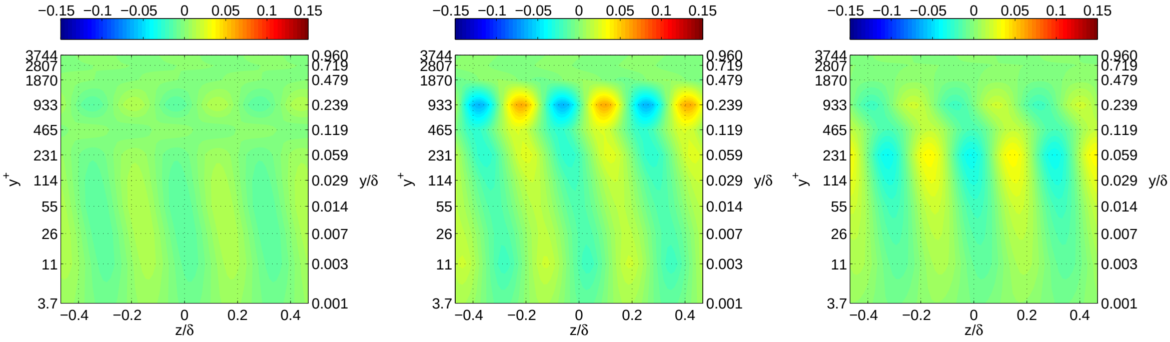

(g) t=0.233 s.

(h) t=0.266 s.

(i) t=0.316 s.

Figure 7.34: Reconstructed velocity fluctuations using only the first POD and fourth spanwise Fourier modes at $Re_\theta = 9800$. Different time steps are as given in the captions.

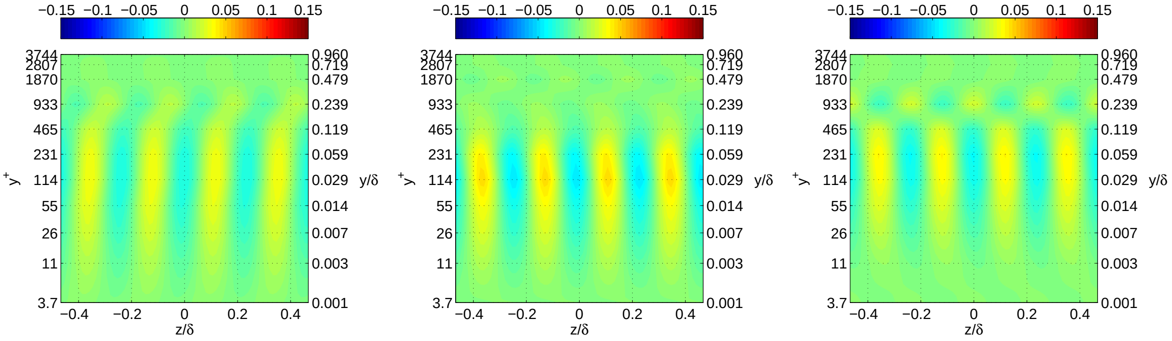

(a) t=0.033 s. (b) t=0.050 s. (c) t=0.066 s.

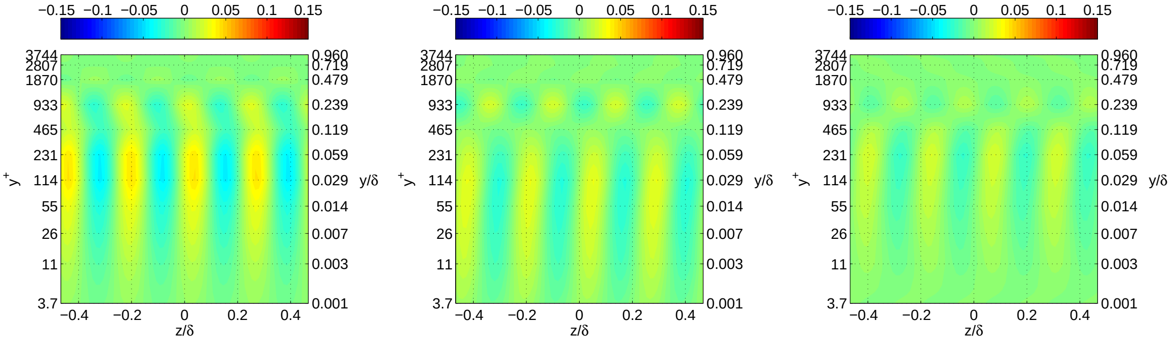

(d) t=0.133 s. (e) t=0.150 s. (f) t=0.200 s.

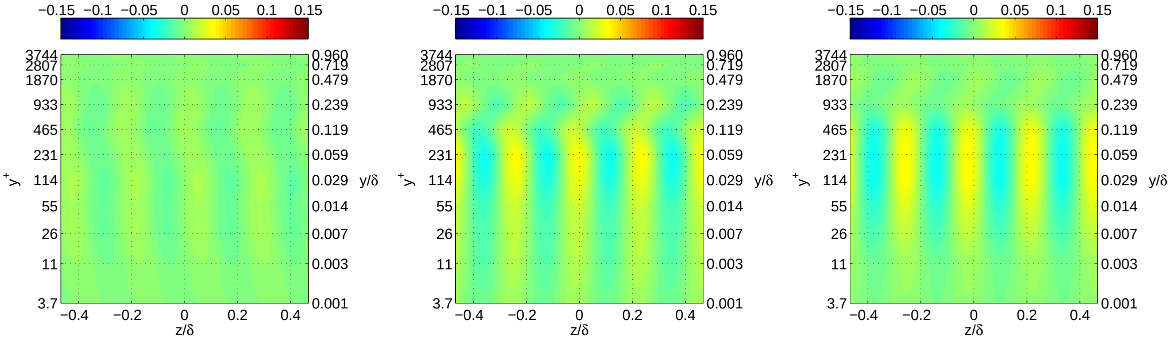

(g) t=0.233 s. (h) t=0.266 s. (i) t=0.316 s.

Figure 7.35: Reconstructed velocity fluctuations using only the first POD and fifth spanwise Fourier modes at $Re_\theta = 9800$. Different time steps are as given in the captions.

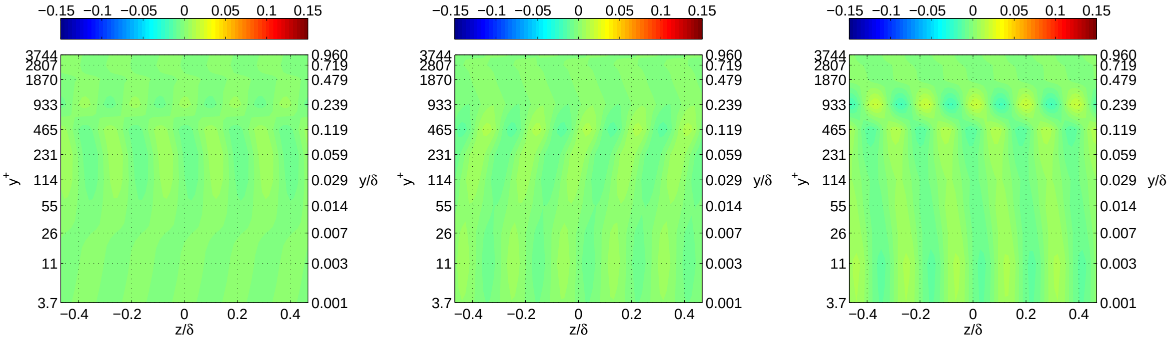

(a) t=0.033 s.

(b) t=0.050 s.

(c) t=0.066 s.

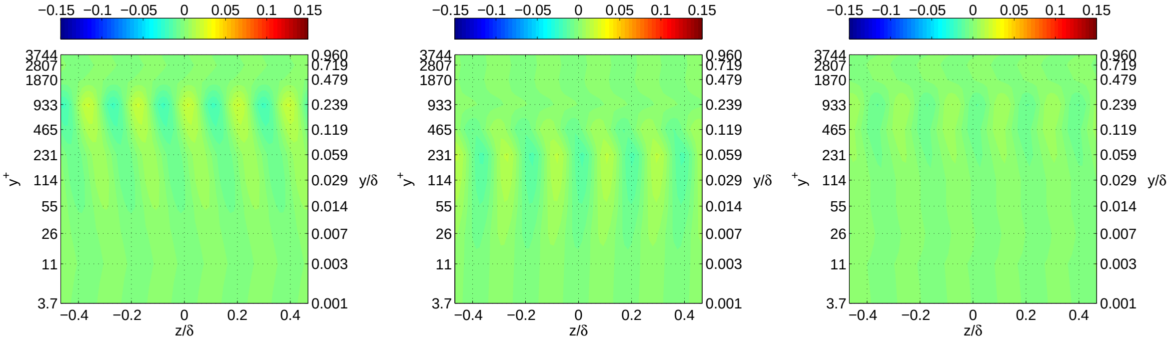

(d) t=0.133 s.

(e) t=0.150 s.

(f) t=0.200 s.

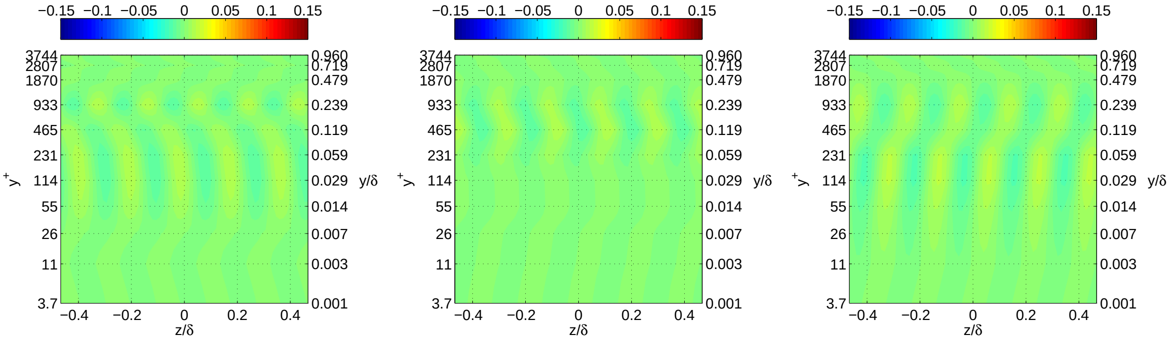

(g) t=0.233 s.

(h) t=0.266 s.

(i) t=0.316 s.

Figure 7.36: Reconstructed velocity fluctuations using only the first POD and sixth spanwise Fourier modes at $Re_\theta = 9800$. Different time steps are as given in the captions.

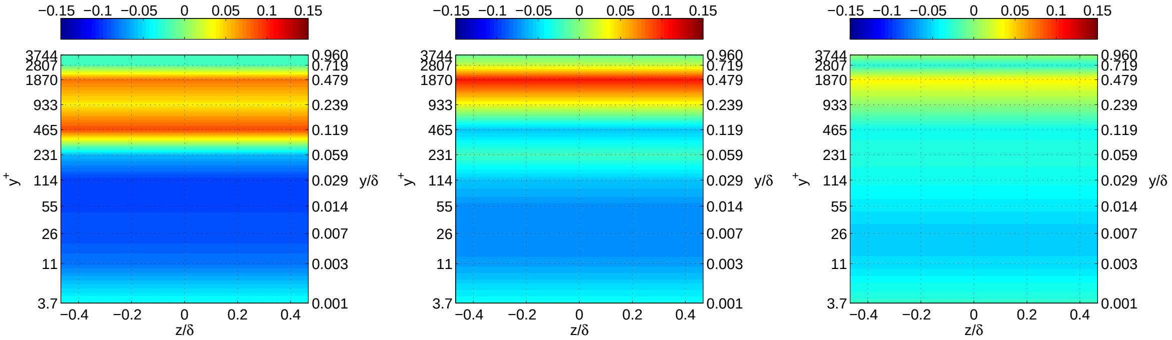

(a) t=0.033 s. (b) t=0.050 s. (c) t=0.066 s.

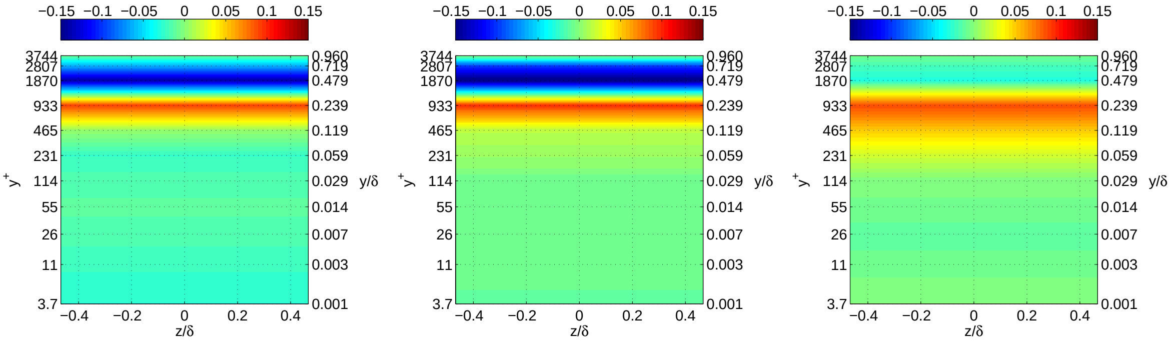

(d) t=0.133 s. (e) t=0.150 s. (f) t=0.200 s.

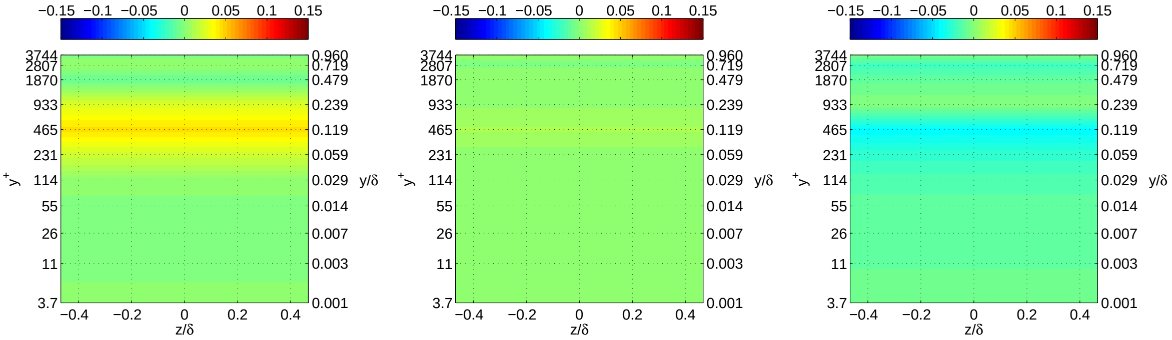

(g) t=0.233 s. (h) t=0.266 s. (i) t=0.316 s.

Figure 7.37: Reconstructed velocity fluctuations using the first four POD modes and first spanwise Fourier mode at $Re_\theta = 9800$. Different time steps are as given in the captions.

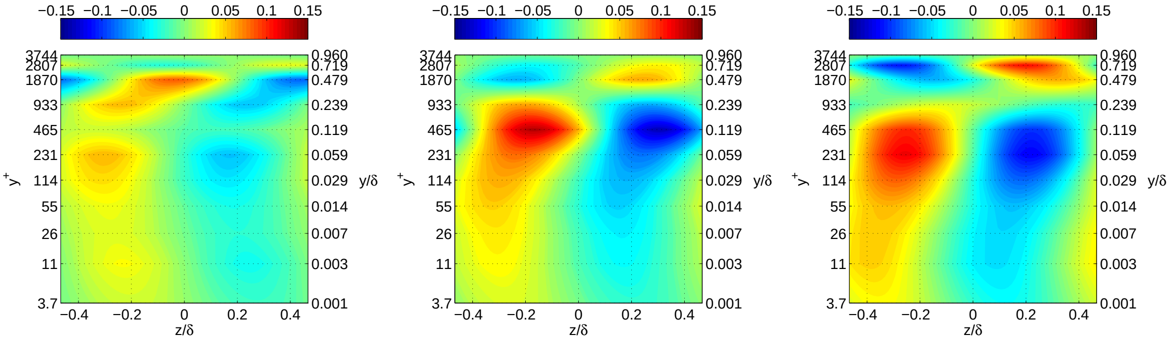

(a) t=0.033 s.

(b) t=0.050 s.

(c) t=0.066 s.

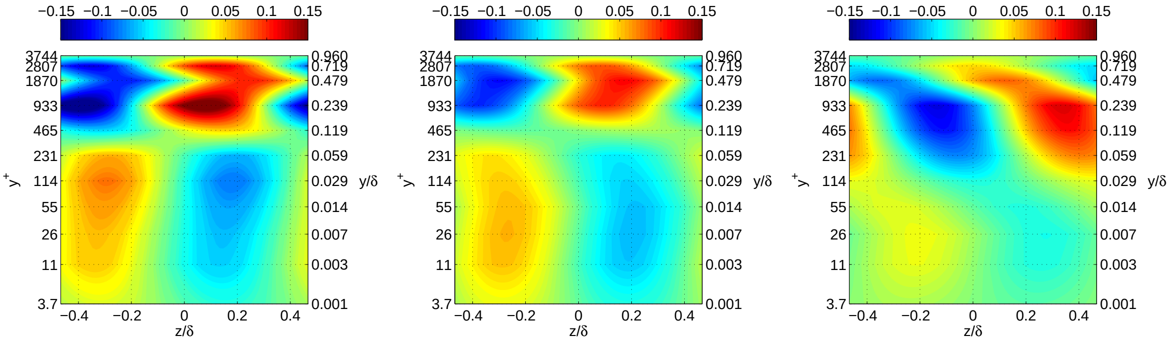

(d) t=0.133 s.

(e) t=0.150 s.

(f) t=0.200 s.

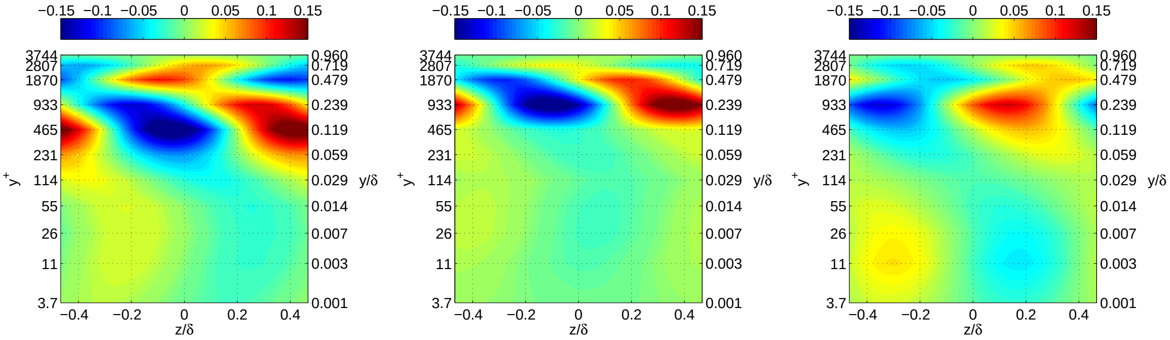

(g) t=0.233 s.

(h) t=0.266 s.

(i) t=0.316 s.

Figure 7.38: Reconstructed velocity fluctuations using the first four POD modes and second spanwise Fourier mode at $Re_\theta = 9800$. Different time steps are as given in the captions.

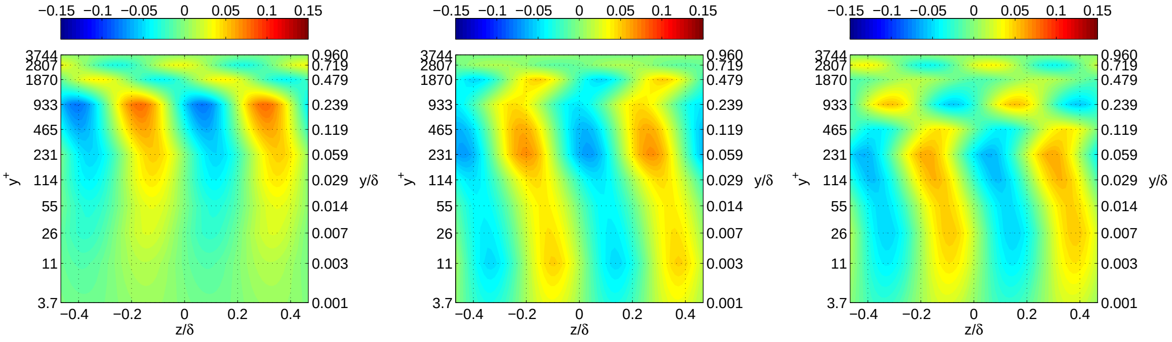

(a) t=0.033 s.

(b) t=0.050 s.

(c) t=0.066 s.

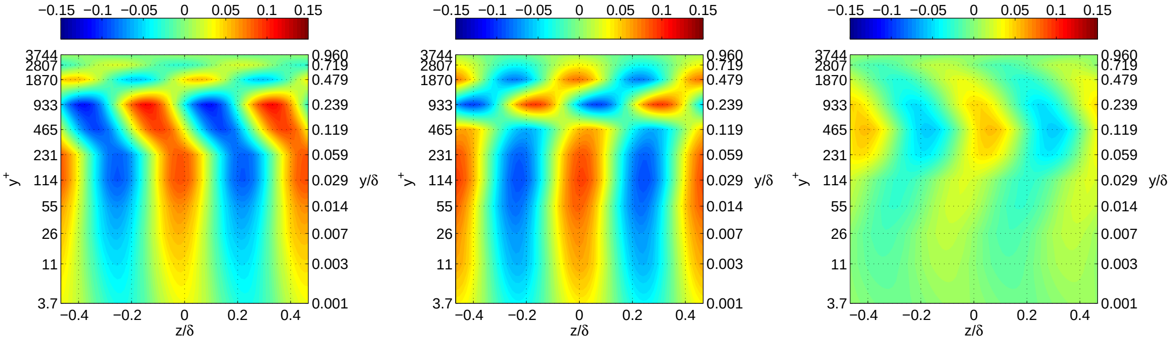

(d) t=0.133 s.

(e) t=0.150 s.

(f) t=0.200 s.

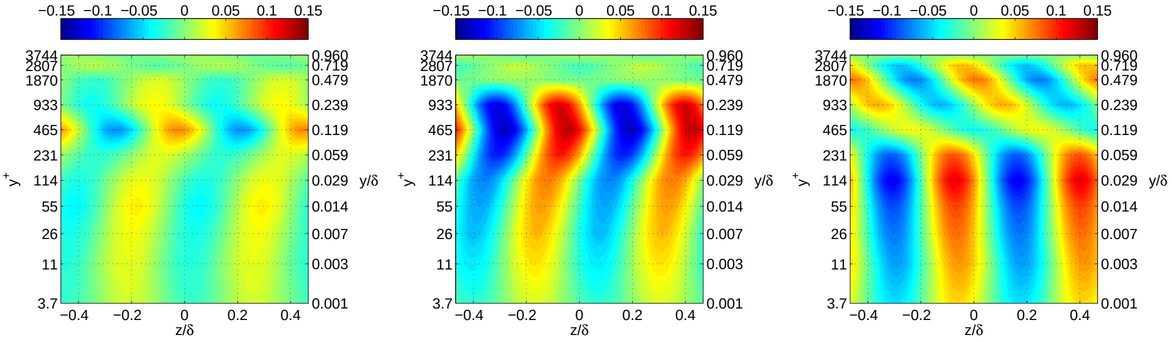

(g) t=0.233 s.

(h) t=0.266 s.

(i) t=0.316 s.

Figure 7.39: Reconstructed velocity fluctuations using the first four POD modes and third spanwise Fourier mode at $Re_\theta = 9800$. Different time steps are as given in the captions.

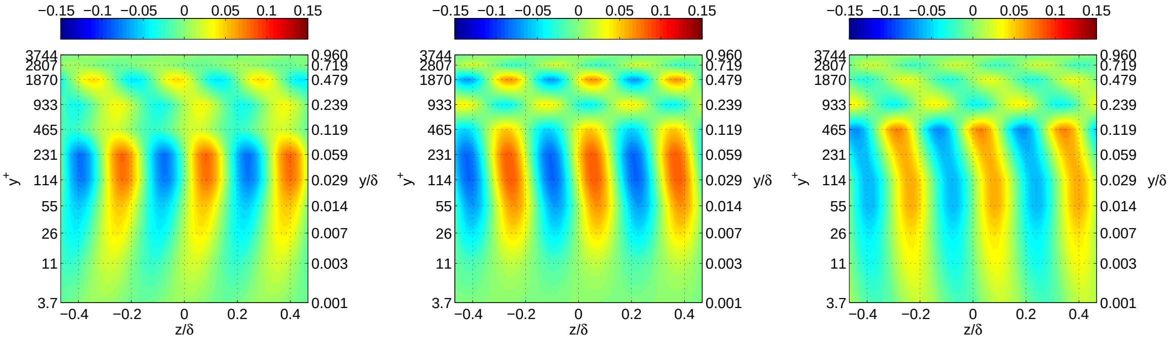

(a) t=0.033 s.

(b) t=0.050 s.

(c) t=0.066 s.

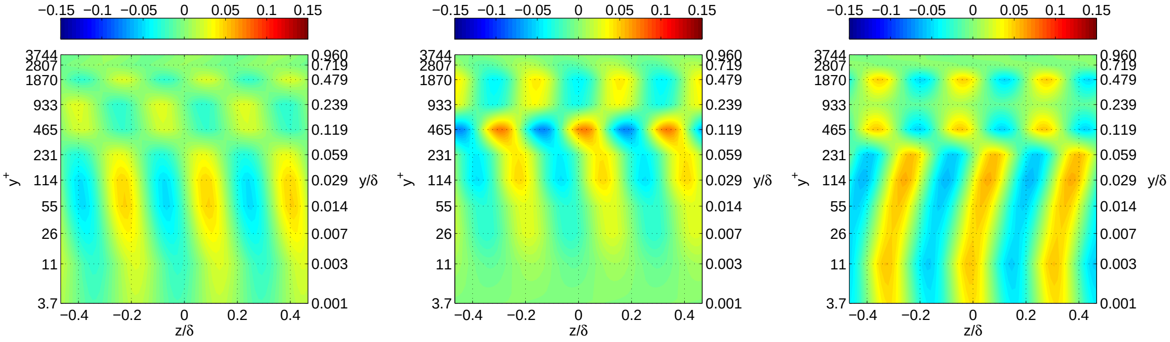

(d) t=0.133 s.

(e) t=0.150 s.

(f) t=0.200 s.

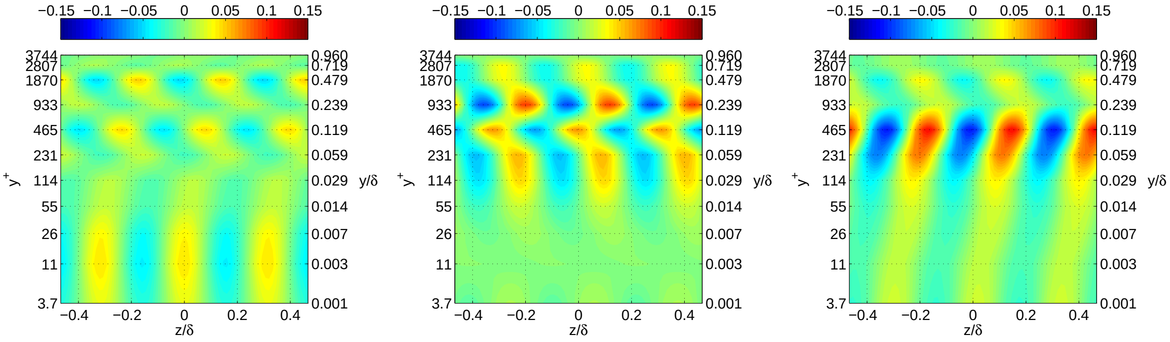

(g) t=0.233 s.

(h) t=0.266 s.

(i) t=0.316 s.

Figure 7.40: Reconstructed velocity fluctuations using the first four POD modes and fourth spanwise Fourier mode at Re_θ =9800. Different time steps are as given in the captions.

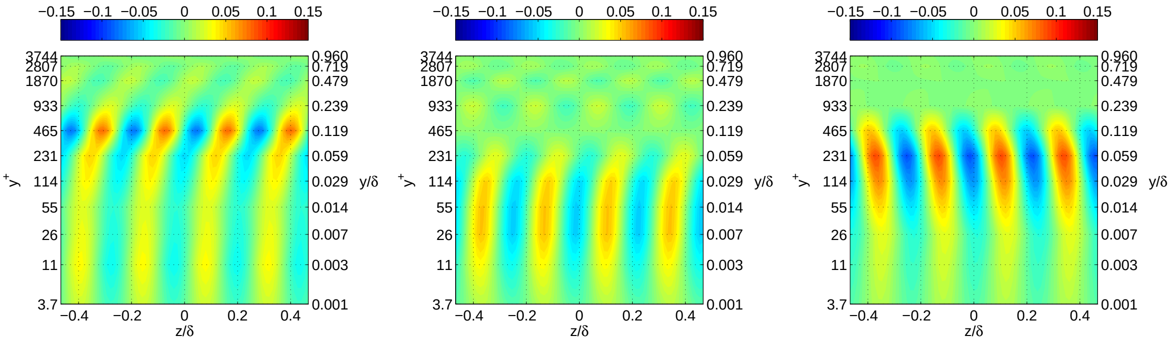

(a) t=0.033 s.

(b) t=0.050 s.

(c) t=0.066 s.

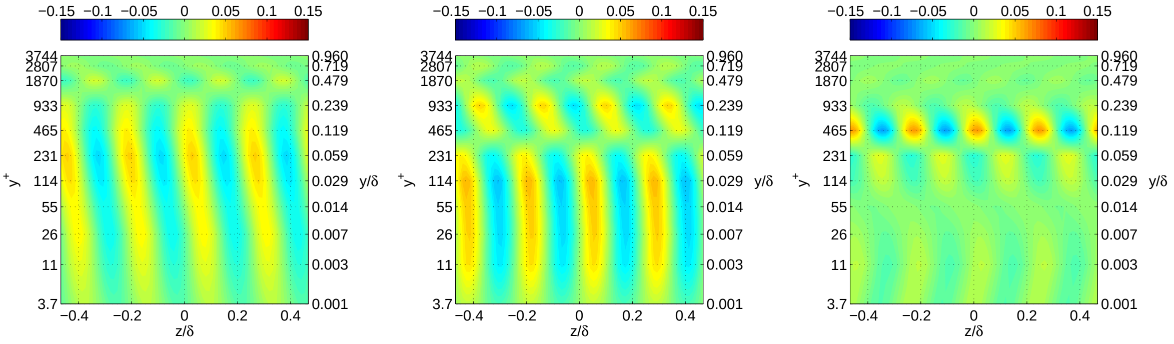

(d) t=0.133 s.

(e) t=0.150 s.

(f) t=0.200 s.

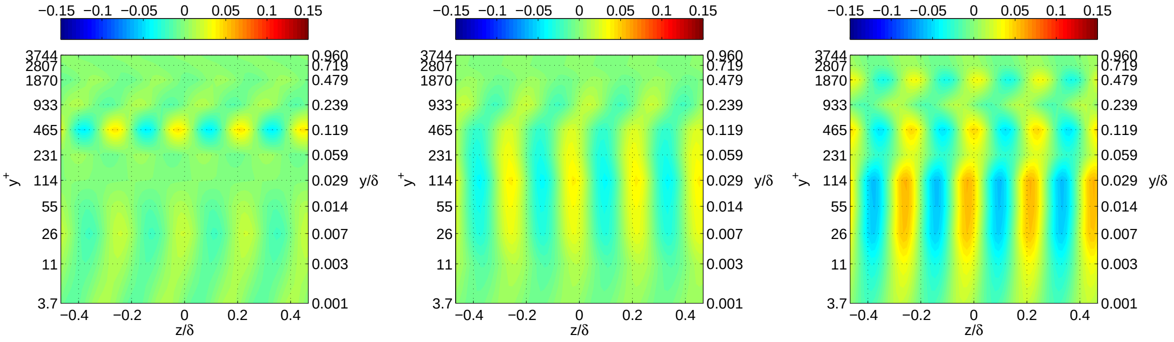

(g) t=0.233 s.

(h) t=0.266 s.

(i) t=0.316 s.

Figure 7.41: Reconstructed velocity fluctuations using the first four POD modes and fifth spanwise Fourier mode at Re_θ =9800. Different time steps are as given in the captions.

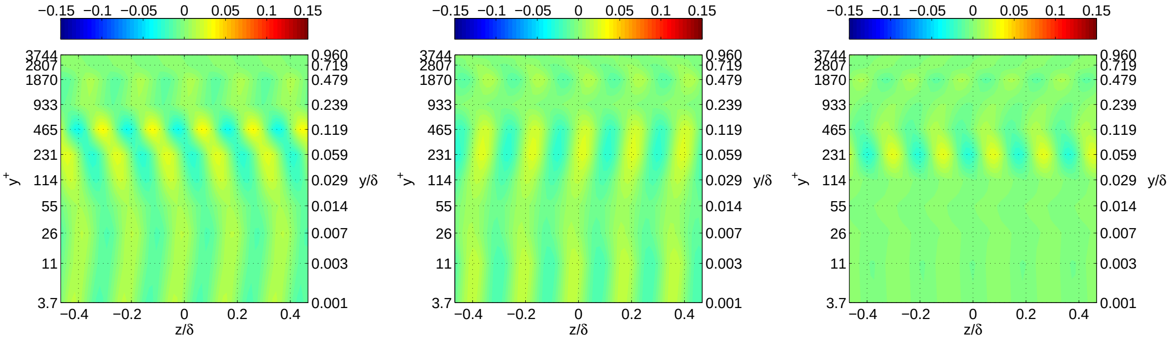

(a) t=0.033 s.

(b) t=0.050 s.

(c) t=0.066 s.

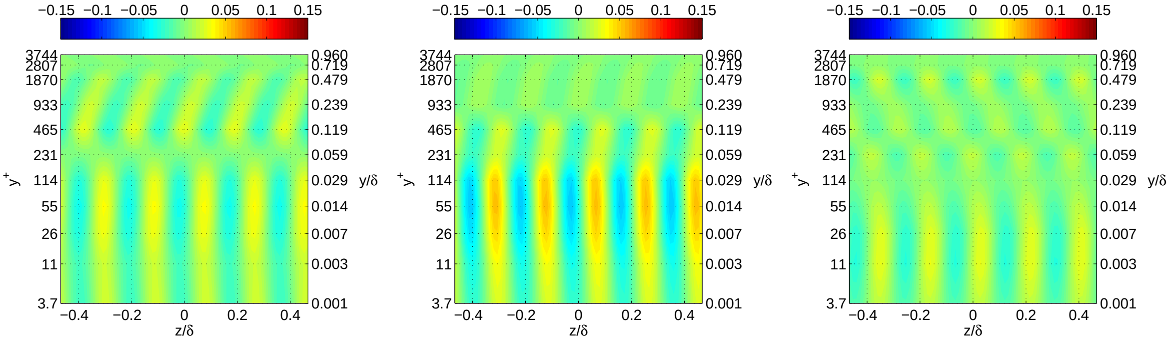

(d) t=0.133 s.

(e) t=0.150 s.

(f) t=0.200 s.

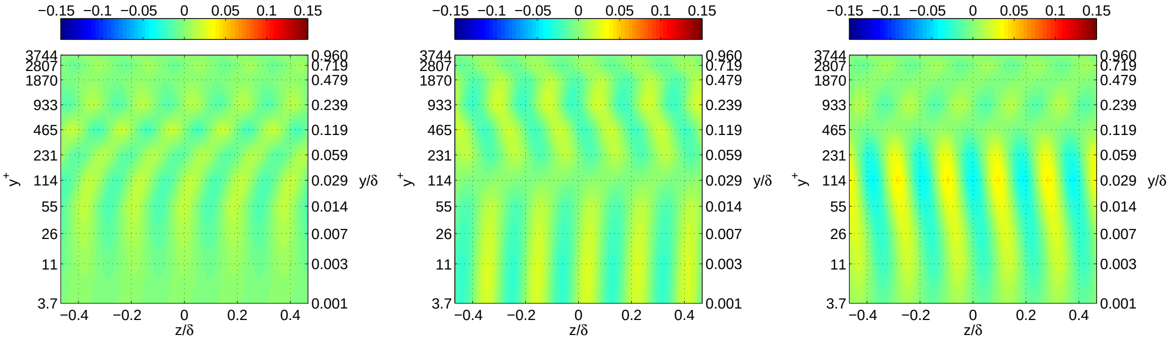

(g) t=0.233 s.

(h) t=0.266 s.

(i) t=0.316 s.

Figure 7.42: Reconstructed velocity fluctuations using the first four POD modes and sixth spanwise Fourier mode at $Re_\theta = 9800$. Different time steps are as given in the captions.

Chapter 8

Summary and Conclusions

This thesis presents part of the large research program funded by the European Commission called *Wallturb: A European synergy for the assessment of wall turbulence*. The main aim of this research program is to create new experimental and numerical databases on the characteristics of turbulent wall-bounded flows, especially turbulent boundary layers. The goal is that these databases will be used to gain more insight into the physical mechanisms governing the dynamics of these flows. This knowledge is deemed essential for the future development of efficient and physical turbulence modeling strategies, which are in turn crucial to aircraft and other industries for sustainable development, especially under the pressure of high oil prices and operational costs.

One of the main aims of this thesis was to perform experiments in the large LML wind tunnel using synchronized, multipoint flow measurement systems to acquire data within a flow volume comparable to the size of boundary layer thickness cubed. The experiments were performed using three synchronized stereo PIV systems and a hot-wire rake of 143 single wire probes distributed on an array of 30×30 cm^2 normal to the flow in the streamwise direction. This thesis presents the analysis of only the hot-wire anemometry data collected for the zero pressure gradient case at two different Reynolds numbers, namely Re_θ of 9800 and 19 100. The thesis includes a description of the experimental setup for the measurements performed in the LML wind tunnel, and the *in situ* calibration methodology developed in the course of these experiments. It presents some of the basic single point statistics, the results from a detailed investigation of the two-point cross-correlations, and finally results from a proper orthogonal decomposition (POD) including the kinematics of the reconstructed velocity fields using the POD eigenmodes.

The attachment of the 143 probe hot-wire rake to the wind tunnel prevented a conventional hot-wire probe calibration because of the mechanical difficulties. Therefore a new hot-wire calibration method was developed and utilized for this investigation. The method is based on a polynomial curve fitting approximation which expresses the instantaneous velocity as a function of instantaneous voltage. There is only one freestream velocity needed in this method; since the method employs the higher order velocity statistics obtained at only one external velocity instead of obtaining classical freestream velocity versus voltage curves. The key to the method was the measurement before, during and after the experiment using single hot-wires and PIV of the mean velocity and higher velocity moments just upstream of the individual probes. The results showed that even a second order polynomial approximation yields very good agreement between the measured profiles (or computed profiles after the calibration) and the reference profiles used in the calibration. The method also provides an opportunity to do the calibration on the fly as long as the convergence of the high order voltage statistics can be satisfied. The calibration scheme can be executed for different blocks of hot-wire data to correct the coefficients, thus classical correction methodologies due to the changes in physical conditions can be eliminated by the proposed method.

A primary goal of the measurement was to establish the spatial and temporal structure of the high Reynolds number turbulent boundary layer by taking time-resolved data simultaneously at many spatial locations. Single point statistics were not the main interest in this study, because extensive investigations on the characteristics of the turbulent boundary layers within the same facility in the same range of Reynolds numbers had already been performed and documented by Carlier & Stanislas (2005); Stanislas *et al.* (2008). Comparisons with this earlier data, however, provided an important opportunity to verify the multipoint and calibration methodology. Single point statistics (e.g., rms velocity profiles, profiles for the third and fourth central moments) of the turbulent velocity field together with the power spectral densities at different wall-normal positions showed excellent agreements with the previously obtained results in the same facility. Moreover, the single point spectral analysis revealed some important findings. First, the $k^{-5/3}$ range develops only after y^+ of 220 and reaches a significant length after y^+ of 450, consistent with the existence of a mesolayer. Second, the k^{-1} range is found only in a very small region. The corresponding flat region in the premultiplied spectra is seen only near approximately $y^+ = 100$ for both of the Reynolds numbers studied here. Third, the different shapes of the premultiplied spectra in the overlap region of the boundary layer suggest strongly a dependence on Reynolds number consistent with different inner and outer character of this developing flow.

The large scale motions of the turbulence were studied in detail using two-dimensional two-point cross-correlations maps on different planes within the measurement domain. It was observed that the elongated correlations exist at every wall-normal position above the buffer layer. (The single exception was the very thin streaky features observed within the viscous layer of the low Reynolds number case.) These elongated structures were relatively more significant in the log layer. Also, their spatial extent in the streamwise direction, utilizing the Taylor's frozen field hypothesis, was found to be extremely large (i.e., many boundary layer thicknesses). Data analysis using different algorithms revealed similar results, suggesting that the source of these very long correlations is not the algorithm. Clearly there is a need for physical explanation of their existence. Correlation between different layers of the boundary layer was also observed, even between the most intermittent outer region and the near wall region, suggesting strongly that coherent structures link different regions across the boundary layer.

The investigation using the proper orthogonal decomposition showed that the POD (in conjunction with Fourier analysis in the statistically homogeneous and stationary directions) can effectively represent the total kinetic energy with a small number of modes. It was possible to recover for both Reynolds numbers almost 90% of the total turbulence kinetic energy within the entire boundary layer with only four POD modes. The eigenspectra of the POD modes showed that most of the activity is located in the spectrum below 50 Hz and 100 Hz for the low and high Reynolds number respectively. Therefore, low-pass filtering of turbulence kinetic energy by means of truncating the number of POD and Fourier modes is very effective, and causes no significant change to the large scale features of the turbulent boundary layer. The reconstructed velocity fluctuations on the spanwise-wall-normal plane show how organized motions of turbulence with significant amounts of energy interact with each other across the boundary layer. It is also possible to observe the strength of the interaction between the inner and outer layers of turbulence using these reconstructed velocity fields. The reconstructed fields suggest that any attempt to develop uncoupled models for different layers of turbulence will result in failure, since interactions exist between the large scale energetic scales of turbulence across the entire boundary layer. The reconstructions also appears to contradict the classical view that it is the inner layer that drives the outer. In fact, the opposite appears to be true.

In summary, the results of the two-point cross-spectral analysis and the proper orthogonal decomposition analysis suggest that the turbulent boundary layer is full of organized motions extending in both the transverse and streamwise directions, and greatly elongated in the latter. The results also reveal that the different layers of the turbulent boundary layer are actively communicating because of the structures connecting them.

Bibliography

ADRIAN, R. J. 2007 Hairpin vortex organization in wall turbulence. *Physics of Fluids* **19** (041301), 1–16.

ADRIAN, R. J., MEINHART, C. D. & TOMKINS, C. D. 2000 Vortex organization in the outer region of the turbulent boundary layer. *Journal of Fluid Mechanics* **422**, 1–54.

DEL ÁLAMO, J. C. & JIMENEZ, J. 2003 Spectra of the very large anisotropic scales in turbulent channels. *Physics of Fluids* **15** (6), L41–L44.

DEL ÁLAMO, J. C., JIMENEZ, J., ZANDONADE, P. & MOSER, R. D. 2004 Scaling of the energy spectra of turbulent channels. *Journal of Fluid Mechanics* **500**, 135–144.

BAKEWELL, H. P. & LUMLEY, J. L. 1967 Viscous sublayer and adjacent wall region in turbulent pipe flow. *Physics of Fluids* **10** (9), 1880–1889.

BALAKUMAR, B. J. & ADRIAN, R. J. 2007 Large- and very-large-scale motions in channel and boundary-layer flows. *Philosophical Transactions of the Royal Society A* **365**, 665–681.

BLACKWELDER, R. F. & KOVASZNY, L. S. G. 1972 Time scales and correlations in a turbulent boundary layer. *Physics of Fluids* **15** (9), 1545–1554.

BREUER, K. S. 1995 Stochastic calibration of sensors in turbulent flow fields. *Experiments in Fluids* **19** (2), 138–141.

BRUUN, H. H. 1995 *Hot-Wire Anemometry*. New York: Oxford University Press.

BUCHAVE, P. 1979 The measurement of turbulence with the burst-type laser dopler anemometery - errors and correction methods. Ph.D. Dissertation, State University of New York at Buffalo.

CARLIER, J. & STANISLAS, M. 2005 Experimental study of eddy structures in a turbulent boundary layer using particle image velocimetry. *Journal of Fluid Mechanics* **535**, 143–188.

CHATELLIER, L. & FITZPATRICK, J. 2005 Spatio-temporal correlation analysis of turbulent flows using global and single-point measurements. *Experiments in Fluids* **38** (5), 563–575.

CITRINITI, J. H. 1996 Experimental investigation into the dynamics of the axisymmetric mixing layer utilizing the proper orthogonal decomposition. Ph.D. Dissertation, State University of New York at Buffalo.

CITRINITI, J. H. & GEORGE, W. K. 2000 Reconstruction of the global velocuty field in the axisymmetric mixing layer utilizing the proper orthogonal decomposition. *Journal of Fluid Mechanics* **418**, 137–166.

CITRINITI, J. H., TAULBEE, K. D., WOODWARD, S. H. & GEORGE, W. K. 1994 Design of multiple channel hot wire anemometers. In *Fluid Mechanics and Instrumentation*, , vol. 183, pp. 67–73. ASME-FED.

COUDERT, S., FOUCAUT, J. M., KOSTAS, J., STANISLAS, M., BRAUD, P., FOURMENT, C., DELVILLE, J., TUTKUN, M., MEHDI, F., JOHANSSON, P. B. V. & GEORGE, W. K. 2007 Double large field stereoscopic PIV in a high Reynolds number turbulent boundary layer. *Experiments in Fluids* **Under review**.

DELVILLE, J. 1994 Characterization of the organization in shear layers via the proper orhogonal decomposition. *Applied Scientific Research* **53**, 263–281.

DELVILLE, J., UKEILEY, L., CORDIER, L., BONNET, J. P. & GLAUSER, M. 1999 Examination of large-scale structures in a turbulent plane mixing layer. Part 1. Proper orthogonal decomposition. *Journal of Fluid Mechanics* **391**, 91–122.

DENNIS, D. J. C. & NICKELS, T. B. 2007 On the use of Taylor's hypothesis in constructing long structures in wall-bounded turbulent flow. In *Advances in Turbulence XI: Proceedings of the 11th EUROMECH European Turbulence Conference* (ed. J. M. L. M. Palma & A. Silva Lopes), *Springer Proceedings in Physics*, vol. 117, pp. 236–238. Porto, Portugal: Springer, Heidelberg.

EWING, D., FROHNAPFEL, B., GEORGE, W. K., PEDERSEN, J. & WESTERWEEL, J. 2007 Two-point similarity in the round jet. *Journal of Fluid Mechanics* **577**, 309–330.

FAVRE, A. J., GAVIGLIO, J. J. & DUMAS, R. 1957*a* Further space-time correlations of velocity in a turbulent boundary layer. *Journal of Fluid Mechanics* **3** (4), 344–356.

FAVRE, A. J., GAVIGLIO, J. J. & DUMAS, R. 1957*b* Space-time double correlations and spectra in a turbulent boundary layer. *Journal of Fluid Mechanics* **2** (4), 313–342.

FAVRE, A. J., GAVIGLIO, J. J. & DUMAS, R. 1967 Structure of velocity space-time correlations in a turbulent boundary layer. *The Physics of Fluids* **Supplement**, S138–S145.

GAMARD, S. 2002 Axisymmetric turbulent jets. Ph.D. Dissertation, Chalmers University of Technology, Göteborg, Sweden.

GAMARD, STEPHAN, JUNG, DAEHAN & GEORGE, WILLIAM K. 2004 Downstream evolution of the most energetic modes in a turbulent axisymmetric jet at high reynolds number. Part 2. The far-field region. *Journal of Fluid Mechanics* **514**, 205–230.

GANAPATHISUBRAMANI, B., HUTCHINS, N., HAMBLETON, W. T., LONGMIRE, E. K. & MARUSIC, I. 2005 Investigation of large-scale coherence in a turbulent boundary layer using two-point correlations. *Journal of Fluid Mechanics* **524**, 57–80.

GANAPATHISUBRAMANI, B., LONGMIRE, E. K. & MARUSIC, I. 2003 Characteristics of vortex packets in turbulent boundary layers. *Journal of Fluid Mechanics* **478**, 35–46.

GEORGE, W. K. 1988 Insight into the dynamics of coherent structures from a proper orthogonal decomposition. In *The Structure of Near Wall Turbulence, Proceedings of Symposium on Near Wall Turbulence* (ed. S. Kline), pp. 168–180. Dubrovnik, Yugoslavia, Hemisphere, NY.

GEORGE, WILLIAM K. 1999 Some thoughts on similarity, the POD, and finite boundaries. In *Trends in Mathematics* (ed. A. Gyr & A. Tsinober), pp. 117–128. Birkhauser, Basel.

GEORGE, W. K. 2006 Recent advancements toward the understanding of turbulent boundary layers. *Applied Mechanics Review* **44**, 2435–2449.

GEORGE, W. K., BEUTHER, P. D. & SHABBIR, A. 1989 Polynomial calibrations for hot wires in thermally varying flows. *Experimental Thermal and Fluid Science* **2** (2), 230–235.

GEORGE, W. K. & CASTILLO, L. 1997 Zero-pressure-gradient turbulent boundary layer. *Applied Mechanics Review* **50**, 689–729.

GLAUSER, M. N. 1987 Coherent structures in the axisymmetric turbulent jet mixing layer. Ph.D. Dissertation, State University of New York at Buffalo.

GLAUSER, M. N. & GEORGE, W. K. 1987 Orthogonal decomposition of the axisymmetric jet mixing layer including azimuthal dependence. In *Advances in Turbulence* (ed. G Comte-Bellot & J. Mathieu), pp. 357–366. Berlin: Springer.

GLAUSER, M. N. & GEORGE, W. K. 1992 Application of mulitpoint measurements for flow characterization. *Experimental Thermal and Fluid Science* **5**, 617–632.

GLAUSER, M. N., LEIB, S. J. & GEORGE, W. K. 1985 Coherent structures in the axisymmetric turbulent jet mixing layer. In *Turbulent Shear Flows 5* (ed. F. Durst, B. E. Launder, J. H. Lumley, F. W. Schmidt & J. H. Whitelaw), pp. 134–145. Springer-Verlag.

GORDEYEV, S. V. & THOMAS, F. O. 2000 Coherent structure in the turbulent planar jet. Part 1. Extraction of proper orthogonal decomposition eigenmodes and their self-similarity. *Journal of Fluid Mechanics* **414**, 145–194.

GORDEYEV, S. V. & THOMAS, F. O. 2002 Coherent structure in the turbulent planar jet. Part 2. Structural topology via POD eigenmode projection. *Journal of Fluid Mechanics* **460**, 349–380.

GUALA, M., HOMMEMA, S. E. & ADRIAN, R. J. 2006 Large-scale and very-large-scale motions in turbulent pipe flow. *Journal of Fluid Mechanics* **554**, 521–542.

HEAD, M. R. & BANDYOPADHYAY, P. 1981 New aspects of turbulent boundary-layer structure. *Journal of Fluid Mechanics* **107**, 297–338.

HERZOG, S. 1986 The large scale structure in the near-wall region of turbulent pipe flow. Ph.d. dissertation, Cornell University, Ithaca, NY.

HOLMES, P., LUMLEY, J. H. & BERKOOZ, G. 1996 *Turbulence, Coherent Structures, Dynamical Systems and Symmetry*. U.K.: Cambridge University Press.

HOMMEMA, S. E. & ADRIAN, R. J. 2002 Similarity of apparently random structures in the outer region of wall turbulence. *Experiments in Fluids* **33** (1), 5–12.

HUTCHINS, N. & MARUSIC, I. 2007 Evidence of very long meandering features in the logarithmic region of turbulent boundary layers. *Journal of Fluid Mechanics* **579**, 1–28.

IQBAL, M. O. & THOMAS, F. O. 2007 Coherent structure in a turbulent jet via a vector implementation of the proper orthogonal decomposition. *Journal of Fluid Mechanics* **571** (281-326).

JOHANSSON, PETER 2007 Report on wallturb joint experiments equipment setup. Technical Report WT-070806-TR-TUCh. Wallturb Project Consortium, Laboratoire de Mécanique de Lille (LML UMR CNRS 8107), Bd. Paul Langevin, Cité Scientifique, 59655 Villeneuve d'Ascq Cedex, France.

JOHANSSON, P. B. V. & GEORGE, W. K. 2006*a* The far downstream evloution of the high reynolds number axisymmetric wake behind a disk. Part 1. Single point statistics. *Journal of Fluid Mechanics* **555**, 363–385.

JOHANSSON, P. B. V. & GEORGE, W. K. 2006*b* The far downstream evloution of the high reynolds number axisymmetric wake behind a disk. Part 2. Slice proper orthogonal decompositioon. *Journal of Fluid Mechanics* **555**, 387–408.

JOHANSSON, P. B. V., GEORGE, W. K. & WOODWARD, S. H. 2002 Proper orthogonal decomposition of an axisymmetric turbulent wake behind a disk. *Physics of Fluids* **14** (7), 2508–2514.

JUNG, D. 2001 An investigation of the Reynolds-number dependence of the axisymmetric jet mixing layer using a 138 hot-wire probe and the POD. Ph.D. Dissertation, State University of New York at Buffalo, Buffalo, NY.

JUNG, D., GAMARD, S. & GEORGE, W. K. 2004 Downstream evolution of the most energetic modes in a turbulent axisymmetric jet at high reynolds number. Part 1. The near-field region. *Journal of Fluid Mechanics* **514**, 173–204.

KIM, K. C. & ADRIAN, R. J. 1999 Very large-scale motion in the outer layer. *Physics of Fluids* **11** (2), 417–422.

KLINE, S. J., REYNOLDS, W. C., SCHRAUB, F. A. & RUNSTADLER, P. W. 1967 The structure of turbulent boundary layers. *Journal of Fluid Mechanics* **30** (4), 741–773.

KOVASZNAY, L. S. G., KIBENS, V. & BLACKWELDER, R. F. 1970 Large-scale motion in the intermittent region of a turbulent boundary layer. *Journal of Fluid Mechanics* **41** (2), 283–325.

KROGSTAD, P.-Å., KASPERSEN, J. H. & RIMESTAD, S. 1998 Convection velocities in a turbulent boundary layer. *Physics of Fluids* **10** (4), 949–957.

LEIB, S. J., GLAUSER, M. N. & GEORGE, W. K. 1984 An application of lumley's orthogonal decomposition to the axisymmetric turbulent jet mixing layer. In *Proceedings of the 9th Rolla Symposium on Turbulence in Fluids* (ed. G. L. Patterson & J. L. Zakin). Rolla, Missouri: University of Missouri-Rolla.

LIU, Z., ADRIAN, R. J. & HANRATTY, T. J. 2001 Large-scale modes of turbulent channel flow: Transport and structure. *Journal of Fluid Mechanics* **448**, 53–80.

LIU, Z. C., ADRIAN, R. J. & HANRATTY, T. J. 1994 Reynolds number similarity of orthogonal decomposition of the outer layer of turbulent wall flow. *Physics of Fluids* **6** (8), 2815–2819.

LUMLEY, J. L. 1967 The structure of inhomogeneous turbulent flows. In *Atmospheric Turbulence and Radio Wave Propogation* (ed. A. M. Yaglom & V. I. Tatarsky), pp. 166–176. Moscow, USSR: Publishing House Nauka.

LUMLEY, J. L. 1970 *Stochastic Tools in Turbulence*. New York and London: Academic Press.

MCKEON, B. J. & MORRISON, J. F. 2007 Asymptotic scaling in turbulent pipe flow. *Philosophical Transactions of the Royal Society A* **365**, 771–787.

MOIN, P. & MOSER, R. D. 1989 Characteristic-eddy decompostion of turbulence in a channel. *Journal of Fluid Mechanics* **200**, 471–509.

MONTY, J. P., STEWART, J. A., WILLIAMS, R. C. & CHONG, M. S. 2007 Large-scale features in turbulent pipe and channel flows. *Journal of Fluid Mechanics* **589**, 147–156.

O'NEILL, P. L., NICOLAIDES, D., HONNERY, D. & SORIA, J. 2004 Autocorrelation functions and the determination of integral length with reference to experimental and numerical data. In *Proceedings of the 15th Australian Fluid Mechanics Conference (CD-ROM)* (ed. M. Behnia, W. Lin & G. D. McBain). The University of Sydney, Sydney NSW 2006 Australia, Paper no: AFMC00064.

PERRY, A. E. 1982 *Hot-Wire Anemometry*. New York: Oxford University Press.

STANISLAS, M., PERRET, L. & FOUCAUT, J.-M. 2008 Vortical structures in the turbulent boundary layer: a possible route to a universal representation. *Journal of Fluid Mechanics* **602**, 327–382.

THEODORSEN, T. 1952 Mechanism of turbulence. In *Proceedings of the Midwestern Conference on Fluid Mechanics*. Ohio State University, Columbus, OH.

TOMKINS, C. D. & ADRIAN, R. J. 2003 Spanwise structure and scale growth in turbulent boundary layers. *Journal of Fluid Mechanics* **490**, 37–74.

TOMKINS, C. D. & ADRIAN, R. J. 2005 Energetic spanwise modes in the logarithmic layer of a turbulent boundary layer. *Journal of Fluid Mechanics* **545**, 141–162.

TOWNSEND, A. A. 1976 *The Structure of Turbulent Shear Flow*, 2nd edn. United Kingdom: Cambridge University Press.

TUTKUN, M., JOHANSSON, P. B.V. & GEORGE, W. K. 2008 Three-component vectorial proper orthogonal decomposition of axisymmetric wake behind a disk. *AIAA Journal* **46** (5), 1118–1134.

WÄNSTRÖM, M., GEORGE, W. K. & MEYER, K.-E. 2006 Stereoscopic PIV and POD applied to far turbulent axisymmetric jet. In *AIAA Paper 2006-3368*.

WOODWARD, S. H. 2001 Progress toward massively parallel thermal anemometry system. M.Sc. Thesis, State University of New York at Buffalo.

WOODWARD, S. H., EWING, D. & JERNQVIST, L. 2001 Anemometer system review. In *In Sixth Annual Symposium on Thermal Anemometry*. Melbourne, Australia.

ZHOU, J., ADRIAN, R. J. & BALACHANDAR, S. 1996 Autogeneration of near-wall vortical structures in channel flow. *Physics of Fluids* **8** (1), 288–290.

ZHOU, J., ADRIAN, R. J., BALACHANDAR, S. & KENDALL, T. 1999 Mechanism for generating coherent packets of hairpin vortices in channel flow. *Journal of Fluid Mechanics* **387**, 353–396.

Appendix A

Details of Rake Design

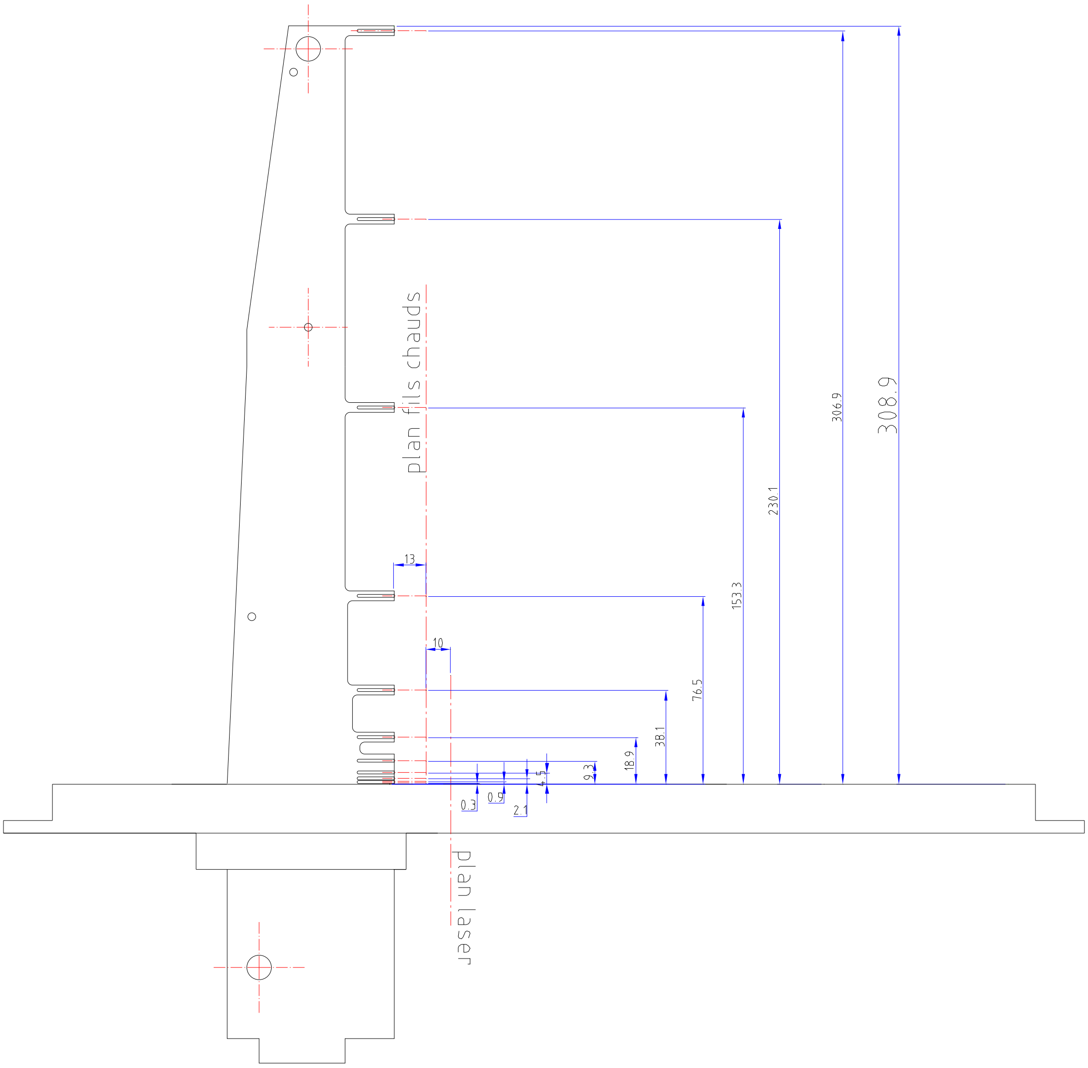

Figure A.1: Side view of the hot-wire rake. All dimensions are in mm.

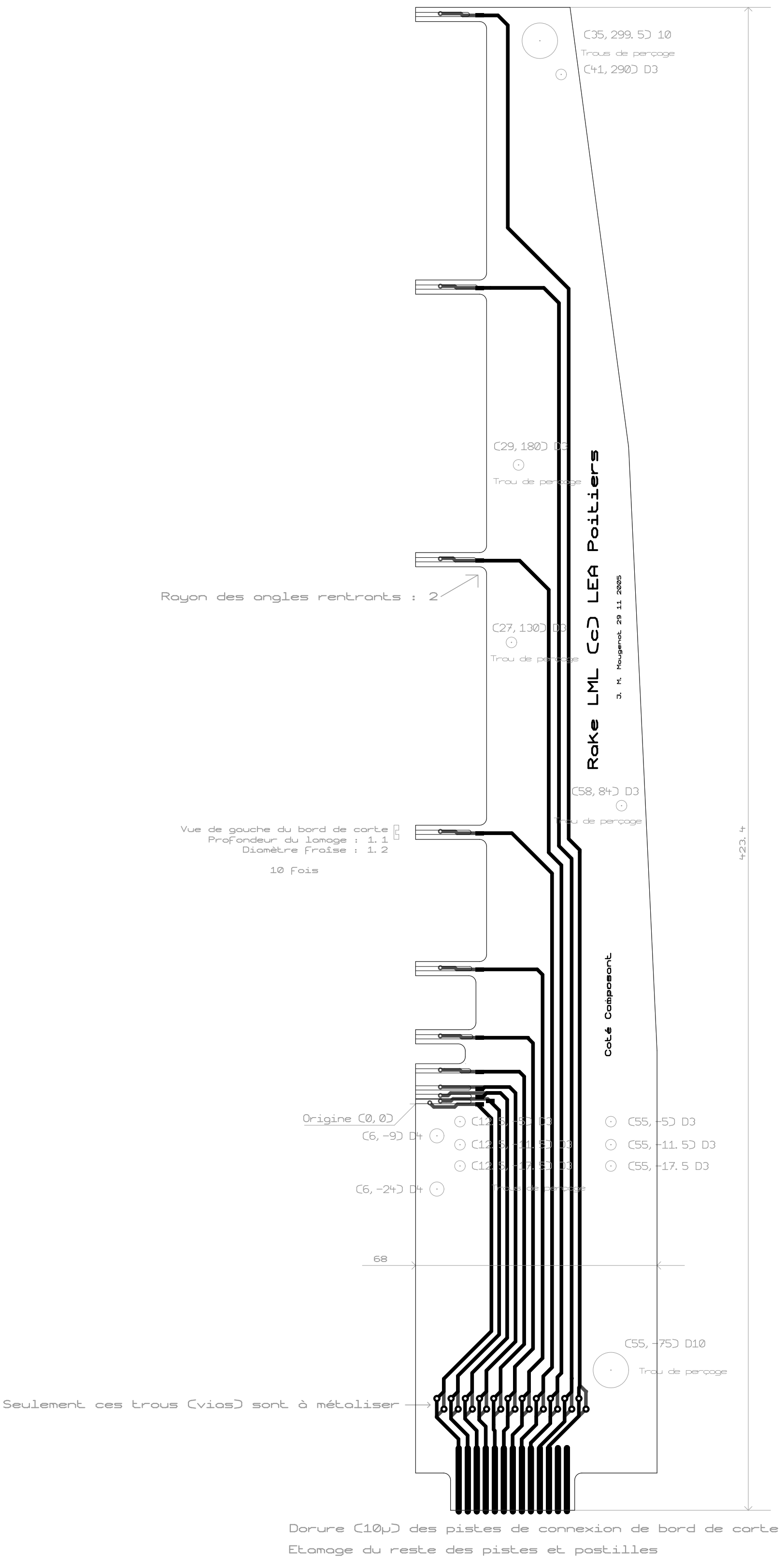

Figure A.2: Diagram of the double-sided circuit board. All dimensions are in mm.

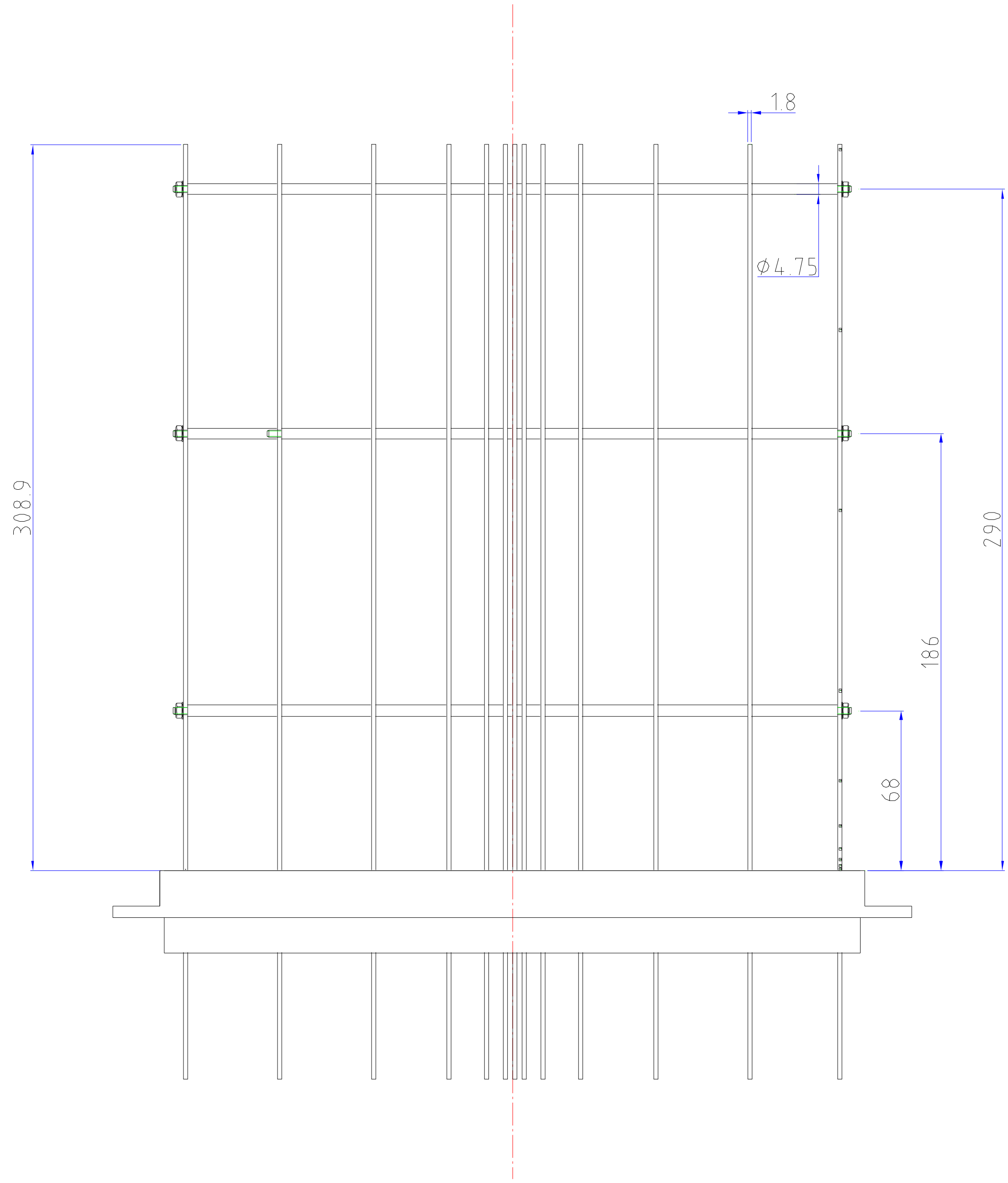

Figure A.3: Front view of the hot-wire rake. All dimensions are in mm.

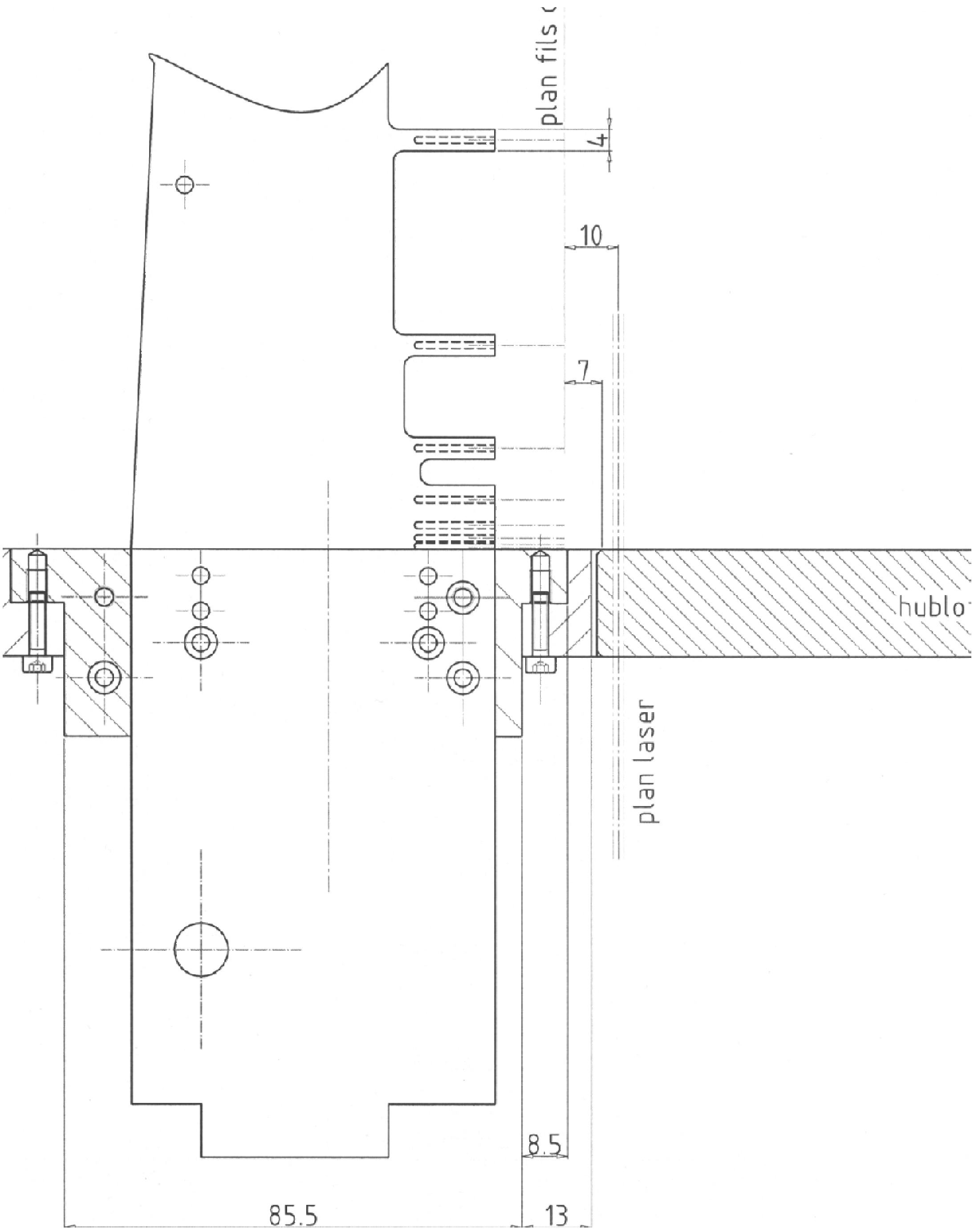

Figure A.4: Attachment of the hot-wire rake to the tunnel wall. All dimensions are in mm.

Appendix B

Two-Point Cross-Correlations by Time-Lag Products

The computation of the two-point cross-correlations presented in this section is performed by directly computing the correlation as given in Eq. (5.2). This method computationally is so expensive and time consuming. As it can be seen from the figures shown in this section, there is essentially no difference between these results and the results computed using the FFT algorithm, as shown in figures 5.1 and 5.2.

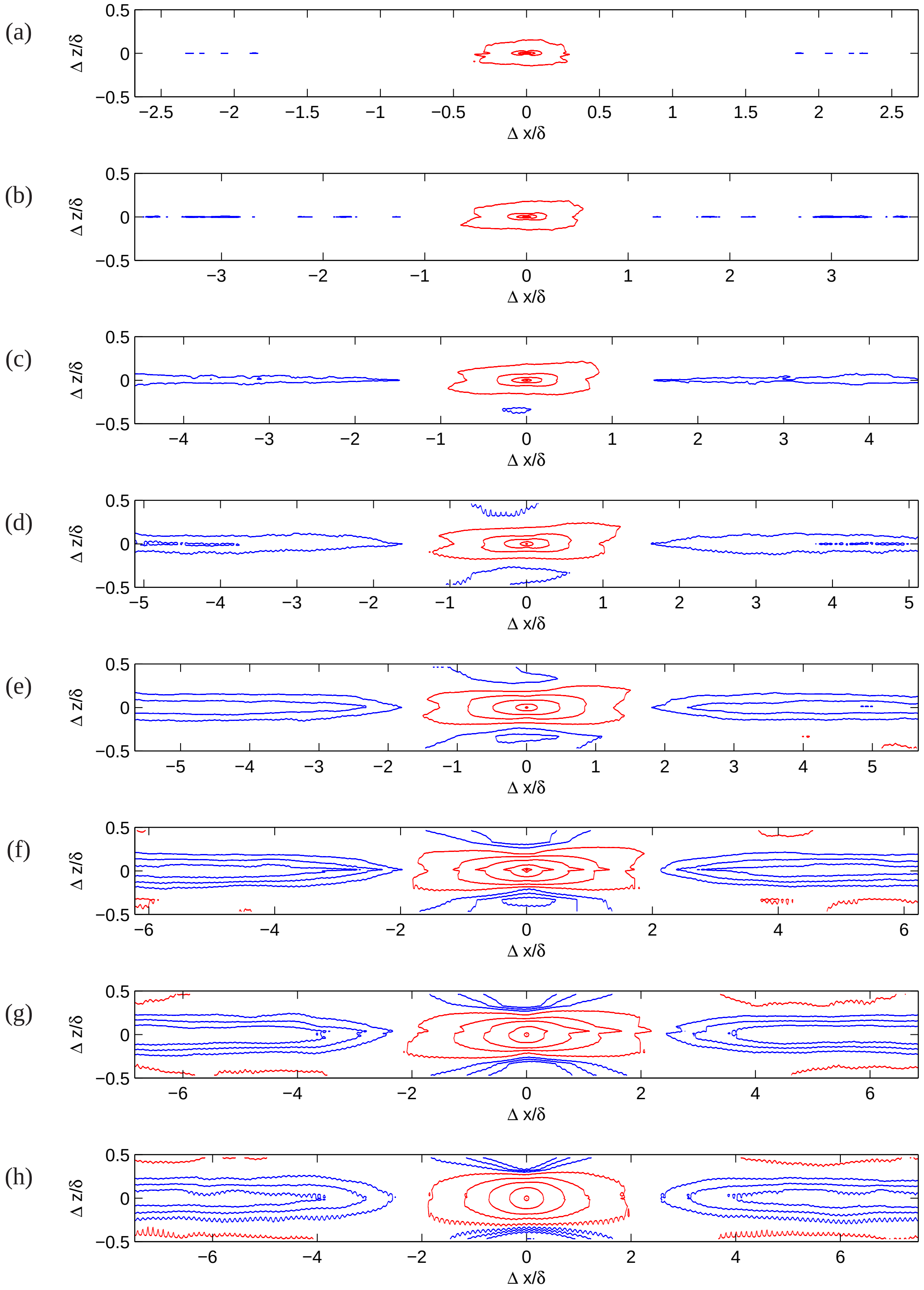

Figure B.1: Two-point cross-correlation coefficients (XZ-plane) at constant wall-normal positions using time-lag products at Re_θ of 19 100. The figures present the correlations between the probe located at z=0 and the probes at the same y^+ location on each plane. (a) $y^+ = 7.5$, (b) $y^+ = 22$, (c) $y^+ = 50$, (d) $y^+ = 100$, (e) $y^+ = 230$, (f) $y^+ = 475$, (g) $y^+ = 950$, (h) $y = 0.2\delta$.

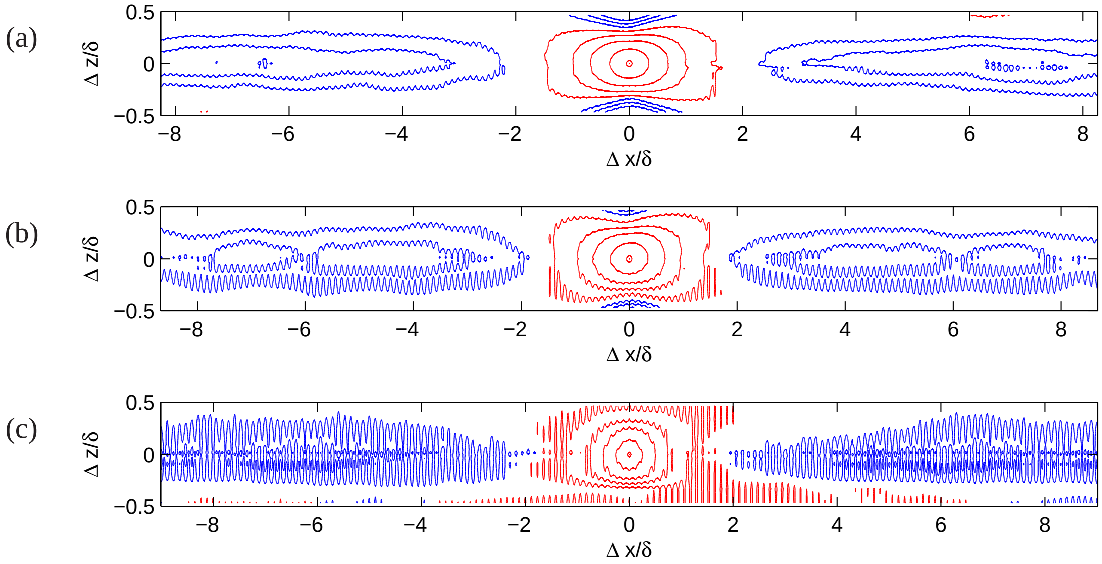

Figure B.2: Two-point cross-correlation coefficients (XZ-plane) at constant wall-normal positions using time-lag products at Re_θ of 19 100. The figures present the correlations between the probe located at z=0 and the probes at the same y^+ location on each plane. (a) y= 0.2δ, (b) y= 0.5δ (c) y= 0.75δ (d) y= δ.

Appendix C

Effect of Seeding Particles

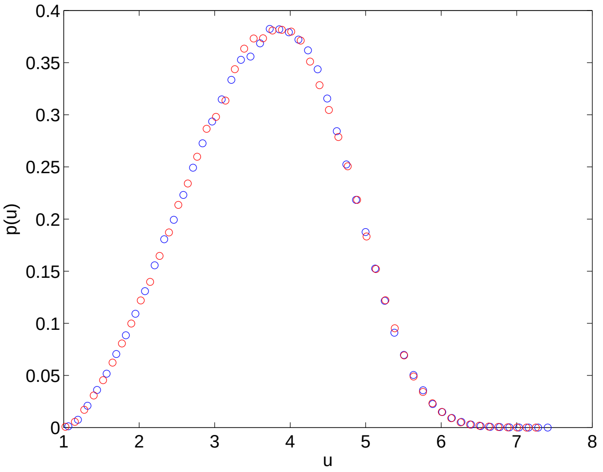

Figure C.1: Probability density function with and without seeding particles. Blue: Without seeding particles, Red: With seeding particles.

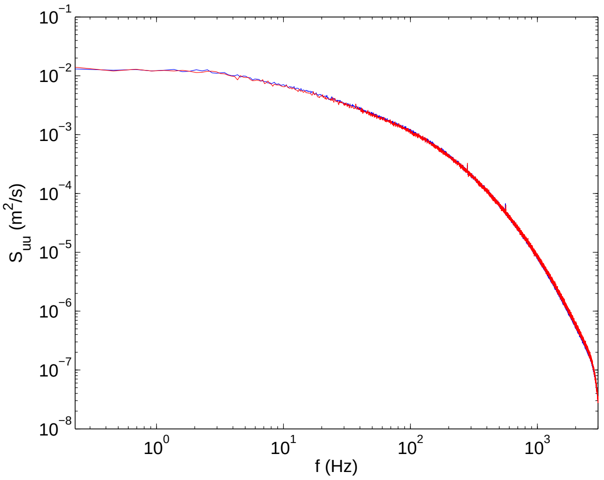

Figure C.2: Frequency spectra with and without seeding particles. Blue: Without seeding particles, Red: With seeding particles.